

THE TRI-WHEEL:

A NOVEL ROBOT LOCOMOTION CONCEPT

MEETING THE NEED FOR INCREASED SPEED

AND CLIMBING CAPABILITY

by

LAUREN M. SMITH

Submitted in partial fulfillment of the requirements
for the degree of Master of Science

Department of Mechanical and Aerospace Engineering
CASE WESTERN RESERVE UNIVERSITY

January, 2015

CASE WESTERN RESERVE UNIVERSITY
SCHOOL OF GRADUATE STUDIES

We hereby approve the thesis of

Lauren M. Smith

Candidate for the degree of Master of Science*.

Committee Chair

Dr. Roger Quinn

Committee Member

Dr. Paul Barnhart

Committee Member

Dr. Joseph Mansour

Date of Defense

December 2, 2014

* We also certify that written approval has been obtained for any proprietary
material contained therein

*To my family,
For instilling in me their
Values of hard work, integrity, and faith
That have shaped me as a person
And carried me through
My graduate studies.*

CONTENTS

CONTENTS	i
LIST OF TABLES	iv
LIST OF FIGURES	v
LIST OF SYMBOLS	ix
ACKNOWLEDGEMENTS	xvi
1 INTRODUCTION	1
1.1 Research Inspiration: First Responders	1
1.2 Existing Locomotion Concepts.....	3
1.2.1 Wheel Locomotion.....	4
1.2.2 Continuous Track Locomotion	5
1.2.3 Wheel-Leg Hybrid Locomotion.....	7
1.2.4 Articulated Leg Locomotion.....	8
1.2.5 Summary of Existing Locomotion Concepts.....	10
1.3 Research Objectives.....	10
1.4 Document Organization	12
2 THE TRI-WHEEL MECHANISM	14
2.1 Introduction to the Tri-Wheel Concept.....	14
2.1.1 Driving Mode.....	15
2.1.2 Tumbling Mode	19
2.2 Tri-Wheel Advantages and Disadvantages.....	23
2.3 Design Strategy.....	26

3 KINEMATIC ANALYSIS	28
3.1 Introduction and Nomenclature	28
3.2 Inching Mode	32
3.3 Tumbling Mode	37
3.4 Stair Climbing Optimization.....	45
4 DESIGN OF GEARING SYSTEM	56
4.1 Introduction.....	56
4.2 Speed and Torque Considerations	61
4.2.1 Motor Selection.....	61
4.2.2 Driving Mode Speed and Gear Ratio.....	64
4.2.3 Tumbling Mode Speed and Gear Ratio	77
4.3 Gearing Spreadsheet Analysis	78
4.3.1 Methodology	78
4.3.2 Nomenclature	81
4.3.3 Sizing Analysis	87
4.3.4 Force Analysis	94
4.3.5 Material Selection and Treatment.....	106
4.3.6 Weight Reduction, Efficiency, Tolerances, and Lubrication.....	113
5 MECHANICAL ASSEMBLY DESIGN	120
5.1 Driving Factors and Design Philosophy	120
5.2 Shaft Design.....	122
5.2.1 Methodology	123
5.2.2 Gear System Free Body Diagrams.....	127
5.2.3 Shaft A	129
5.2.4 Shaft B	134
5.2.5 Shaft C	137
5.2.6 Shaft D2	140
5.2.7 Shaft D1	143
5.3 Power Transmission: Keys	150

5.3.1	Methodology	150
5.4	Bearing Selection	156
5.4.1	General Considerations	156
5.4.2	Plain Bearings	156
5.4.3	Rolling Contact Bearings	160
5.5	Miscellaneous Assembly Components	163
5.5.1	Retaining Rings (Snap Rings)	163
5.5.2	Wheel-Hub Subassembly	164
5.5.3	Shear Pins	166
5.6	Housing Design	167
5.7	Braking Mechanism	175
6	RESULTS	178
6.1	Functional Assembly	178
6.2	Driving Mode	187
6.3	Tumbling Mode	189
7	CONCLUSIONS AND FUTURE WORK	192
7.1	Design Summary	192
7.2	Conclusions	195
7.3	Future Work	197
APPENDIX A: DISCARDED LOCOMOTION CONCEPTS		198
APPENDIX B: TRI-WHEEL DESIGN ITERATIONS		201
APPENDIX C: GEARING SPREADSHEET		208
APPENDIX D: SHEAR AND MOMENT FORMULAS		215
APPENDIX E: MACHINE DRAWINGS		217
APPENDIX F: BILL OF MATERIALS		235
BIBLIOGRAPHY		237

LIST OF TABLES

3.1: RISE AND RUN PARAMETER FOR COMMON STAIRCASES	46
3.2: MAXIMIZE & MINIMIZE CONSIDERATIONS FOR OPTIMIZATION.....	46
3.3: KINEMATICS ANALYSIS DERIVED REQUIREMENTS	49
3.4: SIZING OPTIMIZATION DATA 1	50
3.5: SIZING OPTIMIZATION DATA 2	51
3.6: SIZING OPTIMIZATION DATA 3	51
3.7: KINEMATICS ANALYSIS DERIVED REQUIREMENTS V. CAPABILITY COMPLIANCE	53
4.1: MOTOR PERFORMANCE OPERATING POINTS	63
4.2: FUNDAMENTAL GEARING OPTIMIZATION CONSIDERATIONS.....	79
4.3: DRIVING GEAR SET SIZING INPUT AND OUTPUT PARAMETERS	87
4.4: TUMBLING GEAR SET SIZING INPUT AND OUTPUT PARAMETERS	88
4.5: DRIVING GEAR SET FORCE INPUT AND OUTPUT PARAMETERS	95
4.6: TUMBLING GEAR SET FORCE INPUT AND OUTPUT PARAMETERS	96
4.7: GEAR SIZING AND FORCE ANALYSIS DERIVED REQUIREMENTS.....	104
4.8: GEARING REQUIREMENTS V. CAPABILITY COMPLIANCE.....	105
4.9: RIM THICKNESS SIZING PARAMETERS.....	116
5.1: DEPTH OF KEYSEATS AND KEYWAYS.....	153
5.2: CLASS 2 - FIT FOR PARALLEL AND TAPER KEYS [37]	153
5.3: PV FACTOR DATA FOR SHAFTS C, D1, AND D2.....	159
7.1: CRITICAL DESIGN CHARACTERISTICS	195
7.2: FINAL REQUIREMENTS V. CAPABILITY COMPLIANCE.....	196

LIST OF FIGURES

1.1: MARSHA 1.5 ROBOT & MARSHA 2 ROBOT (INCLUDES A ROBOTIC ARM) [1].....	3
2.1: TRI-WHEEL DESIGN ON A BASIC ROBOT PLATFORM.....	14
2.2: DRIVING MODE	16
2.3: ABSORBING OBSTACLES IN PASSIVE TUMBLING MODE	17
2.4: DRIVING MODE GEARING CONFIGURATION	18
2.5: ACTUATED TUMBLING MODE	20
2.6: TUMBLING MODE GEARING CONFIGURATION.....	21
2.7: TRI-WHEEL PARALLEL GEAR SETS	22
2.8: TRI-WHEEL DESIGN STRATEGY	27
3.1: SPOKE LENGTH AND WHEEL RADIUS ON TRI-WHEEL	28
3.2: TRI-WHEEL KINEMATIC ANALYSIS NOMENCLATURE	29
3.3: FULL ROTATION IN INCHING MODE	35
3.4: INCHING MODE TRAJECTORY PLOT.....	36
3.5: TUMBLING MODE TRAJECTORY PLOT	45
3.6: INITIAL TRI-WHEEL PLACEMENT ON MAXIMUM STEP HEIGHT	47
3.7: TRAJECTORY PLOT FOR SELECTED SIZING – SINGLE TURN	53
3.8: TRAJECTORY PLOT FOR SELECTED SIZING - THREE TURNS	54
3.9: TUMBLING MODE SUBPLOTS FOR SELECTED PARAMETERS	55
4.1: SPUR GEAR TRAIN EXAMPLE	57
4.2: SELECTED GEARING CONFIGURATION	59
4.3: BLY 344D-48V-3200 MOTOR TORQUE CURVE [21]	62
4.4: FREE BODY DIAGRAM OF TRI-WHEEL ROBOT PLATFORM ON FLAT SURFACE	66
4.5: INDIVIDUAL GROUND WHEEL FREE BODY DIAGRAM	69
4.6: TORUS MOMENT OF INERTIA NOMENCLATURE [26].....	73

4.7: SPREADSHEET ANALYSIS GEARING CONFIGURATION	80
4.8: GEAR TEETH NOMENCLATURE [19]	82
4.9: DIAMETRAL PITCH SIZES [20].....	83
4.10: PRESSURE ANGLE DIAGRAM [19].....	85
4.11: VARYING PRESSURE ANGLES AFFECTING TOOTH SHAPE [19]	86
4.12: REVERTED GEAR TRAIN FOR TUMBLING.....	93
4.13: RIM THICKNESS FACTOR [19]	100
4.14: BENDING STRENGTH GEOMETRY FACTOR J FOR 20° SPUR GEAR STANDARD ADDENDUM [19].....	101
4.15: PITTING RESISTANCE GEOMETRY FACTOR I FOR 20° SPUR GEAR STANDARD ADDENDUM [19]	103
4.16: ALLOWABLE CONTACT STRESS NUMBER FOR STEEL GEARS [19].....	107
4.17: ALLOWABLE BENDING STRESS NUMBER FOR STEEL GEARS [19].....	108
4.18: AVERAGE S-N CURVES FOR CONTACT STRESSES [20]	110
4.19: ARMS, WEBBING, AND CORE HOLES ON GEARS, RESPECTIVELY	114
4.20: CROSS-SECTION OF WEBBED GEAR	115
5.1: CROSS-SECTIONAL VIEW WITH SHAFT NOMENCLATURE	124
5.2: SINGLE GEAR BRANCH FREE BODY DIAGRAM FRONT VIEW	128
5.3: SHAFT A CROSS SECTION AND ISOMETRIC.....	130
5.4: REACTION FORCES ON D1 IN DRIVING MODE	130
5.5: SHAFT A DRIVING MODE FREE BODY DIAGRAM	131
5.6: SHAFT A SHEAR AND MOMENT DIAGRAMS	132
5.7: STRESS DISTRIBUTION IN HOLLOW SHAFT [19].....	134
5.8: SHAFT C CROSS-SECTION AND ISOMETRIC	137
5.9: SHAFT C FREE BODY DIAGRAM	138
5.10: SHAFT C SHEAR AND MOMENT DIAGRAMS.....	139
5.11: SHAFT D2 CROSS-SECTION AND ISOMETRIC	141
5.12: SHAFT D2 FREE BODY DIAGRAM.....	141
5.13: SHAFT D2 SHEAR AND MOMENT DIAGRAM	142
5.14: SHAFT D1 CROSS-SECTION AND ISOMETRIC	144

5.15: SHAFT D1 FREE BODY DIAGRAM-MAXIMUM SHEAR.....	145
5.16: SHAFT D1 SHEAR AND MOMENT DIAGRAMS-MAXIMUM SHEAR	146
5.17: SHAFT D1 SHEAR AND MOMENT DIAGRAM-MAXIMUM MOMENT	148
5.18: SHAFT D1 SHEAR AND BENDING DIAGRAMS-MAXIMUM MOMENT	149
5.19: KEY SIZE v. SHAFT DIAMETER [37]	151
5.20: DIMENSIONS FOR PARALLEL KEYSEATS AND KEYWAYS [19]	152
5.21: FORCES ON A PARALLEL KEY [19]	154
5.22: FLANGED SLEEVE BEARING [38].....	157
5.23: FLANGED BALL BEARING AND NEEDLE BEARING [38]	161
5.24: LIFE AND SPEED FACTORS FOR BALL AND ROLLER BEARINGS [19]	162
5.25: EXTERNAL RETAINING RING [39]	164
5.26: WHEEL-HUB SUBASSEMBLY	165
5.27: ALIGNMENT DOWEL PIN [40].....	166
5.28: HOUSING DESIGN 1	168
5.29: HOUSING DESIGN 2	170
5.30: HOUSING DESIGN 3	172
5.31: FINAL HOUSING DESIGN CENTER CARRIER STRUCTURE.....	173
5.32: FINAL HOUSING DESIGN DRIVING CARRIER PLATE	174
5.33: FINAL HOUSING DESIGN TUMBLING CARRIER PLATE	174
5.34: FINAL HOUSING DESIGN ASSEMBLY	175
5.35: INTERNALS OF SELECTED TRI-WHEEL BRAKING MECHANISM.....	177
6.1: COMPLETED TRI-WHEEL.....	178
6.2: BEGINNING OF ASSEMBLY PROCESS	179
6.3: PRESSED-IN BEARINGS	180
6.4: DEPTH MEASUREMENT WITH MICROMETER.....	181
6.5: CLEARANCE MEASUREMENT WITH DIAL INDICATOR	182
6.6: LUBRICATED DRIVING GEARS.....	183
6.7: LUBRICATED TUMBLING GEARS	184

6.8: INITIAL TESTING OF FIRST TRI-WHEEL	185
6.9: RUN-IN OF GEARS IN BOTH TRI-WHEELS.....	185
6.10: VEHICLE WEIGHING.....	186
6.11: DRIVING MODE TIME LAPSE.....	187
6.12: DRIVING MODE	188
6.13: BRAKE CONFIGURATION	190
6.14: TUMBLING MODE.....	191
6.15: TUMBLING MODE ASCENDING STEPS - 7" RISE, 11" RUN	191
7.1: EXPLODED VIEW OF COMPLETE TRI-WHEEL ASSEMBLY	192
7.2: PROCESS DIAGRAM FOR TRI-WHEEL DESIGN.....	193
A.1: VERSION 1.0 GEARING CONFIGURATION.....	201
A.2: PROTOTYPED TRI-WHEEL 1.0.....	202
A.3: TRI-WHEEL 2.0 AND CORRESPONDING GEARING CONFIGURATION.....	203
A.4: TRI-WHEEL 3.0	205
A.5: TRI-WHEEL 3.0 DRIVING MODE AND TUMBLING MODE, RESPECTIVELY	206

LIST OF SYMBOLS

a	Radius of torus cross-section Addendum
a_{max}	Maximum permissible noninterfering addendum
a_y	Vertical acceleration
b	Side length of equilateral triangle, distance between wheel centroids Dedendum
c	Spoke length, distance between Tri-Wheel centroid and wheel center Center distance between gears
\vec{c}	Initial centroid vector with respect to leading ground wheel
\vec{c}'	Transformed centroid vector with respect to leading ground wheel
c_θ	Cosine of the angle theta
C	Point representing Tri-Wheel centroid
C_G	Gradient factor
C_L	Load factor
C_P	Elastic coefficient
C_{rr}	Coefficient of rolling resistance
C_R	Reliability Factor
C_S	Surface finish factor Size factor
CR	Contact ratio
d	Distance between point O and approaching step Diameter of the individual wheel Pitch diameter of gear Inner diameter of hollow shaft
d_b	Dedendum circle diameter
d_o	Outside gear diameter

d_{RIM}	diameter within which cutouts are acceptable to preserve structural integrity
d_t	Distance between O and approaching step at which Tumbling Mode engages
D	Shaft diameter
	Internal diameter of bearing
E	Modulus of elasticity
F	Face width
	Total resultant load acting on bearing
F_R	Radial component of force between mating teeth
F_T	Tangential component of force between mating teeth
F_y	Vertical force
g	Gravitational acceleration
g_{ab}	Rigid body transformation specifying position and orientation of Tri-Wheel
GR_M	Motor gearbox gear ratio
GR_{TOT}	Total gear ratio desired to tumble
F_f	Traction force resulting from rolling and friction
h	Stair approach height of the Tri-Wheel during tumbling mode
h_{max}	Maximum stair approach height of the Tri-Wheel during tumbling mode
h_t	Whole depth of gear tooth
H	Key height
I	Identity matrix
	Geometry factor for pitting resistance
I_{DISK}	Moment of inertia of a solid disk
I_{TOR}	Moment of inertia of hollow torus
I_W	Moment of inertia of the wheel system
J	Geometry factor for bending strength
k_{ms}	Mean stress factor
k_r	Reliability factor
k_t	Temperature factor
K_B	Rim thickness factor
K_O	Overload factor

K_v	Dynamic factor
K_s	Size factor
K_m	Load distribution factor
K_t	Stress concentration factor
K_T	Rim thickness factor
\vec{l}_1	Initial top wheel vector with respect to leading ground wheel
\vec{l}'_1	Transformed top wheel vector with respect to leading ground wheel
\vec{l}_2	Initial trailing ground wheel vector with respect to leading ground wheel
\vec{l}'_2	Transformed trailing ground wheel vector with respect to leading ground wheel
L	Lagrangian function
	Key length
m_B	Backup ratio
m_c	Mass of the robot chassis
m_s	Mass of the Tri-Wheel-robot system
m_T	Mass of one full Tri-Wheel assembly
m_{TOT}	Total robot mass, including Tri-Wheels, controls, etc.
M	Bending moment
n	rotational speed in RPM
N	Number of teeth per gear
	Normal force
	Safety factor
O	Point representing centroid of leading ground wheel
p	Circular pitch
	Load capacity
p_{ab}	Position vector in g_{ab} transformation
p_b	Base pitch
P	Diametral pitch
	Power transmitted by gear
q	Generalized coordinate variable
Q'_i	Generalized forces not derivable from a potential function

Q'_{TOT}	Total generalized forces not derivable from a potential function
r	Individual wheel radius
$r_{a_{max}}$	Maximum noninterfering addendum circle radius
r_b	Base circle radius
R	Gear pitch radius
	Radius of torus
R_{ab}	Rotation matrix in g_{ab} transformation
\mathbb{R}^3	3-dimension Euclidian space
\mathbb{R}^4	4-dimension Euclidian space
RPM_M	Input speed of motor without attached gearbox
RPM_{GM}	Gear-motor input speed
s	Horizontal distance traveled by point O during tumbling mode
\hat{s}	Vector representing horizontal distance traveled by leading ground wheel
Δs	Displacement of leading ground wheel between two points
s_{ac}	Allowable contact stress number
s_{at}	Allowable bending stress number
s_c	Contact stress number
$s_{h_{max}}$	Horizontal distance traversed to arrive at maximum height
s_t	Bending stress number
s_y	Yield strength
s_θ	Sine of the angle theta
S	Depth of shaft keyseat
S_h	Surface fatigue strength estimation
S_n	Fatigue strength
S_n'	Standard R.R. Moore endurance limit
S_u	Ultimate tensile strength
t	Tooth thickness
t_R	Rim thickness
T	Total kinetic energy
	Depth of hub keyway

	Torque transmitted through gear by key
v	Maximum horizontal speed of an individual wheel
v_{max}	Maximum computed linear driving speed
V	Potential energy
	Gear pitch line velocity
	Shear stress
	Relative speed between the moving and stationary components
VR	Velocity ratio/gear ratio
v_θ	$1 - \cos \theta$
\dot{W}_{GM}	Transmitted power from gearmotor
x	Generalized coordinate for Lagrangian analysis
Δx	Horizontal displacement
\dot{x}	Linear velocity
\ddot{x}	Linear acceleration
x_h	Horizontal position at which a particular value of h occurs
x_0	Initial horizontal position of leading ground wheel
x_{run}	Horizontal distance measuring run of step
y_{rise}	Vertical distance measuring rise of step
Z_p	Polar section modulus

GREEK

α	Angle measuring amount of rotation during Tumbling Mode
β	Angle measuring amount of rotation during Tumbling Mode
γ	Angle of inclination
$\delta\theta$	Virtual angular displacement
δW	Virtual work
δx	Virtual horizontal displacement
η_M	Motor planetary gearbox efficiency
θ	Angle between equilateral triangle base and Tri-wheel spoke
	Angle through which rolling wheel rotates

μ_s	Coefficient of static friction
μ	Poisson's ratio
σ_d	Design stress for compression
τ_d	Design shear stress
τ_{GM}	Total motor + gearbox output torque
τ_{max}	Maximum applied torque
τ_M	Applied motor torque
τ_s	Motor stall torque
	Torque developed in a shaft
τ_T	Torque required to tumble
φ	Pressure angle
ω	Unit vector representing axis of rotation during Tumbling Mode
	Angular velocity of gear
$\hat{\omega}$	Skew-symmetric matrix representation of ω
ω_{max}	Motor free speed
ω_W	Angular velocity of each driving wheel
ω_x	x-component of unit vector
ω_y	y-component of unit vector
ω_z	z-component of unit vector

SUBSCRIPTS

$\alpha=120^\circ$	Occurring when the Tri-Wheel has completed a full 120° rotation
c_{max}	Occurring at the maximum vertical displacement of the centroid
D	Driving gear train
h_{max}	Occurring at the maximum step approach height
$h=5$	Occurring when step approach height is equal to 5 in
$h=8_{LHS}$	Occurring when step approach height is 8 in on left-hand-side of trajectory
$h=8_{RHS}$	Occurring when step approach height is 8 in on right-hand-side of trajectory
i	References inner (air) torus
$i-j$	References two gear numbers

- o* References outer (solid rubber) torus
- T* Tumbling gear train
- 1* References the input gear
- 2* References the output gear
- 1...4* References gears numbered 1 through 4, inclusively

ACKNOWLEDGEMENTS

This research is a result of not only my efforts but of the contributions of friends, family, and mentors who have helped me learn and grow exceedingly more than expected as an individual and as an engineer throughout this entire process. I have thoroughly enjoyed my time at Case Western and would like to thank the members of my panel for their advice and guidance in my time here as a student. I also extend my sincerest gratitude to the Ohio Space Grant Consortium, NASA Glenn Research Center, and the Department of Mechanical and Aerospace Engineering at Case Western for funding me and this project.

I have been fortunate to have outstanding mentorship at NASA Glenn. I would like to thank Mike Krasowski and Larry Greer for allowing me to further their hopes for the Tri-Wheel concept and for their continued encouragement throughout the victories and struggles encountered along the way. I would also like to thank Kyle Johnson, Colin Creager, Phil Abel, Steve Bauman, and Dave Lewicki for their contributions and constructive feedback in many design reviews. Lastly, I must heartily thank Roger Tuck for his willingness to share his time and his years of experience with me; were it not for his expertise, I would not know what I now know about assembling a gearbox. His help has been indispensable in bringing the Tri-Wheel to life.

Finally, I must acknowledge my mother Lori Smith, my father Warren Smith, and my brother Justin Smith for their continued love and support without which I would not be where I am today. I can never fully thank my parents for the sacrifices they have made

or for how arduously they have worked to provide for me. They inspire me to work harder and not give up. I am truly blessed to have friends and family beyond those already named who make me smile even after the longest days of report writing.

The Tri-Wheel: A Novel Robot Locomotion Concept Meeting the Need for Increased
Speed and Climbing Capability

Abstract

by

LAUREN M. SMITH

A need has been expressed for a robot locomotion concept that incorporates both efficient, rapid motion on smooth surfaces as well as the capacity to traverse a variety of challenging terrain obstacles, including but not limited to: stairs, rubble, and other environmental impediments. Currently, this dual capability has not been optimized successfully for existing locomotion concepts. This research seeks to meet this need with a novel mobility concept called the Tri-Wheel and chronicles its theoretical conception, design, and preliminary testing. An in-depth discussion of the design process and determination of derived requirements is first presented to substantiate the final configuration. The Tri-Wheel is then manufactured and installed on an existing robot chassis for testing, ultimately proving the concept successful by meeting the stated research objectives.

1 INTRODUCTION

1.1 Research Inspiration: First Responders

The need to improve robot locomotion was initially brought to the attention of NASA Glenn Research Center by members of Cleveland Fire Department and the New York City Fire Department. The method of fighting fires is more complex than movies and popular culture relay, and new advances in technology hope to make it safer. In many cities, abandoned buildings and warehouses that line the streets can be particularly dangerous for firefighters. These buildings are often past homes to chemical plants and other industries that leave behind flammable, toxic, or explosive materials that have sat unattended for years. The consequences of entering such a hazardous environment without all the information necessary can be fatal.

Traditionally, humans have been required to enter these treacherous premises carrying sensors to gain information about the contents of these buildings and the potentially harmful chemical traces in the air. The knowledge of who, or what, is in a burning building is essential to the safety of firefighters and civilians alike. Through the use of a robot equipped with a very robust locomotion system, unmanned ground systems can be tasked with bringing in HazMat sensors, relieving firefighters from the risky assignment. Furthermore, the additions of voice communication devices and cameras hold great promise to help firefighters locate people who may be trapped and even allow them to communicate with rescuers.

These first responders have reached out to the Optical Instrumentation and NDE Branch at NASA Glenn Research Center and expressed a need for a simple, robust ground traction drive mechanism for remotely controlled vehicles that can operate quickly on level ground, as wheels would, but also effectively and reliably slog through inclement environments (such as mud, snow, sand, gravel, and miscellaneous debris), climb stairs and grades, and power over railroad ballast.

The NDE Branch produced initial prototype robots named MARSHA (Mobile and Remote Sensing Hazmat Activity). MARSHA 1.5 (without robotic arm) and MARSHA 2 (with robotic arm) are shown in Figure 1.1. Equipped with a continuous track system, each version of MARSHA has ultimately proven ineffective in testing because the robot could not climb stairs and moved too slowly in time-sensitive situations. Despite the effectiveness of sensors included in the platform, MARSHA conclusively was not robust enough in its locomotion capability to transport those sensors to their desired locations. As noted by one Department of Homeland Security Bomb Assessment Officer, “The compromise with robots is that they take too long to drive to the scene.” There is an innate tradeoff in the use of electric motors between speed and torque, yet both quantities are needed in excess for various phases of a mission. This in itself is a unique design challenge to be solved.

In hopes of engineering a locomotion solution to overcome obstacles and travel at higher speeds, a partnership is forged with the Simulated Lunar Operations Laboratory (SLOPE Lab) at NASA Glenn Research Center and Case Western Reserve University. The SLOPE Lab is experienced in alternate forms of mobility and maintains its own interest in improving robotic exploration capabilities. In addition to first responder

reconnaissance, such a locomotion alternative holds great promise in the fields of explosive ordinance disposal, various military applications, chemical or radiological crises, and perhaps even extraterrestrial exploration.



Figure 1.1: MARSHA 1.5 Robot & MARSHA 2 Robot (Includes a Robotic Arm) [1]

1.2 Existing Locomotion Concepts

Before initiating the design of a new locomotion platform, it is essential to establish a true cause for this research by examining the four most relevant locomotion systems currently in use: wheels, continuous tracks, Whegs, and articulated robotic legs. This preliminary research is critical in helping to identify both the advantages and disadvantages of each mobility system so that these observations can be addressed in the investigation and design of a new locomotion concept.

1.2.1 Wheel Locomotion

Wheels are arguably the most common locomotion platform used in mobile robotics, presenting a number of distinct benefits. The wheel is easy to implement mechanically, and unlike some platforms, there is no need to develop a mechanism for balance control as long as the vehicle has at least three wheels [2]. In addition, wheeled locomotion is relatively power efficient, even when traveling at high speeds [3]. Wheeled systems are also smooth over even terrain. For these reasons, many robots continue to be designed with wheels, such as Northrop Grumman's Mobile Armed Dismount Support System (MADSS) vehicle [4]. Yet traction, stability in rough terrain, and maneuverability prove difficult for wheeled robotic systems—three characteristics that are particularly important for critical robot applications in rugged and unpredictable environments.

Front or rear wheel steer robots are often unable to traverse sideways along additional directions without enacting several parking maneuvers consisting of repeated changes in wheel direction and forward and backward movement. This process requires additional time and clear operator visibility of the robot, which are certainly not guaranteed factors when operations are occurring in non-ideal environments. In the case of a firefighter utilizing an unmanned ground system, for instance, it is probable that the robot will be completely obscured by smoke once it enters a burning building.

Wheeled systems are also only sufficient to move over depressions and obstacles which are less than or equal to the radius of the wheel, which is most detrimental to the application of climbing stairs. This limits the robot's motion in that it cannot climb obstacles encountered in the field if these obstructions exceed its wheel radius [5]. In order to effectively ascend steps, large wheels would be required.

On loose ground or in snow, the wheels must also provide sufficient surface area to prevent sinking and must be fitted with treads of sufficient texture to maintain traction. Despite their optimal performance on flat ground, it has been shown in testing that wheels do not perform well when faced with hindrances such as stairs and rubble. Some of the problems associated with wheel locomotion can be overcome in part through the use of an articulated robot body or through the use of a bogie system. However, this involves a more complex design that may not be as robust or cost-effective as desired for certain applications such as first responder reconnaissance.

1.2.2 Continuous Track Locomotion

Continuous track systems are implemented on a variety of existing robot and vehicle platforms, particularly those designed for military purposes such as tanks. The system utilizes a continuous band of treads, typically driven by two or more wheels. The band is often made of either steel plates in the case of some military/construction vehicles, or rubber reinforced with steel wires in the case of lighter vehicles. The main advantage of continuous track locomotion derives from increased surface area in contact with the ground, which effectively distributes the weight of the vehicle. This characteristic causes continuous track vehicles to perform favorably in traversing soft surfaces without sinking, which is why they are so successful in desert environments.

Despite this benefit, track assemblies are complex, and operators often face maintenance issues such as tracks being dislodged or thrown during normal operation [3]. While the impact of such a problem may be minimal in some environments, it can result in mission failure in others. Explosive ordinance disposal, extraterrestrial exploration,

and the other previously mentioned applications provide minimal opportunity for serviceability, meaning that the locomotion system selected should be as robust and redundant as possible. Additionally, continuous track locomotion often results in lower speed operation when used on smaller robots, though these platforms do tend to handle small holes and ditches effectively [3].

Tracked vehicles are capable of changing direction through skidding—the process of sliding tracks against the ground and rotating to change the orientation of the chassis. However, when the ground is firm, the vehicle cannot easily slide against it, increasing the friction during steering and consequently the power consumption of the vehicle [2]. Depending on the friction between the tracks and the ground, the skidding motion can also be quite inaccurate if the operator is trying to achieve a particular orientation. This inaccuracy is undesirable for critical applications.

Climbing obstacles is also quite difficult to accomplish successfully with continuous track systems. Climbing requires a track leading end radius greater than tread height (similar to the wheel), or requires separate mechanisms such as articulated secondary track assemblies. Many of the unmanned ground systems at Northrop Grumman's Remotec utilize conventional or articulated tracks. Andros F6, for instance, uses a patented articulated track to traverse rough terrain [6]. Utilizing articulated tracks has proven effective in practice to climb some obstacles, but ultimately this climbing process is slow and not necessarily optimized to climb obstacles in unpredictable, uneven terrain. To overcome a given obstruction, the surface of the landing preceding the obstruction must afford sufficient traction to even initiate climbing. Wet or otherwise slippery landing surfaces also thwart attempts to climb.

1.2.3 Wheel-Leg Hybrid Locomotion

There are numerous wheel-leg hybrid locomotion platforms that have already been explored in the last 15 years. The first instance to note is RHex—a power autonomous, compliant-legged hexapod robot designed to travel at up to one body length per second [7]. The concept has evolved into a variant of this original design known as the RHex Quattroped Wheel Transformer. This wheel-leg hybrid robot uses a transformable wheel to combine advantages of circular and legged wheels via a passive transformation [8].

Whegs robots use a hybrid wheel-leg locomotion mechanism that rolls like a wheel, but has curved, protruding spokes that allow for climbing over obstacles. One motor drives all of the wheel-legs. Torsional spring-clutches in their axles allow the wheel-legs to move in response to terrain irregularities [9]. Whegs were developed by Dr. Roger Quinn and the Center for Biologically Inspired Robotics at Case Western Reserve University in order to autonomously navigate uneven terrain. The advantage of this system is that it approximates legged locomotion with a one-motor drive system because its mechanical system allows the wheel-legs to passively adapt to the terrain [9].

While Whegs are effective at climbing over some objects and traversing irregular terrain, Whegs do not move as smoothly over flat, even terrain. This creates an advancing motion that sometimes shakes and rattles sensors and other electrical equipment as the robot bounces along. This jerky operation further stresses payloads and also disrupts video, negatively impacting navigation and surveillance.

As is the case for any locomotion platform, Whegs are dependent upon friction with the ground to advance the robot platform forward. However, the torsional element

of the Wheg is not always robust enough to push through extremely inclement conditions.

Other systems are available that include legs with wheels on the ends in addition to wheeled systems that rotate to attempt climbing. The RIMRES hybrid wheel-leg rover Sherpa combines both a wheeled system and legged system into a single concept via an electro-mechanical interface. Both systems can be actuated independently to take advantage of their respective locomotion advantages [10]. Another unique concept is the Lockheed TerraStar Marginal-Terrain Amphibian [11]. This vehicle utilizes novel major and minor wheel about a single axle that passively tumble around obstacles. However, this particular vehicle is also scaled to be driven by humans rather than controlled remotely as a small robot.

1.2.4 Articulated Leg Locomotion

Articulated robotic legs are the most complex and impressive case of existing mobility technology. Legs are the most effective method to climb over obstacles, and articulated robotic legs offer the highest degree of similarity to human walking. However, the motion of these robots can be slow and short in duration and typically involve a complex, expensive, and cumbersome actuator system [3]. At times, the many degrees of freedom present in articulated legs can be more of an engineering problem than a solution, creating additional controls and balance issues. The number of legs can vary from one to six typically, but in each case, the issue of dynamic stability must be solved even if the configuration (such as four legs) is statically stable [2].

Locomotion via conventional robot legs is also the least efficient means of motion over flat surfaces. While human beings are able to absorb positive and negative obstacles with relative ease, many will attest that there is significant effort that must be exerted to run quickly on flat surfaces when compared to the ease of wheeled motion on level ground. Efficient legged locomotion further requires an even more complex system of springy elements in the actuation system.

NASA's All-Terrain Hex-Limbed Extra-Terrestrial Explorer (ATHLETE) vehicle concept is based on six wheels at the ends of six multi-degree-of-freedom limbs or articulated legs [12]. While each limb has enough degrees of freedom for use as a general purpose leg, the robot has yet to reach a technical level where it can walk effectively. In some applications, the benefits may outweigh the additional engineering challenges presented by articulated leg locomotion. However, if a more simplified locomotion concept is conceivable and performs at a comparable level, it would be desirable for the qualities of robustness, cost efficiency, and overall decreased complexity. Though an intricate system such as that designed for NASA's ATHLETE Rover is not appropriate for this application, the concept to combine two existing locomotion concepts is certainly something to consider.

The ASTERISK robot is a smaller-scale example of an articulated leg robot platform, presenting a unique rolling-walk motion for a multi-legged robot inspired by bipedal robots. The robot is able to switch between two phases in order to achieve its desired motion. The ASTERISK has a six-legged radial arrangement to attempt rotational walking motion.

1.2.5 Summary of Existing Locomotion Concepts

No single application of these four platforms has solved the stated problems associated with remote vehicle navigation. While it is unlikely that any concept could be optimal in every aspect, the intent of this research is to design a locomotion platform optimized to function suitably for the critical operations discussed. In investigating potential solutions to the issues of low speed and obstacle climbing, due consideration will be given to the advantages and disadvantages of the wheel, continuous track, wheel-leg and articulated robotic leg concepts. At the same time, this proposed research seeks to absorb some of the positive attributes of these four conventional systems and incorporate them in the design of a new locomotion platform when possible.

1.3 Research Objectives

The purpose of this project is to develop and assess the viability of a locomotion concept that can be implemented on an existing robot platform to increase overall mobility. The design will also be robust enough to ensure reliability in the midst of vital operations. This new technology enables a robot to move quickly and efficiently over flat terrain but also overcome obstacles and maneuver through rugged conditions when necessary.

This capability is currently missing in robots carrying out critical missions as previously noted including but not limited to first responder reconnaissance, explosive ordnance disposal, military tasks, and extraterrestrial exploration. Using current mobility mechanisms, robots that can move over irregular terrain are typically too slow to perform time-sensitive tasks, yet robots that can move rapidly become immobilized in rough environments. Testing and field experience reveal that no single application of the four

stated locomotion systems solves the problems associated with natural and man-made impediments to remote vehicle navigation. As a result, this new mechanism attempts to move toward a more general solution. However, the concept of a ‘quick’ robot must be better defined. After speaking with first responders, it is evident that the ideal robot will not always be required to speed past them into the distance; frequently, what matters is whether the robot can traverse at the typical walking pace of approximately 2.95 – 3.31 MPH to keep up with them [13]. This is the minimum linear speed that should be achieved.

Particularly with respect to first responder reconnaissance, it is important to keep the locomotion system cost effective. Frequently, large sums of money are spent developing complex robotic systems that are ultimately too expensive to send into environments that will likely cause significant damage to the system. For this reason, the resulting mechanism should be designed with consideration of the final cost with respect to existing locomotion platforms currently available.

This innovation, when applied to robots for use by first responders (and others) provides a ground traction mechanism which moves in the direction of optimizing a single vehicle for the objectives of:

- 1.** Smooth and quick operation on level ground (with a linear speed of at least 3.3 MPH).
- 2.** The ability to navigate rough terrain, including obstacles such as rocks or stairs of common sizes in addition to loose terrains such as sand and mud.
- 3.** A robust design that will not fail mechanically during normal operations.

- 4.** Full mission capability that includes quick motion to a site of interest as well as the ability to actuate with more torque when necessary to overcome a range of obstacles and terrain characteristics—not being designed for one mode over the other.
- 5.** The ability to be implemented on a previously constructed robotic platform as a hardware upgrade.
- 6.** Initial sizing such that it is suitable for a robot of no greater than 150 – 200 lbs.
- 7.** Potential for implementation of a system to switch between objectives 1 and 2 above either passively, through user command, and/or autonomously.

The result is a mechanism which can be used to drive a vehicle of any conceivable size through a wide range of terrain features and characteristics through modifications to material selection. In other words, for a heavier chassis, more sturdy metals can be utilized whereas a smaller robot body can allow for lighter material choices, though the sizing will be kept the same to preserve the analysis. The most important objective is to develop new technology that allows first responders to perform their jobs in a more safe and efficient manner while keeping them out of dangerous environments when possible.

1.4 Document Organization

Chapter 1 is largely intended to orient the reader to the current need for a new locomotion platform and provide context for applications that could benefit from its development. In addition, this introductory chapter characterizes existing locomotion platforms and their potential influences on a new design. In Chapter 2, the selected design named the Tri-

Wheel is discussed at a high level, identifying its general modes of operation, advantages, and disadvantages. The overall design strategy followed will also be laid out, and the framework through which derived requirements are arrived at will be explained.

Chapters 3, 4, and 5 delve further into the technical design of the Tri-Wheel mechanism. Chapter 3 begins with the kinematic analysis required to constrain the basic size of the Tri-Wheel mechanism such that it successfully climbs stairs and performs the desired tasks. Chapter 4 contains the gearing analysis performed in order to ensure that the Tri-Wheel mechanism functions with the desired speed and torque. Chapter 5 takes all of this analysis and compiles it into a firm design, discussing mechanical assembly analyses required to transmit power through the system, protect the gearing system, and ultimately produce a functional prototype.

Following this technical analysis, Chapter 6 examines the manufactured Tri-Wheel assemblies implemented on an existing robot platform and discusses preliminary results. Finally, Chapter 7 states the conclusions of this research and defines future work.

2 THE TRI-WHEEL MECHANISM

2.1 Introduction to the Tri-Wheel Concept

In an effort to develop a novel locomotion platform that successfully meets the stated research objectives, a number of configurations are considered. After comparing the advantages and disadvantages of the various configurations, it is clear that the Tri-Wheel concept holds the most promise for ease of implementation, robustness, and maneuverability in various terrains. Information regarding the rejected mechanisms is included in Appendix A: Discarded Locomotion Concepts.

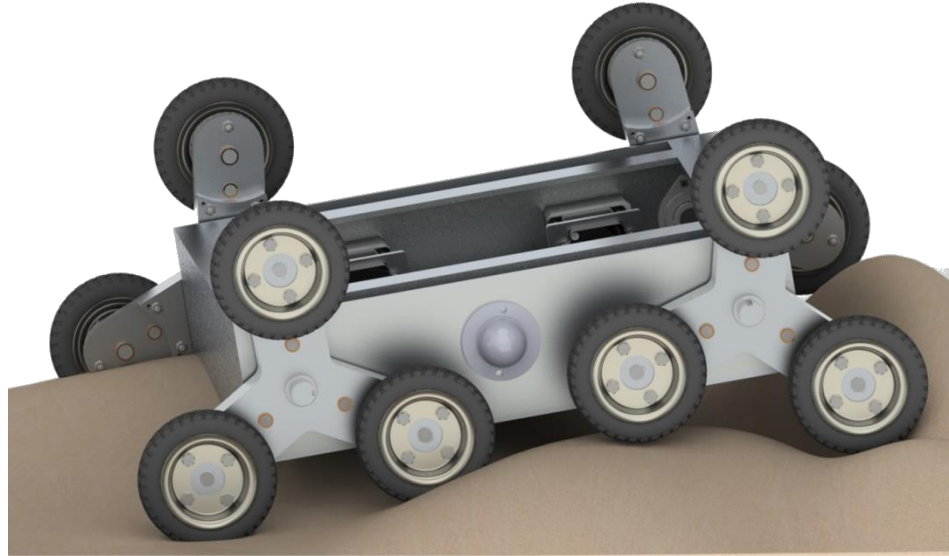


Figure 2.1: Tri-Wheel Design on a Basic Robot Platform

The Tri-Wheel locomotion mechanism shown in Figure 2.1 is a three-wheeled, spoked drive mechanism capable of two rotational modes: Driving Mode and Tumbling Mode. This concept is roughly explained as an equilateral triangle with powered wheels

at each vertex. Driving Mode and Tumbling Mode are actuated through two separate but connected parallel gear sets powered by a brushless DC electric motor. One Tri-Wheel assembly is intended to replace each wheel of a typical robot, and each assembly is powered by its own electric motor. Figure 2.1 displays four Tri-Wheel assemblies or mechanisms on a robot platform, though two could conceivably be used on small robot or with an idling wheel in the back for balance.

At the center of each Tri-Wheel assembly, there is a gear that receives power directly from the electric motor and transmits it radially out to rotate the three wheels. In Driving Mode, two of these three rotating wheels in each Tri-Wheel mechanism are in contact with the ground and roll across level surfaces just as a wheeled robot would. This produces a capable means to traverse smooth surfaces efficiently and quickly. However in many cases, an obstacle (stairs, debris, etc.) may be encountered or the terrain could be loose, resulting in poor traction. In these instances, a mechanism can be engaged to act upon the gearing system such that it forces the three wheels to rotate around the center of the Tri-Wheel assembly and enter Tumbling Mode. When this occurs, the Tri-Wheel has the appearance of “walking” like a Whegs robot over obstacles as it rotates about its central shaft. The mechanism inducing Tumbling Mode may be engaged passively via operator command or autonomously using feedback from sensors indicating a stall state, potential slippage, or a particular distance from the obstacle to be overcome.

2.1.1 Driving Mode

Because two wheels (of the three present in each Tri-Wheel assembly) are in contact with the ground and operate as normal wheels, this concept takes advantage of

the wheel's optimal performance on flat terrain. Because the Tri-Wheel's orientation is not locked in place relative to the robot body, the wheels are able to passively pivot about the main drive shaft located at the centroid of each Tri-Wheel assembly. This allows for effective adaptation to grades and slopes. Figure 2.2 shows this ability to pivot and maintain contact with a smooth, sloped surface. The red arrows surrounding each wheel indicate the same angular velocity as the three wheels spin during driving mode. In this scenario, two wheels are in contact with the ground and contributing to the driving motion of the robot or vehicle. The black arrow located at the centroid of each Tri-Wheel represents the overall linear velocity induced in each mechanism as a result of the rotation of the wheels.

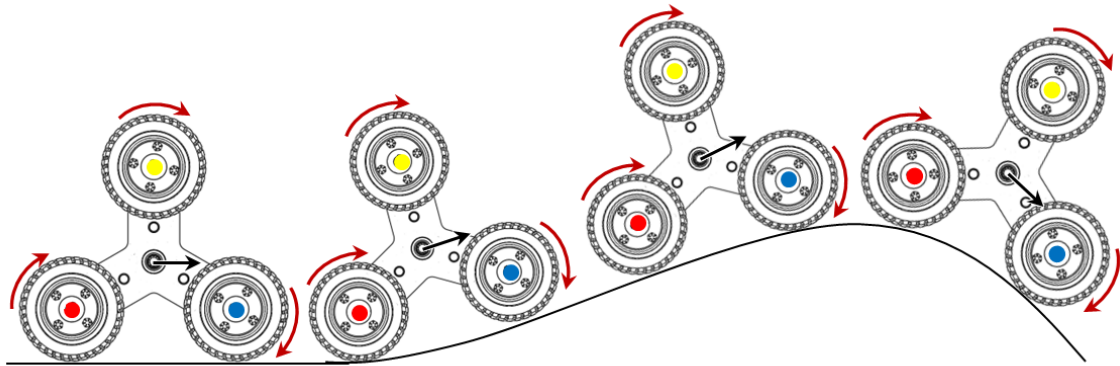


Figure 2.2: Driving Mode

While this mode does allow for smooth operation on even surfaces, it also has the advantage of absorbing obstacles encountered such as rocks or other debris that are larger than the diameter of one wheel. When moving across a surface, if the leading ground wheel of one Tri-Wheel assembly comes into contact with an obstruction, that wheel will kick back, and the third wheel (top wheel) that was previously not in contact with the ground will rotate forward and assume the position of the leading ground wheel. The

assembly will then continue its linear motion. For this reason, the Tri-Wheel is optimal for uneven terrain; each assembly is independently operated, and if an obstacle is encountered on only the left side of the vehicle, for instance, the others Tri-Wheel assemblies can maintain balance and continue to propel the robot forward.

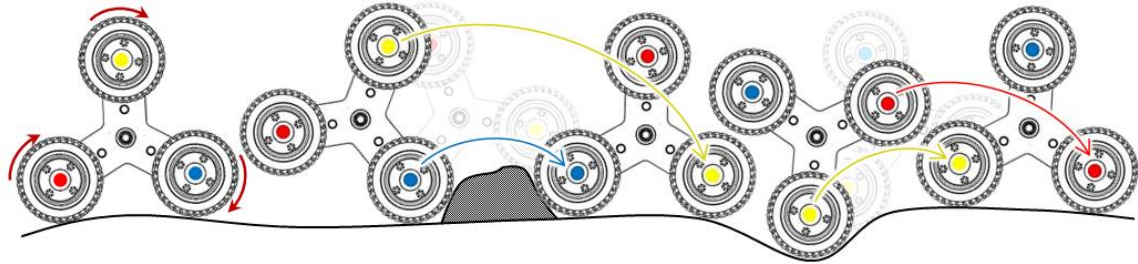


Figure 2.3: Absorbing Obstacles in Passive Tumbling Mode

Figure 2.3 illustrates this process of passively absorbing obstacles while in driving mode. Note that the arrows encircling the three wheels once again represent the angular velocity as the mechanism to advances forward. These wheels continue to rotate throughout the entire figure; arrows are omitted after the first Tri-Wheel instance for clarity of the image. This figure displays the Tri-Wheel mechanism reaction to a positive obstacle (a rock or some debris) and a negative obstacle (a crevice or depression). Beginning with the leftmost instance, the Tri-Wheel proceeds forward in normal driving mode. When the leading (blue) wheel comes into contact with the positive obstacle, the natural reaction of the mechanism is to rotate forward such that the top (yellow) wheel assumes the position of the blue wheel to absorb the obstacle and continue its forward motion. When the negative obstacle is encountered, the leading (yellow) wheel becomes somewhat stuck in the depression. As a response, the Tri-Wheel continues to spin its wheels, and the top (red) wheel flips forward to assume the yellow wheel's previous

position. Once the negative obstacle is cleared, the Tri-Wheel continues to drive forward in its typical driving mode.

Recall that in general, a wheel can only surmount an obstacle that is less than or equal to the radius of the wheel. However with the Tri-Wheel mechanism, if an obstruction of height greater than the radius of a single wheel is encountered, the assembly absorbs the obstacle and rotates about its central axel to flip over the object and continue moving.

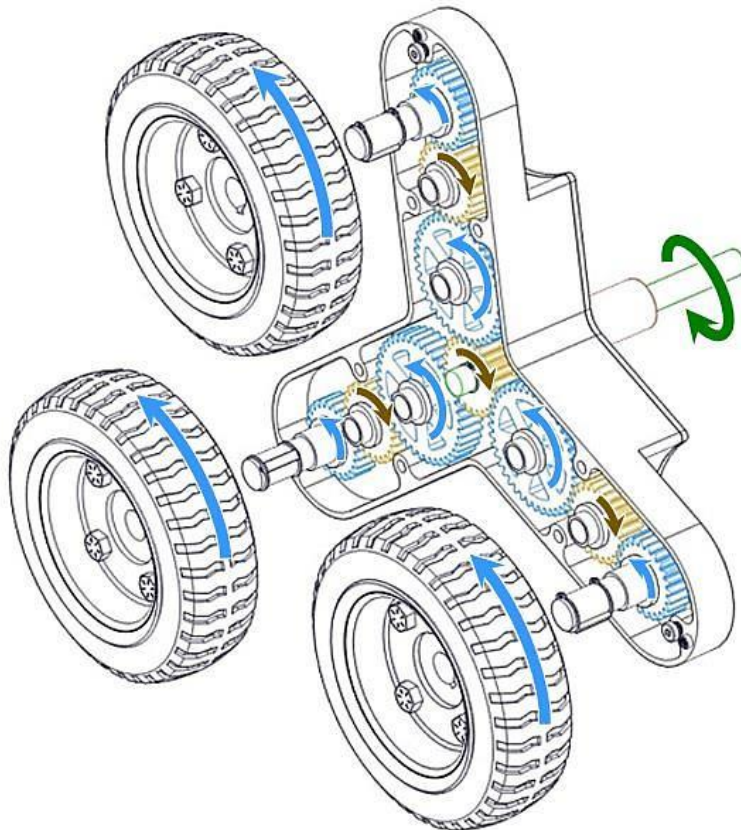


Figure 2.4: Driving Mode Gearing Configuration

In Figure 2.4, the inside of the Tri-Wheel is shown to provide a view of the gearing that makes Driving Mode possible. The parallel gear set that enables Tumbling Mode is obscured in this picture but exists directly behind the gears shown within the

same housing structure. In Driving Mode, the gear set used in Tumbling Mode has no significant effect on the driving motion. An in-depth analysis of this gearing system can be found in Chapter 4, but in order to understand how the Tri-Wheel works at a high level, a brief discussion of the gearing is necessary. The blue and gold colors are used in Figure 2.4 to relay the alternating rotational directions within the gear set as power is transmitted from gear to gear. Blue represents a counterclockwise rotational direction, and gold represents a clockwise rotational direction. The green-outlined drive shaft receives power directly from a brushless DC motor. The green arrow indicates that the motor power output entering the Tri-Wheel mechanism is clockwise in direction. After the power travels completely through each leg of the gearing system, the final result is that each of the three wheels spins in the same direction (counterclockwise, assuming a clockwise power input) at the same angular velocity.

All of the gears shown are keyed to their shafts, providing a means to transmit power. The drive shaft is keyed to the center gold gear, which receives power from the DC motor and transmits it radially outward to the large blue gear, to the small gold gear, to the small blue gear, and finally to the wheels which are keyed to the same shaft as the small blue gear.

2.1.2 Tumbling Mode

In Tumbling Mode, a braking mechanism is engaged to cause the entire Tri-Wheel mechanism to rotate about a shaft located at its centroid. This rotation will intentionally occur in the same direction in which the three wheels are spinning. This braking mechanism can be a disk brake, band brake, or even an additional motor. The

selected braking mechanism and its implementation will be discussed in coming chapters. This capability provides a powered mode that enables a robot to surmount obstacles such as stairs that cannot simply be absorbed passively in Driving Mode. The braking of the center mechanism can be modulated to any value from free wheel to full braking.

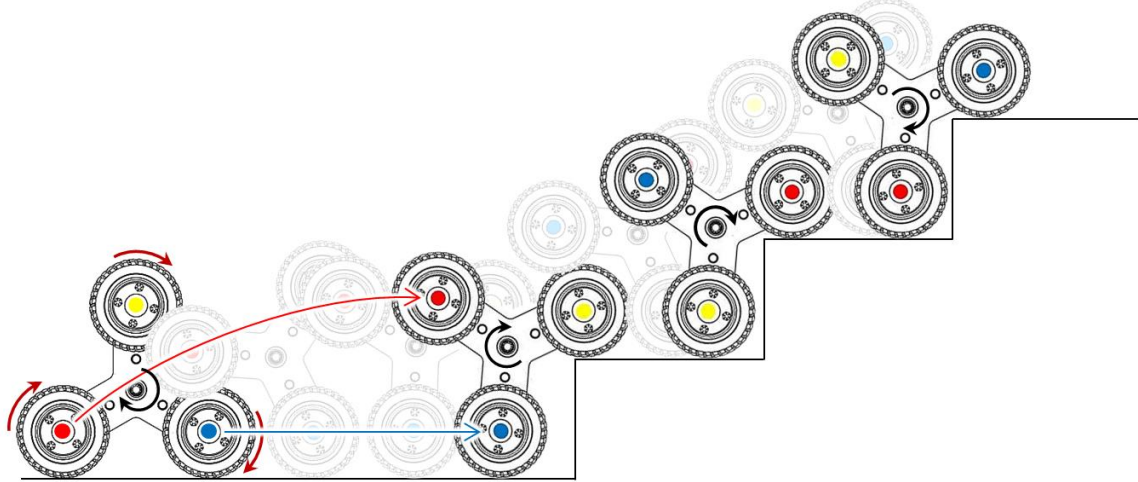


Figure 2.5: Actuated Tumbling Mode

Figure 2.5 depicts the actuation of Tumbling Mode as the Tri-Wheel mechanism ascends stairs. Because of its dual ability to roll and climb, the Tri-Wheel is able to rotate about its central axel to approach a step and then roll along the step surface until it reaches an optimal position to flip over itself once again and continue the climbing process. Both the individual wheels and the entire body rotate about the braked central gear, causing a tumbling motion. The leftmost Tri-Wheel instance in Figure 2.5 begins in Driving Mode with all three wheels spinning in a clockwise direction. The arrow encircling the centroid of the mechanism indicates the initiation of the braking mechanism to induce tumbling. As the Tri-Wheel body begins to rotate about its centroid, it simultaneously continues to translate in a horizontal direction, as indicated by the blue horizontal arrow. As the leading (blue) wheel rolls forward on the flat surface, the top

(yellow) wheel begins to rotate forward and lands on the first step and assumes the position as the new leading wheel. At this point, the leading (yellow) wheel rolls forward. As the leading (yellow) wheel approaches the next step, the top (red) wheel swings over top of the yellow wheel and lands on the next step. The pattern continues as the Tri-Wheel mechanism effectively “walks” itself up the set of stairs.

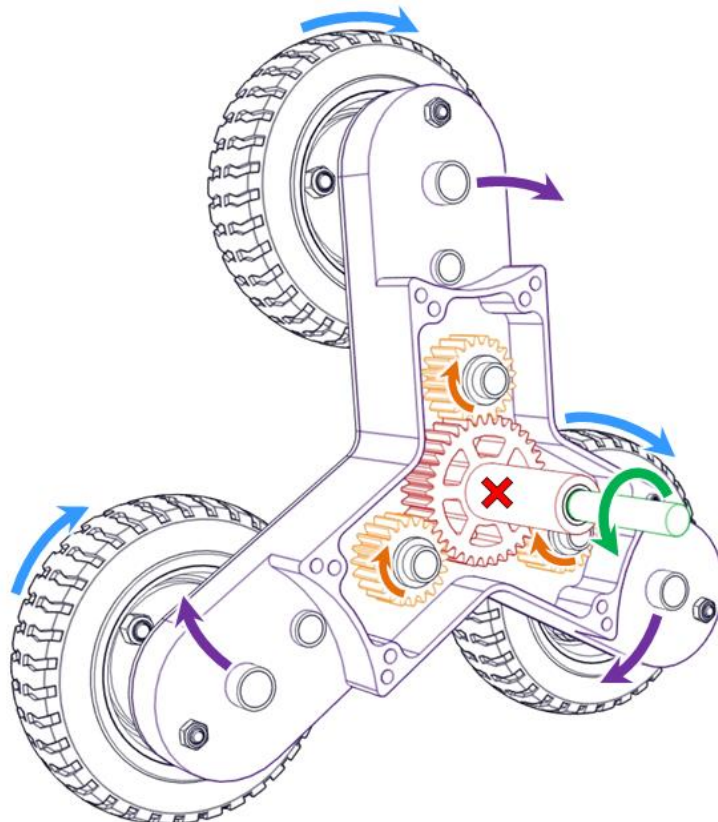


Figure 2.6: Tumbling Mode Gearing Configuration

This unique tumbling capability is achieved through Tri-Wheel’s novel gearing configuration. Figure 2.6 provides an internal view of the tumbling gear set. Note that directly in front of these gears on the other side of the housing wall, the driving gear set as seen in Figure 2.4 has been obscured by the housing but is still present. Please keep in mind that the arrows represented in this figure are in the reverse direction of those in

Figure 2.4 because Figure 2.6 is shown from the opposite side of the Tri-Wheel mechanism. In this figure, the colors serve to distinguish the varying clockwise or counterclockwise rotational directions of the Tri-Wheel components. It is important to note that three smaller orange gears are keyed to the same shaft as the three larger blue gears shown in Figure 2.4. The center red gear shown has a hollow shaft extruded from it; the gear and the shaft constitute a single manufactured part. The green drive shaft passes through the red hollow shaft and connects to the center gold gear shown in Figure 2.4. When a braking mechanism is applied to the hollow shaft (indicated by the red X in Figure 2.6), the center red gear is held stationary and locked in place relative to the robot chassis. The motor continues to provide power to the green drive shaft (indicated by the green counterclockwise arrow), which drives the small center gold gear and subsequently drives the larger blue gears.

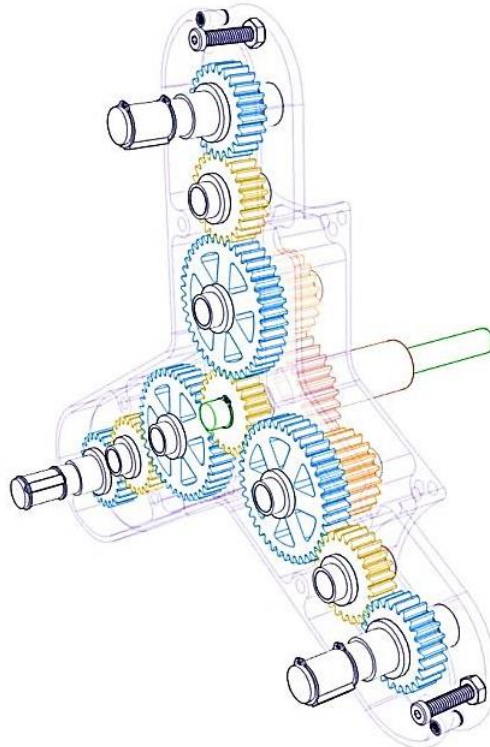


Figure 2.7: Tri-Wheel Parallel Gear Sets

In Figure 2.7, the housing of the Tri-Wheel is made transparent, and the wheel subassemblies are removed so that the parallel driving and tumbling gear sets are clearly visible in their typical orientation. Because the small orange gears and large blue gears are keyed to the same shaft as shown, the small orange gears will rotate with the same angular velocity and in the same direction as the larger blue gears and will effectively walk themselves around the stationary center gear, forcing the entire Tri-Wheel body to rotate as indicated by the purple arrows. As the rotational force is applied to the central tumbling gear by the three small orange gears, the braking mechanism prevents the red gear from rotating as it would in driving mode and forces the orange gears to climb around the fixed center gear, causing the entire assembly to spin. While the rotation of the entire body occurs in a clockwise direction, the three wheels continue to rotate in a clockwise direction. The wheel rotation helps to pull the Tri-Wheel along as its entire body rotates about its center shaft. The relative speeds of rotation and their implications will be discussed in Chapter 4.

2.2 Tri-Wheel Advantages and Disadvantages

As previously stated, no single application of the four currently utilized locomotion concepts (wheels, continuous tracks, wheel-leg hybrids, and articulated robotic legs) has been optimized to combat the problems associated with remote vehicle navigation. The Tri-Wheel design concept moves toward a more comprehensive solution to make robots more maneuverable, reliable and robust. However, like each of the four reviewed locomotion platforms, the Tri-Wheel design comes with its own unique set of advantages and disadvantages that must be considered.

The emphasis is on the full mission capability that includes quick motion to a site of interest as well as the ability to actuate with more torque when necessary to overcome a range of obstacles and terrain characteristics. This depends upon the selected gear ratios but is theoretically feasible. The most challenging research objective is the ability of a locomotion mechanism to allow for stair climbing. Yet because of the Tri-Wheel's dual ability to roll and climb as it enters Tumbling Mode, this goal is achievable even with different grades of stairs, as discussed in Chapter 3. With this design requirement met, the Tri-Wheel is well on its way to fulfilling the desired performance characteristics.

Previous observations of wheeled locomotion systems have heavily influenced the design of the Tri-Wheel. The ability to roll until an object is encountered allows the system to move freely and efficiently over even terrain, including over slopes, and the use of three wheels means that the system would be stable even when faced with unexpected obstacles at high speeds as it could flip over itself and tumble passively as shown in Figure 2.3. The maneuverability issue regarding multiple parking turns can be addressed in the future through the use of two motors to torque forward and backward (as in the inverted pendulum problem) to balance up on one wheel for a smaller turning radius. Future testing will provide information regarding this research objective.

The study of continuous track motion also provides significant insight regarding how the Tri-Wheel or another locomotion concept should operate for the research criteria. In driving mode, two wheels out of three will be in contact with the ground for each triangular unit or assembly. Thus, if the Tri-Wheel is installed on a typical four wheeled robot, the robot will have eight wheels in contact with the ground at one time when rolling. This produces twice the surface area as when there were four wheels,

helping to distribute the weight of the robot and hopefully prevent some sinkage into loose soil.

Furthermore, the structure will be less susceptible to damage since the braking mechanisms that lock the center shaft will act inside the robot, out of reach of mud or other potentially hazardous elements anticipated when navigating debris or rugged terrain. The wheels can also be easily replaced unlike tank treads, and if a wheel is disabled, the other two wheels can be used until a repair could be made. This redundancy makes the design more reliable and serviceable. The Tri-Wheel holds potential to be utilized for a wide variety of tasks, and many of those tasks would not lend themselves well to excessive robot downtime caused by maintenance issues. Moreover, many of these tasks do not provide the operator with a safe opportunity to enter a potentially hazardous environment for maintenance purposes. For this reason, the design redundancy of the Tri-Wheel is critical for mission success.

In some sense, the Tri-Wheel effectively merges Dr. Quinn's existing Whegs concept with the benefits of typical wheeled motion as well as a more robust structure that is more active than passive due to its novel gearing configuration. The rolling, three-spoked platform as proposed would take advantage of the Whegs' climbing capabilities on a larger scale but enables smoother motion over flat surfaces and provide less jostling to the internal components of the vehicle. As discussed, Whegs' usage of frictional forces on the outside of the spokes to propel themselves can lead to failure in inclement environments. In contrast, the Tri-Wheel concept uses gearing and an internal braking mechanism to relocate the frictional force from the outside surfaces to the internal mechanical mechanisms to lock the wheel when needed, relying more on the design itself

than the environment. In addition, the three individual wheels installed in each Tri-Wheel assembly are pneumatic tires that can provide some shock absorption when encountering obstacles. In contrast, a wheel-leg is typically formed from a rigid structure made of carbon fiber or a metal such as aluminum; this affords minimal dampening of the external forces encountered during typical operation.

Despite the advantages of the Tri-Wheel system, the triangle is still the least efficient shape to roll over. Additional testing and experimental data are required to observe the proper operating conditions such that the wheels did not bump and shake the payload unnecessarily. As mentioned, the turning radius of a vehicle utilizing a Tri-Wheel might not be significantly smaller than the radius achieved by existing locomotion platforms. In the future, drive shafts with increased degrees of freedom that swivel could be implemented in conjunction with this strategy to further increase the mobility of the concept. Optimization of the individual wheel spacing in each assembly is also critical to keep debris from becoming lodged between wheels. The two gear sets required to power both driving mode and tumbling mode could also cause the Tri-Wheel add significant mass to the system if not optimized properly.

2.3 Design Strategy

In order to better define this open-ended problem given minimal quantitative constraints, a logical design sequence is developed in an attempt to parameterize the Tri-Wheel. Figure 2.8 is a graphical representation of this design process and explains where the methodology for Tri-Wheel optimization comes from and the steps necessary to take the design from a concept to a fabricated apparatus fit for testing. The following chapters

delve further into the specific analytical steps taken to ultimately yield a final, optimized Tri-Wheel configuration. This design methodology involves a series of iterative processes to converge on a final device. If the gear analysis ultimately yields a configuration that is unsatisfactory for any number of practical reasons including weight, size, or other concerns, the process will begin again and the iteration continues.

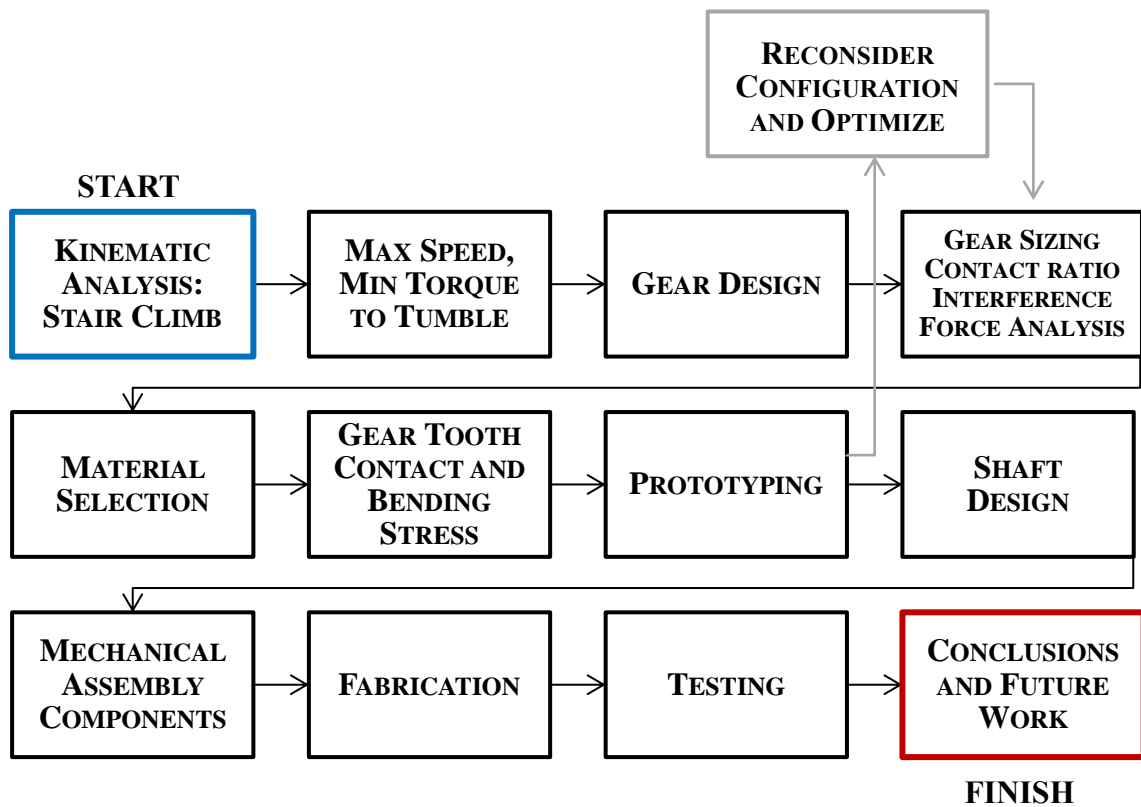


Figure 2.8: Tri-Wheel Design Strategy

3 KINEMATIC ANALYSIS

3.1 Introduction and Nomenclature

Following the selection of the Tri-Wheel concept, derived requirements for a final mechanism that meets the stated research objectives must be obtained. The starting point of this process is a kinematic analysis that explains where the mechanism is in space. This ultimately governs the overall size of the Tri-Wheel that is suitable for stair climbing, the most challenging requirement. The kinematic analysis also seeks to converge on two parameters through optimization: the radius of each individual wheel r and the distance between the centroid of the Tri-Wheel and the center of one wheel c , the spoke length. These variables are shown in Figure 3.1 in relation to a Tri-Wheel.

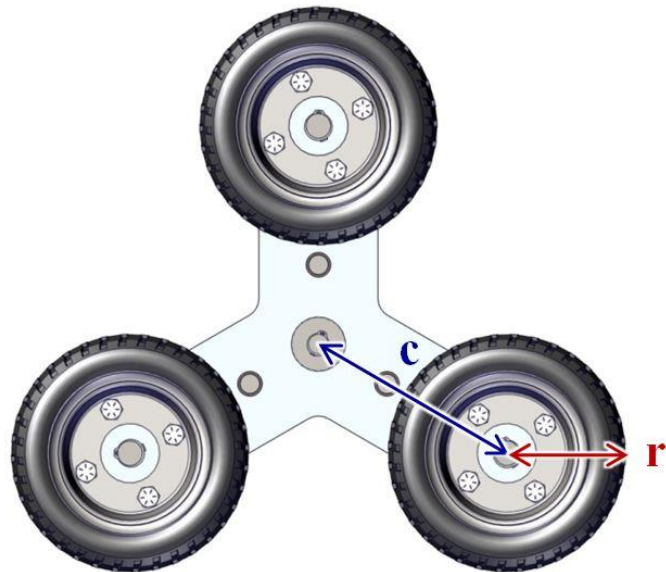


Figure 3.1: Spoke Length and Wheel Radius on Tri-Wheel

In order to derive the optimal values for r and c , an overall analysis of the Tri-Wheel's motion during Tumbling Mode is required since this mode of operation is utilized to climb stairs. Studying this motion provides an understanding of where the three wheels and the centroid of the mechanism are located at strategic points. Once this general relationship is understood, the size of the Tri-Wheel is able to be optimized for the task of climbing stairs from a quantitative perspective. The following sections in this chapter serve to explain the mathematical relationship that relates the three vertices of the mechanism (its three wheels) as well as its centroid and plot each of these four points in space. With this information, optimization for stair climbing can be investigated.

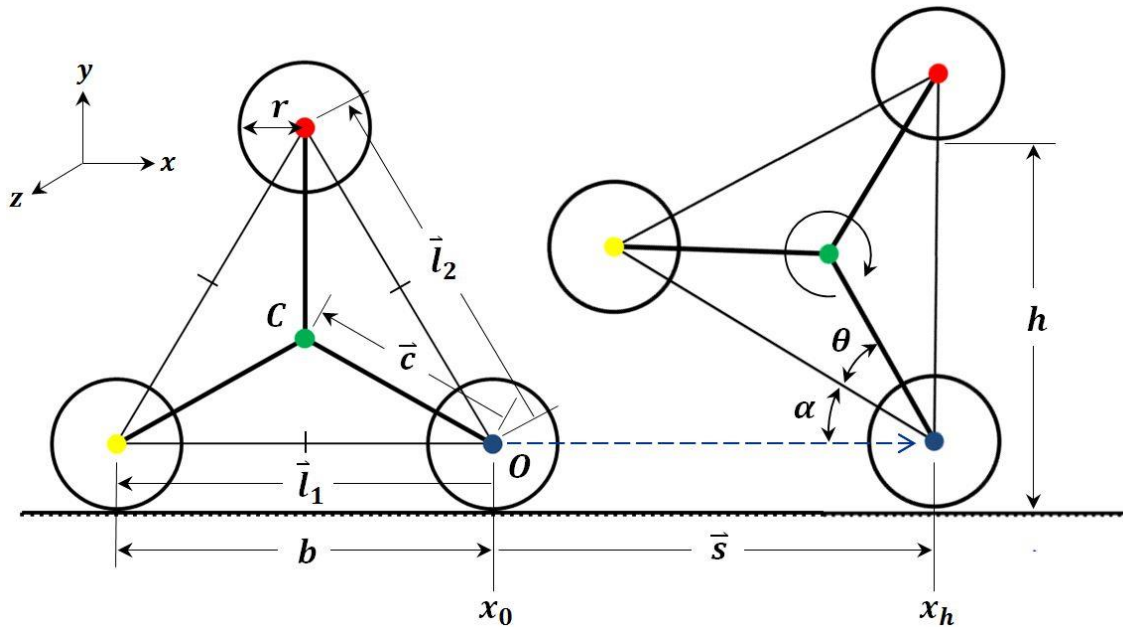


Figure 3.2: Tri-Wheel Kinematic Analysis Nomenclature

Figure 3.2 is a simplified representation of the Tri-Wheel geometry labeled with the vectors, angles, lengths, and points referenced throughout the kinematics analysis. All lengths are measured in units of inches, and angles are measured in degrees. As this figure relays, the basic structure of the Tri-Wheel derives from an equilateral triangle. In

the actual Tri-Wheel mechanism shown in Figure 3.1, notice that each wheel is connected to the centroid C , but there is no physical element connecting one wheel directly to another wheel. For purposes of this analysis, Figure 3.2 includes these lines connecting the three wheels to facilitate easy measurement of angles. In Figure 3.2, each equivalent side length is labeled b and provides the distance between the centroids of any two wheels.

Throughout the process of tumbling, all three individual wheels will assume different positions. In other words, the red wheel will not always be at the top, and the blue wheel will not always be leading. In order to climb over obstacles, the wheels must exchange places in a clockwise or counterclockwise direction (depending on the direction in which the motor is driven) as the assembly walks over these obstructions. For this reason, it is prudent to establish consistent terminology for describing the wheel positions beyond the use of color. Looking at the wheel configuration provided in Figure 3.2, the wheel positions are defined as follows: red—top wheel, yellow—trailing ground wheel, blue—leading ground wheel. The leading ground wheel is the translating pivot point for tumbling motion while the top wheel will land on or above the obstacle to be overcome. During Tumbling Mode, the trailing ground wheel simply serves to complete the cycle.

Point O marks the origin of rotation (the horizontally translating pivot point), which is always placed at the center of the leading ground wheel. Vector \vec{l}_1 has a magnitude equal to the side length b and gives the position of the trailing ground wheel with respect to the leading ground wheel. Vector \vec{l}_2 is similarly of magnitude b and provides the position of the top wheel with respect to the leading ground wheel. The vector \vec{c} represents the spoke length already discussed and gives the position of the Tri-

Wheel centroid C with respect to the leading ground wheel. The initial horizontal position of the leading ground wheel (of point O) is labeled x_0 . Once the braking mechanism has been engaged and the Tri-Wheel begins to rotate about the leading ground wheel, the vector \vec{s} is used to measure the horizontal distance traveled by the leading ground wheel.

As the trailing ground wheel begins to lift off the ground, the angle α emerges as a measure of how much the Tri-Wheel has rotated from its initial state with two wheels planted on the ground. Specifically, α is the angle from the reference horizontal to the theoretical base of the equilateral triangle. Beginning at 0° , α will end at 120° for a full rotation of the Tri-Wheel. Angle θ always equals 30° due to the properties of an equilateral triangle and measures the degree of separation between the triangle's base and the vector \vec{c} . There are six similar θ angles in the Tri-Wheel. In Tumbling Mode, the top wheel will reach its maximum vertical height when it is directly above the leading ground wheel. The horizontal distance at which this occurs is labeled x_h where $h = h_{max}$. Lastly, the distance h represents the distance from the ground to the lowest point of the top wheel—the step approach height. It is evident in examining the diagram that this height h is actually equivalent to the side length b when maximized.

When the Tri-Wheel is engaged in Tumbling Mode, the leading ground wheel advances forward (while rolling) as the rest of the assembly rotates about it. There is a relationship between the angle of rotation, the wheel radius, and the translation. Consider now the case in which the leading ground wheel does not translate during rotation of the assembly. Rather, if the leading ground wheel is imagined to be fixed as the rest of the Tri-Wheel assembly pivots about it, the resulting motion establishes another mode of operation called Inching Mode. While Inching Mode and the means by which the leading

wheel would be fixed during rotation are not investigated in this paper, this motion is the simplest to model and the best place to begin kinematic analysis. In future applications, the ability for one wheel to become fixed in place might prove advantageous for climbing out of soft soils or dislodging the Tri-Wheel assembly from other potential failure modes.

3.2 Inching Mode

Inching Mode is best described as a simplified, theoretical form of Tumbling Mode. In order to obtain the rotational trajectory for each wheel as well as the centroid in a Tri-Wheel mechanism, a rigid body transformation matrix is used to map the coordinates of each of the four points in question. Positions of these four points are expressed uniquely by vectors throughout the rotation. The methodology is to write expressions for these vectors in the initial configuration shown in the leftmost Tri-Wheel of Figure 3.2 and then plot their locations with the help of a rotation matrix. Referencing the right-handed coordinate frame shown in the same figure, the rotation of the assembly occurs in the negative z-direction. In this case, the rotation matrix is modeled as a basic Euler Angle rotation about the z-axis written as [14]:

$$R_z(-\alpha_z) = \begin{bmatrix} \cos (-\alpha_z) & -\sin (-\alpha_z) & 0 \\ \sin (-\alpha_z) & \cos (-\alpha_z) & 0 \\ 0 & 0 & 1 \end{bmatrix} \quad (3.1)$$

Using the properties of the sine and cosine function, this expression can be further simplified as follows for the rotation of a negative angle.

$$R_z(-\alpha_z) = \begin{bmatrix} \cos \alpha_z & \sin \alpha_z & 0 \\ -\sin \alpha_z & \cos \alpha_z & 0 \\ 0 & 0 & 1 \end{bmatrix} \quad (3.2)$$

Next, the vectors \vec{c} , \vec{l}_1 , \vec{l}_2 , are written corresponding to their positions in Figure 3.2. All of these vectors are written with respect to the angle θ , which was previously defined to always equal 30° .

$$\vec{c} = -c \cos \theta \mathbf{i} + c \sin \theta \mathbf{j} + 0\mathbf{k} \quad (3.3)$$

$$\vec{l}_1 = -2c \cos \theta \mathbf{i} + 0\mathbf{j} + 0\mathbf{k} \quad (3.4)$$

$$\vec{l}_2 = -(2c \cos \theta)(\cos 60) \mathbf{i} + (2c \cos \theta)(\sin 60) \mathbf{j} + 0\mathbf{k} \quad (3.5)$$

The value of $\theta = 30^\circ$ can then be substituted into these general expressions:

$$\vec{c} = -\frac{\sqrt{3}}{2}c\mathbf{i} + \frac{1}{2}c\mathbf{j} + 0\mathbf{k} \quad (3.6)$$

$$\vec{l}_1 = -\sqrt{3}c\mathbf{i} + 0\mathbf{j} + 0\mathbf{k} \quad (3.7)$$

$$\vec{l}_2 = -\frac{\sqrt{3}}{2}c\mathbf{i} + \frac{3}{2}c\mathbf{j} + 0\mathbf{k} \quad (3.8)$$

These vectors expressions can now be rearranged into column vectors and multiplied by the rotation matrix given by Equation (3.2). This matrix multiplication is shown below.

$$[\vec{c}'] = [R_z(-\alpha_z)] * [\vec{c}] \quad (3.9)$$

$$[\vec{c}'] = \begin{bmatrix} \cos \alpha & \sin \alpha & 0 \\ -\sin \alpha & \cos \alpha & 0 \\ 0 & 0 & 1 \end{bmatrix} * \begin{bmatrix} -\left(\frac{\sqrt{3}}{2}\right)c \\ \left(\frac{1}{2}\right)c \\ 0 \end{bmatrix} \quad (3.10)$$

$$[\vec{c}'] = \begin{bmatrix} -\left\{\left(\sqrt{3}/2\right)\cos \alpha\right\}c + \left\{(1/2)\sin \alpha\right\}c \\ \left\{\left(\sqrt{3}/2\right)\sin \alpha\right\}c + \left\{(1/2)\cos \alpha\right\}c \\ 0 \end{bmatrix} \quad (3.11)$$

$$[\vec{l}_1'] = [R_z(-\alpha_z)] * [\vec{l}_1] \quad (3.12)$$

$$[\vec{l}_1'] = \begin{bmatrix} \cos \alpha & \sin \alpha & 0 \\ -\sin \alpha & \cos \alpha & 0 \\ 0 & 0 & 1 \end{bmatrix} * \begin{bmatrix} -\sqrt{3}c \\ 0 \\ 0 \end{bmatrix} \quad (3.13)$$

$$[\vec{l}_1'] = \begin{bmatrix} -(\sqrt{3}\cos \alpha)c \\ (\sqrt{3}\sin \alpha)c \\ 0 \end{bmatrix} \quad (3.14)$$

$$[\vec{l}_2'] = [R_z(-\alpha_z)] * [\vec{l}_2] \quad (3.15)$$

$$[\vec{l}_2'] = \begin{bmatrix} \cos \alpha & \sin \alpha & 0 \\ -\sin \alpha & \cos \alpha & 0 \\ 0 & 0 & 1 \end{bmatrix} * \begin{bmatrix} -\left(\sqrt{3}/2\right)c \\ (3/2)c \\ 0 \end{bmatrix} \quad (3.16)$$

$$[\vec{l}_2'] = \begin{bmatrix} -\left\{\left(\sqrt{3}/2\right)\cos \alpha\right\}c + \left\{(3/2)\sin \alpha\right\}c \\ \left\{\left(\sqrt{3}/2\right)\sin \alpha\right\}c + \left\{(3/2)\cos \alpha\right\}c \\ 0 \end{bmatrix} \quad (3.17)$$

Equations (3.11), (3.14), and (3.17) are the final desired expressions. The prime symbol next to each vector on the left hand side of each equation denotes a transformation. Code is then written to iterate through these three expressions and

determine the x and y positions of the three vectors during a full rotation of the Tri-Wheel in Inching Mode.

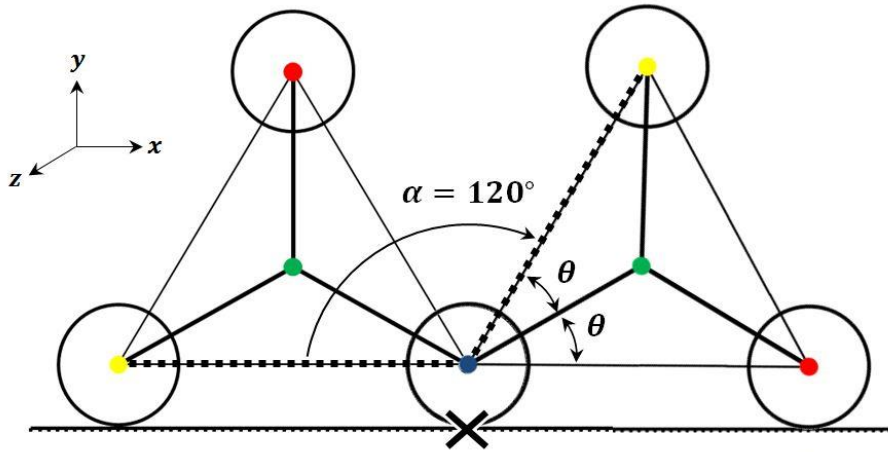


Figure 3.3: Full Rotation in Inching Mode

Figure 3.3 shows one full rotation of the mechanism. Here, the X denotes a fixed leading ground wheel such that the entire assembly can pivot and rotate about it. Because each angle in an equilateral triangle is equal to 60° , the Tri-Wheel undergoes a rotation of 120° for a full rotation. Thus, Equations (3.11), (3.14), and (3.17) are iterated through for values of $0^\circ < \alpha < 120^\circ$ and any given value of c . Once the red top wheel rotates 120° such that it is firmly planted on the ground, the red wheel is fixed in place and becomes the new leading ground wheel.

It is important to note that in writing these vector expressions, the zero reference horizontal is located at the center of the leading ground wheel. For purposes of plotting the data, the zero horizontal will be relocated to beneath the wheels. In other words, the data obtained through the vector expressions is still valid, but it will be translated vertically to account for the wheel radius.

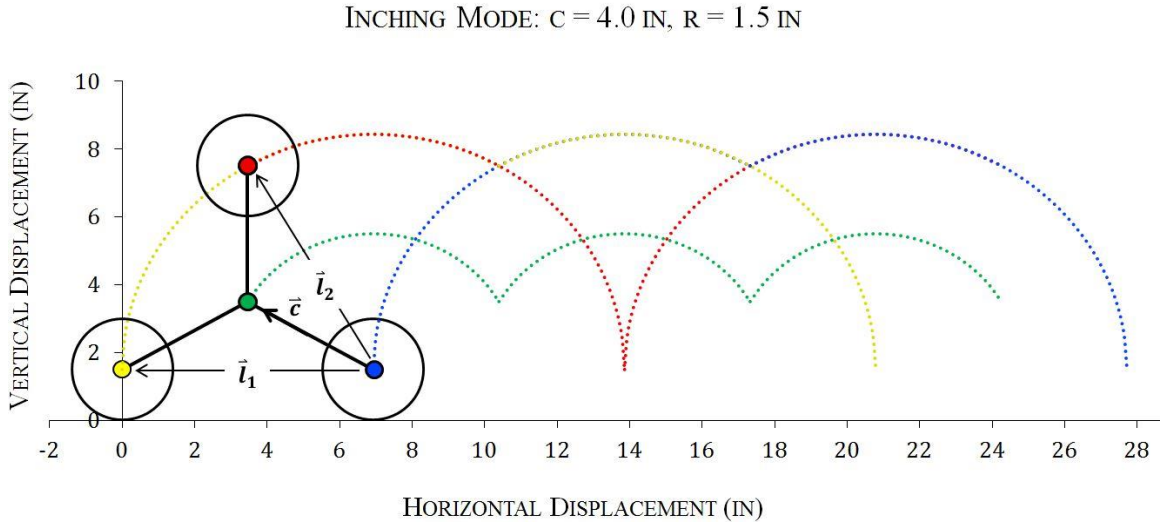


Figure 3.4: Inching Mode Trajectory Plot

Figure 3.4 is a plot of the horizontal and vertical displacements of these vectors for a Tri-Wheel with arbitrary sizing $c = 4.0$ in with a wheel radius $r = 1.5$ in. The value of r in Inching Mode is not significant from the standpoint that its only function is to increase all vertical positions by some fixed constant value equal to the wheel radius. In fact, r does not have influence on the horizontal position of the apparatus. In Figure 3.4, all of the y-values returned by the vector expressions are increased by 1.5 in. before they are plotted to account for the wheel height. Three rotational cycles are plotted in the graph with a single rotational cycle occurring from $\alpha = 0^\circ$ to $\alpha = 120^\circ$.

From this graph, it is possible to determine what the maximum vertical displacement is and where it occurs in the rotational cycle. For this sizing, Figure 3.4 reveals that the maximum vertical displacement reached by the three wheel centers is equal to 8.43 in. The maximum vertical displacement reached by the centroid is 5.5 in. Another important observation is the angle of α at which the top wheel, centroid, and trailing ground wheel reach their maximum vertical displacements. The vectors reach

their maximum vertical displacements as follows: \vec{l}_2 at $\alpha = 30^\circ$, \vec{c} at $\alpha = 60^\circ$, and \vec{l}_1 at $\alpha = 90^\circ$. This observation is valid for Tumbling Mode as well. Because Inching Mode is not being pursued in this project beyond the point of kinematic analysis, further investigation of optimization is not required. A more in-depth analysis and optimization discussion are left for the following sections in which Tumbling Mode is plotted and further examined for the purposes of stair climbing.

3.3 Tumbling Mode

The main distinction between Tumbling Mode and Inching Mode is that the leading ground wheel rolls forward as a typical, unconstrained wheel in Tumbling Mode as the rest of the Tri-Wheel assembly rotates about it. Thus, in addition to tracking the rotation (orientation) of the Tri-Wheel vertices, an expression is required to also account for the translation (position) that occurs. When the leading ground wheel of radius r rolls without slip across a horizontal surface, the distance through which the wheel's center travels (as the wheel turns by some angle $0^\circ < \alpha < 120^\circ$) is equivalent to the arc length through which a point on the rim of the wheel moves. This relationship is captured by the following general equation:

$$\Delta x = s = r\theta \quad (3.18)$$

In this kinematic analysis, the Tri-Wheel is treated as a rigid body—a collection of particles such that the distance between the particles does not change when the body moves with time. For this reason, a rigid body transformation is used to capture the position of the Tri-Wheel as it moves through space. A rigid body transformation is

simply a mapping function that preserves both length between points and the cross product between vectors (also implying that angles are preserved) [15]. By this definition, rotation matrices are, in fact, rigid body transformations. There are multiple valid approaches that can be used to express rigid body motion involving rotation and translation. Because all subsequent design stages are constrained by the spoke length c (the gearing configuration in particular), two of these methods are selected and compared to ensure that the results are consistent and accurate. The first is a simple modification of the equations used in section 3.2, and the second is a more formal method involving Rodrigues' Formula and the homogeneous representation transformation.

METHOD 1: In order to account for the horizontal translation, a 3x1 translation vector \vec{s} is written. Note that this expression agrees with Equation (3.18). In this equation, the value of α must be given in radians while the radius is still measured in inches.

$$\vec{s} = (r * \alpha)\mathbf{i} + 0\mathbf{j} + 0\mathbf{k} \quad (3.19)$$

The same vector representations given by Equations (3.6) - (3.8) are adopted for this analysis. The vectors are rearranged into column vectors as done in the previous analysis and multiplied by the rotation matrix given by Equation (3.2). The horizontal translation component is then appended via matrix addition.

$$[\vec{c}'] = [R_z(-\alpha_z)] * [\vec{c}] + [\vec{s}] \quad (3.20)$$

$$[\vec{c}'] = \begin{bmatrix} -\left\{\left(\sqrt{3}/2\right)\cos \alpha\right\}c + \left\{(1/2)\sin \alpha\right\}c \\ \left\{\left(\sqrt{3}/2\right)\sin \alpha\right\}c + \left\{(1/2)\cos \alpha\right\}c \\ 0 \end{bmatrix} + \begin{bmatrix} (r * \alpha) \\ 0 \\ 0 \end{bmatrix} \quad (3.21)$$

$$[\vec{c}'] = \begin{bmatrix} -\left\{\left(\frac{\sqrt{3}}{2}\right) \cos \alpha\right\} c + \left\{\left(\frac{1}{2}\right) \sin \alpha\right\} c + (r * \alpha) \\ \left\{\left(\frac{\sqrt{3}}{2}\right) \sin \alpha\right\} c + \left\{\left(\frac{1}{2}\right) \cos \alpha\right\} c \\ 0 \end{bmatrix} \quad (3.22)$$

$$[\vec{l}_1'] = [R_z(-\alpha_z)] * [\vec{l}_1] + [\vec{s}] \quad (3.23)$$

$$[\vec{l}_1'] = \begin{bmatrix} -(\sqrt{3} \cos \alpha)c + (r * \alpha) \\ (\sqrt{3} \sin \alpha)c \\ 0 \end{bmatrix} \quad (3.24)$$

$$[\vec{l}_2'] = [R_z(-\alpha_z)] * [\vec{l}_2] + [\vec{s}] \quad (3.25)$$

$$[\vec{l}_2'] = \begin{bmatrix} -\left\{\left(\frac{\sqrt{3}}{2}\right) \cos \alpha\right\} c + \left\{\left(\frac{3}{2}\right) \sin \alpha\right\} c + (r * \alpha) \\ \left\{\left(\frac{\sqrt{3}}{2}\right) \sin \alpha\right\} c + \left\{\left(\frac{3}{2}\right) \cos \alpha\right\} c \\ 0 \end{bmatrix} \quad (3.26)$$

Equations (3.22), (3.24), and (3.26) are then iterated through incrementally from $0^\circ < \alpha < 120^\circ$ per Tri-Wheel rotation, and the resulting x and y-coordinates are plotted. The resolution of each rotation is set at 1000 points per rotation.

METHOD 2: Rodrigues' Rotation Formula gives an efficient method for computing the rotation matrix $R(\omega, \theta)$ corresponding to a rotation by an angle θ (given in radians) about a fixed axis through the origin specified by the unit vector $\omega = (\omega_x, \omega_y, \omega_z) \in \mathbb{R}^3$ at unit velocity [15]. The rotation matrix can be analogously written in terms of exponential coordinates for rotation. This relationship is quickly derived by considering

the velocity of a point attached to a rotating body, as shown in [15]. A time-invariant linear differential equation is written and integrated to yield the simple relationship:

$$R(\omega, \theta) = e^{\hat{\omega}\theta} \quad (3.27)$$

Here, $\hat{\omega}$ is a skew-symmetric or antisymmetric matrix which is defined analogously to the differential matrix representation of the curl operator [15]:

$$\hat{\omega} = \begin{bmatrix} 0 & -\omega_z & \omega_y \\ \omega_z & 0 & -\omega_x \\ -\omega_y & \omega_x & 0 \end{bmatrix} \quad (3.28)$$

The hat operator promotes a vector to a matrix, essentially acting as the cross-product operator. Using a general variable example, $v \times \omega = \hat{v}\omega$. Geometrically, the skew-symmetric matrix corresponds to the axis of rotation while the exponential map generates the rotation about that axis by some specified amount θ . Rodrigues' Formula uses this relationship to compute a rotation matrix as given by [15]:

$$e^{\hat{\omega}\theta} = I + \hat{\omega} \sin\theta + \hat{\omega}^2(1 - \cos\theta) \quad (3.29)$$

where I is the 3x3 identity matrix composed of ones on the diagonal and zeros elsewhere. Defining $v_\theta = 1 - \cos\theta$, $s_\theta = \sin\theta$, and $c_\theta = \cos\theta$, this equation can be expanded in matrix form as follows [15]:

$$e^{\hat{\omega}\theta} = \begin{bmatrix} \omega_1^2 v_\theta + c_\theta & \omega_1 \omega_2 v_\theta - \omega_3 s_\theta & \omega_1 \omega_3 v_\theta + \omega_2 s_\theta \\ \omega_1 \omega_2 v_\theta + \omega_3 s_\theta & \omega_2^2 v_\theta + c_\theta & \omega_2 \omega_3 v_\theta - \omega_1 s_\theta \\ \omega_1 \omega_3 v_\theta - \omega_2 s_\theta & \omega_2 \omega_3 v_\theta + \omega_1 s_\theta & \omega_3^2 v_\theta + c_\theta \end{bmatrix} \quad (3.30)$$

Substituting in α for the rotation angle θ and using $\omega = (\omega_1, \omega_2, \omega_3) = (0, 0, 1)$ as the rotation axis, the rotation matrix can be simplified and computed. Substituting the correct values of ω for this analysis, the simplified rotation matrix is:

$$e^{\hat{\omega}\theta} = \begin{bmatrix} c_\theta & -s_\theta & 0 \\ s_\theta & c_\theta & 0 \\ 0 & 0 & 1 \end{bmatrix} \quad (3.31)$$

As expected, this rotation matrix is exactly the same as the Euler angle rotation matrix used in Equation (3.1) and then again in Method 1.

The rotation and translation of vectors and points as a result of rigid body transformations can be represented easily in terms of vectors and matrices in \mathbb{R}^4 . The homogeneous representation of a transformation is a uniform representation of points and vectors. The number 1 is appended to the coordinates of any point to produce a vector in \mathbb{R}^4 . The coordinates of the top wheel, trailing ground wheel, and centroid are modified as follows:

$$[\vec{c}] = \begin{bmatrix} -\left(\sqrt{3}/2\right)c \\ (1/2)c \\ 0 \\ 1 \end{bmatrix} \quad (3.32)$$

$$[\vec{l}_1] = \begin{bmatrix} -\sqrt{3}c \\ 0 \\ 0 \\ 1 \end{bmatrix} \quad (3.33)$$

$$[\vec{l}_2] = \begin{bmatrix} -\left(\sqrt{3}/2\right)c \\ \left(3/2\right)c \\ 0 \\ 1 \end{bmatrix} \quad (3.34)$$

Using the preceding point notation, it is possible to represent the rigid body transformation as a 4x4 matrix g_{ab} where $g_{ab} = (p_{ab}, R_{ab})$. The matrix $g_{ab} \in SE(3)$ is a member of the special Euclidian set in three dimensions. This means that a right-handed coordinate frame is used and that space is flat. The subscript ‘a’ represents the spatial frame fixed in space, and the ‘b’ subscript represents some body frame attached to the Tri-Wheel while rotating. Thus, g_{ab} specifies the configuration of the ‘b’ frame relative to the ‘a’ frame. This specification involves two components: first, a 3x1 vector p_{ab} that gives the position of the origin of the ‘b’ frame with respect to the fixed ‘a’ frame, and second, a 3x3 rotation matrix R_{ab} that provides the orientation of frame ‘b’ in space relative to the fixed frame ‘a’. Then for some point q , $q_a = g_{ab} * q_b$ maps coordinates of q from the moving body frame to the fixed spatial frame [15]. This transformation is written as a 4x4 augmented matrix such that its dimensions ensure matrix multiplication with the 4x1 homogeneous representations of the Tri-Wheel points of interest.

$$g_{ab} = \begin{bmatrix} R_{ab} & p_{ab} \\ 0 & 1 \end{bmatrix} \quad (3.35)$$

In this analysis, p_{ab} is used to represent the horizontal translation experienced during Tumbling Mode.

$$p_{ab} = \begin{bmatrix} (r * \alpha) \\ 0 \\ 0 \end{bmatrix} \quad (3.36)$$

Using the rotation matrix obtained in Equation (3.31), the complete transformation is written for some angle of rotation $-\alpha$.

$$g_{ab} = \begin{bmatrix} \cos \alpha & \sin \alpha & 0 & (r * \alpha) \\ -\sin \alpha & \cos \alpha & 0 & 0 \\ 0 & 0 & 1 & 0 \\ 0 & 0 & 0 & 1 \end{bmatrix} \quad (3.37)$$

This position mapping matrix is then applied to the points in question to provide a linear form of an affine transformation (a transformation that preserves straight lines, points, and planes) [15].

$$[\vec{c}'] = \begin{bmatrix} \cos \alpha & \sin \alpha & 0 & (r * \alpha) \\ -\sin \alpha & \cos \alpha & 0 & 0 \\ 0 & 0 & 1 & 0 \\ 0 & 0 & 0 & 1 \end{bmatrix} * \begin{bmatrix} -(\sqrt{3}/2)c \\ (1/2)c \\ 0 \\ 1 \end{bmatrix} \quad (3.38)$$

$$[\vec{c}'] = \begin{bmatrix} \left\{ -(\sqrt{3}/2)\cos \alpha + (1/2)\sin \alpha \right\} c + (r * \alpha) \\ \left\{ (\sqrt{3}/2)\sin \alpha + (1/2)\cos \alpha \right\} c \\ 0 \\ 1 \end{bmatrix} \quad (3.39)$$

$$[\vec{l}_1'] = \begin{bmatrix} \cos \alpha & \sin \alpha & 0 & (r * \alpha) \\ -\sin \alpha & \cos \alpha & 0 & 0 \\ 0 & 0 & 1 & 0 \\ 0 & 0 & 0 & 1 \end{bmatrix} * \begin{bmatrix} -\sqrt{3}c \\ 0 \\ 0 \\ 1 \end{bmatrix} \quad (3.40)$$

$$[\vec{l}_1'] = \begin{bmatrix} -(\sqrt{3} \cos \alpha)c + (r * \alpha) \\ (\sqrt{3} \sin \alpha)c \\ 0 \\ 1 \end{bmatrix} \quad (3.41)$$

$$[\vec{l}_2'] = \begin{bmatrix} \cos \alpha & \sin \alpha & 0 & (r * \alpha) \\ -\sin \alpha & \cos \alpha & 0 & 0 \\ 0 & 0 & 1 & 0 \\ 0 & 0 & 0 & 1 \end{bmatrix} * \begin{bmatrix} -(\sqrt{3}/2)c \\ (3/2)c \\ 0 \\ 1 \end{bmatrix} \quad (3.42)$$

$$[\vec{l}_2'] = \begin{bmatrix} \left\{ -(\sqrt{3}/2)\cos \alpha + (3/2)\sin \alpha \right\}c + (r * \alpha) \\ \left\{ (\sqrt{3}/2)\sin \alpha + (3/2)\cos \alpha \right\}c \\ 0 \\ 1 \end{bmatrix} \quad (3.43)$$

The value of 1 located in position [4, 1] of each matrix is simply used to ensure a point to point mapping. Removing it from Equations (3.39), (3.41), and (3.43), it is evident that these expressions for the transformed points of interest are identical to those obtained in Method 1 Equations (3.22), (3.24), and (3.26). The cost of the convenience to have a homogeneous (linear) representation of the Tri-Wheel rigid body motion is the increase in number of dimensions of the quantities from 3 to 4 [15].

Now that the mapping technique has been confirmed using two different methods, Equations (3.39), (3.41), and (3.43) are then iterated through incrementally from $0^\circ < \alpha < 120^\circ$ per Tri-Wheel rotation, and the resulting x and y-coordinates are plotted. The leading ground wheel horizontal displacement is calculated using Equation (3.18). For purposes of comparison, this first plot uses values of $c = 4.0$ and $r = 1.5$ in as is used in Figure 3.4.

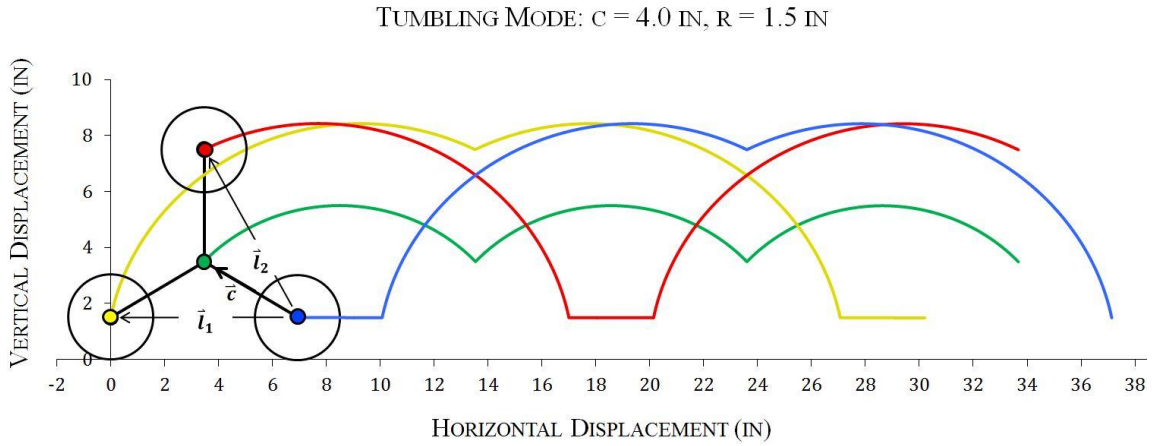


Figure 3.5: Tumbling Mode Trajectory Plot

The resulting graph shows a clear stretching of the plot in the horizontal direction when compared to the graph derived from the same parameters for Inching Mode seen in Figure 3.4. This is expected due to the continuous rolling of the leading ground wheel, which is represented by the horizontal line segments on the graph. The maximum displacement reached by the three wheel centers is once again equal to 8.43 in, as evaluated in Inching Mode. The maximum vertical displacement reached by the centroid is 5.5 in. The framework is now in place to vary the parameters r and c for optimization of stair climbing.

3.4 Stair Climbing Optimization

Research is conducted to determine five typical pairs of rise and run measurements for common staircase sizes. This data is provided in Table 3.1 below [16]. Note that the parameter β represents the approximate angle of ascent for each staircase with a given rise and run. It is assumed that the rise and run values remain fixed along the stairs.

<i>Rise (in)</i>	<i>Run (in)</i>	β ($^{\circ}$)
7.875	10	38.2
7.625	10.5	36.0
7	11	32.5
6	12	26.6
5	13	21.0

Table 3.1: Rise and Run Parameter for Common Staircases

From these data, it is concluded that the maximum achievable approach height h_{max} must be greater than or equal to 8 in to clear the maximum height of one step, 7.875 in. The clearance of 0.125 in at minimum is included to account for any unknown depression of the pneumatic tires.

<i>Maximize</i>	<i>Justification</i>	<i>Minimize</i>	<i>Justification</i>
Stair climbing adaptability	Research objective; Tri-Wheel must be sized appropriately for any given common staircase.	Overall envelope size of Tri-Wheel	Sizing any larger than absolutely necessary to climb stairs may interfere with missions occurring in tight spaces. Also, if multiple Tri-Wheels are to be used on one vehicle, they cannot intersect.
Wheel Diameter	Lower RPM is required to achieve a higher speed in driving mode.	Distance between leading edge of robot and stairs	Interference between robot chassis and steps could impede stair climbing.
Wheel Diameter	Allows for more ground clearance and creates larger buffer between gearing behind spokes and the environment.	Horizontal translation s while tumbling	Enables Tri-Wheel to rotate fully on steps with short runs.
h_{max}	Enables Tri-Wheel to climb over larger obstacles in excess of stair climbing		

Table 3.2: Maximize & Minimize Considerations for Optimization

To begin the general thought process for sizing optimization, consideration is given to which parameters or characteristics should be maximized and which should be minimized by the final design. This information is organized in Table 3.2. Notice that this is not a clear list of what should be done and what should not be done. There are certain parameters such as the wheel diameter that have good reason to be maximized, but doing so also increases the horizontal translation s while tumbling. The goal is to determine a configuration which optimizes the Tri-Wheel such that it finds a balance between these sometimes conflicting characteristics and determines how much of a difference increasing one variable may have on the whole system.

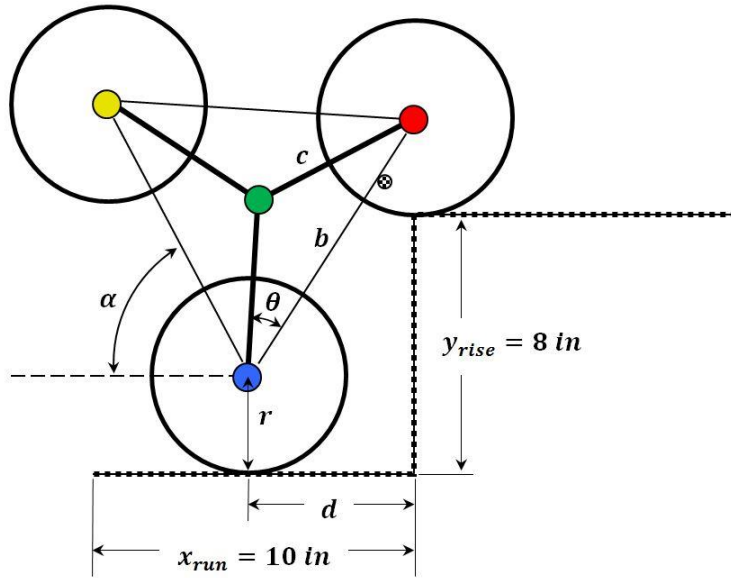


Figure 3.6: Initial Tri-Wheel placement on Maximum Step Height

Assuming a solid staircase, it is important to determine the distance away from the step at which Tumbling Mode should be initially engaged, d_t . This distance is crucial when determining the wheel radius since the horizontal rolling distance is proportional to the radius r . The objective is to specify this distance such that the centroid of the top wheel is collinear with the vertical edge of the step when the step rise is maximized at 8

in to ensure that there is sufficient contact made with the step. If this is the case, then the wheel centroid will be located to the right of the step's vertical edge for lower step rise values, ensuring even better contact with the flat step surface. Figure 3.6 shows the maximum case of rise is being considered: $x_{run} = 10$ in and $y_{rise} = 8$ in. The variable d is calculated using the Pythagorean Theorem:

$$b^2 = y_{rise}^2 + d^2 \quad (3.44)$$

where:

$$b = 2 * (c \cos \theta) \quad (3.45)$$

Because this relationship is desired for the maximum step height, substitutions can be made for a value of $y_{rise} = 8$ in, and it is known that $\theta = 30^\circ$. Equation (3.44) can then be rearranged as:

$$d^2 = -8^2 + (\sqrt{3}c)^2 \quad (3.46)$$

which results in:

$$d = \sqrt{3c^2 - 64} \quad (3.47)$$

Keeping this relationship in mind as well as the considerations presented in Table 3.2, a list of derived requirements is formulated in order to achieve the research objectives presented and ultimately create a Tri-Wheel sized to tackle stair climbing. These derived requirements and justifications for their inclusion are summarized in Table 3.3 below. Recall that h is the step approach height. The value h_{max} then represents the maximum possible step approach height. The position x_0 marks the initial starting position

for the leading ground wheel before it begins to tumble, and as the leading ground wheel rolls forward, it moves some horizontal distance s .

<i>Derived Requirement</i>	<i>Justification</i>
$h_{max} \geq 8 \text{ in}$	Maximum step approach height must exceed maximum step height.
$d_t = (s_{h=8_{RHS}} + d) < 10$	The distance away from the step at which Tumbling Mode is initially engaged must be less than the minimum run of a step.
$s_{\alpha=120^\circ} < (10 - r)$	This requirement ensures that there is enough leading ground wheel roll space to allow the Tri-Wheel to rotate fully back to the desired h value once ascending the second, third, etc. steps. On a step with minimum run of 10 in, the distance available to roll without the wheel bumping into the next step is equal to $(10-r)$. Thus, if the Tri-Wheel can complete a full rotation and translate forward by $s_{\alpha=120^\circ}$ in a distance less than $(10-r)$, there is no interference between the next step and the wheel. This is not to say that it would be a failure mode if the wheel bumped into an object before tumbling. However, that mode is best explored in testing due to differences in potential robot chassis locations relative to the Tri-Wheel.
$(d_t - r - s_{h=5}) > 0$	When the Tri-Wheel begins to tumble at d_t , there must be enough rolling distance left for the leading ground wheel to allow the assembly to plant its top wheel on a step with the minimum rise of 5 in without the leading ground wheel bumping into the step.
$(13 - r) - s_{\alpha=120^\circ} > 0$	Assume that the Tri-Wheel has approached a step with rise of 5 in and run of 13 in after beginning to tumble at d_t and successfully planted its top wheel on the first step. After this point, there must be enough roll space for the new leading ground wheel to advance forward along subsequent steps until the new top wheel reaches $h = 5$ in once again to continue the cycle.

Table 3.3: Kinematics Analysis Derived Requirements

After studying numerous values of c and r , a smaller range of possibilities for the spoke length and wheel radius are converged upon after consideration of the derived requirements criteria. For each combination of spoke length and wheel radius, the maximum approach height h , the horizontal distance traversed by the leading ground wheel to arrive at that maximum height $s_{h_{max}}$, the initial starting position of the leading ground wheel x_0 , and the graphed x- and y-coordinates for maximum values of the centroid $(x, y)_{c_{max}}$ and stair approach height $(x, y)_{h_{max}}$ are included in Table 3.4 below.

c	r	h_{max}	x_0	$(x, y)_{h_{max}}$	$s_{h_{max}}$	$(x, y)_{c_{max}}$
5.2	2	9.007	9.007	(10.054, 11.007)	1.047	(11.101, 7.200)
5.2	2.5	9.007	9.007	(10.316, 11.507)	1.309	(11.625, 7.700)
5.2	3	9.007	9.007	(10.577, 12.007)	1.571	(12.148, 8.200)
5.2	3.5	9.007	9.007	(10.839, 12.507)	1.833	(12.672, 8.700)
5.5	2	9.526	9.526	(10.573, 11.526)	1.047	(11.621, 7.500)
5.5	2.5	9.526	9.526	(10.835, 12.026)	1.309	(12.144, 8.000)
5.5	3	9.526	9.526	(11.097, 12.526)	1.571	(12.668, 8.500)
6	2	10.392	10.392	(11.440, 12.392)	1.047	(12.487, 8.000)
6	2.5	10.392	10.392	(11.701, 12.892)	1.309	(13.010, 8.500)
6	3	10.392	10.392	(11.963, 13.392)	1.571	(13.534, 9.000)

* Please Note: All units are inches.

Table 3.4: Sizing Optimization Data 1

From this preliminary information, a few trends are apparent. Increasing the spoke length is the only way to increase the maximum approach height. Wheel radius has no effect because any height added by the radius of the leading ground wheel is counteracted by the wheel radius of the top wheel, resulting in a maximum stair approach height of $h_{max} = r + b - r = b$. As c is increased, the overall envelope size of the Tri-Wheel increases as indicated by x_0 . Also as expected, $s_{h_{max}}$ increases when wheel radius increases and is independent of the spoke length. The x- and y-positions of the maximum approach height and centroid are affected proportionally by both the spoke length and the wheel radius.

Because the step approach height $h = 8$ in is critical to this analysis as the worst case scenario, Table 3.5 provides the x-coordinate, angle, and distance traveled to reach an approach height of 8 in. Note that for $c = 5.2$, $h = 8$ on the left hand side of h_{max} and

on the right hand side of h_{max} whereas spoke lengths of 5.5 and 6.0 yield a Tri-Wheel configuration that provides a value of h greater than 8.0 even before tumbling begins.

c	r	$x_{h=8_{LHS}}$	$\alpha_{h=8_{LHS}}$	$s_{h=8_{LHS}}$	$x_{h=8_{RHS}}$	$\alpha_{h=8_{RHS}}$	$s_{h=8_{RHS}}$
5.2	2	4.970	2.800	0.098	15.138	57.400	2.004
5.2	2.5	4.997	2.800	0.122	15.638	57.400	2.505
5.2	3	5.017	2.800	0.147	16.138	57.400	3.005
5.2	3.5	5.041	0.000	0.000	16.638	57.400	3.506
5.5	2	♦	0.000	0.000	16.879	62.900	2.196
5.5	2.5	♦	0.000	0.000	17.427	62.900	2.745
5.5	3	♦	0.000	0.000	17.975	62.900	3.293
6	2	§	0.000	0.000	19.446	69.700	2.433
6	2.5	§	0.000	0.000	20.054	69.700	3.041
6	3	§	0.000	0.000	20.661	69.700	3.649

* Please Note: Lengths and coordinates are measured in inches. Angles are measured in degrees.

♦ $h = 8.25$ before tumbling is initiated.

§ $h = 9.00$ before tumbling is initiated.

Table 3.5: Sizing Optimization Data 2

c	r	$x_{h=5}$	$\alpha_{h=5}$	$s_{h=5}$	$s_{\alpha=120^\circ}$	$\Delta s_{h=8_{RHS} \rightarrow h=5}$
5.2	2	20.069	86.400	3.016	4.189	1.012
5.2	2.5	20.822	86.400	3.770	5.236	1.265
5.2	3	21.575	86.400	4.524	6.283	1.518
5.2	3.5	22.328	86.400	5.278	7.330	1.772
5.5	2	20.763	88.400	3.086	4.189	0.890
5.5	2.5	21.521	88.400	3.857	5.236	1.113
5.5	3	22.291	88.400	4.629	6.283	1.335
6	2	21.853	91.300	3.187	4.189	0.754
6	2.5	22.649	91.300	3.984	5.236	0.942
6	3	23.445	91.300	4.780	6.283	1.131

* Please Note: Lengths and coordinates are measured in inches. Angles are measured in degrees.

Table 3.6: Sizing Optimization Data 3

After considering the step highest rise of 8 in, the lowest rise of 5 in must also be considered to bound the results and ensure that the distance at which tumbling occurs allows the Tri-Wheel to successfully climb lower stairs. All the same values are investigated in Table 3.6. In addition, this table provides information about the horizontal displacement of the leading ground wheel for a full 120° rotation, $s_{\alpha=120^\circ}$ and the difference between the horizontal displacement to reach an approach height of 5 in from an approach height of 8 in, $\Delta s_{h=8_{RHS} \rightarrow h=5}$.

The spoke length of 5.2 is eliminated since its resting stair approach height before tumbling is less than 8 inches. While it technically still meets the derived requirements, it is less advantageous than the other options. A wheel radius of 3 inches is selected due to the benefits discussed in Table 3.2 related to maximizing the wheel diameter. Though this causes greater horizontal displacement of the leading ground wheel, the benefits outweigh the cost and still provide an opportunity to satisfy the derived requirements. The spoke length of 6.0 in is eliminated because the additional length increases the overall envelope size of the Tri-Wheel and makes it difficult to satisfy the derived requirements laid out previously. As a result, the desired configuration converged upon is a spoke length $c = 5.5$ in and a wheel radius $r = 3.0$ in.

In order to ensure that all derived requirements are met, the previous table is revisited, and the derived requirements are computed for the selected values. Table 3.7 presents this information and clearly shows that all derived requirements are met by the selected configuration.

<i>Derived Requirement</i>	<i>Computed Values for c = 5.5 in & r = 3 in</i>	<i>Capability</i>
$h_{max} \geq 8 \text{ in}$	$h_{max} = 9.526 \geq 8 \text{ in}$	Meets
$d_t = (s_{h=8_{RHS}} + d) < 10$	$d_t = (3.293 + 5.1720) < 10$ $d_t = 8.465 < 10$	Meets
$s_{\alpha=120^\circ} < (10 - r)$	$s_{\alpha=120^\circ} = 6.283 < (10 - 3)$ $6.283 < 7$	Meets
$(d_t - r - s_{h=5}) > 0$	$(8.465 - 3 - 4.629) > 0$ $0.863 > 0$	Meets
$(13 - r) - s_{\alpha=120^\circ} > 0$	$(13 - 3) - 6.283 > 0$ $3.717 > 0$	Meets

Table 3.7: Kinematics Analysis Derived Requirements v. Capability Compliance

A plot of the selected Tri-Wheel sizing for a single rotation is provided in Figure 3.7. The total horizontal span of the trajectory is 25.34 in, and the horizontal leading ground wheel advances 6.28 in as it goes through one full rotation. This sizing is optimal for the research objectives stated and fulfills all derived requirements.

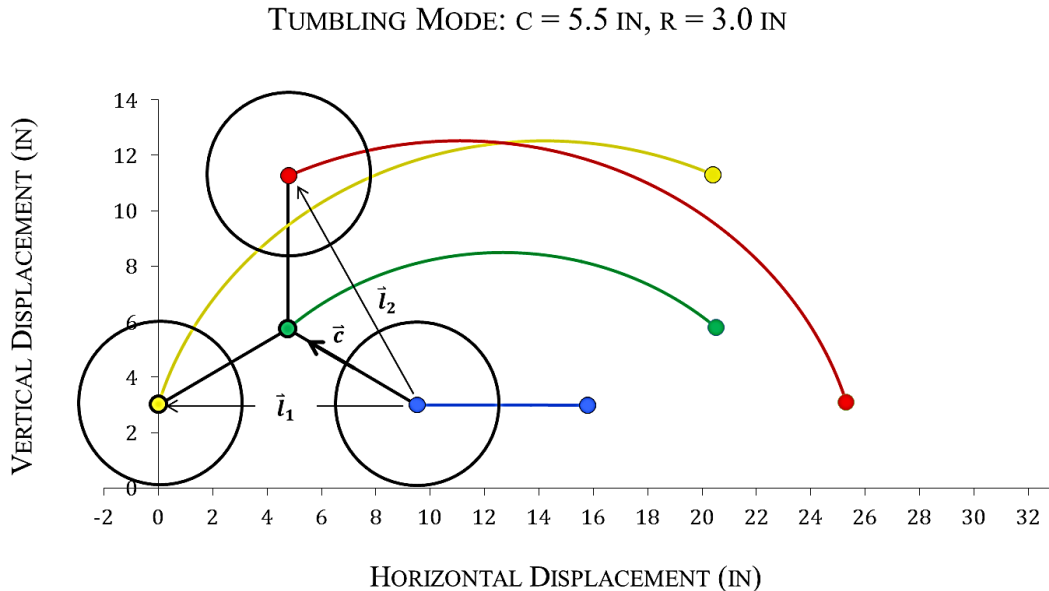


Figure 3.7: Trajectory Plot for Selected Sizing – Single Turn

The trajectory plot for three turns of the Tri-Wheel with this sizing is given in Figure 3.8. For comparison, this plot can be viewed in relation to Figure 3.4: Inching Mode Trajectory Plot and Figure 3.5: Tumbling Mode Trajectory Plot to see how the sizing has ultimately changed the Tri-Wheel motion in space.

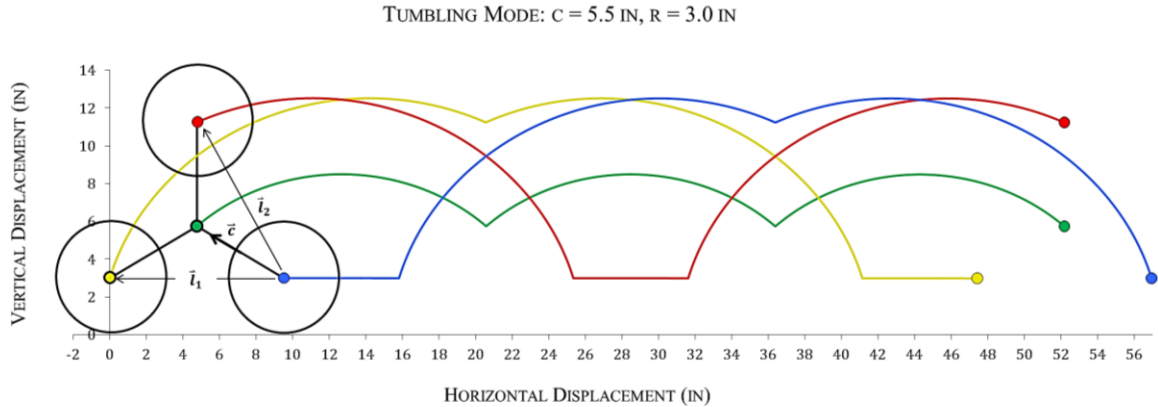


Figure 3.8: Trajectory Plot for Selected Sizing - Three Turns

This information is further dissected in Figure 3.9: Tumbling Mode Subplots for Selected Parameters. These subplots yield individual trends for each of the Tri-Wheel vertices and the centroid. It is clear that the three vertices cyclically operate in the same trend depending on which position each is in from the beginning of Tumbling Mode. Note that the cusps and sharp turns in behavior indicate the beginning or ending of one turn into the next.

TUMBLING MODE INDIVIDUAL VERTICES: $C = 5.5$ IN, $R = 3.0$ IN

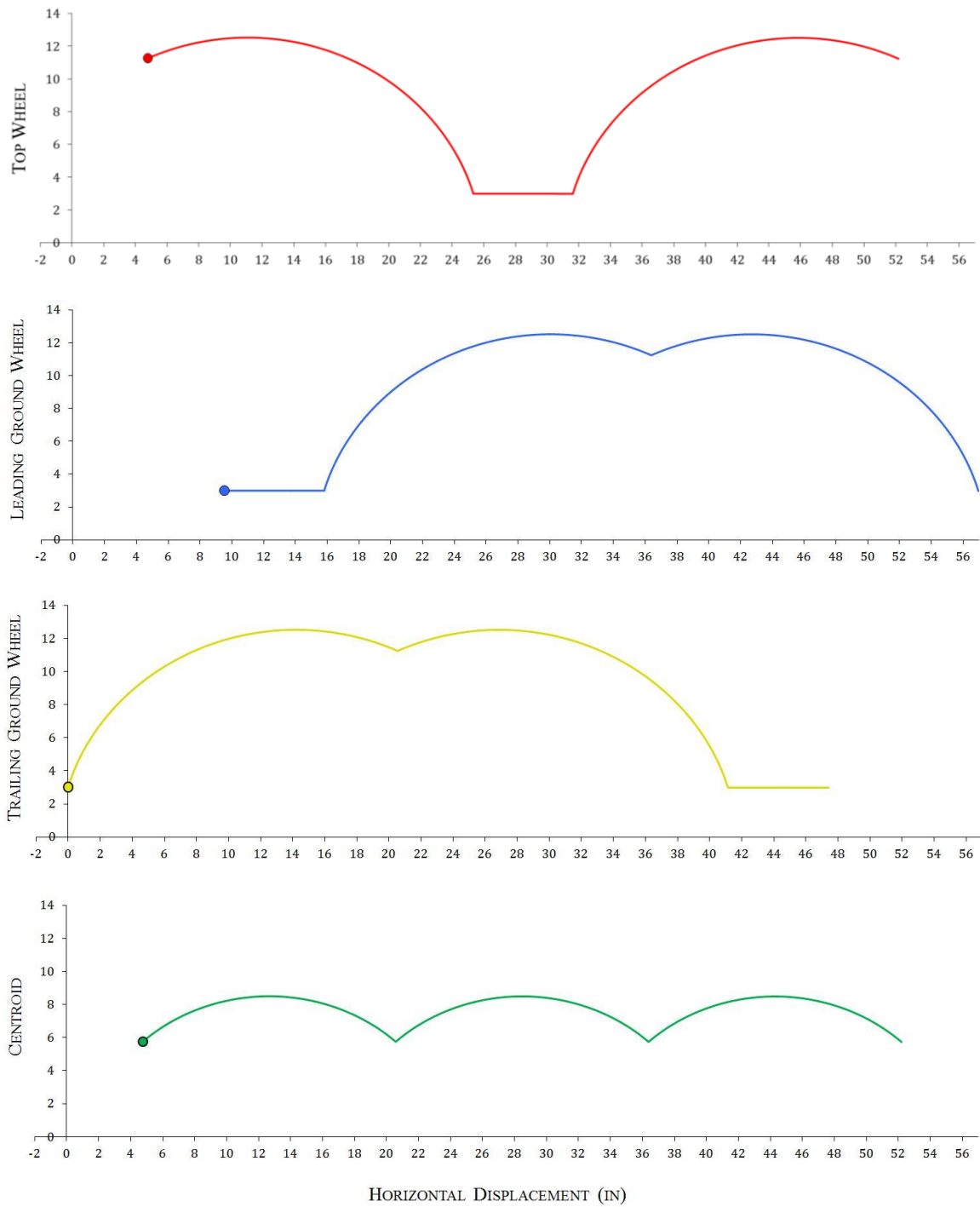


Figure 3.9: Tumbling Mode Subplots for Selected Parameters

4 DESIGN OF GEARING SYSTEM

4.1 Introduction

Once the overall envelope size of the Tri-Wheel is constrained by the kinematic analysis performed in Chapter 3, the mechanism of power transmission must be specified. Power transmission is best explained as the transfer of energy from its place of generation or storage to some location where it does work [17]. In order to transmit power from the DC motor to the wheels, a gearing system is designed and optimized. Gears are toothed members that transmit rotary motion between shafts. Other means of transmitting the mechanical power such as belts and pulleys are considered but ultimately not selected. As stated in the research objectives, one of the most integral features of this design is that the mechanism is robust and will not fail during critical missions. For this reason, gears are selected for their reliability and ruggedness at the expense of weight. Gears are also an extremely efficient method of transmitting power at any desired speed ratio; in fact, many gears have efficiencies of approximately 98% or more [18].

Spur gears are selected for the Tri-Wheel due to their ease of manufacturing and installation as well as their relative low cost when compared with other options such as helical gears. Spur gears are characterized by teeth that are straight and parallel to the axis of the shaft carrying the gear [19]. It is helpful to think of a gear modeled as a lever, transmitting a new value of torque depending on the radius (lever arm) at which the teeth of one gear push with some force against teeth of another gear meshed with it. Again,

torque and speed (angular velocity, in this case), are inversely proportional. This being the case, gears can be combined in a variety of configurations to increase or decrease speed or torque as desired. This relationship is expressed by the fundamental law of gearing [19]:

$$VR = \frac{\omega_1}{\omega_2} = \frac{n_1}{n_2} = \frac{R_2}{R_1} = \frac{N_2}{N_1} = \frac{\text{speed}_1}{\text{speed}_2} = \frac{\text{size}_2}{\text{size}_1} \quad (4.1)$$

where VR is the velocity ratio of the gear train (also called the gear ratio), ω is the angular velocity, n is the rotational speed in RPM, R is pitch radius of the gear, and N is the number of teeth per gear. The subscript 1 refers to the input gear receiving power, and subscript 2 refers to the output gear. Gearing nomenclature will be discussed in greater detail later in this chapter. The takeaway of this equation is the recognition of the difference between a gear train classified as a speed reducer (decrease speed, increase torque) and one classified as a speed increaser (increase speed, decrease torque). For a speed reducer, $VR > 1$; for a speed increaser, $VR < 1$.

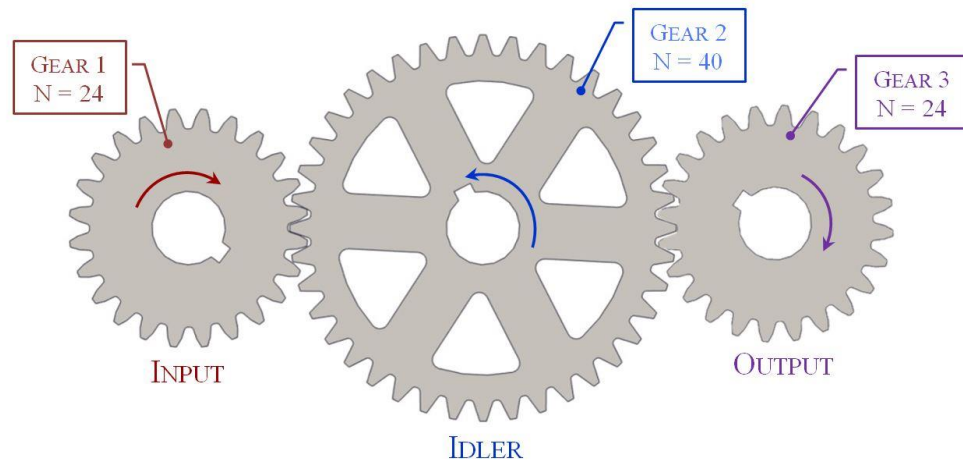


Figure 4.1: Spur Gear Train Example

Figure 4.1 provides an example of a gear train to be analyzed. Any gear that is situated between the input and output gears is known as an idler gear; idler gears are used to alter the direction of rotation rather than the numerical value of the speed ratio. An odd number of idlers causes the input and output shafts to rotate in the same direction while an even number of idlers causes rotation in opposite directions. By multiplying together the individual velocity ratios present between gears in a complete gear train, the total velocity ratio is obtained. In the case of the gear train presented in Figure 4.1, the following calculation is performed:

$$VR = \frac{N_2}{N_1} \cdot \frac{N_3}{N_2} = \frac{40}{24} \cdot \frac{24}{40} = 1 \quad (4.2)$$

This calculation illustrates the fact that any increase/decrease in velocity (and inversely proportional increase/decrease in torque) occurs as a direct result of the ratio between the input gear and the output gear regardless of the characteristics of any idler gears used in between. In general, when a smaller gear drives a larger gear, torque increases; when a larger gear drives a smaller gear, torque decreases.

It is also pertinent to clarify that the basic requirement of gear tooth geometry is the provision of angular velocity ratios that are exactly constant as gears mesh [20]. For instance, the velocity ratio between a 20-tooth and an 80-tooth gear should be precisely 4 in every position. The velocity ratio must not equal 3.99 or 4.01 as various gear tooth pairs come into mesh or out of mesh, respectively. The involute tooth profile ensures that this condition known as conjugate gear tooth action is satisfied and is therefore selected for use in the Tri-Wheel gearing design. For more information regarding the construction of an involute tooth shape and its unique properties, please reference [20].

The Tri-Wheel gearing system presents a design challenge in that it must be contained closely behind the spokes of the Tri-Wheel; ideally, this system should be compact enough that it can be contained in a housing that does not cut significantly into the 120° space between each of the three Tri-Wheel spokes. Figure 4.2 shows the final driving (left) and tumbling (right) gear sets and how compactly the system is configured to take up minimal space. The remainder of this chapter provides a detailed explanation of how this configuration is selected and what design factors were considered to ultimately converge upon this number of gears and their unique characteristics. Note that each gear is labeled with a letter and a number. The driving gears are designated by the letter “D,” and the tumbling gears are designated by the letter “T.” Each gear in the train receives a number beginning with 1 at the center gear and increasing toward the wheel to 4 in the case of the driving gears and 2 in the case of the tumbling gears. Though it is not shown clearly in the figure below, recall that the gears D2 and T2 are connected directly and keyed to a common shaft, ultimately enabling Tumbling Mode to occur.

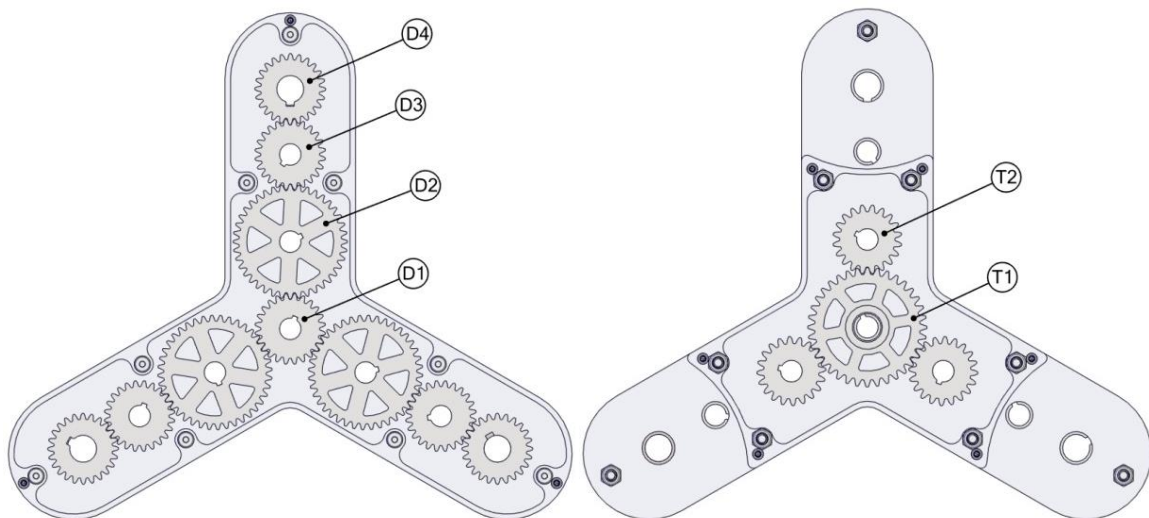


Figure 4.2: Selected Gearing Configuration

A gearing system for the Tri-Wheel locomotion concept must seek to balance the requirement for rapid linear velocity in Driving Mode and a high torque capacity in Tumbling Mode in order to ascend stairs and pull along a robot chassis weighing at most 200 lbs. Because speed and torque are inversely proportional, it is important that the ratio of the driving speed to the tumbling speed is not too large, lest the wheels will spin much too fast during Tumbling Mode and skid as the assembly rotates. Recall that when Tumbling Mode is engaged, the entire Tri-Wheel body rotates at one angular velocity defined by the gear ratio of Tumbling Mode; simultaneously, the three individual wheels will be rotating at a different (faster) angular velocity defined by the gear ratio between the central driving gear and the gear attached at the wheel shaft (D1 and D4). This is beneficial since the rotation will occur in the same direction, and the spinning wheels will help to pull along the rotating body. However, it is important to consider that the velocity ratio between the wheels and the Tri-Wheel body is reasonable.

There is no set minimum or maximum number of gears required to transmit power through the parallel gear sets. It is desirable to reduce the number of gears in general if possible given that some losses in efficiency occur with every gear mesh interaction. On the other hand, the use of too few gears to span the spoke length c establishes a need for large gears that cut into the tumbling space between the spokes. Chapter 4 reviews the calculations that lead to the final selected gearing configuration for the Tri-Wheel. Earlier versions of the Tri-Wheel gearing and an explanation of why those configurations have been discarded can be found in Appendix B: Tri-Wheel Design Iterations.

Before initiating detailed gearing analysis, it is a vital first step to understand how much power, speed, and torque is available for the Tri-Wheel system. This requires a brief evaluation of the motor selected. Next, analyses are performed to derive requirements for the maximum speed and corresponding gear ratio desired in Driving Mode and the minimum torque and corresponding gear ratio required to enter Tumbling Mode. With these gear ratios defined, appropriate gears can be specified for loading and size constraints imposed and then further optimized.

4.2 Speed and Torque Considerations

4.2.1 Motor Selection

The speed, torque, and acceleration that the Tri-Wheel achieves both in Driving Mode and in Tumbling Mode are functions of many factors: the power and torque characteristics of the motor used, the gear ratio defined, robot chassis weight, efficiency of the system transferring power from the motor to the wheels, and the wheel radius. The only explicit requirement of these mentioned is the motor to be used. The SLOPE Lab at NASA Glenn strives to make use of the same motors on all of their vehicles. For this reason, the motor selected is the Anaheim Automation BLY 344D-48V-3200RPM motor—a dual shaft brushless DC motor with high power density that weighs approximately 8.82 lbs [21]. Four of these motors would ideally be installed on the selected robot chassis to power each of the four anticipated Tri-Wheel assemblies. The motor torque curve is given in Figure 4.3, showing trends for Speed v. Torque as well as Current Draw v. Load Torque.

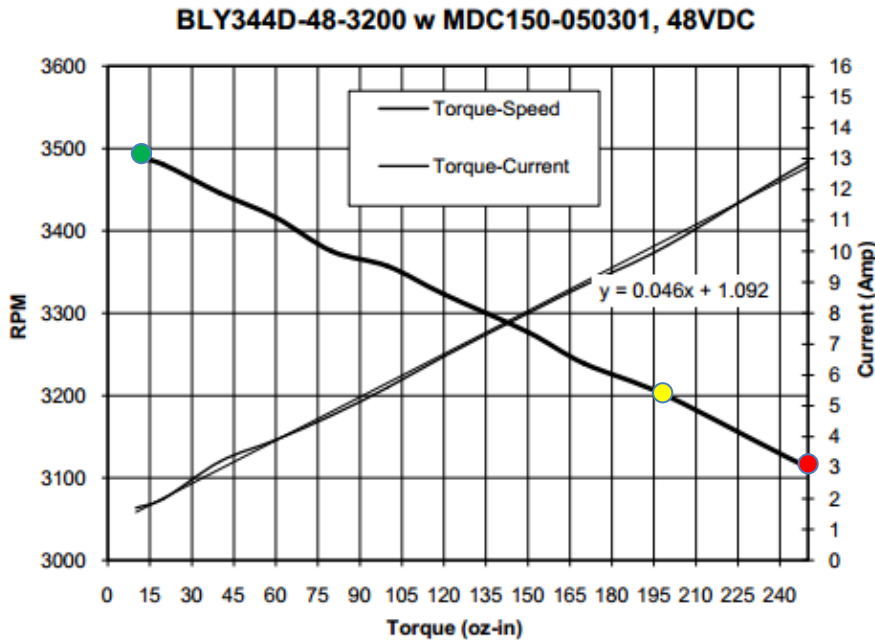


Figure 4.3: BLY 344D-48V-3200 Motor Torque Curve [21]

The motor converts electrical energy into mechanical energy using electromagnetic fields and rotating coils of wire. A voltage is applied to the motor, causing it to output some fixed amount of mechanical power [17]. This, in turn, causes the output shaft to spin and transmit power to the gear that is keyed to it at some given speed with a corresponding amount of torque. The motor outputs a fixed amount of power; thus, when more torque is required to overcome some load, the speed (RPM) will decrease. This general trend is shown by the closely approximated negative linear slope for the Torque-Speed curve. Depending on the amount of load placed on the motor, it also draws a specific amount of electrical current. The Torque-Current curve shows that at low loads, there is low current draw, and at high loading conditions, there is high current draw. This is accounted for by the nearly linear positive slope shown in Figure 4.3. The motor draws more electrical current depending on how much load is placed on it. So with a given load, the motor can only spin certain speeds.

Torque (oz-in)	Speed (RPM)	Torque-10:1 (oz-in)	Speed-10:1 (RPM)	P_{out} (W)	Current (A)	P_{in} (W)	η_m (%)
10	3490	100	349.0	25.83	1.7	81.6	31.65
20	3480	200	348.0	2	96	53.66	20
40	3446	400	344.6	3.2	153.6	66.41	40
60	3416	600	341.6	3.9	187.2	81.03	60
80	3375	800	337.5	4.7	225.6	88.57	80
100	3357	1000	335.7	5.6	268.8	92.43	100
120	3323	1200	332.3	6.6	316.8	93.16	120
150	3277	1500	327.7	8	384	94.74	150
170	3239	1700	323.9	8.9	427.2	95.39	170
200	3199	2000	319.9	473.51	10.2	489.6	96.71
250	3113	2500	311.3	12.9	619.2	93.02	250
300	3038	3000	303.8	674.51	15.2	729.6	92.45

Table 4.1: Motor Performance Operating Points

Table 4.1 contains test data provided by the manufacturer relating the motor's performance characteristics at a variety of operating points. Here, the cases of highest speed and lowest torque (green), average operating conditions (yellow), and lowest speed and highest torque (red) are featured. A 10:1 gearbox is then installed on each motor; this increases the output torque tenfold and simultaneously reduces the output RPM tenfold. These compact gearboxes are frequently in the range of 97% efficient [22]. Electric motors with an attached gearbox are often referred to as gearmotors. The resulting speed and torque for this gearmotor configuration are included in columns three and four of Table 4.1: Motor Performance Operating Points. The remaining columns reference the power in and out of the motor, current, and the actual performance efficiency of the unit, which is already accounted for in the quoted RPM and torque quantities. Thus, for

calculation purposes, Anaheim Automation does not recommend multiplying by an additional efficiency for the motor itself.

4.2.2 Driving Mode Speed and Gear Ratio

In order to select the proper gear ratio to increase or decrease the torque or RPM produced during Driving Mode as desired, basic calculations are performed to determine the velocity and acceleration of a theoretical robot platform that is outfitted with four Tri-Wheel assemblies. These calculations are performed under the assumption that the gear ratio between gears D1 and D4 is 1:1 (meaning that there is no increase in torque or speed between the input and output gears) as a baseline for the analysis. Assuming that the wheel rolls without slip, the maximum theoretical velocity obtained at the highest RPM, lowest torque operating point for the motor is calculated:

$$v = \frac{(RPM)}{60} \cdot \pi d \cdot \frac{2.237 \text{ MPH}}{1 \text{ m/s}} \quad (4.3)$$

Here, v is the maximum horizontal speed of one of the eight wheels contacting the ground for four Tri-Wheel assemblies in units of miles/hour. RPM measures the number of revolutions per minute that each individual wheel experiences as a result of the gearmotor output shaft, and the value of d in Equation (4.3) represents the 6 in diameter of the individual wheel used in units of m.

$$v = \frac{(348 \text{ RPM})}{60s} \cdot \pi \cdot 0.1524m \cdot \frac{2.237 \text{ MPH}}{1 \text{ m/s}} \quad (4.4)$$

$$v_{max} \approx 6.21 \text{ MPH} \quad (4.5)$$

This meets the explicit requirement to travel at the walking pace of approximately 3.31 MPH quoted in Chapter 1 as a minimum linear speed for the Tri-Wheel platform [13].

Considering frictional and rolling losses at the wheels and power losses from the gearing system, it is still absolutely reasonable to believe that the maximum speed will exceed this minimum requirement.

In order to analyze the acceleration of the system, the motor's stall torque or starting torque τ_s and free speed ω_{max} are determined. Stall torque is the maximum torque that the motor produces, at zero speed, which is associated with starting or overloading the motor [23]. The no-load speed or free speed is the maximum sustained speed the motor can attain when no load or torque is applied to the motor [23]. With the given data points from Table 4.1, a linear curve fit with R^2 value of 0.999 produces the following equation to relate torque and speed:

$$RPM = -0.015687 * \tau_m + 350.9 \quad (4.6)$$

From this equation, the motor free speed ω_{max} is the y-intercept of this line, meaning that $\omega_{max} = 350.9 \text{ RPM}$. This equation is rearranged to solve for τ_m (the motor torque in oz-in) as a function of RPM (the motor speed), substituting $RPM = 0$ for the case of stall torque:

$$\tau_s = 0 + \left(\frac{-350.9}{-0.015687} \right) = 22,368.8 \text{ (oz · in)/motor} \quad (4.7)$$

This is the stall torque for a single motor. However, each Tri-Wheel is powered by its own motor, totaling four motors total per robot platform. In this case, the torque and current specifications sum together, but the no-load speed does not [17]. For the case of four Tri-Wheels, the total stall torque is thus 89,475.4 oz-in, or 631.83 N-m. For

computational simplicity, some calculations are performed in SI units and then converted to English units.

Maximum acceleration will be experienced only for a fraction of a second when the motors accelerate the robot from rest. The torque will subsequently decrease as the *RPM* increases to a desired operating speed. This acceleration is calculated by using an approach defined by Lagrange's equations. Lagrange's method of evaluating dynamic systems provides a relatively direct technique by which the energy of the system is used to derive equations of motion. More detail regarding the particulars of Lagrangian dynamics can be found in [14].

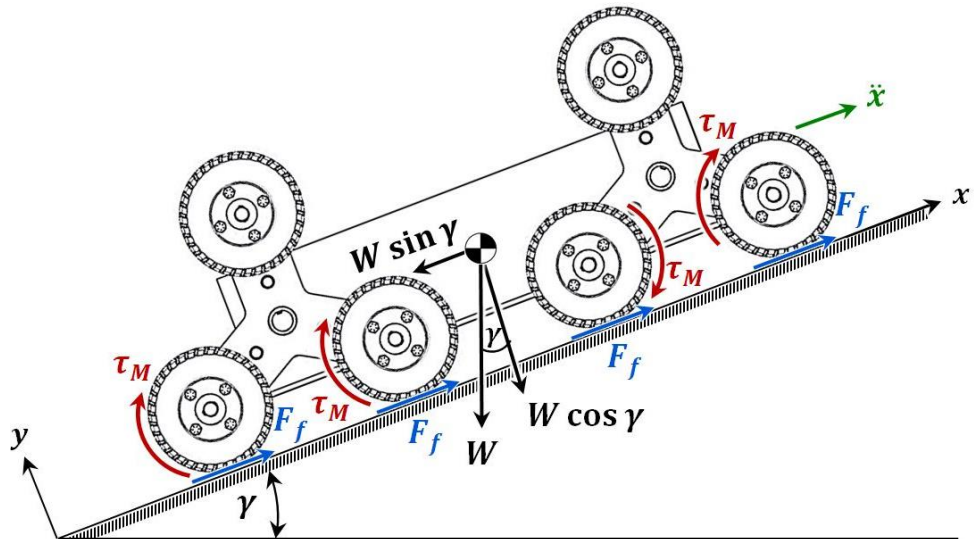


Figure 4.4: Free Body Diagram of Tri-Wheel Robot Platform on Flat Surface

The first step in writing Lagrange's equations is determining which generalized forces are wholly derivable from a potential function and writing energy equations that capture those forces. For the entire system, a single generalized coordinate x has been selected to describe the motion. The total mass of the system is expressed as:

$$m_S = m_C + 4 \cdot m_T \quad (4.8)$$

where m_S is the total mass of the system, m_C is the mass of the robot chassis, and m_T is the mass of one full Tri-Wheel assembly, including: gears, shafts, housing, wheels, and fasteners. Using conservative estimates, $m_C = 240 \text{ lb}$ and $m_T = 15 \text{ lb}$.

Next, an expression for the kinetic energy is written in terms of the generalized coordinate x accounting for the translational energies of the chassis and Tri-Wheels as well as the rotational kinetic energy of all 12 spinning wheels. The rotational kinetic energy of the gears in the Tri-Wheels is neglected because all moments of inertia with the exception of gear T1 ($I = 1.1 \text{ lb-in}^2$) are significantly less than 1.0 lb-in^2 .

$$T = \frac{1}{2} m_C \dot{x}^2 + 4 \left[\frac{1}{2} m_T \dot{x}^2 \right] + 12 \left[\frac{1}{2} I_W \omega_W^2 \right] \quad (4.9)$$

where \dot{x} is the linear velocity, I_W is the moment of inertia of the wheel system (including the inner tube, hub, and keyed flange that attaches the wheel to the shaft), and ω_W is the angular velocity of each driving wheel.

The angular velocity ω_W can be rewritten in terms of the linear velocity \dot{x} and substituted back into Equation (4.9):

$$\dot{x} = r \cdot \omega_W \quad (4.10)$$

$$\omega_W = \frac{\dot{x}}{r} \quad (4.11)$$

$$T = \frac{1}{2} m_C \dot{x}^2 + 4 \left[\frac{1}{2} m_T \dot{x}^2 \right] + 12 \left[\frac{1}{2} I_W \left(\frac{\dot{x}}{r} \right)^2 \right] \quad (4.12)$$

An expression for the potential energy is developed. Note that the force W in Figure 4.4: Free Body Diagram of Tri-Wheel Robot Platform on Flat Surface is expressed as the total system mass multiplied by the gravitational acceleration. This force acting at the angle of the incline γ produces potential energy computed as:

$$V = [m_C + 4 \cdot m_T] \cdot g \cdot \sin \gamma \cdot x \quad (4.13)$$

The Lagrangian function L is defined as the difference between the kinetic and potential energies and is written as follows:

$$L = T - V \quad (4.14)$$

$$L = \frac{1}{2} m_C \dot{x}^2 + 4 \left[\frac{1}{2} m_T \dot{x}^2 \right] + 12 \left[\frac{1}{2} I_W \left(\frac{\dot{x}}{r} \right)^2 \right] - [m_C + 4 \cdot m_T] g \sin \gamma \cdot x \quad (4.15)$$

The general form used to construct Lagrange's equation for any given generalized coordinate q is a function of the partial derivatives of L with respect to q described by the expression [14]:

$$\frac{d}{dt} \left(\frac{\partial L}{\partial \dot{q}_i} \right) - \frac{\partial L}{\partial q_i} = Q'_i \quad (i = 1, 2, \dots n) \quad (4.16)$$

If more than one generalized coordinate were to be used, Equation (4.55) would be written for each of the i generalized coordinates. In this case, q is simply replaced with the generalized coordinate x :

$$\frac{d}{dt} \left(\frac{\partial L}{\partial \dot{x}_i} \right) - \frac{\partial L}{\partial x_i} = Q'_i \quad (4.17)$$

Here, Q'_i are the generalized forces not derivable from a potential function, such as traction force resulting from rolling and friction F_f and the applied motor torque that powers each wheel τ_M . The traction/friction force and applied torque are applied to each of the eight wheels theoretically in contact with the ground. Thus, a free body diagram for an individual wheel is considered to introduce expressions for these generalized forces.

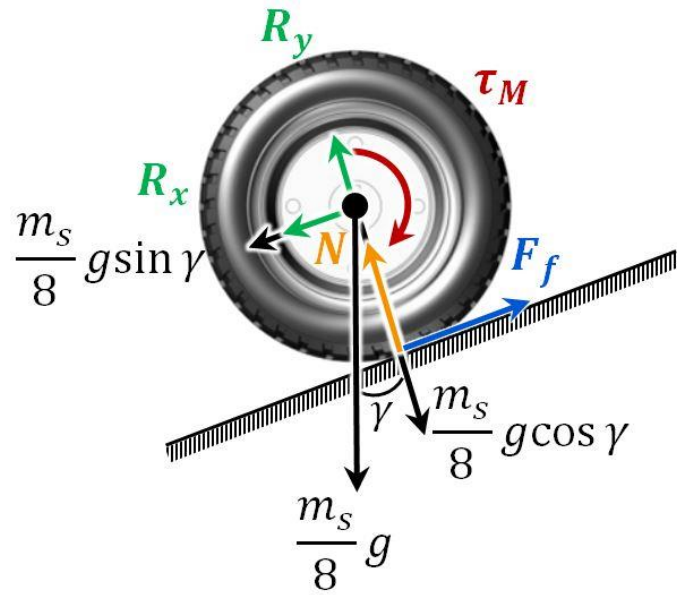


Figure 4.5: Individual Ground Wheel Free Body Diagram

The free body diagram in Figure 4.5 includes the traction/friction force, the applied motor torque, the weight of the entire system distributed to each wheel, the normal reaction force from the ground, and the hub reaction forces. Please note that while the hub reaction forces R_x and R_y have been included for completeness since this close-up view is simply of the wheel, these forces are disregarded for calculation purposes since they are internal forces that cancel out with respect to the entire system. From this diagram, expressions for the torque and the traction are written in terms of virtual work

and summed. These quantities are multiplied by eight to account for the individual forces acting on each of the eight wheels in contact with the ground.

First, the case of applied torque is considered. Consistent with previous notation, the variable r refers to the radius of each of the three individual wheels used in a Tri-Wheel assembly. The motor torque must be divided by two since each of the eight loaded wheels receives half the input torque from each of the four motors due to the gear trains connecting the motor input from the wheel output. The wheel torque is expressed as:

$$\delta W = \frac{\tau_M}{2} \cdot \delta\theta \quad (4.18)$$

$$x = r \cdot \theta \quad (4.19)$$

$$\delta x = r \cdot \delta\theta \quad (4.20)$$

$$\delta W = \frac{(\tau_M/2)}{r} \delta x \quad (4.21)$$

Next, the case of friction/traction is considered. The forces are summed in the y-direction and set equal to zero assuming no vertical acceleration. This allows for the virtual work of the frictional force to be similarly expressed in terms of the generalized coordinate x as an expression of virtual work:

$$\sum F_y = m \cdot a_y \quad (4.22)$$

$$N - \frac{m_S}{8} g \cdot \cos\gamma = 0 \quad (4.23)$$

$$N = \frac{m_s}{8} g \cdot \cos \gamma \quad (4.24)$$

$$\delta W = [C_{rr} \cdot N] \delta x \quad (4.25)$$

$$\delta W = \left[C_{rr} \left(\frac{m_s}{8} g \cdot \cos \gamma \right) \right] \delta x \quad (4.26)$$

Here, the coefficient C_{rr} is the coefficient of rolling resistance. Frequently, the static or kinetic friction force is used for an ideal rolling wheel depending on slippage. Rolling friction, also called traction, exists whenever one surface is rolling over another but not sliding [24]. It is used in this model because it more realistically reflects the friction resulting from any depression of the pneumatic tire. A frictional force is represented by multiplying the appropriate coefficient of friction by the normal force. The coefficient of rolling friction is less than that of either kinetic or static friction [24]. In fact, rolling friction can be thought of as a specialized case of static friction in that the wheel does not slide. Static friction is caused by imperfections in the surfaces of two objects that lock together and resist sliding. Rolling friction, however, is caused when one molecular surface is essentially peeled away from another. The coefficient of rolling resistance for a car tire on road ranges from approximately 0.010 to 0.035 [25]. The total generalized forces not derivable from a potential function are written as:

$$Q'_{TOT} = 8 \cdot \frac{(\tau_M/2)}{r} - 8 \cdot \left[C_{rr} \left(\frac{m_s}{8} g \cdot \cos \gamma \right) \right] \quad (4.27)$$

With the nonconservative generalized forces known, the partial derivatives in Lagrange's equation are evaluated. Referencing Equation (4.17), the partial of the

Lagrangian function with respect to the linear velocity \dot{x} is evaluated. Then, the time derivative of that quantity is calculated:

$$\frac{\partial L}{\partial \dot{x}} = m_C \dot{x} + 4[m_T \dot{x}] + 12 \left[I_W \left(\frac{\dot{x}}{r^2} \right) \right] \quad (4.28)$$

$$\frac{d}{dt} \left(\frac{\partial L}{\partial \dot{x}} \right) = m_C \ddot{x} + 4[m_T \ddot{x}] + 12 \left[I_W \left(\frac{\ddot{x}}{r^2} \right) \right] \quad (4.29)$$

In order to complete the expression of Lagrange's equation, the partial of the Lagrangian function with respect to the generalized coordinate x is evaluated:

$$\frac{\partial L}{\partial x} = -[m_C + 4 \cdot m_T] \cdot g \cdot \sin \gamma \quad (4.30)$$

Equations, (4.27), (4.29), and (4.30) are then substituted back into Equation (4.17) to yield:

$$\begin{aligned} & m_C \ddot{x} + 4[m_T \ddot{x}] + 12 \left[I_W \left(\frac{\ddot{x}}{r^2} \right) \right] + [m_C + 4 \cdot m_T] \cdot g \cdot \sin \gamma \\ &= 8 \cdot \frac{(\tau_M / 2)}{r} - 8 \cdot \left[C_{rr} \left(\frac{m_S}{8} g \cdot \cos \gamma \right) \right] \end{aligned} \quad (4.31)$$

This expression is rearranged to solve for the acceleration \ddot{x} :

$$\ddot{x} = \frac{8 \left\{ \frac{\tau_M}{2r} - \left[C_{rr} \left(\frac{m_S}{8} g \cdot \cos \gamma \right) \right] \right\} - [m_C + 4 \cdot m_T] \cdot g \cdot \sin \gamma}{m_C + 4m_T + 12 \left(\frac{I_W}{r^2} \right)} \quad (4.32)$$

As previously mentioned, the equation will be evaluated using SI units and converted to the English units. The torque $\tau_M = 157.96$ Nm, and the wheel radius $r =$

0.0762 m. The system mass in English units is: $m_S = (m_C + 4 \cdot m_T) = (240 \text{ lb} + 4 \cdot 15 \text{ lb}) = 300 \text{ lb}$. The system mass in SI units is: $m_S = (m_C + 4 \cdot m_T) = (108.86 \text{ kg} + 4 \cdot 6.80 \text{ kg}) = 136.06 \text{ kg}$. Lastly, the moment of inertia of the wheel is represented as the moment of inertia of hollow torus (the inner tube) + the moment of inertia of a solid disk roughly approximating the hub and flange. The moment of inertia for an entire wheel assembly about the central axis perpendicular to the wheel is calculated as [26]:

$$I_W = I_{TOR} + I_{DISK} \quad (4.33)$$

$$I_W = \left[\left(m_o R_o^2 + \frac{3}{4} m_o a_o^2 \right) - \left(m_i R_i^2 + \frac{3}{4} m_i a_i^2 \right) \right] + \left[\frac{1}{2} m_d R_d^2 \right] \quad (4.34)$$

Note that the calculation for the hollow torus involves subtracting the inner (air) torus from the outer (solid rubber) torus. The variables R and a are depicted in Figure 4.6, and the subscripts i and o denote the inner (air) torus and outer (solid rubber) torus, respectively.

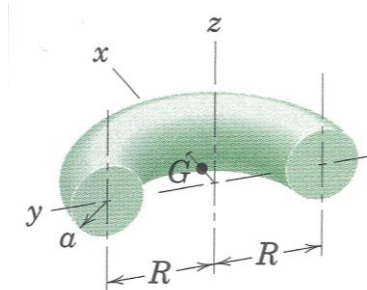


Figure 4.6: Torus Moment of Inertia Nomenclature [26]

Using approximate estimates of the mass and size properties from the McMaster-Carr Air Ride 6-in diameter wheel as well as for the hub flange disk, the moment of inertia is calculated [27]:

$$\begin{aligned}
I_W = & \left[\left(1.56 \text{ lb} \cdot 2.35^2 \text{ in} + \frac{3}{4} \cdot 1.56 \text{ lb} \cdot 1^2 \text{ in} \right) \right. \\
& - \left(1.32 \text{ lb} \cdot 2.35^2 \text{ in} + \frac{3}{4} \cdot 0.5 \text{ lb} \cdot 0.75^2 \text{ in} \right) \left. \right] \\
& + \left[\frac{1}{2} \cdot 0.5 \text{ lb} \cdot 1.44^2 \text{ in} \right]
\end{aligned} \quad (4.35)$$

$$I_W = 2.79 \text{ lb} \cdot \text{in}^2 = 0.00082 \text{ kg} \cdot \text{m}^2 \quad (4.36)$$

Lastly, this value is substituted into Equation (4.32). The stall torque is used in this calculation to provide an estimate for the initial acceleration from rest. The previously mentioned values for the chassis mass, wheel radius, and Tri-Wheel mass are converted into kilograms for this calculation. The value $C_{rr} = 0.02$ is used as an average of the previously quoted range of typical rolling resistance coefficients. Initially, the initial acceleration on a flat surface is desired, so $\gamma = 0^\circ$.

$$\ddot{x} = \frac{8 \left\{ \frac{157.96 \text{ Nm}}{2 \cdot 0.0762 \text{ m}} - \left[0.02 \left(\frac{136.06 \text{ kg}}{8} \cdot 9.81 \frac{\text{m}}{\text{s}^2} \cdot \cos 0 \right) \right] \right\}}{136.06 \text{ kg} + 12 \left(\frac{0.00082 \text{ kg} \cdot \text{m}^2}{(0.0762 \text{ m})^2} \right)} \quad (4.37)$$

$$\ddot{x} = 60.0 \frac{\text{m}}{\text{s}^2} = 196.85 \frac{\text{ft}}{\text{s}^2} \quad (4.38)$$

This acceleration is extremely high, but it is anticipated as an initial peak acceleration lasting for only a fraction of a second, if it is fully produced. Performing this same computation with a nominal torque of 400 oz-in (2.83 Nm) in which case the motor output is 345 RPM, the horizontal acceleration $\ddot{x} = 0.89 \frac{\text{m}}{\text{s}^2} = 2.92 \frac{\text{ft}}{\text{s}^2}$. As a rough

approximation, this gives an average acceleration of $100 \frac{ft}{s^2}$. Dividing the desired maximum velocity reached at this torque output (Approximately 9 ft/s) by this average acceleration produces a time of nearly 0.1 s to reach the desired operating RPM. The purpose of this analysis is to verify that for the desired output velocity, the vehicle will be able to accelerate in a reasonable amount of time. This minimal acceleration time satisfies this requirement.

Next, Equation (4.32) is evaluated for the maximum stair ascent angle in Table 3.1— 38.2° — to ensure that the vehicle is able to at least accelerate up a smooth ramp of this inclination.

$$\ddot{x} = \frac{8 \left\{ \frac{157.96}{2 \cdot 0.0762} - \left[0.02 \left(\frac{136.06}{8} \cdot 9.81 \cdot \cos 38.2 \right) \right] \right\} - 136.06 \cdot 9.81 \cdot \sin 38.2}{136.06 + 12 \left(\frac{0.00082}{0.0762^2} \right)} \quad (4.39)$$

$$\ddot{x} = 54.04 \frac{m}{s^2} = 177.30 \frac{ft}{s^2} \quad (4.40)$$

The minimum torque required to make this acceleration positive is roughly 17 Nm or 2407.4 oz-in, which is well within the capabilities of the motor. Substituting in this value for the torque, the acceleration up the incline is approximately $0.33 \frac{m}{s^2}$ or $1.10 \frac{ft}{s^2}$. This confirms that the Tri-Wheel assemblies can theoretically drive up an incline at the same ascent angles as the steepest set of stairs.

It is logical to assume that four Tri-Wheel assemblies will not be in contact with the ground at all times during operation. As a worst case scenario, Equation (4.32) is modified for only two Tri-Wheel assemblies:

$$\ddot{x} = \frac{4 \left\{ \frac{\tau_M}{2r} - \left[C_{rr} \left(\frac{m_s}{4} g \cdot \cos \gamma \right) \right] \right\} + [m_c + 2 \cdot m_t] \cdot g \cdot \sin \gamma}{m_c + 2m_t + 6 \left(\frac{I_w}{r^2} \right)} \quad (4.41)$$

Substituting the stall torque into this equation yields an acceleration of $\ddot{x} = 24.1 \frac{m}{s^2}$. This acceleration is positive for values of at least roughly 33 Nm or 4673.2 oz-in, which is reasonably easy to achieve with the selected motor.

The last check of this gear ratio is determination of whether or not the wheel skids when it comes in contact with the ground during Tumbling Mode. This is a function of the wheel spin (driving gear ratio) since only one wheel comes into contact with the ground at a time, regardless of the angular velocity of the Tri-Wheel body. Revisiting the wheel free body diagram in Figure 4.5, it is clear that the torque applied to the wheel creates a force that acts opposite the traction force. If this produced force does not exceed the theoretical static frictional force, sliding or slippage should not occur. The coefficient of static friction for rubber on dry pavement is in the range of $0.6 < \mu_s < 0.7$ [28].

$$\frac{\tau_M}{2r} < \mu_s \cdot N \quad (4.42)$$

$$\frac{\tau_M}{2r} < \mu_s \cdot \left(\frac{m_s}{8} g \right) \quad (4.43)$$

$$\frac{2.83 \text{ Nm}}{2 \cdot 0.0762 \text{ m}} < 0.7 \cdot \left(\frac{136.06 \text{ kg}}{8} \cdot 9.81 \frac{\text{m}}{\text{s}^2} \right) \quad (4.44)$$

$$18.57 \text{ N} < 116.79 \text{ N} \quad (4.45)$$

Taking into consideration all of these calculations, it is determined that a driving gearset velocity ratio of 1:1 is sufficient for the task at hand. The Tri-Wheel assembly is able to travel at a maximum of roughly 6 MPH, which exceeds the minimum required 3.1 MPH. Any increase in speed past this value is excessive. In addition, on flat ground, the acceleration time is very brief to reach that top speed, and the robot is capable of driving up rather steep inclines successfully, even in driving mode before the additional torque from the Tumbling Mode gearing is taken into consideration. Even with only two Tri-Wheels, there is sufficient power to accelerate. Lastly, a factor of safety for additional components is built in by adding 40 extra pounds to the chassis mass.

4.2.3 Tumbling Mode Speed and Gear Ratio

Next, the amount of torque required to tumble must be approximated. Assuming that the mass of the entire robot and Tri-Wheel system is concentrated at the centroid C of an individual Tri-Wheel, a rough approximation of the tumbling torque is:

$$\tau_T = \frac{m_s}{2} g \cdot c \cos 30 \quad (4.46)$$

$$\tau_T = \frac{90.72 \text{ kg}}{2} \cdot 9.81 \frac{\text{m}}{\text{s}^2} \cdot 0.1397 \cdot \cos 30 \quad (4.47)$$

$$\tau_T = 53.84 \text{ Nm} = 39.71 \text{ ft} \cdot \text{lb} \quad (4.48)$$

where τ_T is the required torque to tumble, m_s is the mass of the system, which here is simply equal to 200 lb, and c is once again the spoke length. The mass of the system is divided by two as a safety factor to say that one Tri-Wheel should be capable of pulling along half the mass of the robot system. For this reason, an additional factor of safety in

the way of increasing the theoretical mass of the system is not needed. Note that the answer is also provided in units of ft-lbs because the gearing spreadsheet outputs torque values in these units.

As an even more conservative estimate, the cosine term can be removed to yield a value of $\tau_T = 62.16 \text{ Nm} = 45.84 \text{ ft} \cdot \text{lb}$. Referencing the gearmotor torque operating points provided in Table 4.1, the highest torque output of 3000 oz-in (15.625 ft-lb) is selected for analysis. Noting again that the 10:1 gearbox on the motor is approximately 97% efficient, the incoming torque to begin with is 15.16 ft-lb. Thus, to determine the appropriate gear ratio, the most conservative estimate of torque to tumble is divided by the incoming torque:

$$GR_{TOT_T} = \frac{45.84 \text{ ft} \cdot \text{lb}}{15.16 \text{ ft} \cdot \text{lb}} \cong 3.02 \quad (4.49)$$

Therefore, a velocity ratio of 3:1 is required in Tumbling Mode in order to rotate the Tri-Wheel body and pull along the robot frame.

4.3 Gearing Spreadsheet Analysis

4.3.1 Methodology

With the desired gear ratios and spoke length c constrained, the gears required to fulfill those requirements can be specified. A comprehensive spreadsheet incorporating the entire gearing assembly is created to address both the general size and number of gears in each branch of the gear train. Gear force analysis is also incorporated in order to ensure within a reasonable factor of safety that the gears can adequately handle loads without

failure. This spreadsheet analysis facilitates an iterative design process to optimize the gearing system with the following considerations in mind:

Maximize	Justification	Minimize	Justification
System efficiency	Want to provide as much power as possible to the Tri-Wheel system.	Gearing system weight	Increases overall weight of robot platform and places more load on the motors.
Tumbling space between spokes	Creates more space between spokes to latch on to objects during tumbling.	Diameter of individual gears	Gears of smaller diameter protrude less into the tumbling space.
Similarity to off-the-shelf gears	Any gears that can be purchased or modified and not completely customized are more cost-effective.	Thickness of assembly	Compactness of system allows the Tri-Wheel to enter smaller spaces and climb narrow staircases.
		Number of gears	Efficiency decreases with more gear interactions.

Table 4.2: Fundamental Gearing Optimization Considerations

In addition, this spreadsheet analysis allows the system to be evaluated at numerous operating points of interest for the motor provided in Table 4.1. The cases of high torque/low RPM, low torque/high RPM, and a typical manufacturer-specified operating point are all evaluated to ensure that the gearing withstands the loads and stresses developed in each of these cases. As mentioned, prior iterations of the Tri-Wheel gearing configuration are included for reference in Appendix B. For conciseness, only the selected gearing configuration will be discussed in this chapter.

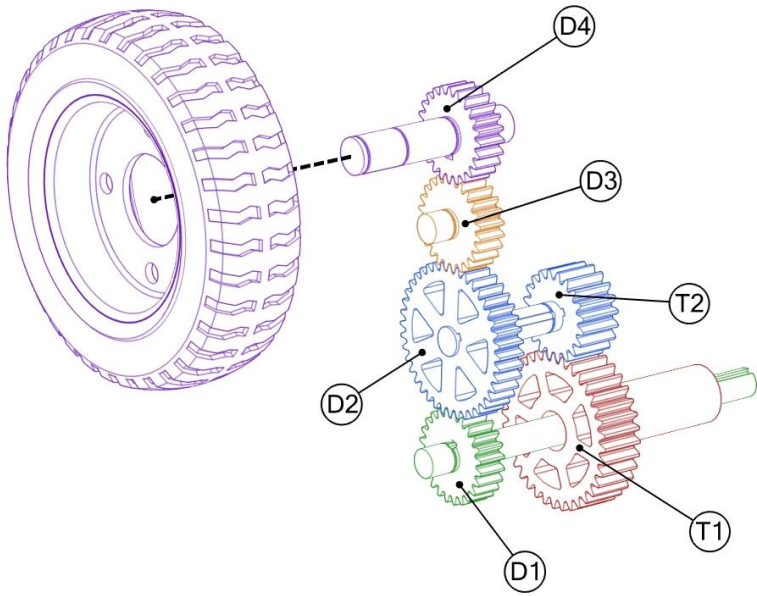


Figure 4.7: Spreadsheet Analysis Gearing Configuration

There are three branches of the gearing system linking the power input at D1 to each of the three individual wheels. Figure 4.7 is an exploded view of one branch of this selected configuration. The spreadsheet analysis is performed on a single branch since in the worst case loading scenario (in Tumbling Mode), only one wheel will be loaded and in contact with the ground. Incorporating a safety factor, the analysis is also performed such that one branch of one Tri-Wheel can pull along half the total mass of the entire robot chassis. In practical application, it is not unlikely that four Tri-Wheel assemblies will be in perfect contact with the ground simultaneously, given the rough terrain anticipated. It is a reasonable assumption that only two Tri-Wheels might be in contact with the ground at a single instant, attempting to drive ahead with the associated masses of the entire robot system.

Reviewing the selected configuration shown in Figure 4.7, this gearing branch contains four driving gears and two tumbling gears, totaling fourteen gears per Tri-Wheel

assembly. In previous iterations discussed in Appendix B, three gears were desired for the driving gear set, replacing gears D2 and D3 with a single gear. This concept was discarded because the single gear had to be quite large to mesh with the input and output gears. In addition, the driving and tumbling gear sets were originally linked by a common shaft at the wheel axle rather than at gears D2 and T2. However, it was found that many gears could be eliminated from the tumbling gear set simply by linking the parallel gear sets at D2 and T2. The spreadsheet analysis for this configuration incorporates information for each individual gear in one branch. Note that the use of color in Figure 4.7 indicates a relationship between gears and the important shafts that they transmit power to/receive power from. For instance the input shaft and gear D1 are both green, indicating the same angular velocity and torque.

4.3.2 Nomenclature

The first step in performing a comprehensive analysis involves extensive research to determine which metrics define a gear system and how those metrics can be calculated or bounded to form derived requirements. This section serves to provide an explanation of gear nomenclature and then summarize the associated constraints that will be used to optimize the gear train.

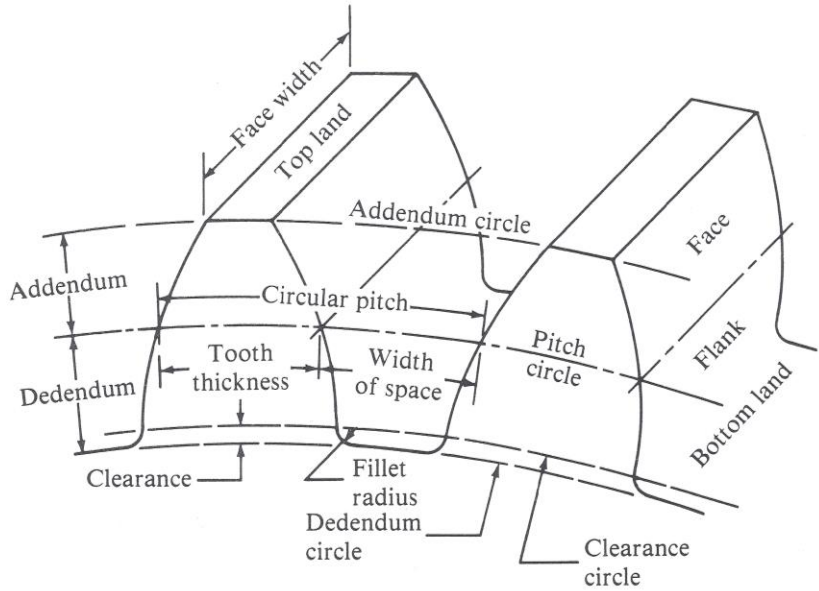


Figure 4.8: Gear Teeth Nomenclature [19]

Figure 4.8 shows two teeth from a spur gear with the involute tooth profile discussed earlier. This image is labeled appropriately with common terminology. Important definitions are provided below:

- **PITCH CIRCLE:** When two spur gears are meshed and rotating, there are two circles, one from each gear, that remain tangent. These circles are called pitch circles [19].
- **PITCH DIAMETER (d , in):** diameter of the pitch circle; lies somewhere in middle of gear tooth and must be calculated rather than measured directly.
- **CLEARANCE CIRCLE:** the largest circle generated at the gear center that is not penetrated by the teeth of the mating gear.
- **CLEARANCE:** radial distance between the top of a tooth and the bottom of a tooth space of the mating gear when the gear tooth is fully engaged [19].

- **CIRCULAR PITCH (p , in):** the distance from one point on a gear tooth at the pitch circle to the corresponding point on the next adjacent tooth, measured along the pitch circle [19]; an arc length. Computed as:

$$p = \frac{\pi \cdot d}{N} \quad (4.50)$$

Notice that the size of the gear tooth increases proportionally to the circular pitch.

- **DIAMETRAL PITCH (P , teeth/in):** number of teeth per inch of pitch diameter:

$$P = \frac{N}{d} \quad (4.51)$$

Diametral pitch is often referred to as simply the “pitch” of the gear [20]. For instance, a 16-pitch gear refers to a gear with 16 teeth per inch of pitch diameter. For high speed, low torque applications, a high pitch (smaller tooth size) is desired; for low speed, high torque applications, a low pitch (larger tooth size) is desired.

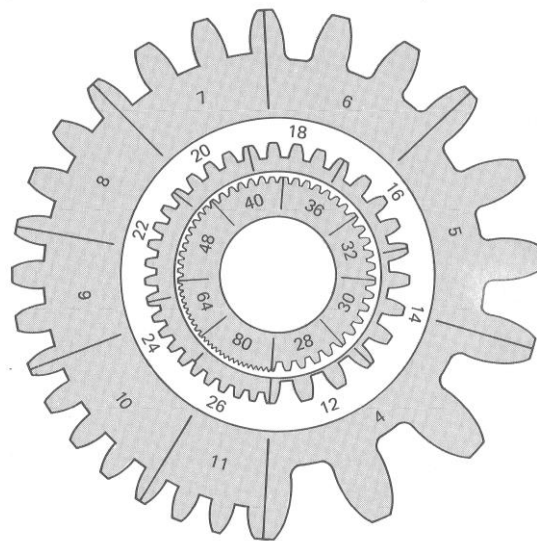


Figure 4.9 shows the approximate sizes of gear teeth with various diametral pitches.

A fine-pitch gear has $P \geq 20$, whereas a coarse-pitch gear has $P < 20$ [19]. A coarse diametral pitch is desirable for the Tri-Wheel gearing since the gears will be handling heavy loads during tumbling and will benefit from a reasonably robust tooth. Note that diametral pitch is often referenced simply as the pitch of a gear.

- ADDENDUM (a , in): radial distance from the pitch circle to the top land [29].
- DEDENDUM (b , in): radial distance from the bottom land to the pitch circle [29].
- OUTSIDE DIAMETER (d_o , in): the diameter of the addendum circle; in other words, the diameter of a circle that would enclose the outermost points of the gear teeth.
- TOOTH THICKNESS (t , in): the arc length, measured along the pitch circle, from one side of a tooth to the other side.
- FACE WIDTH (F , in): tooth width measured parallel to the gear axis; as face width gets wider, gears are more difficult to manufacture and to mount such that contact is uniform across the full face width [20]. While face width is not standardized, a general range for a reasonable value can be calculated as a function of the diametral pitch. Note that even if the face width does not fall within this range exactly, the gearing system is still viable if it is determined that the teeth satisfy the conditions described later for bending and contact stress. This range is calculated as [19]:

$$\frac{8}{P} < F < \frac{16}{P} \quad (4.52)$$

This concludes the definitions associated with Figure 4.8. Additional nomenclature used in the Tri-Wheel gear analysis is included below:

- **PRESSURE ANGLE (ϕ , °):** the angle between the tangent to the pitch circles and the line drawn normal (perpendicular) to the surface of the gear tooth (known as the line of action), as shown in Figure 4.10 [19].

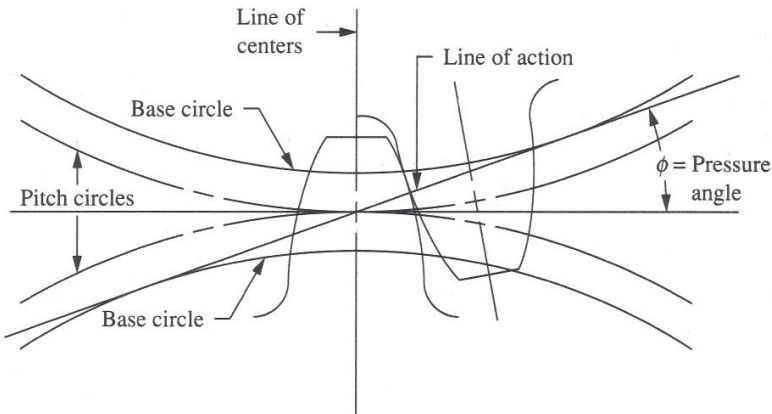


Figure 4.10: Pressure Angle Diagram [19]

Gear manufacturers have established standard values of pressure angles over time. Current standard pressure angles are 14.5° , 20° , and 25° [19]. However, the 14.5° pressure angle is declared obsolete by many manufacturers today [19]. Though tooth thickness is the same for any given gear with the same metrics but different pressure angles, the actual shape of the tooth does vary, as shown in Figure 4.11. The base circle in this figure references the circle on which the involute curve is generated by any point on a taut thread as it unwinds from a circle [20]. The pressure angle determines the size of the base circle, increasing in diameter with increasing pressure angle. The gear teeth in this figure are also described as having standard full-depth, which is explained in the following definition. The pressure angle selected for the Tri-Wheel is the most common and widely used— 20° . This increases the chance of being able to purchase gears off the shelf.

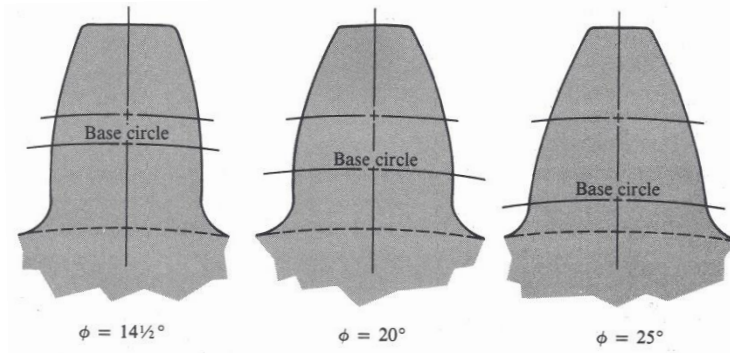


Figure 4.11: Varying Pressure Angles Affecting Tooth Shape [19]

- **WORKING DEPTH**: the radial distance that a gear tooth projects into the tooth space of the mating gear. Note that standard full-depth gear teeth have a working depth equal to $2/P$.
- **BACKLASH**: the difference between tooth space and tooth thickness, measured along the pitch circle. Backlash is intended to prevent jamming and allow for gear lubrication. However, too much backlash leads to inaccurate gear motion and high shock loads.
- **CENTER DISTANCE (c , IN)**: the distance between the centers of two meshing gears, or the sum of the pitch radii of two gears in mesh.

This explanation of nomenclature is not all-encompassing but does provide enough information to contextualize the subsequent calculations and analysis. It is important to note that in order for two spur gears to mesh properly, they must share the following characteristics: pressure angle, diametral pitch, and typically the addendum and dedendum [19]. Now that the basic operation of gearing systems and the corresponding terminology has been reviewed, more specific calculations used to evaluate and optimize

the Tri-Wheel gearing system are studied. This leads to the compilation of a clear set of derived requirements for the selected gearing configuration.

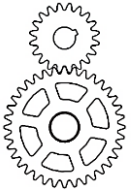
4.3.3 Sizing Analysis

The spreadsheet analysis is divided into two subsections: sizing analysis and force analysis. Sizing analysis references determination of the number of gears, overall size characteristics of those gears and their teeth, and how those teeth interact in mesh. In this section, pitch diameter, number of teeth, interference, and contact ratio are calculated.

<i>Configuration</i>	<i>Input Parameters</i>	<i>Output Parameters</i>
DRIVING 	c_{TOT_D}	Total center distance (5.5 in) N_{1D} Tooth number for D1
	GR_{TOT_D}	Total velocity ratio (1:1) N_{4D} Tooth number for D4
	P_D	Diametral Pitch (16) F_D Face width of gears
	φ	Pressure Angle (20°) c_{i-j} Center distance from gears Di-Dj
	N_{2D}	Tooth number for D2 (40) GR_{i-j} Velocity ratio between gears Di-Dj
	N_{3D}	Tooth number for D3 (24) a_D Addendum
	GR_{TOT}	Total gear ratio desired to tumble, including driving and tumbling gears (3:1) $r_{1\dots 4D}$ Pitch radii for driving gears $d_{1\dots 4D}$ Pitch diameters $r_{b_{1\dots 4D}}$ Base circle radii $r_{a_{max1\dots 4D}}$ Maximum noninterfering addendum circle radii $a_{max,1\dots 4D}$ Maximum permissible noninterfering addendum p_{bD} Base pitch $r_{a_{1\dots 4D}}$ Addendum circle radii CR_{i-j} Contact ratio between gears Di-Dj

Table 4.3: Driving Gear Set Sizing Input and Output Parameters

The sizing analysis input and output parameters for Driving Mode are summarized in Table 4.3. Quantities in parentheses indicate the values iteratively determined for the selected gearing configuration. Note that some of the variables use subscripts i and j as indices to denote various gear numbers. The subscript D designates a particular quantity as a Driving Mode parameter if an identical value exists in Tumbling Mode. The sizing analysis input and output parameters for Tumbling Mode are, in large part, a result of the input and output of the driving mode parameters since the power flow for the system travels first through the driving gears before transmitting through the tumbling gears. However, there are still some specific input parameters for Tumbling Mode sizing analysis. These variables are summarized in Table 4.4 below and designated with a T , respectively, to indicate Tumbling Mode:

<i>Configuration</i>	<i>Input Parameters</i>	<i>Output Parameters</i>
TUMBLING 	c_{TOT_T} Total center distance (2.0 in) *	$N_{1\dots 2T}$ Number of teeth for T1 and T2
	GR_{TOT_T} Total velocity ratio (1.8:1)*	F_T Face width of gears
	P_T Diametral Pitch (14)	a_T Addendum
	φ Pressure Angle (20°)	$r_{1\dots 2T}$ Pitch radii for tumbling gears
	GR_{TOT} Total gear ratio desired to tumble, including driving and tumbling gears (3:1)	$d_{1\dots 2T}$ Pitch diameters
		$r_{b_{1\dots 2T}}$ Base circle radii
		$r_{a_{max1\dots 2T}}$ Maximum noninterfering addendum circle radii
		$a_{max,1\dots 4T}$ maximum permissible noninterfering addendum
		p_{bT} Base pitch
		$r_{a_{1\dots 2T}}$ Addendum circle radii
		CR_{2-1} Contact ratio between gears Di-Dj

* Parameters with an asterisk represent input values that result from the Driving Mode sizing analysis.

Table 4.4: Tumbling Gear Set Sizing Input and Output Parameters

In this analysis, the number of teeth for gears D2 and D3 are selected as inputs for two reasons: first, this helps to constrain the overall size of the gears to fit behind a Tri-Wheel spoke that is defined to be less than 3 inches across, and second, this allows the size of D2 to be changed freely in the pursuit of an overall tumbling velocity ratio of 3:1. The pitch diameters for these gears are calculated using Equation (4.51) and then divided in half to obtain the pitch radii. Then, the values of r_{1D} and r_{4D} are calculated. The total distance between D1 and D4 is expressed as:

$$c_{TOT_D} = r_{1D} + d_{2D} + d_{3D} + r_{4D} \quad (4.53)$$

Because the total gear ratio is known, an expression can be formed to relate the input gear D1 to the output gear D4:

$$GR_{TOT_D} = \frac{r_{4D}}{r_{1D}} \quad (4.54)$$

This is rearranged as:

$$r_{4D} = GR_{TOT_D} * r_{1D} \quad (4.55)$$

Given the known values of c_{TOT_D} , d_{2D} , and d_{3D} , Equation (4.53) is then rearranged, and Equation (4.55) is substituted into the expression to solve for r_{1D} :

$$r_{1D} = \frac{(c_{TOT_D} - d_{2D} - d_{3D})}{(1 + GR_{TOT_D})} \quad (4.56)$$

With r_{1D} known, this value is substituted back into Equation (4.55) in order to obtain r_{4D} .

Given the diametral pitch and pitch diameter (multiplying the pitch radii each by two)

known, Equation (4.51) is once again used to fill in the missing values of tooth number for gears D1 and D4. Another constraint of this analysis is that the number of teeth must be an integer value. For logical reasons, it does not make sense to end up with 20.4 gear teeth. This is a requirement for all iterations of the gearing configuration.

By summing values of the pitch radii between two meshing gears, the individual center distances between the gears in the train are all determined. For instance, c_{1-2} is calculated by summing r_{1D} and r_{2D} . In like manner, values of the individual gear interaction velocity ratios are obtained through the fundamental law of gearing expressed in Equation (4.1). The velocity ratio between D3 and D4 GR_{3-4} would be calculated by dividing r_{4D} by r_{3D} , for example. Remember that the angular velocity of the gears switches direction (clockwise versus counterclockwise) with each gear interaction. This can be represented by placing a negative sign in front of the velocity ratios for clockwise rotation. Expression (4.52) can also be evaluated given a known diametral pitch. This range is not an absolute requirement to meet (since force analysis will determine whether the stresses can be mitigated), but the quick calculation does provide a reasonable range to be aware of.

Next, the gears must be checked for interference. Interference between meshing gear teeth occurs if either of the addendum circles extends beyond tangency points called interference points, preventing rotation [20]. As a general recommendation to avoid interference, it is advisable to use gears with no fewer than 18 teeth for the 20 full-depth involute system [19]. However, determination of interference can easily be calculated using a technique modified from [19]. First, the base radius is calculated for each of the gears:

$$r_{b_{iD}} = r_i \cos \varphi \quad (4.57)$$

Next, the maximum noninterfering addendum circle radius $r_{a_{max,1\dots 4D}}$ is calculated for each of the four gears using the following formula:

$$r_{a_{max,1\dots 4D}} = \sqrt{r_{b_{1\dots 4D}}^2 + c_{i-j}^2 * \sin^2 \varphi} \quad (4.58)$$

The addendum circle radius is calculated simply by:

$$r_{a_{1\dots 4D}} = r_{1\dots 4D} + a_D \quad (4.59)$$

Using $r_{a_{max,1\dots 4D}}$ in place of $r_{a_{1\dots 4D}}$, this equation is rearranged to solve for $a_{max,1\dots 4D}$, the maximum permissible noninterfering addendum:

$$a_{max,1\dots 4D} = r_{a_{max,1\dots 4D}} - r_{1\dots 4D} \quad (4.60)$$

Four values of the maximum permissible noninterfering addendum are calculated (one for each gear) and compared to the basic calculation for the addendum of a standard full-depth tooth, which is a function only of the diametral pitch:

$$a_D = \frac{1}{P} \quad (4.61)$$

It can therefore be said that if the following condition is met for each gear, interference does not occur:

$$a_D < a_{max,1\dots 4D} \xrightarrow{yields} no\ interference \quad (4.62)$$

Once the gearing configuration is checked for interference, the contact ratio between meshing gear teeth is analyzed. The contact ratio between two mating gears is best explained as the average number of gear teeth in contact during rotation. Depending on the design application, contact ratio may be desired to be extremely high. A high contact ratio ultimately creates a quieter and more smoothly operating gear set. If a contact ratio is less than 1, there is some interval of time during which no gear teeth are in contact; this is very undesirable. In general, a contact ratio of at least 1.2 is often deemed adequate and can be interpreted as having one pair of teeth always in contact and two pairs in contact 20% of the time [22]. Upon the recommendation of a NASA Glenn Tribology employee, the minimum contact ratio for this application is set at 1.6. The addendum circle radius for each of the four gears is calculated using Equation (4.59). With this and the base circle radius known from the calculation of interference, the following equation determines contact ratio:

$$CR_{i-j} = \frac{\sqrt{r_{a_{iD}}^2 - r_{b_{iD}}^2} + \sqrt{r_{a_{jD}}^2 - r_{b_{jD}}^2} - c_{i-j} * \sin \varphi}{p_b} \quad (4.63)$$

where p_b is the base pitch calculated as:

$$p_b = p \cos \varphi \quad (4.64)$$

The contact ratio is calculated three times for each of the three gear interactions in the driving gear set (gears 1-2, 2-3, and 3-4). This concludes the sizing analysis for the driving gear set.

The tumbling gear set analysis consists of identical calculations for the interference check and contact ratio, substituting in the appropriate value of diametral

pitch and other recomputed quantities for the tumbling gear set version of the analysis.

The real difference lies in the dependence of this portion of the analysis upon the already completed sizing analysis. For instance, the parameters c_{TOT_T} and GR_{TOT_T} are determined by the driving gear analysis. There is also a stipulation that:

$$GR_{TOT} = GR_{1-2D} * GR_{TOT_T} \quad (4.65)$$

This reflects the reverted gear train configuration selected to achieve the total velocity ratio of 3:1 yielding the necessary torque increase by a factor of 3. A reverted gear train is one in which two sets of parallel shaft gears are arranged such that the output shaft is concentric with the input [30]. This configuration requires equal center distances for the two trains and complicates calculations to specify gears that satisfy ratio requirements with standard pitch values. Looking at only gears D1, D2, T1, and T2 from Figure 4.7: Spreadsheet Analysis Gearing Configuration, the reverted gear train is clearly visible. Figure 4.12 below shows how the two velocity ratios compound to increase torque in order to meet the derived torque requirement for tumbling.

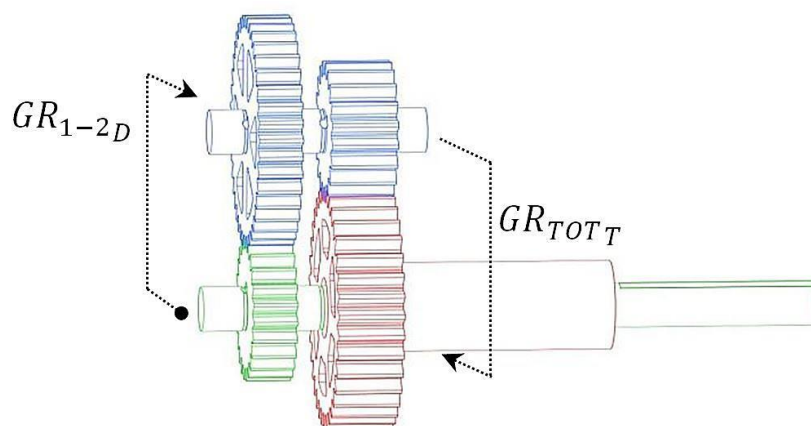


Figure 4.12: Reverted Gear Train for Tumbling

Thus, Equation (4.65) is rearranged to solve for the total gear ratio used to analyze the tumbling gear set based on a known value of the total desired velocity ratio and the existing velocity ratio between gears D1 and D2 for the driving gears. Additionally, there are no idler gears between T2 and T1. The equations used previously are identical except that the there are no pitch diameter values included in the total center length expression. This concludes the Tri-Wheel gear sizing analysis.

4.3.4 Force Analysis

The main goal of the gearing force analysis is to determine the torque transmitted through each gear interaction in the pursuit of answering two questions: 1. Do the loads created produce acceptable bending and contact stresses in the gear teeth that will not lead to failure? 2. Is the amount of torque developed during Tumbling Mode sufficient to meet the theoretically calculated estimate of what is required, within a reasonable factor of safety? As in the sizing analysis, a list of the inputs and outputs for the force analysis are compiled for both the driving gears and the tumbling gears. This is followed by an explanation of the appropriate assumptions and calculations required to answer the stated two questions.

Table 4.5 contains the various input and output parameters that are seen in the force analysis for Driving Mode. Note that for the analysis of bending stress number and contact stress number, various factors are included to capture characteristics of the gear's size, loading, and shape in order to produce a more accurate result. Some textbooks recommend a modified version of the bending and contact stress equations without the various factors, but they have been included in this analysis to increase correctness.

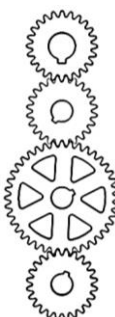
<i>Configuration</i>	<i>Input Parameters</i>		<i>Output Parameters</i>	
DRIVING 	GR_M	Motor gearbox gear ratio	V_D	Gear pitch line velocity (ft/min)
	m_{TOT}	Total robot mass, including Tri-Wheels (lb)	F_{T_D}	Tangential component of force between mating teeth (lb)
	τ_M	Motor torque (minus gearbox) (ft-lb)	F_{R_D}	Radial component of force between mating teeth (lb)
	η_M	Motor planetary gearbox efficiency	$\tau_{1\dots 4D}$	Torque produced about center of each gear (ft-lb)
	RPM_M	Input speed of motor without attached gearbox (rev/min)	R_{f_D}	Resultant force of tangential and radial components (lb)
	\dot{W}_{GM}	Transmitted power from garmotor (HP)	$s_{t_{i,i-j_D}}$	Bending stress number for gear D_i if D_i and D_j are in mesh (lb/in ²)
	τ_T	Torque required to enact Tumbling Mode (ft-lb)	$s_{t_{j,i-j_D}}$	Bending stress number for gear D_j if D_i and D_j are in mesh (lb/in ²)
	$J_{i,i-j_D}$	Geometry factor for gear D_i if D_i and D_j are in mesh	$s_{c_{i,i-j_D}}$	Contact stress number for gear D_i if D_i and D_j are in mesh (lb/in ²)
	$J_{j,i-j_D}$	Geometry factor for bending strength for gear D_j if D_i and D_j are in mesh	$s_{c_{j,i-j_D}}$	Contact stress number for gear D_j if D_i and D_j are in mesh (lb/in ²)
	I_{i-j_D}	Geometry factor for pitting resistance between gears D_i & D_j	τ_{GM}	Total motor + gearbox output torque (ft-lb)
	C_P	Elastic coefficient [lb/in ²] ^{0.5}	RPM_{GM}	Gear-motor input speed (rev/min)
	K_B	Rim thickness factor		
	K_O	Overload factor		
	K_v	Dynamic factor		
	K_S	Size factor		
	K_m	Load distribution factor		

Table 4.5: Driving Gear Set Force Input and Output Parameters

The input and output parameters used in the force analysis of the gears in Tumbling Mode is included in Table 4.6. The primary difference is that the torque and speed (power) input does not come directly from the gear-motor itself but from the gear D2, which is keyed to the same shaft as gear T2.

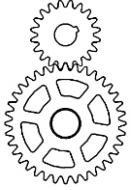
<i>Configuration</i>	<i>Input Parameters</i>		<i>Output Parameters</i>	
TUMBLING 	τ_{D2}	Input torque from gear D2 (ft-lb)	V_T	Gear pitch line velocity (ft/min)
	m_{TOT}	Total robot mass, including Tri-Wheels (lb)	F_{TT}	Tangential component of force between mating teeth (lb)
	RPM_{D2}	Input speed from gear D2 (rev/min)	F_{RT}	Radial component of force between mating teeth (lb)
	\dot{W}_{GM}	Transmitted power from gearmotor (HP)	$\tau_{1\dots 2T}$	Torque produced about center of each gear (ft-lb)
	τ_T	Torque required to enact Tumbling Mode (ft-lb)	R_{fT}	Resultant force of tangential and radial components (lb)
	$J_{i_{i-jT}}$	Geometry factor for gear T_i if T_i and T_j are in mesh	$s_{t_{i,i-jT}}$	Bending stress number for gear T_i if T_i and T_j are in mesh (lb/in^2)
	$J_{j_{i-jT}}$	Geometry factor for bending strength for gear T_j if T_i and T_j are in mesh	$s_{t_{j,i-jT}}$	Bending stress number for gear T_j if T_i and T_j are in mesh (lb/in^2)
	I_{i-jT}	Geometry factor for pitting resistance between gears D_i & D_j	$s_{c_{i,i-jT}}$	Contact stress number for gear T_i if T_i and T_j are in mesh (lb/in^2)
	C_P	Elastic coefficient [lb/in^2] ^{0.5}	$s_{c_{j,i-jT}}$	Contact stress number for gear T_j if T_i and T_j are in mesh (lb/in^2)
	K_B	Rim thickness factor		
	K_O	Overload factor		
	K_v	Dynamic factor		
	K_s	Size factor		
	K_m	Load distribution factor		

Table 4.6: Tumbling Gear Set Force Input and Output Parameters

This analysis begins where the power enters the system—the driving gear set. To begin the force analysis, the first quantity that must be calculated is the pitch-line velocity, defined as the linear velocity of a point on the pitch circle of the gear [19]. All of the gears in one branch of the gear train will have the same pitch-line velocity [20]. Thus, this quantity can be calculated using any of the gears in the gear train:

$$V_D = \frac{\pi \cdot d_i \cdot n_i}{12} \quad (4.66)$$

where d_i is again the pitch diameter (in), and n_i is the angular velocity in RPM.

Next, the force between mating teeth is evaluated. The resultant force R_{f_D} can be broken down into F_{T_D} & F_{R_D} , its tangential and radial components, respectively. The tangential component can be multiplied by pitch-line velocity to determine transmitted power, and the radial component does not do work but tends to push the gears apart [20]. Rearranging the equations in [20], the tangential and radial force components as well as their resultant force are calculated as:

$$F_{T_D} = \frac{33,000 \cdot \dot{W}_{GM}}{V_D} \quad (4.67)$$

$$F_{R_D} = F_{T_D} \cdot \tan \phi \quad (4.68)$$

$$R_{f_D} = \sqrt{{F_{T_D}}^2 + {F_{R_D}}^2} \quad (4.69)$$

These calculations reflect the assumption of a uniform applied load. Treating the gear as a lever that transmits a tangential force at some distance from the center of the gear (the pitch radius), the torque in ft-lb about the center of each gear is computed as:

$$\tau_{1\dots4_D} = r_{1\dots4_D} \cdot F_{T_D} \cdot \frac{1 \text{ ft}}{12 \text{ in}} = \frac{33,000 \cdot P}{V_D} \quad (4.70)$$

Next, the bending stress number and contact stress number must be evaluated for each gear in each of the three gear mesh interactions. The American Gear Manufacturers Association provides a basic procedure for computing both of these values. ANSI/AGMA

2001-D04 provides the standard calculation to evaluate the bending stress number of a gear tooth in mesh [31]:

$$s_t = F_{T_D} K_O K_V K_S \cdot \frac{P}{F} \cdot \frac{K_M K_B}{J} \quad (4.71)$$

Differences in established nomenclature for this method can be substituted into this equation, yielding:

$$s_{t,i-j_D} = F_{T_D} K_O K_V K_S \cdot \frac{P}{F} \cdot \frac{K_M K_B}{J_{i-j_D}} \quad (4.72)$$

Calculations for uniform tangential load, pitch, and face width have been discussed. Now, determination of the other modification factors (constants) is required.

K_O is known as the overload factor; this constant reflects the degree of nonuniformity of driving and load torques [20]. According to the AGMA standard, the overload factor is more or less intended to account for any externally applied loads in excess of the normal tangential load for a given application [31]. Using Table 15.1 in [20], the value of 1.25 is selected to represent a moderate shock from a uniform source of power.

K_V is the dynamic factor and accounts for internally generated gear tooth loads induced by non-conjugate meshing action of mating gear teeth [31]. Using a rough approximation method presented in [20] involving determination of the dynamic factor as a function of the pitch-line velocity and an estimation of the manufacturing method employed, the dynamic factor is determined to be 1.0. In prior work, the dynamic factor was set as less than 1, but a recent edition of the AGMA standard has altered this

conception. Because the pitch-line velocity of the gears in use is so low, the dynamic factor presents as approximately 1.0 regardless of the quality of the manufacturing used.

K_S is the size factor, reflecting non-uniformity in the gear material. This constant takes into account a variety of operating conditions: tooth size, diameter of parts, ratio of tooth size to diameter of part, face width, area of stress pattern, ratio of case depth to tooth size, and hardenability and heat treatment of materials [31]. Despite all of this, the size factor is recommended to be taken as unity for most gears, so long as a reasonable choice of steel and heat treatment are selected. This AGMA assertion is supported by Table 11-4 in [19], which recommends a value of 1.00 for any value of K_S applied to gears with a pitch greater than or equal to 5.

K_M is known as the load distribution factor and is one of the most difficult factors to specify. This parameter is dependent upon not only the gears themselves but the shafts, bearings, housing, and the structure upon which the gear train is installed [19].

Distortions due to centrifugal and thermal effects, assembly variations, manufacturing variation, and deflections resulting from applied loads are also considered to make up this complex constant [31]. Table 15.2 in [20] recommends that for gears of face width less than 2 in, $K_M = 1.3$ considering accurate mountings, small bearing clearances, and minimum deflection. Figure 11-27 in [19] supports this estimate with a plot of load distribution factor vs. face width for enclosed gearing.

Lastly, K_B is the rim thickness factor. Frequently, a rim or cutouts are used to reduce the weight of a gear and thus the weight of the overall system. These cutouts can be in the form of wagon wheel spokes, lightening holes, or even an extrude cut cylinder into each side of a gear. What this produces, ultimately, is a stress concentration point if

the rim of the gear is too thin, creating undesirable deformation. The inclusion of these cutouts is to be discussed in greater detail in a coming section, but for purposes of this analysis, a design requirement is that the rim thickness factor $K_B = 1.00$. As shown in Figure 4.13: Rim Thickness Factor, when the ratio of the rim thickness to the tooth whole depth is greater than or equal to 1.2, the rim thickness factor is equal to 1.00.

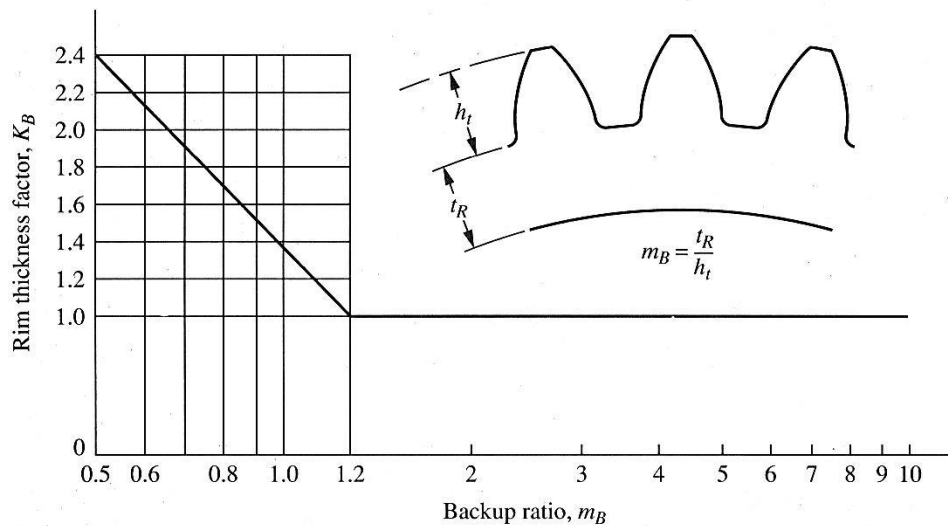


Figure 4.13: Rim Thickness Factor [19]

In addition to the various K correction factors, the geometry factor for bending strength J must be determined. Another AGMA standard provides the background information for what this factor is and how it can be determined. AGMA 908-B89 states that the bending strength geometry factor is a dimensionless number that takes into account the effects of tooth shape, worst load position, stress concentration, and load sharing between oblique lines of contact when applied to helical gears [32]. This standard provides a number of tables for different pressure angles, addendum ratio, and load placement that are summarized and compiled into the following graph:

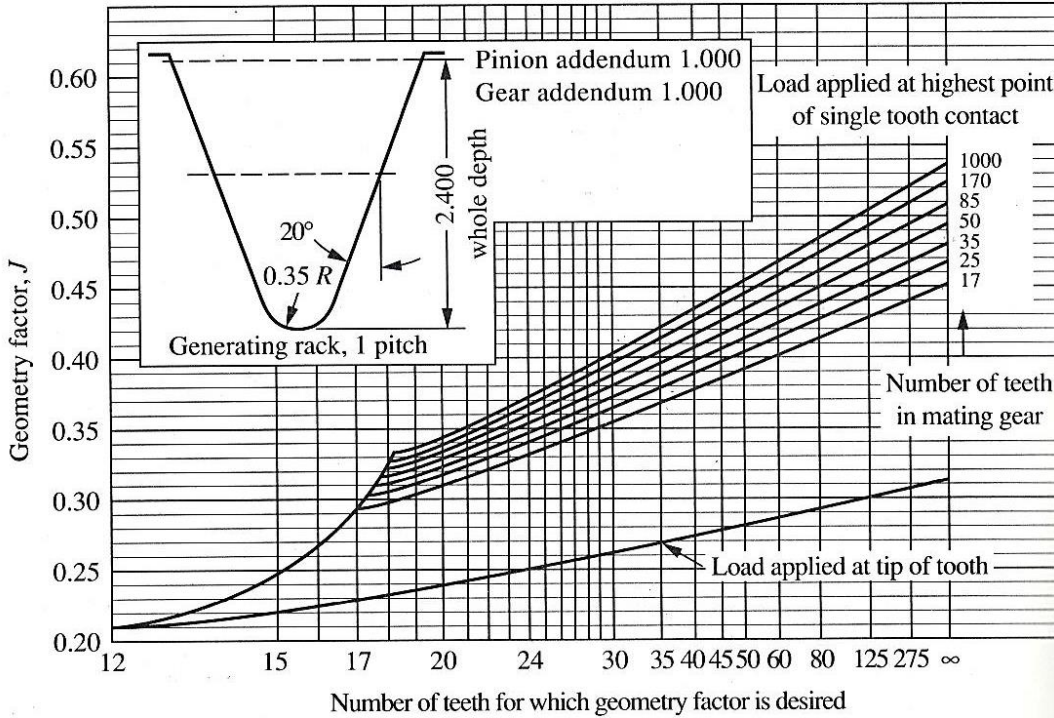


Figure 4.14: Bending Strength Geometry Factor J for 20° Spur Gear Standard Addendum [19]

This graph utilizes the number of teeth for both meshing gears to determine a unique geometry factor for both gears in each of the three gear meshes.

The contact stress number is calculated using an equation found in [31]:

$$s_c = C_p \sqrt{F_{T_D} K_O K_V K_S \cdot \frac{K_M}{d \cdot F} \cdot \frac{C_f}{I}} \quad (4.73)$$

The contact stress number, representing what is commonly referred to as the Hertz contact stress, provides a metric by which the gear teeth are assessed for pitting failure. There are three new constants to be determined in order to evaluate this expression: the elastic coefficient C_p , the surface condition factor for pitting resistance C_f , and the geometry factor for pitting resistance I .

The elastic coefficient C_p takes into consideration the actual material properties of both gears in mesh. The pitting characteristics of two steel gears in mesh are very different than the characteristics resulting from a tin bronze gear and a steel gear in mesh, for instance. The elastic coefficient is defined by the following equation [31]:

$$C_p = \sqrt{\frac{1}{\pi \left(\frac{1 - \mu_i^2}{E_i} \right) + \left(\frac{1 - \mu_j^2}{E_j} \right)}} \quad (4.74)$$

where the values of μ_i and μ_j are the values of Poisson's ratio for the driving gear and the driven gear, respectively, and the values of E_i and E_j are the modulus of elasticity metrics in lb/in². Material selection will be discussed in the subsequent section. The gears will be made of steel, and as such, $C_p = 2300 \sqrt{psi}$.

The surface condition factor C_f is dependent upon residual stress, plasticity effects, and the surface finish as affected by the manufacturing method of the gears in question [31]. At this time, values for C_f have not yet been established for cases in which the surface finish has a detrimental effect on the system. In that case, some value of $C_f > 1$ would be used. Otherwise, a value of $C_f = 1$ can be assumed [31].

Lastly, the pitting resistance geometry factor I is considered. As explained by [31], this geometry factor evaluates the radii of curvature of the contacting tooth profiles based on the tooth geometry. These radii are then used to evaluate Equation (4.73), the Hertzian contact stress in the tooth flank. Effects on the system resulting from load sharing and modified tooth proportions are also captured by this parameter. An analytical method that results in the derivation of I is located in [32]. Similar to J , the values of I in this AGMA standard are presented in tables for a variety of tooth forms. Utilizing both

these tables and the associated graph of that trend shown in Figure 4.15, three values of I are determined for each gear interaction. Note that while there are six required values for J , one for each gear in each of the three gear meshes, only three values of I are required since the parameter is based on the gear ratio and the gear mesh rather than each individual gear. This concludes the force analysis for the driving gear set.

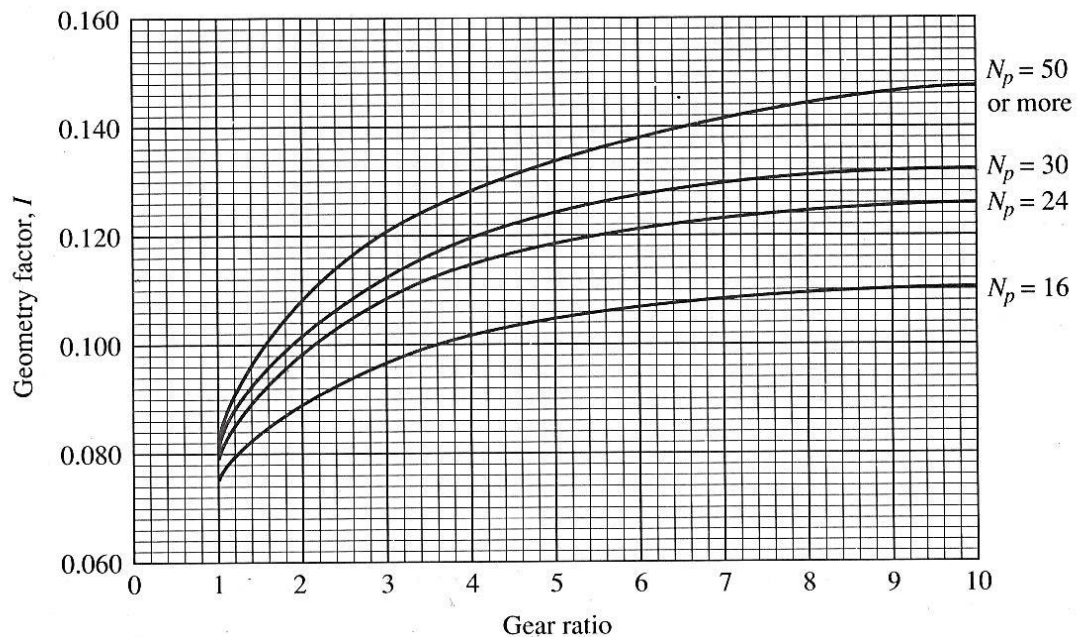


Figure 4.15: Pitting Resistance Geometry Factor I for 20° Spur Gear Standard Addendum [19]

In computation, the methods used to evaluate the forces, torques, and stresses in the tumbling gear set are identical to those just described. As mentioned, the primary difference is that the input power is not coming directly from the motor but is being transmitted through a keyed shaft from gear D2 to gear T2. The calculations are simpler only because there are two gears to be considered rather than four. The selected gear configuration is a product of iteration to meet derived requirements for size as well as required speed and torque followed by consideration of material properties that would be

able to reasonably handle the loads developed. The most important derived requirements are included in Table 4.7 below.

<i>Derived Requirement</i>	<i>Justification</i>
$GR_{TOT_D} = 1: 1$	Enables Tri-Wheel to travel at desirable driving speed.
$GR_{TOT_T} = 3: 1$	Necessary to achieve torque to tumble.
$\phi = 20^\circ$	This pressure angle is common to many off-the-shelf gears and provides satisfactory tooth strength.
$N > 18$	All gears must have at least 18 teeth to avoid backlash.
$\frac{8}{P} < F < \frac{16}{P}$	Face width of gears is recommended to exist in this range for satisfactory operating performance.
$d_o < 3 \text{ in}$	Maximum outer diameter of gears must be less than 3 in to prevent the gearing from taking up valuable space required to tumble between the three spokes.
$P < 20$	Coarse pitch gears are desired for adequate bending strength properties.
$N = \{1, 2, 3, \dots\}$	The computed number of teeth for all gears must be an integer number to avoid adverse rounding consequences.
$c_{TOT_D} = 5.5 \text{ in}$	The total center distance from gears D1 to D4 must be equal to the spoke length selected in Chapter 3.
$c_{1-2_D} = c_{2-1_T}$	The center distance between gears D1 and D2 must be identical to the center distance between gears T2 and T1 for the reverted gear train concept to be made possible.
$CR \geq 1.6$	This recommended contact ratio is meant to improve smoothness and reduce noise of the gearing system.
$a < a_{max}$	The standard addendum for a full-depth tooth must be less than the maximum computed noninterfering addendum.
$(P, p, \phi, a, d)_D = const.$	These characteristics must be common for all gears in the driving gear train to ensure proper meshing.
$(P, p, \phi, a, d)_T = const.$	These characteristics must be common for all gears in the tumbling gear train to ensure proper meshing.

Table 4.7: Gear Sizing and Force Analysis Derived Requirements

While each of these requirements individually may appear simple to fulfill, the optimization of a system that comprehensively satisfies all of these conditions is quite a design challenging. These same requirements were used to eliminate the gearing

configurations in Appendix B: Tri-Wheel Design Iterations. By using both Table 4.7 and Table 4.2 as guidelines, the number of gears and their respective characteristics are arrived at for both gear trains. An assessment of the derived requirements versus compliance for the selected gearing configuration is found below in Table 4.8.

<i>Derived Requirement</i>	<i>Calculations and Metrics For Selected Tri-Wheel Gearing Configuration</i>	<i>Capability</i>
$GR_{TOT_D} = 1:1$	$GR_{TOT_D} = \frac{40}{24} \cdot \frac{24}{40} \cdot \frac{24}{24} = \frac{1}{1}$	Meets
$GR_{TOT_T} = 3:1$	$GR_{TOT_T} = \frac{40}{24} \cdot \frac{36}{20} = \frac{3}{1}$	Meets
$\phi = 20^\circ$	$\phi = 20^\circ$	Meets
$N > 18$	$N_{1D} = N_{3D} = N_{4D} = 24; N_{2D} = 40; N_{1T} = 36; N_{2T} = 20$	Meets
$P < 20$	$P_D = 16; P_T = 14$	Meets
$\frac{8}{P} < F < \frac{16}{P}$	$0.5 < F_D < 1.0 \rightarrow F_D = 0.5$ $0.57 < F_T < 1.14 \rightarrow F_D = 0.75$	Meets
$d_o < 3 \text{ in}$	$d_{oD_2} = 2.62 \text{ in}; d_{oT_2} = 2.71 \text{ in}$	Meets
$N = \{1, 2, 3, \dots\}$	$N = \{20, 24, 36, 40\}$	Meets
$c_{TOT_D} = 5.5 \text{ in}$	$c_{TOT_D} = 2.0 + 2.0 + 1.5 = 5.5 \text{ in}$	Meets
$c_{1-2D} = c_{2-1T}$	$c_{1-2D} = 2.0 \text{ in} = c_{2-1T}$	Meets
$CR \geq 1.6$	$CR_{1-2D} = 1.66; CR_{2-3D} = 1.66;$ $CR_{3-4D} = 1.60; CR_{2-1T} = 1.63$	Exceeds
$a < a_{max}$	$(a_D = 0.063) < (a_{max} = 0.109)$ $(a_T = 0.071) < (a_{max} = 0.103)$	Meets
$(P, p, \phi, a, d)_D = const.$	$(P, p, \phi, a, d)_D = (16, 0.196, 20^\circ, 0.063, 0.077)_D = const$	Meets
$(P, p, \phi, a, d)_T = const.$	$(P, p, \phi, a, d)_D = (14, 0.224, 20^\circ, 0.071, 0.089)_D = const$	Meets

Table 4.8: Gearing Requirements v. Capability Compliance

This table provides a summary of the final gearing design iteration that fulfills the derived requirements set forth. More detailed information regarding the constants used and other quantitative data can be found in Appendix C: Gearing Spreadsheet. To highlight a few key design choices, a larger face width was used for the tumbling gears to help combat the bending stress around the fixed center gear T1. The contact ratios meet or exceed the stated recommendation of 1.6 to ensure that the gears operate smoothly. In addition, the largest gears, D2 and T2, are also small enough to fit behind a housing that is 3 in across for each leg of the Tri-Wheel assembly. Now that the derived requirements for the sizing and force analyses are satisfied, the next step is to determine whether the properties of a reasonable material can satisfy the bending and contact stresses of the system.

4.3.5 Material Selection and Treatment

The calculation of various bending stress numbers s_t and contact stress numbers s_c in the previous section provides a firm foundation upon which various material properties can be assessed for viability. Two strategies are considered; first, The American Gear Manufacturers Association has developed a set of allowable bending stress numbers s_{at} as well as a set of allowable contact stress numbers s_{ac} which can be compared to computed bending stress and contact stress levels in a gear tooth to rate the acceptability of a design.

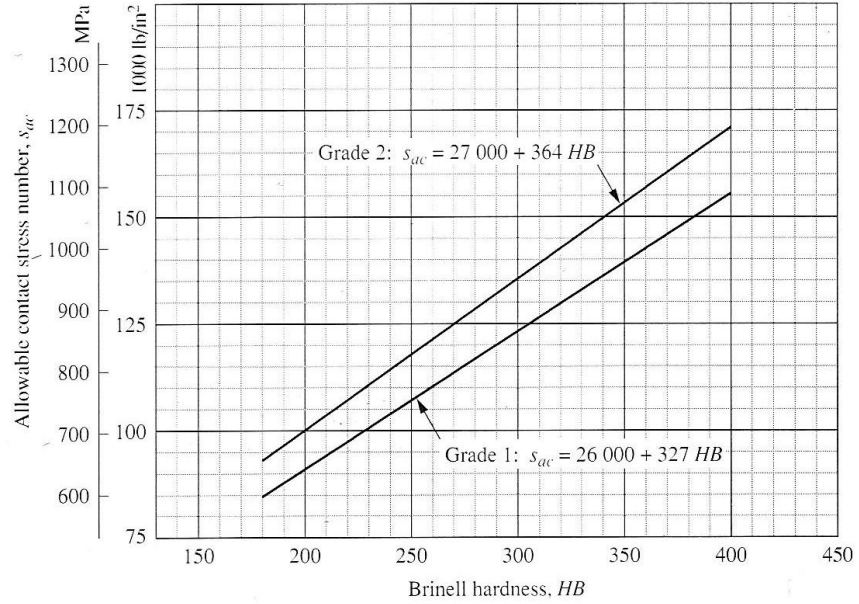


Figure 4.16: Allowable Contact Stress Number for Steel Gears [19]

A thorough explanation of the method used to obtain s_{ac} and s_{at} as well as the various modification factors considered and their respective derivations is included in [31]. For conciseness, only graphs of the allowable bending and contact stress numbers as a function of the Brinell Hardness HB are included in this report. Figure 4.16 and Figure 4.17 are graphical representations of the information presented in [31], displaying typical values for allowable contact stress numbers and bending stress numbers, respectively. The condition must be met that $s_c < s_{ac}$ and $s_t < s_{at}$.

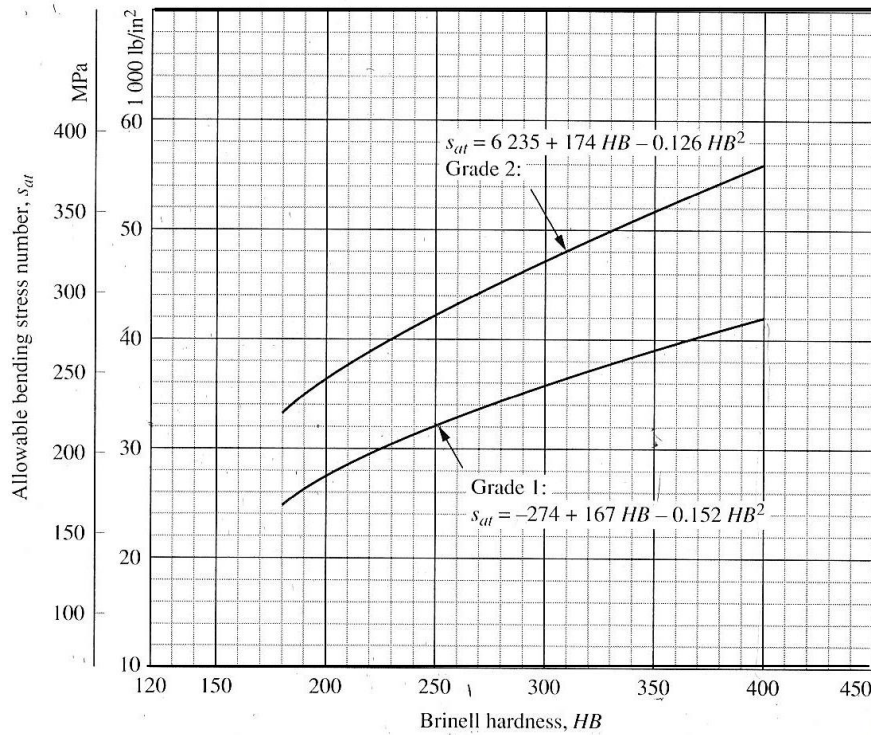


Figure 4.17: Allowable Bending Stress Number for Steel Gears [19]

In addition to this method, [20] recommends that s_t simply be compared with the corresponding fatigue strength, estimated as a function of the endurance limit. This source also recommends that s_c be compared to values plotted in a surface fatigue strength S-N curve obtained experimentally from tests in which factors of thermal stresses, changes in pressure distribution, and stresses from sliding friction are considered. Because this information is not readily available, an approximate surface fatigue strength curve for spur gears is utilized. The fatigue strength is calculated as [20]:

$$S_n = S_n' C_L C_G C_S k_r k_t k_{ms} \quad (4.75)$$

where S_n' is the standard R.R. Moore endurance limit (approximated as $0.5 \cdot S_u$ for steel). The endurance strength of a material is its ability to withstand fatigue loads, providing an

estimate of the stress level that a material can withstand for a given number of loading cycles. Eliminating the load factor C_L , gradient factor C_G , reliability factor k_r , and temperature factor k_t which are all equal to 1.0 for this case, the equation becomes:

$$S_n = S_n' C_S k_{ms} \quad (4.76)$$

C_S is the surface finish factor and accounts for the reduction in endurance limit due to surface finish. Figure 8.13 in [20] is a graph of surface factor as a function of Brinnel Hardness and tensile strength and is used to estimate this parameter for steel parts. The mean stress factor k_{ms} is equal to 1.0 for idler gears subjected to bending in two directions and 1.4 for input and output gears that experience one-way bending. Depending upon where the maximum bending stress values occur, the value of 1.4 might have to be incorporated. The condition must be met that $s_t < S_n$.

In order to estimate the surface fatigue strength S_h , an average $S-N$ curve for contact stress is considered in Figure 4.18. Note that the line being considered is explicitly for spur gears. This line does not provide the most accurate data about the particular Tri-Wheel application, but it provides information about the trend of the data and approximate values that can be viewed quickly and also compared to the values obtained through the first method discussed. The requirement for this quick estimation is that $s_c < S_h$. Finally, it is necessary to mention that the equations and related graphs used in both methods are representative of an analysis that is valid for gears operating at temperatures less than 250°F with up to 10^7 cycles of tooth loading and a reliability of 99% [19].

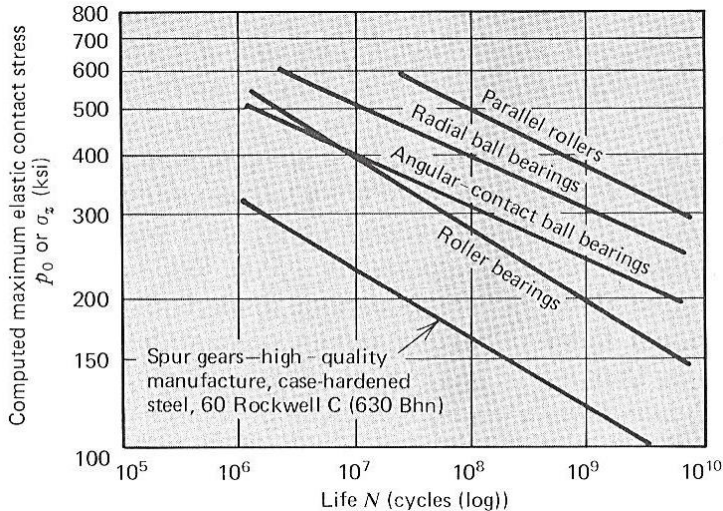


Figure 4.18: Average S-N Curves for Contact Stresses [20]

There is a wide range of available materials that can be used for gearing, but it is fairly easy to narrow down the options depending on the gearing application. Durability (wear resistance) and strength are the most critical properties to consider, though weight, cost, noise, and ease of machinability are also important factors. For the selected gearing configuration, the maximum bending and contact stress numbers present for any gear in either the driving or tumbling gear sets are, respectively: $s_{t_{1T}} = 34,913 \text{ lb/in}^2$ and $s_{c_{1T}} = 176,367 \text{ lb/in}^2$. It makes sense that the largest bending and contact stress values occur in the teeth of the small T2 gears that are tumbling around the fixed T1 gear in Tumbling Mode. Remember that these values reflect the assumption that one Tri-Wheel assembly should be able to pull along or tumble half the total mass of a 200 lb robot on its own. Furthermore, when in Tumbling Mode, one branch of the gear train must be able to move half of the robot mass since only one wheel is in contact with the ground at a time during tumbling. The mass assumption builds a safety factor of approximately 2 into

the calculations already. The goal is thus to select a material that meets or slightly exceeds these bending and contact stress numbers, as dictated by the AGMA procedures.

For a wide variety of materials considered (plastics, aluminum, steel, bronze, etc.), the approximate range determined for allowable bending stress numbers is $5,000 \text{ psi} \leq s_t \leq 75,000 \text{ psi}$. The corresponding range for the allowable contact stress number is $30,000 \text{ psi} \leq s_t \leq 255,000 \text{ psi}$. These values are arrived at considering the maximum possible values with various hardening and heat treatment conditions seen in [19]. Considering where the computed values fall within these ranges, some type of steel is a reasonable material choice. Two grades of steel are considered: grade 1 and grade 2. The grades differ in the degree of control of the microstructure, alloy composition, prior heat treatment, cleanliness, and other characteristics. Grade 2 materials are more closely controlled and permit nearly 10% to 30% higher stress levels [19]. However, for this application and budget, a grade 1 steel should suffice. Furthermore, a heat treatment process can be applied to augment existing material properties if needed.

Next, the type of steel and any specifications for heat treatments are investigated. For machine elements, it is advisable to select a material with the percent elongation of at least 12% to account for repeated loads, shock, and impact expected to occur [19]. A medium carbon steel with 0.30% to 0.50% carbon is desirable for its high strength, moderate hardness, and relatively good ductility [19]. Appendix 3 in [19] provides the design properties of a wide range of carbon and alloy steels, including ductility, tensile strength, and yield strength. Either of the two methods mentioned previously can be used to rule out materials whose bending stresses are not sufficient. For estimation purposes of the bending stress, endurance strength (approximated by half the ultimate strength) of the

material is used to assess the viability of untreated materials. It is thus determined that some type of treatment is required to meet the requirements of this gearing. This is not a surprising conclusion, as it is very common for machine parts to be heat treated in an attempt to produce high strength with acceptable toughness and ductility.

In [19], a wealth of information is available regarding heat treating options available and their effects on the material properties of steel. Case-hardening and through-hardening are the options considered. Through-hardening occurs through quenching and/or tempering. Through-hardening is achieved by heating steel to a specified temperature and placing it in a quenching medium, often oil. This increases the brittleness and internal stresses of the material, though it does also increase hardness and strength. Following quenching, tempering is often performed. This decreases the yield and tensile strength and increases the ductility. On the other hand, case-hardening is used to create a new surface (case) around the existing gear to generate high hardness to a depth of 0.010 to 0.040 inches. The core of the gear is only slightly affected by this process, if at all. This makes case-hardening particularly attractive for gears since the core remains ductile for impact and the teeth have high surface strength for wear. For this reason, case-hardening is the selected treatment.

Flame hardening, induction hardening, nitriding, and carburizing are all processes through which steel can be case-hardened. These processes actually alter the surface composition of a material by exposing it to carbon-bearing solids, liquids, or gases at high temperatures. This produces carbon and diffuses it into the surface of the component. The time of exposure and nature of the steel selected determine the depth and concentration of the carbon penetration [19]. Cyaniding and nitriding tend to result in

very thin, hard cases that are suitable for general wear resistance. Where high wear resistance and load capacity is required, as in the case of gear teeth, carburizing is preferable due to the thicker case produced. Appendix 5 in [19] provides the properties of some carburized steels. It is recommended that the core properties be used to analyze bending strength but that the case hardness should be used to estimate the contact stress [19].

Once the Brinnel hardness HB is determined, Figure 4.16 and Figure 4.17 are used in conjunction with the methods outlined in [31] to determine an approximation for the allowable contact stress number and the allowing bending stress number, respectively. Ultimately, it was determined that by the time gear blanks were bought and modified (keyways, face width, heat treatment) by different machine shops, the final cost of submitting a full order to one machine shop that can make the gears and perform heat treating is less. The manufacturer is given specifications to use a grade 1 steel that can at least meet $s_{ac} = 180 \text{ ksi}$ and $s_{at} = 55 \text{ ksi}$, while maintaining a core ductility of at least 5% for shock absorption. AISI 8620 steel is selected and carburized to meet these specifications.

4.3.6 Weight Reduction, Efficiency, Tolerances, and Lubrication

Because steel is selected as the gear material, the weight of each gear and of the entire 14-gear system is a concern. AISI 8620 alloy steel has a density of 0.284 lb/in^3 [33]. Roughly approximating one of the larger gears in the system D2 as a solid disk with a bore cutout, this produces a mass of nearly 0.71 lb for just that gear alone. For this reason, a few options are considered to physically modify the body of the gears to reduce

mass. In general, gears up to 60" in outside diameter are either webbed, given arms/spokes with cutouts, or cored with various holes to reduce weight [34]. Figure 4.19 shows all of these options individually on gear blanks. These weight reduction strategies are often combined; for instance, it is not uncommon to have a webbed gear with arms.



Figure 4.19: Arms, Webbing, and Core Holes on Gears, Respectively

The first option considered is webbing—the removal of donut-shaped volumes of steel on both sides of the gear to ultimately leave a web of steel in the center to support loads distributed on the full face width of a gear. While there are no absolute rules regarding the design of webbed gears, it is logical that any removal of material as enacted by webbing introduces additional stress concentrations into each gear where the web meets the rim of the gear. Sharp corners and small fillet radii should be avoided if possible in an attempt to reduce these stress concentrations. Figure 4.20 shows a front view and cross-sectional view of a general webbed gear.

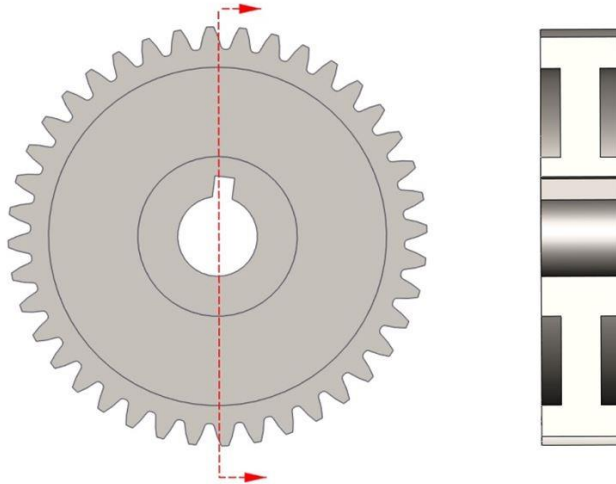


Figure 4.20: Cross-Section of Webbed Gear

Note that there is material left around the hub to provide adequate surface area for power transmission via a square key. To the right of the front view, the cross-sectional view of the gear is shown. The bright white sections represent areas where a theoretical cutting tool would pass through a solid surface. This gives the effect of what could be called a radial I-beam all the way around the gear hub and rim. The American Machinist Gear Handbook provides a variety of equations to be used as rules of thumb for the minimum thickness of this web that still supports the structural integrity of a gear. Because the face width of the driving gears is relatively thin at 0.5 inches, this does not leave much room to cut into the gear and leave enough material for structural soundness, so webbing is eliminated as an option.

Creating arms (also referred to as spokes) in a gear or bore holes (also known as lightening holes) are examined next. Again, structural soundness of the gear is the primary concern. The rim thickness factor K_B discussed previously is considered to ensure that the rim does not deform. Referencing Figure 4.13 for rim thickness factor, t_R is the rim thickness, h_t is the whole depth of the gear tooth, and m_B is a geometry

parameter known as the backup ratio. Using the following equation for each gear, the minimum rim thickness at any point in the gear is determined:

$$m_B = \frac{t_R}{h_t} \quad (4.77)$$

where $m_B > 1.2$ is required in order for the rim thickness factor to equal 1, as specified in the gearing spreadsheet analysis. For the selected gearing configuration, there are really only four sizes of gears to consider—small and large driving gears and small and large tumbling gears. Table 4.9 shows parameters relevant to the rim thickness factor for these four gear sizes. The variable d_b is the dedendum circle diameter, and d_{RIM} represents the diameter for each gear within which cutouts of any kind are acceptable to preserve structural integrity. Values of d_{RIM} are calculated by subtracting the rim thickness from the dedendum circle diameter and are rounded up slightly for more even numbers.

	<i>Small Driving (D1, D3, D4)</i>	<i>Large Driving (D2)</i>	<i>Small Tumbling (T2)</i>	<i>Large Tumbling (T1)</i>
h_t (in)	0.14	0.14	0.16	0.16
t_R (in)	0.168	0.168	0.192	0.192
m_B	1.2	1.2	1.2	1.2
d_b (in)	1.35	2.35	1.25	2.4
d_{RIM} (in)	≈ 1.00	≈ 2.00	≈ 0.875	≈ 2.00

Table 4.9: Rim Thickness Sizing Parameters

It is clear that for the small driving and small tumbling gears, cutouts of any kind are either impractical or inconsequential when factoring in a reasonable diameter for clearance around the hub. The gears T2 and D2 are thus the only gears for which mass

reduction is possible. Incorporating arms/spokes for the gears, the average width of each spoke is 0.375 in for D2 and 0.25 in for T2. These values are approximated using rules of thumb and general advice provided by [34]. The depths of these gears remain at full face width at 0.50 in and 0.75 in, respectively. Using core holes within the acceptable diameter d_{RIM} , it is determined that the volume of steel able to be removed from the gears while maintaining structural soundness is less than that removed using the arms. Therefore, all D2 and T2 gears receive cutouts that ultimately remove 0.79 lb from the Tri-Wheel assembly.

Calculation of efficiency for gearing is largely a function of the sliding velocity present between gear teeth, which is dependent upon specific measurements of the angles of interaction during mesh. According to [18], gear efficiencies are often in the range of 98% or more, and for this reason, it is common for many gear designers to neglect this small loss in their calculations. This source continues to stress that in many applications, this small friction loss causes concern only because it must be dissipated as heat throughout the gear system. For the Tri-Wheel application, heat dissipation is not a large concern as the pitch-line velocity is very low compared to values expressed in Figures 14-1 through 14-5 of [18] on the order of 1,000 to 4,000 ft/min. These figures show various trends relating the coefficient of friction, pitch-line velocity, and efficiency.

Furthermore, the true losses in a gearbox are not simply due to the gear mesh itself. Bearing losses which are discussed in a future chapter, as well as other losses that are more difficult to quantify without testing, are expected to reduce the overall power output of the Tri-Wheel system. Figure 14-5 in [18] shows nominal efficiency of spur gears using standard petroleum oil and a hardened surface similar to the heat treatment

selected for this application. This efficiency ranges from 98% to 100% and increases with increasing pitch-line velocity. Table 12-2 in [18] adds that the total range of losses per mesh can range from $\frac{1}{2}$ to 3% in some cases. Therefore, it is reasonable and conservative to estimate that 98% of the power will be transferred in each gear-mesh interaction. There are three mesh interactions per gear train in Driving Mode, yielding approximately $(0.98)^3$ or nearly 94.1% power efficiency. There are two mesh interactions per gear train in Tumbling Mode, producing $(0.98)^2$ or roughly 96% power efficiency. Due to the factors of safety included in the calculations for required torque to tumble and maximum desired speed, 94.1% of the maximum power output in Driving Mode still produces a speed exceeding 5.8 MPH, and the maximum torque produced still exceeds the theoretically calculated value of about 45 ft-lbs. Because precision in the gearing design beyond its ability to meet these derived requirements without failing is not imperative, this discussion of efficiency is sufficient.

The tolerances present in any gearbox are critical to its functionality. Tolerances related to the individual gears are less important to specify since there are well-known standards for tolerancing that are applied by the gear manufacturer. Assembly tolerances related to installation of gears in a housing should however be specified by the designer. Gear center distance tolerance is the primary concern since it directly affects gear function with respect to backlash and contact ratio [18]. Excessive backlash, binding, or a low contact ratio can result from improper tolerance specification. Center-to-center dimensioning is an acceptable strategy for a housing in which gear centers are single bearing plate or pairs bored together, which is the case for the Tri-Wheel housing to be discussed later. For commercial gear trains, a tolerance of ± 0.002 is recommended for

center distances under 1 in, and a tolerance of ± 0.003 in is recommended for center distances from 1-6 in [18]. A gearing engineer in the Tribology department at NASA Glenn recommends that no additional clearance be added between the centers of gears when precision is important and backlash is undesirable. Additional tolerance considerations are addressed in subsequent chapters as the individually designed and specified Tri-Wheel components are assembled into one functional system.

The final consideration for the Tri-Wheel gearing is lubrication. All gears regardless of their material and type incur greater life expectancies with proper lubrication. Due to the relatively low rotational speeds of the gears in this configuration, a paddle, brush, or drip cup is recommended to lubricate the gearing rather than using an oil pump or other continuous application mechanism [18]. The housing of the Tri-Wheel to be discussed later is designed such that lubrication can be reapplied when necessary, but it is anticipated that a single application of lubricant for testing purposes will be sufficient. A variety of standard AGMA lubricants are available. These lubricants are numbered from 1 to 8 and represent different viscosity ranges at different operating temperatures. As noted in [18], there is really no infallible rule used to obtain the exact viscosity of the lubricant that is needed for particular ratings or sizes of gear units. However, it is recommended that for parallel shaft single reduction gear trains with center distances up to 8 in operating between 15-60°F, AGMA No. 2 is one potential appropriate lubricant that is available.

5 MECHANICAL ASSEMBLY DESIGN

5.1 Driving Factors and Design Philosophy

While the gearing specification and kinematic analysis theoretically designate whether or not the Tri-Wheel is able to operate as desired in different terrain, the mechanism itself will not function in the real world without an adequate mechanical assembly design.

Depending on the industry, the importance of cost on the overall design is variable. In the aerospace sector, for instance, mass is often the driving factor over cost. However for purposes of this project, the cost to produce a Tri-Wheel is very important. Working within a limited budget, the choices made in this chapter reflect a desire to minimize overall cost while modeling a layout that will function for preliminary testing and proof of the concept.

Every engineer has a unique design philosophy. Some prefer to specify everything on paper with numbers and analyze the system in great detail before bringing the product to life and manufacturing. Others prefer to prototype along the way if it is cost-effective (or if cost is not a concern) and learn from those real models to modify their existing calculations and theoretical models. This project ideally requires a combination of both. Because the Tri-Wheel is a novel concept, there are certain design factors affecting its operation that might not become noticeably important until one is built and tested. Furthermore, any individual who has assembled a gearbox or some mechanical system should agree that it is rare indeed for an assembly to slip together perfectly as desired the

first time without any modification required to improve the installation process or the performance of the mechanism itself.

Taking this bit of logic into consideration, the cost to produce early Tri-Wheel prototypes has still made the fabrication of any early working prototypes unfeasible. An attempt was made to use rapid prototyping for the gears and housing along with metal bearings and bushings, as the gears and housing are the most costly components. While this provided a good sense of scale and size and a model to begin critique of, the 3D-printed version was not functional to test. With the rapid prototyping machines immediately available, the size of the Tri-Wheel housing exceeded the build volume of the machine, so the assembly was broken into thirds. This created mismatches in bearing alignment and poor tolerance control. The plastic model was, however, sufficient to spark conversation regarding how parts could be modified to reduce some cost.

The mechanical assembly design discussed in this chapter therefore describes the design of the first real, functional Tri-Wheel assembly fabricated with the specified materials. While thorough analysis has been performed, it is essential to prove the concept with working prototypes. For this reason, this design leaves room for mechanical modification that might be found necessary during assembly. Following this model and subsequent testing, it is expected that some changes will be made to increase functionality or ease of assembly. Along with those changes, it is hopeful that a future version of the Tri-Wheel can be manufactured in which the cost of the housing and other assembly components is not quite as restrictive. In summary, the Tri-Wheel mechanical assembly design chronicled in this chapter is based on sound analysis and fit for testing, but given the restrictions of cost and the limited availability of prior physical models to

study, room for improvement is predicted and will conceivably be accounted for in a future working model.

5.2 Shaft Design

With the gearing configuration specified and the transmitted forces and torques known, the next logical step is to design shafts that support the gears in the Tri-Wheel mechanism. The shafts transmit rotational motion and power produced by the gears, and as such, they are integral to a successful gearing design. As discussed, manufacturing cost is an overarching constraint for the mechanical assembly design and will help to shape certain choices in this analysis. Of course, the primary concern is that the shafts are strong enough to withstand the maximum cases of shearing force and bending moment. A satisfactory material selection and shaft diameter specification are required to prevent failure. Deflection of the shafts is not a primary concern of this analysis because they are relatively short. Intentionally, the shafts are kept as short as possible and are straddle-mounted (supported by two bearings on each end) to best support each rotating member.

It is important to note that there are simplifications in this analysis deemed reasonable by sources including [19], [20], and [29]. Particularly with short shafts, it is not entirely accurate to model bearing loads as point loads, as the load is truly distributed across the length of the bearing. Furthermore, the loading might not always be equally distributed between the bearings as a free body diagram may suggest. The mode of operation (driving versus tumbling) and a variety of other environmental conditions such as the grade of a slope and the orientation of the robot chassis could load the bearings unequally. However, these sources model shaft diagrams using point loads and

reasonable model of the maximum load distribution; thus, incorporating a judicious factor of safety, this simplified analysis is deemed sufficient. Examining the gears, it can be recalled that the contact ratio for this design is set at 1.6 or greater, meaning that the transmitted tangential load will be distributed across more than one gear tooth. The distribution of this loading within the gears is simplified and treated as resultant tangential and radial loads, which is satisfactory for this analysis in which the resultant gear forces on the shafts are ultimately desired. Overall, this analysis is detailed and accurate enough to compute a valid estimate for each shaft diameter, given a particular material selection.

5.2.1 Methodology

There are five different shaft specifications required for the Tri-Wheel assembly. As shown in Figure 5.1, shaft D1 supports the wheel, shaft D2 supports the driving gear idler, shaft C links gears C2 and D2, shaft A is the primary driving gear set drive shaft, and shaft B is a hollow shaft affixed directly to gear T1. Because of the simultaneous presence of normal stresses due to bending and torsional shear stresses, the stress analysis method utilized for shaft design involves a combined stress approach. Bending stresses are created as a result of power-transmitting components (spur gears, in this analysis) which exert forces on their respective shafts perpendicular to the shaft axis in the transverse direction. While transmitting power and some rotational speed, each shaft is also inevitably subjected to torque that leads to torsional shear stress development in the shaft. The particulars of the bearings and other mechanical components shown in Figure 5.1 are addressed in subsequent sections of this chapter. For now, the shaft analysis

mentions bearings to the extent of determining the bearing support loads present for each shaft arrangement.

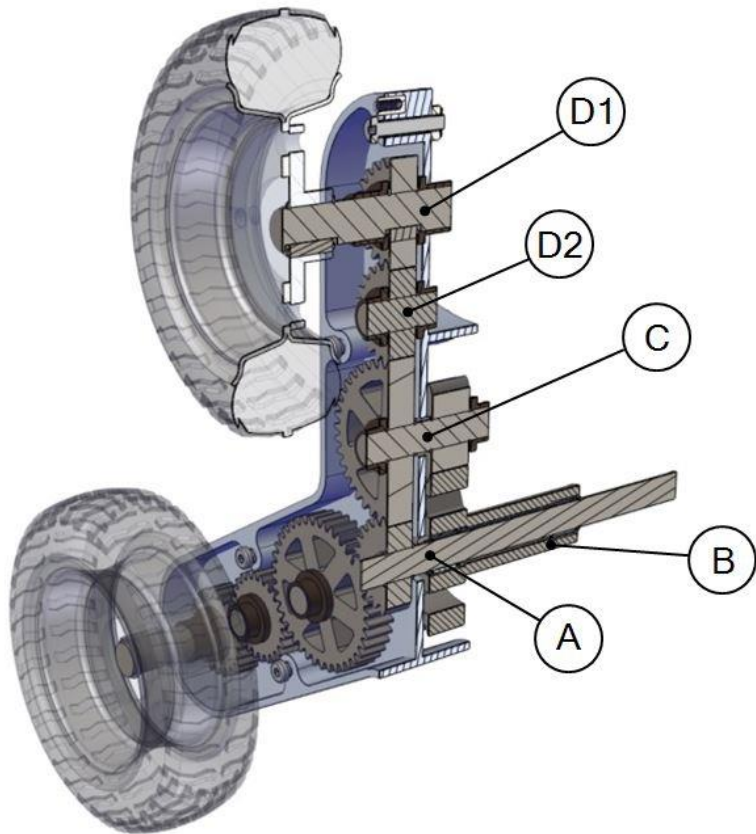


Figure 5.1: Cross-Sectional View With Shaft Nomenclature

Bending and moment diagrams are thus created and analyzed for each shaft. Then, the forces in the vertical and horizontal planes are used to chart the shearing force and bending moment developed throughout each shaft. The case of maximum stress for each shaft (also called the critical point) is considered, which leads to the determination of an adequate shaft diameter that ensures safety under the loading at that location. The following equation is used to solve for the diameter D of a shaft in units of inches [19]:

$$D = \left[\frac{32N}{\pi} \sqrt{\left[\frac{K_t M}{s'_n} \right]^2 + \frac{3}{4} \left[\frac{\tau_s}{s_y} \right]^2} \right]^{1/3} \quad (5.1)$$

where N is the design factor or safety factor, K_t is the stress concentration factor, M is the bending moment (in-lb), s'_n is the modified endurance strength (psi), τ_s is the torque developed in the shaft (in-lb), and s_y is the yield strength (psi).

The bending moment M is computed as the resultant moment of the applied horizontal and vertical forces. The safety factor N is recommended under typical operating conditions as 2 or 3 [19]. The torque in a shaft developed from a spur gear is computed simply as [19]:

$$\tau_s = \frac{63,000P}{n} \quad (5.2)$$

where P is the power being transmitted in units of HP and n is the rotational speed in RPM. The stress concentration factor $K_t = 1.6$ is appropriate for the type of keyseat selected for the shafts (to be further discussed in another section of this chapter). To account for retaining ring grooves that will be used for axial location, it is recommended that the resulting computed diameter from Equation (5.1) be increased by approximately 6% as a safety precaution [19].

The modified endurance strength s'_n is calculated by multiplying the endurance strength s_n by a size factor C_S and a reliability factor C_R :

$$s'_n = s_n C_S C_R \quad (5.3)$$

The size factor accounts for the stress gradient within the shaft material and for the probability of a given section having some sort of damaging occlusion that might initiate a fatigue crack [19]. For shaft diameters less than 2.0 in, the size factor is evaluated using the given expression:

$$c_s = \left(\frac{D}{0.3} \right)^{-0.068} \quad (5.4)$$

Endurance strength data are typically obtained by repeated testing of materials and then averaging values over many trials. This implies that a typical reliability for the value is roughly 50%. Under the assumption that actual failure data would follow a normal distribution, higher reliability can be achieved by adjusting by the reliability factor. Desired reliability of 90% is deemed sufficient, and the corresponding reliability factor $C_R = 0.90$ is used. Lastly, the yield strength is described as the point at which a material has elongated plastically, to a large degree, and permanently. Values of the yield strength are available for a wide variety of materials in credible online databases as well as in the appendices of many engineering textbooks.

In order to minimize cost and manufacturing time, stepped shafts will not be used, though they could be used in future Tri-Wheel models. The purpose of increasing or decreasing shaft diameter is to axially locate the gears. This means that each shaft will have a constant diameter along its entire length, and the maximum resultant bending moment will be used to determine that shaft diameter in each analysis.

In the pursuit of creating representative bending and moment diagrams for each shaft, it is important to make sure that the direction of applied forces and reaction forces between the mating gears are going in the correct direction. As discussed in the gearing

analysis, the two types of forces are radial forces and tangential forces, related by the pressure angle. According to [35], there are simple qualitative rules that describe the force direction between two gears in mesh. For the driving gear (which first receives power and transmits it to the driven gear), the tangential force occurs opposite to the direction of motion and applied at the pitch point. For the driven gear, the tangential force occurs in the direction of motion and applied at the pitch point. The radial force for either driving or driven gears is directed radially inward to the gear center and applied at the pitch point [35].

The subsequent analysis is performed for the final Tri-Wheel configuration, reflecting the exact shaft lengths. While this report includes analysis of the optimized mechanism, it is important to note that this process was repeated iteratively along with the gearing analysis until a satisfactory gearing and shaft design was achieved. It is desirable to minimize shaft length when possible in order to decrease potential deflections. Additionally, use of the minimum diameter that results in a viable shaft design is advised to reduce weight of the Tri-Wheel system.

5.2.2 Gear System Free Body Diagrams

Depending on whether the Tri-Wheel is in Driving Mode or Tumbling Mode, different forces will be experienced by the shafts. In Driving Mode, the torque transmitted through gear D1 is divided evenly between the two gear train branches linking D1 to the two wheels on the ground. The weight of the robot is also divided between the normal forces of two wheels per assembly versus a single wheel in Tumbling Mode. Because only one wheel and thus a single gear train branch is theoretically in contact with the ground at any

one time in Tumbling Mode, the forces experienced are greater in this case. In order to ensure that the shafts are designed to meet the loads in the highest loading condition, a single gear branch in Tumbling Mode is considered for the free body diagrams of the gears and shafts. Following the rules presented in [35], the gear force directions for one branch are included in Figure 5.2: Single Gear Branch Free Body Diagram Front View

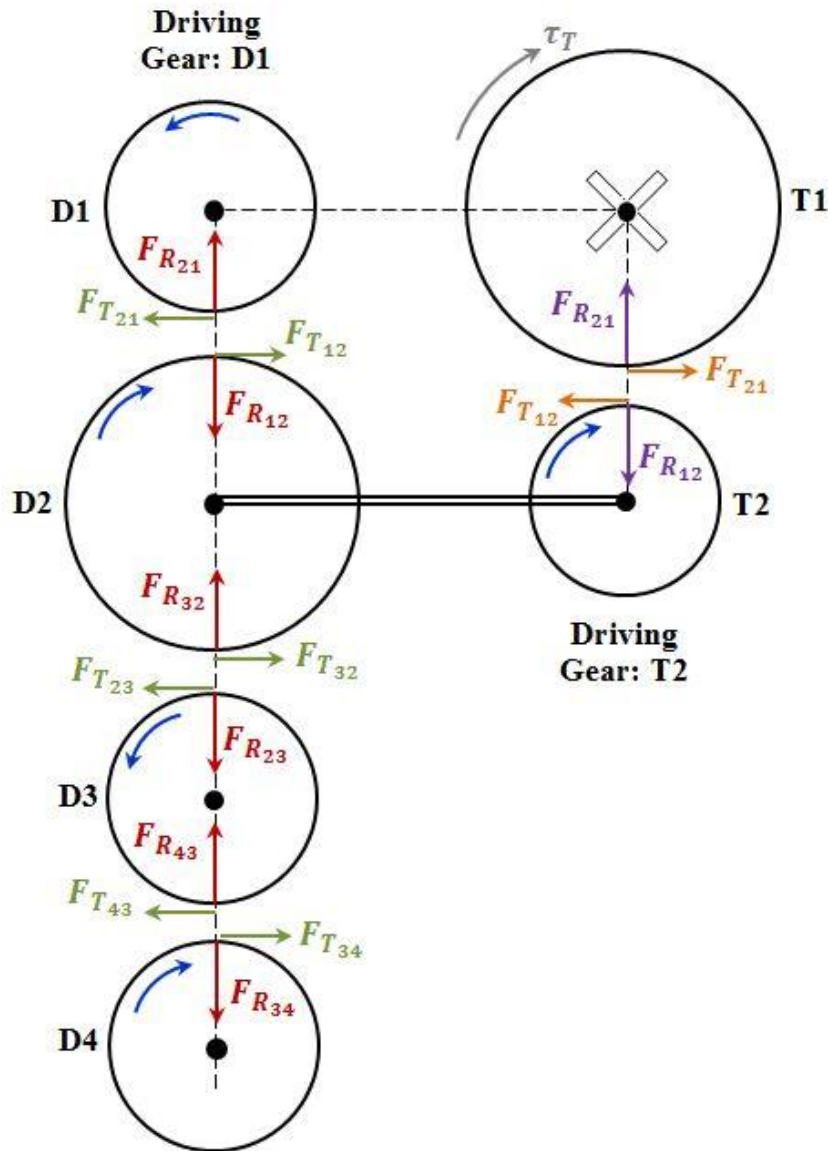


Figure 5.2: Single Gear Branch Free Body Diagram Front View

This diagram does not show reaction forces with bearings or the shaft but is a simple depiction of the gear forces themselves. Note that this is a front view, so typically the right-hand gears T1 and T2 would be concentrically located behind gears D1 and D2. For clarity, these gears have been moved to the right so that they are visible to the reader. The double thickness horizontal line connecting gears D2 and T2 symbolize that these particular gears are keyed to the same shaft and rotate at the same angular velocity. The nomenclature $F_{T_{12}}$ denotes the tangential force from gear 1 applied to gear 2. The same naming convention applies to the radial forces such as $F_{R_{12}}$. The blue arrows represent the direction of rotation. It is also important to observe that, because there is a distinction drawn between driving gears and driven gears for purposes of force direction, the initial driving gears for the Driving and Tumbling Mode gear sets are D1 and T2, respectively. The gray applied torque τ_T represents the braking torque applied that enables the Tri-Wheel to tumble and prevents gear T1 from rotating.

According to [18], if only the input and output shafts are used and a constant horsepower is driven through the train, the load on all the gear teeth in the train is the same. This source also notes that when idlers are in a line, the radial force components cancel, and the tangential loads add directly. The resultant bearing load distributed between bearings supporting the shaft is thus twice the tangential force.

5.2.3 Shaft A

Shaft A is unique in that it is partially encapsulated by hollow shaft B and gear T1. There are six points of interest for shaft A, as labeled in Figure 5.3. These points of interest are color coded as follows: gray for gears, brown for bearings, and black for other forces.

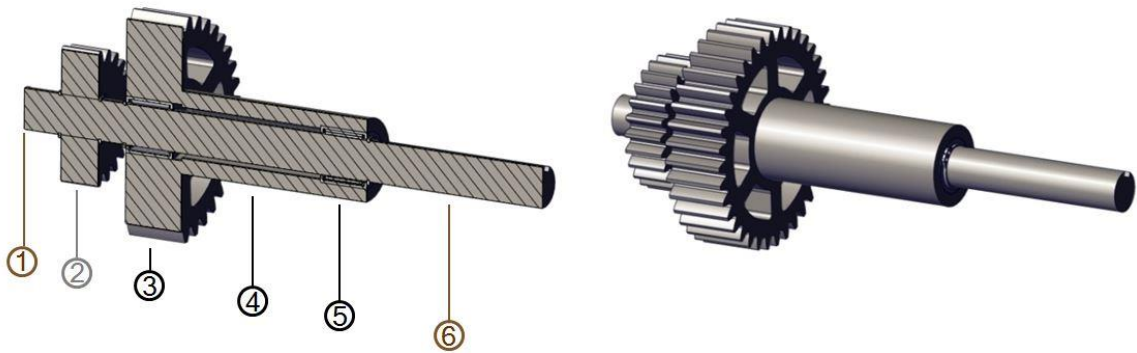


Figure 5.3: Shaft A Cross Section and Isometric

Shaft A is supported inside gear T1 and shaft B by two needle bearings located at points 3 and 6. Because shaft B rotates around shaft A, there is no power transmission between gear T1 and shaft A. For this reason, it is assumed that the only effect of gear T1 on shaft A would be the weight of T1 itself acting upon shaft A, and the reactions from the needle bearings could be approximated as reaction forces to the weight of the gear.

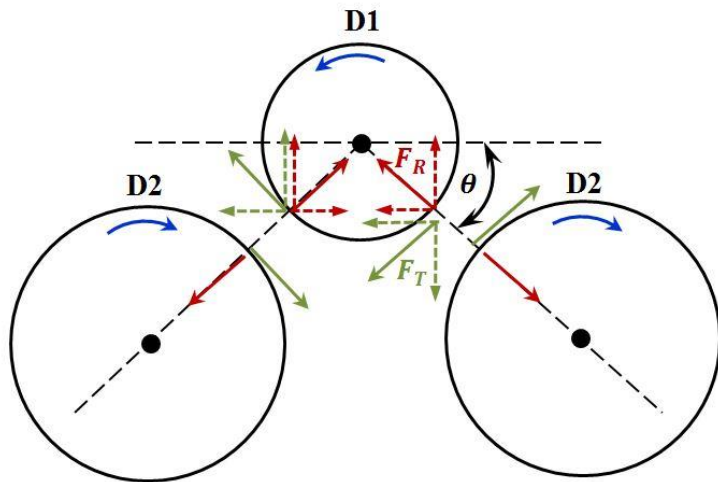


Figure 5.4: Reaction Forces on D1 in Driving Mode

In Driving Mode, gear D1 experiences loading from two gears rather than one gear as in Tumbling Mode. For completeness, a general free body diagram of gear D1 in Driving Mode is shown in Figure 5.4. Forces from the third D2 gear directly above D1

are not included since the last D2 gear is unloaded. Any weight felt in the system by the omitted gear branch is accounted for and discussed later in the analysis. Here, the vertical components of the radial forces add, and the horizontal components cancel out. The horizontal components of the tangential forces sum together, and the vertical components cancel out. The angle θ at which the gears are inclined is 30° . Thus, the total horizontal force acting on gear D1 from the gears is equal to $2F_{T_{21}} \cos 30$. The resultant vertical force acting on gear D1 is equal to $2F_{R_{21}} \sin 30$.

The gearing spreadsheet analysis in Chapter 4 is performed with the requirement that one branch of the Tri-Wheel gearing must be able to pull along half the mass of the entire vehicle. In other words, one branch of the gearing receives all the power. For this particular shaft analysis, the values of radial and tangential force are equal to half of the values obtained in the gearing analysis spreadsheet since the power is divided between the two loaded gear branches in Driving Mode. Thus, $A_x = -212.3 \text{ lb}$, $A_y = -77.27 \text{ lb}$, $B_x = -27.69 \text{ lb}$, $B_y = -10.08 \text{ lb}$, $F_{R_{21}} = 43.68 \text{ lb}$, and $F_{T_{21}} = 120 \text{ lb}$.

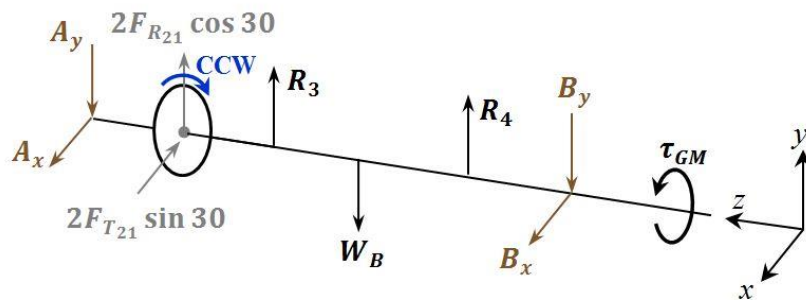


Figure 5.5: Shaft A Driving Mode Free Body Diagram

The free body diagram for shaft A is shown in Figure 5.5. Because this diagram is for Driving Mode, the radial and tangential gear forces are modified as discussed. Yet this does not produce the maximum case of shear and bending, so the case for Tumbling

Mode with all the power applied and the branch in a vertical position as in Figure 5.2 is considered. Notice that the weight of gear T1 and two reaction forces from the needle bearings modeled as simple supports are included. However upon further examination, the weight of T1 is only approximately 1.0 lb, and this force is safely deemed negligible given that the other forces are at least one order of magnitude larger. Forces W_B , R_3 , and R_4 are removed from the free body diagram, and then the forces are split into vertical and horizontal (y and x components). Equations for the case of the simple beam with a concentrated load at any point are used to evaluate the forces, and then the shear and moment diagrams are plotted in Figure 5.6. All equations used for the bending and moment diagrams can be located in Appendix D.

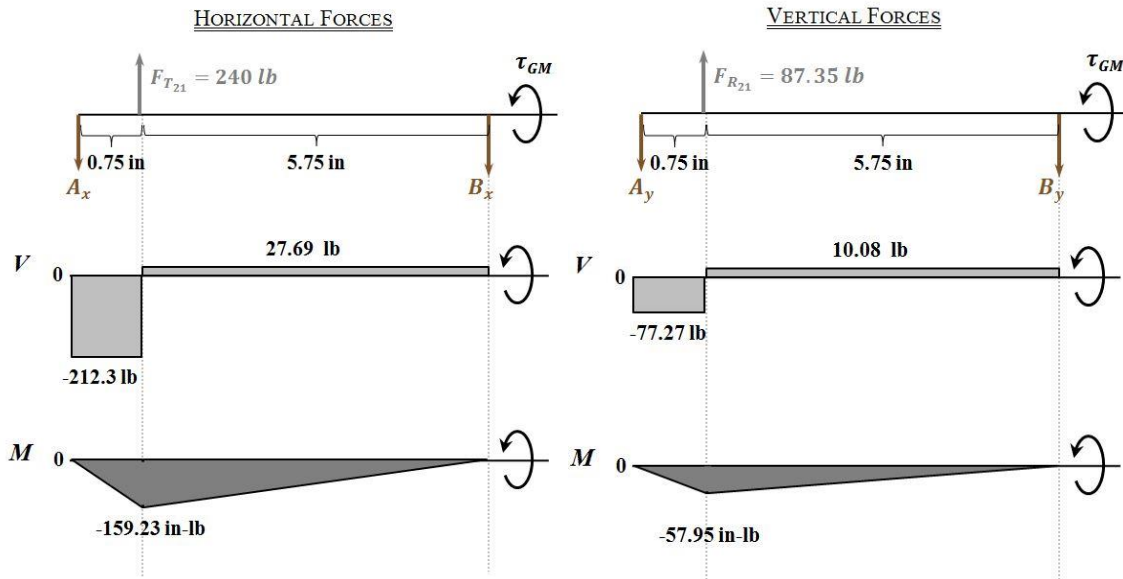


Figure 5.6: Shaft A Shear and Moment Diagrams

Then, the maximum resultant moment is calculated as the sum of the squares of the maximum moment values of the vertical and horizontal moment diagrams:

$$M_{max} = \sqrt{M_x^2 + M_y^2} \quad (5.5)$$

$$M_{max} = \sqrt{(-159.23)^2 + (-57.95)^2} = 169.45 \text{ in} \cdot \text{lb} \quad (5.6)$$

Next, the torque in the shaft is calculated using the power experienced during Tumbling Mode through one gear train operating at the specified speed from the analysis performed in Chapter 4:

$$\tau_s = \frac{63,000P}{n} = \frac{63,000(0.868 \text{ HP})}{303.8 \text{ RPM}} = 180 \text{ in} \cdot \text{lb} \quad (5.7)$$

A number of materials are considered, but AISI 4140 steel is selected due to its material properties and high fatigue strength that keep the computed shaft diameters relatively low. From [19], the yield strength s_y of AISI 4140 is 60,000 psi, and the modified endurance strength $s'_n \approx 45,000$. Using the recommended safety factor of 2, the shaft diameter is calculated as:

$$D_A = \left[\frac{32(2)}{\pi} \sqrt{\left[\frac{1.6 \cdot (169.45 \text{ in} \cdot \text{lb})}{45,000 \text{ psi}} \right]^2 + \frac{3}{4} \left[\frac{180 \text{ in} \cdot \text{lb}}{60,000 \text{ psi}} \right]^2} \right]^{1/3} \quad (5.8)$$

$$D_A \approx 0.511 \text{ in} \quad (5.9)$$

As recommended, this value is increased by 6% to account for the retaining ring grooves that will be cut into the shafts:

$$D_A \approx 0.472 * 1.06 = 0.54 \text{ in} \quad (5.10)$$

Given the compounding safety factors in other areas of the gearing analysis, the final diameter for shaft A is rounded slightly down to an even 0.50 in to enable the purchase of stock shaft with a common diameter, and the chosen material is AISI 4140 steel.

5.2.4 Shaft B

Shaft B is unique in that it is the only hollow shaft used in the Tri-Wheel assembly. Though there are indeed bearing forces supporting the shaft, the most obvious case of failure comes not from bending but from the twisting moment applied to brake the shaft relative to the robot chassis in order to facilitate Tumbling Mode. For this reason, rather than modeling shaft B using bending and moment diagrams as is done for the other shafts, this shaft is simply analyzed for torsional shear stress.

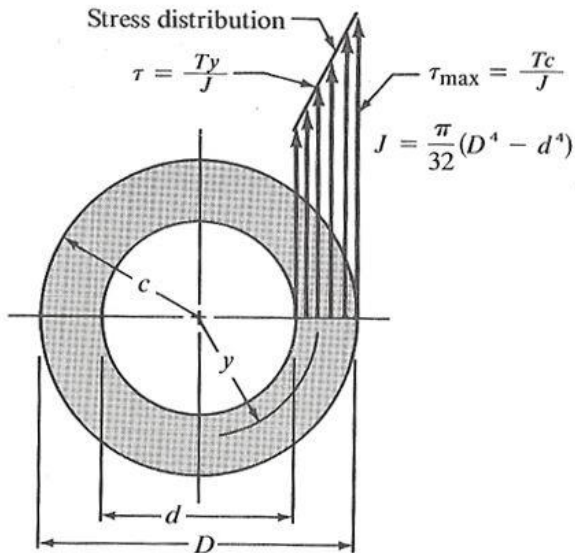


Figure 5.7: Stress Distribution in Hollow Shaft [19]

When subjected to a torque, the outer surface of a round shaft experiences the largest shearing strain and hence the largest torsional shear stress. Figure 5.7 depicts this behavior and provides some basic equations used in this analysis.

Rearranging a number of equations, the outer diameter of this shaft can be solved for. First, the polar section modulus Z_p can be expressed through the following equations found in [19] and then solved for D4:

$$Z_p = \frac{\tau_{max}}{\tau_d} \quad (5.11)$$

$$Z_p = \frac{\pi(D^4 - d^4)}{16D} \quad (5.12)$$

$$\frac{\tau_{max}}{\tau_d} = \frac{\pi(D^4 - d^4)}{16D} \quad (5.13)$$

The design shear stress τ_d is computed simply using the distortion energy theory as:

$$\tau_d = \frac{0.577s_y}{N} \quad (5.14)$$

Using a safety factor of 3 due to the critical nature of this component's resistance to torsional shear and an approximate yield stress for carburized AISI 8620 steel of 83,000 psi from [19], the design shear stress is calculated as:

$$\tau_d = \frac{0.577(83,000 \text{ psi})}{3} = 15,963.7 \text{ psi} \quad (5.15)$$

The maximum estimated required torque to tumble is approximately 45 ft-lb, as derived in Chapter 4. This value can be multiplied by 12 to convert to in-lb, yielding 540 in-lb as τ_{max} . The inner diameter of the hollow shaft d equals 11/16 inches since that is the outer diameter of a needle bearing that will be pressed inside the hollow shaft to support shaft

A. Substituting in these computed values into Equation (5.13), a solver is used to obtain the outer diameter D:

$$\frac{540 \text{ in} \cdot \text{lb}}{15,963.7 \text{ psi}} = \frac{\pi \left[D_B^4 - \left(\frac{11}{16} \text{ in} \right)^4 \right]}{16D_B} \quad (5.16)$$

$$D_B \approx 0.77 \text{ in} \quad (5.17)$$

Therefore, the minimum outer diameter of shaft B is just over $\frac{3}{4}$ of an inch. The existing robot chassis at NASA Glenn that is available for testing (and will be discussed later) utilizes eight bearings that support a 1.0 *in* diameter shaft. Given the fact that this hollow shaft essentially supports the mass of the Tri-Wheel at the connection point to the robot chassis and could see additional shock loading, a decision is made to size up to an outer diameter of 1.0 *in*. This will not increase the mass of the assembly or the cost significantly but will save money on extra bearings and time regarding the mechanical implementation.

Lastly, it is important to comment on the fact that shaft B is directly connected to gear T1. Previously, a flange was considered to attach a hollow shaft to the gear, but this was more complex than desired and increased the overall width of the Tri-Wheel gearing assembly significantly, even when portions of the flange were recessed. Though it is possible, it is also undesirable to key a hollow shaft due to the stress concentrations imparted. The ideal design involves fabrication of the gear and shaft out of the same piece of continuous material to avoid any overly complex of stress-inducing assembly within the gear housing. After obtaining a variety of cost estimates, this was determined to be a viable option within the budget available.

5.2.5 Shaft C

Shaft C is primarily responsible for connecting the driving and tumbling gear sets. Figure 5.8 depicts gears D2 (larger) and T2 (smaller) keyed to their common shaft. Recall from the gearing design that the face width of the tumbling gears is 0.25 *in* larger than the face width of the driving gears. Thought this theoretically distributes the load differently, the assumption is that the radial and tangential loads are applied at the center of those gears at the pitch point. Retaining rings axially locate these gears and ensure that they do not slide axially along the shaft and interfere.

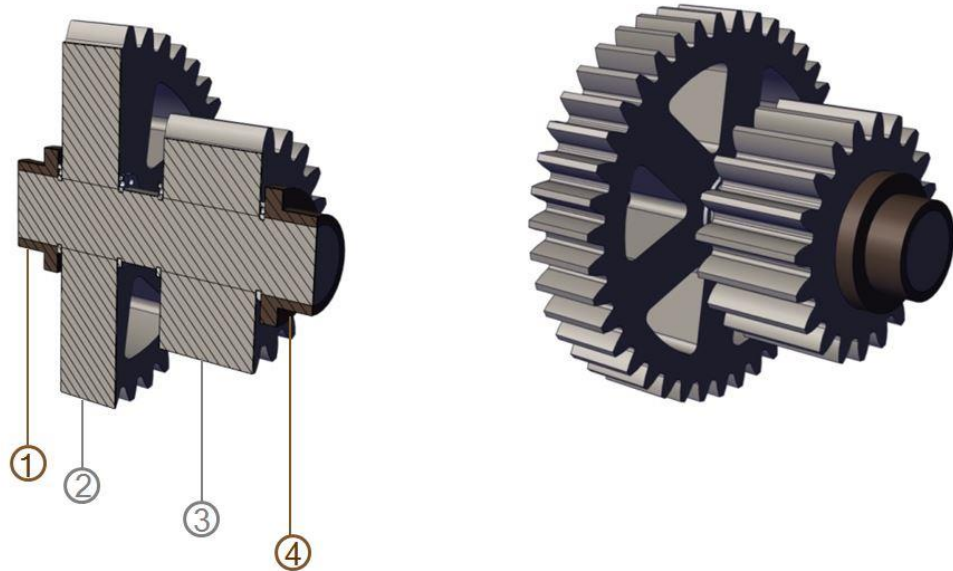


Figure 5.8: Shaft C Cross-Section and Isometric

Because gear D2 is an idler situated between gears D1 and D3, the radial forces cancel out due to equal but opposite bending stresses. The same tangential and radial forces (and the same power) are transmitted through the entire driving gear branch, and as such, there are tangential reaction forces from gear D1 and D2 on D2. It is interesting to note that, while the rotational directions of gears D2 and T2 are both clockwise, the

forces acting on these gears occur in different directions according to the rules outlined in [35] explaining the difference in forces between a driving and driven gear. Gear D₂ is both a driving and a driven gear since it is an idler, but gear T₂ is treated as a driving gear that receives its power from shaft C. The free body diagram of this shaft in Figure 5.9 displays all of the acting forces on shaft C, including the radial forces that will end up cancelling out.

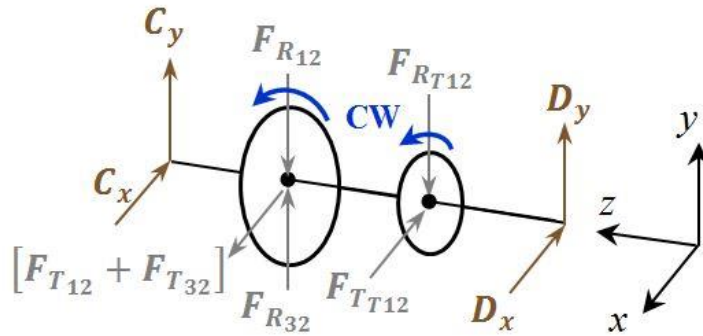


Figure 5.9: Shaft C Free Body Diagram

Next, the vertical and horizontal force must be divided into two force diagrams, and the shear and moment diagrams for the respective planes are created. Figure 5.10 depicts the vertical (radial) and horizontal (tangential) forces in the system. Here, $C_x = 431.68 \text{ lb}$, $C_y = 49.15 \text{ lb}$, $D_x = 75.45 \text{ lb}$, $D_y = 103.28 \text{ lb}$, $F_{R_{T12}} = 152.87 \text{ lb}$, $F_{T_{T12}} = 420 \text{ lb}$, and $F_{T_{12}} = F_{T_{32}} = 240 \text{ lb}$.

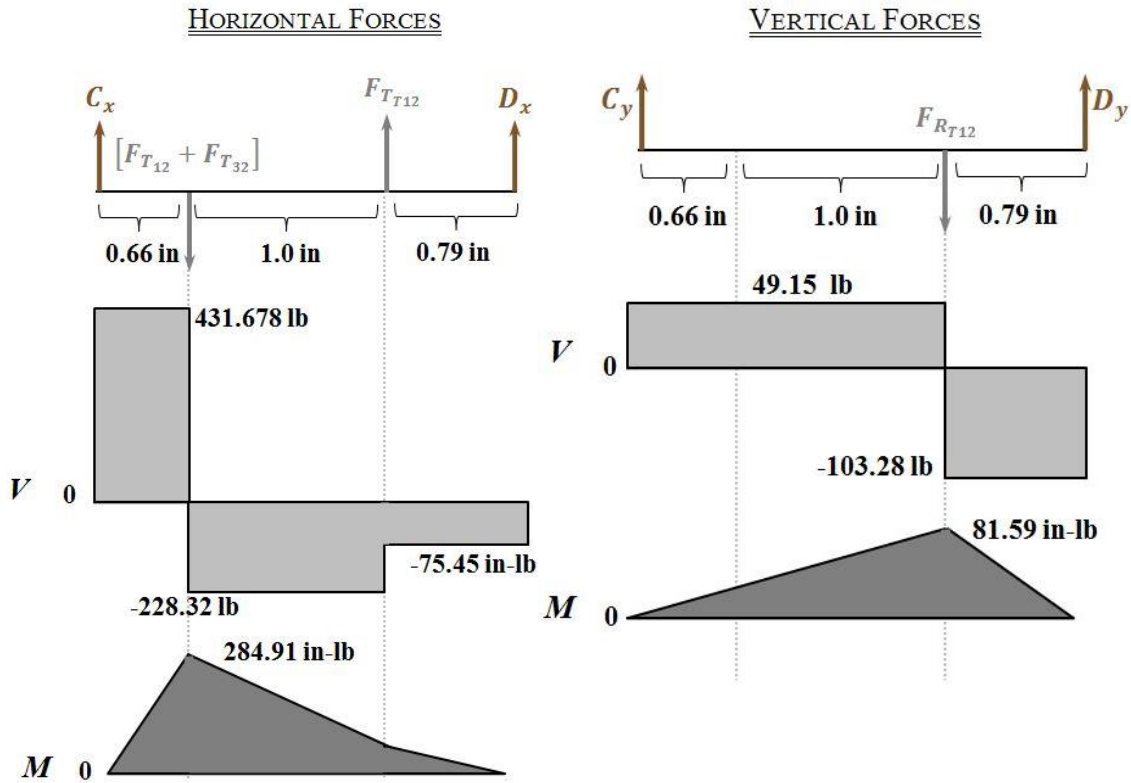


Figure 5.10: Shaft C Shear and Moment Diagrams

The case of maximum resultant moment is evaluated by summing the squares of the maximum moment occurring in the horizontal and vertical planes:

$$M_{max} = \sqrt{(81.59)^2 + (-284.91)^2} = 296.36 \text{ in} \cdot \text{lb} \quad (5.18)$$

Next, this value is substituted into Equation (5.1) along with the constants and power described in the evaluation of the diameter of shaft A. Again selecting AISI 4140 steel as the material choice, the diameter of shaft C is computed as:

$$D_C = \left[\frac{32(2)}{\pi} \sqrt{\left[\frac{1.6 \cdot (296.36 \text{ in} \cdot \text{lb})}{45,000 \text{ psi}} \right]^2 + \frac{3}{4} \left[\frac{180 \text{ in} \cdot \text{lb}}{60,000 \text{ psi}} \right]^2} \right]^{1/3} \quad (5.19)$$

Thus, accounting for the increase in diameter to account for the retaining ring grooves:

$$D_C \approx 0.60 \text{ in} \quad (5.20)$$

As previously discussed, considering the presence of other safety factors throughout this design and the theoretical increase due to the retaining ring grooves, it is reasonable to utilize a reduced shaft diameter and stick with $D_C \approx 0.5 \text{ in}$. This reduces cost by selecting a stock size and is a sound estimation given the conservative nature of the entire Tri-Wheel analysis. Again, the Tri-Wheel is designed such that one branch of the gearing is able to pull along half of the total mass of the robot. This requirement increases the power transmitted through one branch of gearing, which raises the pitch-line velocity, which subsequently increases the radial and tangential forces.

5.2.6 Shaft D2

Shaft D2 supports the small idler gear D3 on the driving side of the Tri-Wheel gearing. This shaft is expected to experience minimal stresses due to its short length and the fact that it is simply supported with the gear exactly in the center as an idler. Figure 5.11 shows this simple shaft and calls to attention the two bearings that support gear D2. Points 1 and 3 reference the simple flanged sleeve bearings to be discussed in a later section, and point 2 references the center of the gear. In this analysis, loads are assumed to be applied at the pitch point of each gear. While the forces may occur at this point and not at the center of the gear, these forces are relocated to the center of the gear in the free body diagrams for purposes of summing only the horizontal and vertical force components of the system. The subsequent moments produced by these forces are accounted for in the moment diagrams.

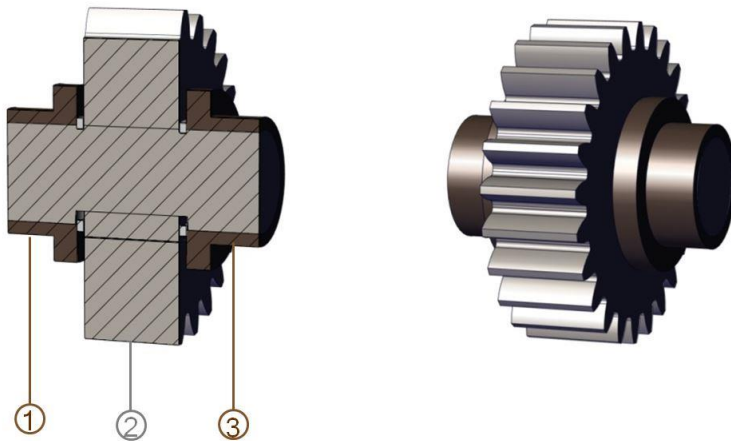


Figure 5.11: Shaft D2 Cross-Section and Isometric

The free body diagram of shaft D2 is shown below in Figure 5.12. Again, because this gear is an idler, there is no bending stress from the radial forces since the radial reaction forces from gears D2 and D4 cancel out. Due to the force direction convention that the tangential force on a driven gear from its driving gear is in its direction of motion and the tangential reaction force on a driving gear from its driven gear is opposite of its direction of motion, the tangential forces on gear D2 both occur in the same direction since it is both a driven and driving gear.

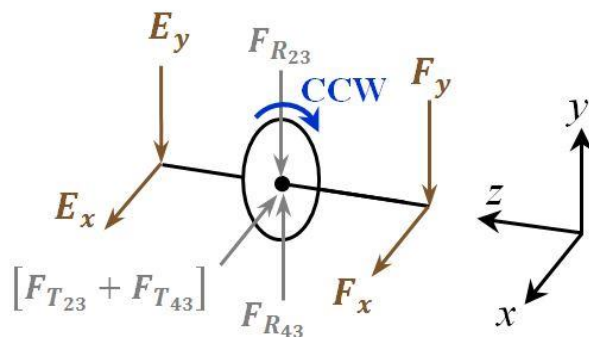


Figure 5.12: Shaft D2 Free Body Diagram

When examining shaft C, it was clear that while the radial forces canceled out for the driving idler gear, there was still an unbalanced radial reaction force acting on driving gear T2 from driven gear T1. For this reason, an analysis of the bearing reaction forces, shear, and moment was still carried out in the radial direction. In this instance, there is no other force that presents itself in the radial direction, so there is no analysis of bending or moment in the vertical direction. The shear and moment diagrams are presented in the horizontal direction in Figure 5.13. Here, $E_x = -240 \text{ lb}$, $F_x = -240 \text{ lb}$, and $F_{T_{23}} = F_{T_{43}} = 240 \text{ lb}$.

HORIZONTAL FORCES

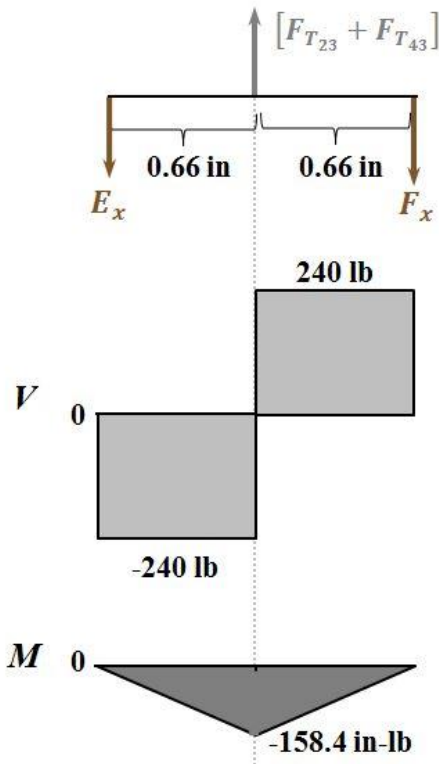


Figure 5.13: Shaft D2 Shear and Moment Diagram

Thus, the maximum moment is calculated as the sum of the squares using 0 lb for the maximum moment present in the vertical direction. This simply yields 158.4 in-lb as the

maximum resultant moment. Substituting this value into Equation (5.1) yields the following expression, again selecting AISI 4140 as the material choice:

$$D_{D2} = \left[\frac{32(2)}{\pi} \sqrt{\left[\frac{1.6 \cdot (158.4 \text{ in} \cdot \text{lb})}{45,000 \text{ psi}} \right]^2 + \frac{3}{4} \left[\frac{180 \text{ in} \cdot \text{lb}}{60,000 \text{ psi}} \right]^2} \right]^{1/3} \quad (5.21)$$

$$D_{D2} \approx 0.502 \text{ in} \quad (5.22)$$

$$D_{D2} \approx 0.502 * 1.06 = 0.53 \text{ in} \quad (5.23)$$

Using logic previously explained in the calculations of diameters for shaft A and shaft C, this number is rounded down slightly to 0.50 in.

5.2.7 Shaft D1

One unique consideration regarding the Tri-Wheel shaft design is the notion that the shafts are not always stationary in space. Textbook examples often utilize one stationary shaft with an input gear and an output gear. However, these shafts are rotating about the Tri-Wheel's centroid along with the rest of the mechanism when in Tumbling Mode. This means that the loading will vary during tumbling.

For instance, when the Tri-Wheel just switches from Driving Mode to Tumbling Mode, the torque applied as a result of the trailing ground wheel just lifting off of the ground is channeled through the outermost shaft (shaft D1), which is directly in contact with the ground since it is keyed to the wheel; this is the instance of maximum moment experienced. When the centroid of the Tri-Wheel is directly above the leading ground wheel (when the leg in contact with the ground is perfectly vertical), the maximum case

of shear occurs. In essence, this is where buckling could potentially occur. Therefore, the separate cases of maximum moment and maximum shear must be considered for shaft D1 since the changing loading (as a result of the shafts not being fixed in space during tumbling) is felt in this particular shaft since it is in contact with the ground. In consequence, is likely that this shaft will need to be more robust.



Figure 5.14: Shaft D1 Cross-Section and Isometric

Looking at Figure 5.14, it is clear that this shaft differs greatly from the others since it supports a wheel at one end. This wheel is bolted together with a keyed flange that slips over the shaft. This specified pneumatic wheel holds a maximum pressure of 50 psi, and its load capacity is 200 lb/wheel [36]. Ideally, there will be eight of these individual wheels making contact with the ground for four Tri-Wheels (or four individual wheels in the instance of a vehicle utilizing two Tri-Wheels) in Driving Mode. Assuming that the load is distributed evenly to these wheels, approximately 25 lb/wheel is

experienced for a robot with four Tri-Wheels, and approximately 50 lb/wheel is experienced for a robot with two Tri-Wheels. It is acknowledged that there is literature detailing the offset of the normal force occurring on each wheel (and thus on each shaft) based upon the flat contact patch that is created when a pneumatic wheel is depressed by the weight of its vehicle. However, with this internal pressure and distributed loading, the analysis is simplified to allow for the normal force acting on the shaft (as a resultant of the wheel's contact with the ground) to be equal in magnitude to half the weight of the entire vehicle applied at the leftmost end of the shaft. In the gearing design spreadsheet discussed in Chapter 4, the design constraint is set that one branch of the Tri-Wheel gearing must have enough torque to pull forward half the weight of the entire vehicle. For this reason, the wheel reaction force on the shaft is equal to half the weight, assuming that Tumbling Mode is occurring.

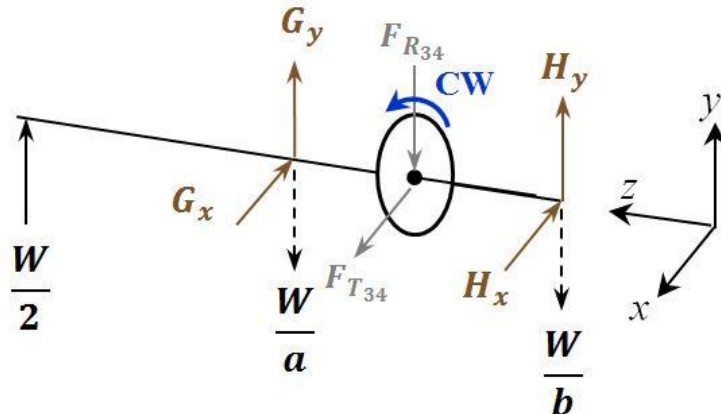


Figure 5.15: Shaft D1 Free Body Diagram-Maximum Shear

The first case considered is the case of maximum shear. Figure 5.15 shows the original free body diagram for the case of buckling in which the Tri-Wheel has lifted 60° off the ground in tumbling. At this point, the Tri-Wheel leg in contact with the ground is

perfectly vertical. The weight being supported in this case is transmitted through bearings G and H. Thus, there are reactions at the bearings countering two types of forces: 1. the upward radial force imparted by the wheel's normal reaction with the ground, and 2. the radial and tangential forces transmitted by gear D4 as it rotates. Again, it is acknowledged that simplifications are made in this representation. It is unlikely that the weight being supported will be divided evenly between the two bearings. For that reason, the forces $\frac{W}{a}$ and $\frac{W}{b}$ are included, where a and b represent the unknown, changing division of loading between the bearings.

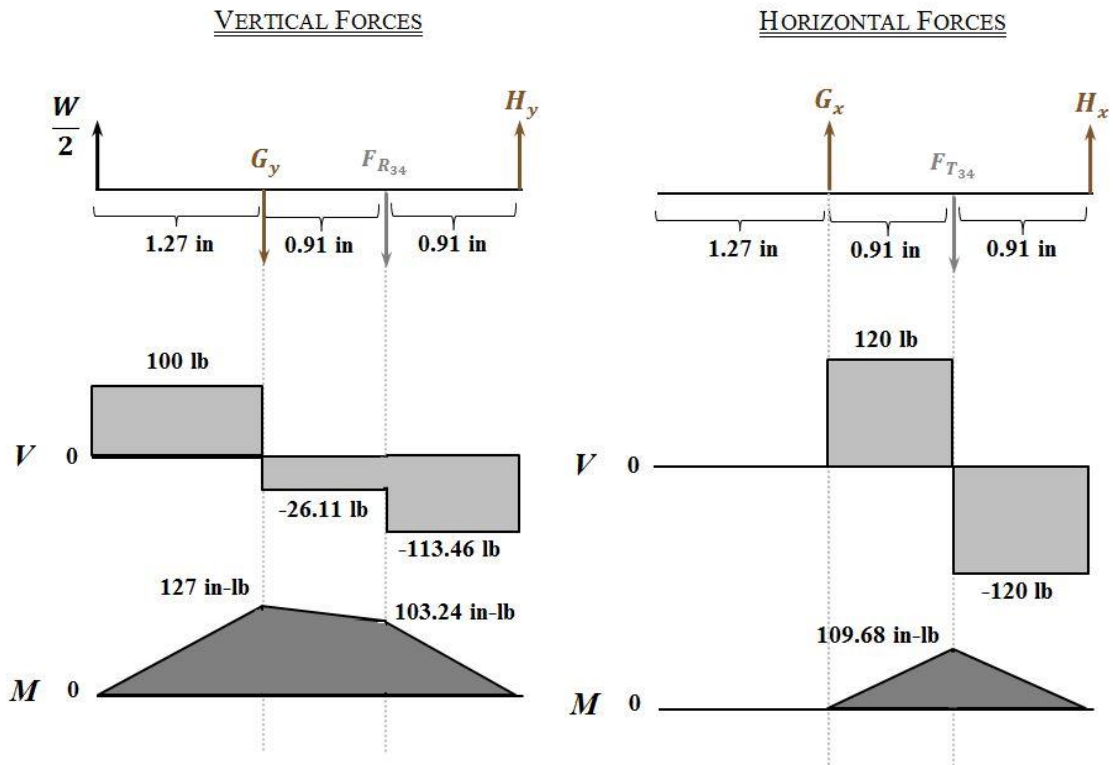


Figure 5.16: Shaft D1 Shear and Moment Diagrams-Maximum Shear

Recognizing that this distribution of loading fluctuates depending on the Tri-Wheel's environment (soft soil versus concrete, for instance) and its orientation on the

ground when $\alpha = 60^\circ$ (referencing nomenclature from Chapter 3), this loading is simplified in Figure 5.16 to reflect net forces at the bearings rather than separating the forces that counteract the wheel force and those that counteract the gear force. If the weight of the vehicle is pushing up on the left hand side of the shaft, the likely reaction will be for bearing G to push down and for bearing H to push up in order to counteract the moment created. Because these forces are assumed larger than the resultant forces at the bearings due to the gear rotation, the forces from the gear rotation are absorbed into the forces acting in these prescribed directions. Assuming a 200-lb robot, $\frac{W}{2} = 100 \text{ lb}$, $G_x = 120 \text{ lb}$, $G_y = -126.11 \text{ lb}$, $H_x = 120 \text{ lb}$, $H_y = 113.46 \text{ lb}$, $F_{R_{34}} = -87.35 \text{ lb}$, and $F_{T_{34}} = -240 \text{ lb}$.

The maximum resultant moment is calculated according to the method previously described in order to solve for the minimum shaft diameter that withstands this described loading scheme:

$$M_{max} = \sqrt{(127)^2 + (109.68)^2} = 167.81 \text{ in} \cdot \text{lb} \quad (5.24)$$

Again using the material properties of AISI 4140 steel, the shaft diameter is computed as:

$$D_{D1} = \left[\frac{32(2)}{\pi} \sqrt{\left[\frac{1.6 \cdot (167.81 \text{ in} \cdot \text{lb})}{45,000 \text{ psi}} \right]^2 + \frac{3}{4} \left[\frac{180 \text{ in} \cdot \text{lb}}{60,000 \text{ psi}} \right]^2} \right]^{1/3} \quad (5.25)$$

$$D_{D1} \approx 0.51 \text{ in} \quad (5.26)$$

Increasing the diameter by 6% in order to account for the presence of retaining ring grooves, this diameter becomes 0.54 in.

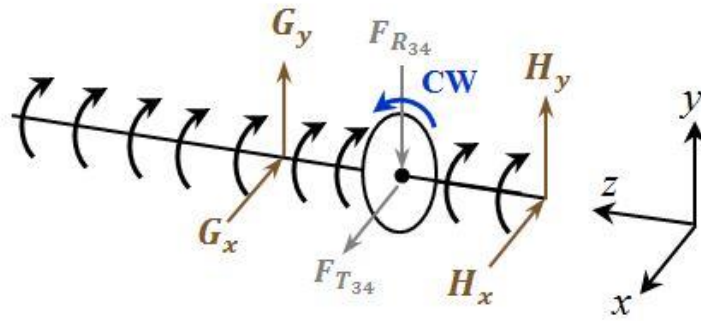


Figure 5.17: Shaft D1 Shear and Moment Diagram-Maximum Moment

Next, the case of maximum moment is considered. Just as the trailing ground wheel lifts off the ground, the maximum moment of approximately 39.69 ft-lb or 476.31 in-lb (as calculated in Chapter 4) is experienced. This estimation assumes that half of the total weight of the robot + Tri-Wheels system is concentrated at the centroid of the Tri-Wheel. According to beam theory, an external moment can be applied anywhere along a beam and still act along that entire beam. Thus, the free body diagram for shaft D2 in Figure 5.17 reflects the moment acting along the entire shaft. The reaction force with the ground is removed in this case due to the fact that the presence of that high moment usurps the normal force at this particular angle since the trailing ground wheel is just barely off the ground.

Figure 5.18 presents the shear and moment diagram for the case of maximum moment experienced by the Tri-Wheel. Note that while the externally applied moment does not affect the shear diagram in any way, the moment does increase both the horizontal and vertical moment diagrams by a constant value all along the shaft. For these figures, under the imposed assumption that the bearings are equally loaded, $G_x = 120 \text{ lb}$, $G_y = 43.68 \text{ lb}$, $H_x = 120 \text{ lb}$, $H_y = 43.68 \text{ lb}$, $F_{T_{34}} = -240 \text{ lb}$, and $F_{R_{34}} = -87.35 \text{ lb}$.

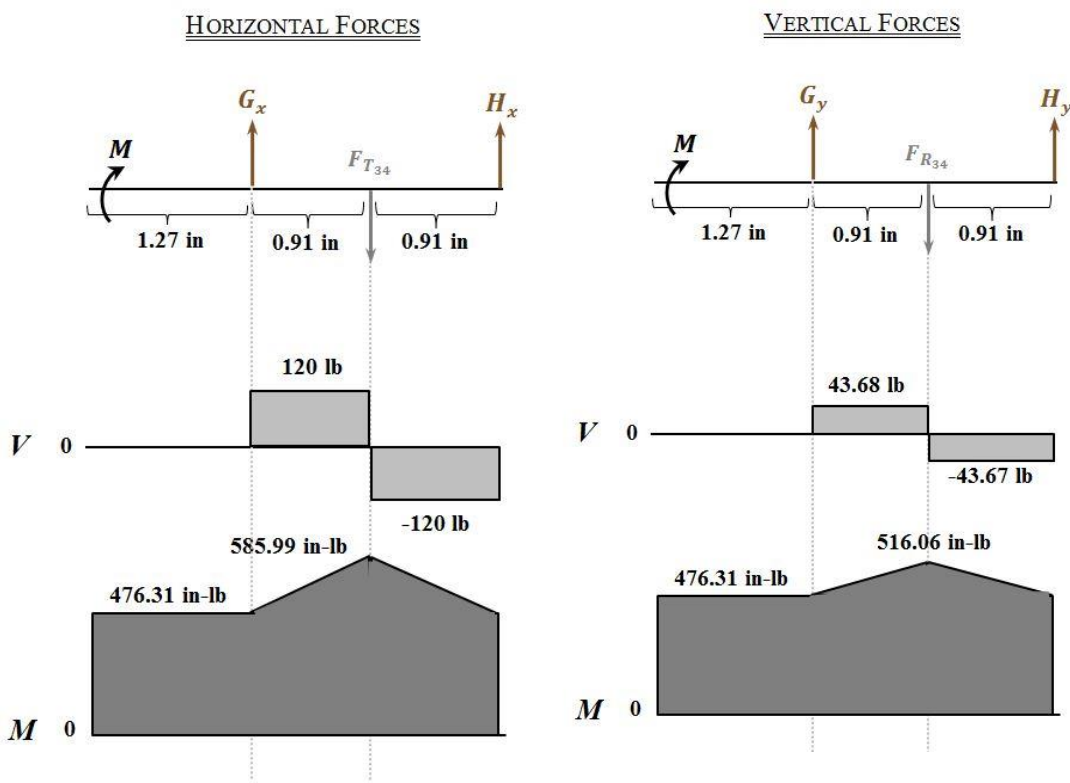


Figure 5.18: Shaft D1 Shear and Bending Diagrams-Maximum Moment

Once again, the maximum moment is computed as the sum of the squares from the vertical and horizontal maximum moment values. This resultant maximum moment is substituted into Equation (5.1) to solve for the minimum required diameter using AISI 4140 steel, and that resulting diameter is increased by 6% in order to account from the shaft weakening that occurs as a result of retaining ring grooves.

$$M_{max} = \sqrt{(585.99)^2 + (516.06)^2} = 780.83 \text{ in} \cdot \text{lb} \quad (5.27)$$

$$D_{D1} = \left[\frac{32(2)}{\pi} \sqrt{\frac{1.6 \cdot (780.83 \text{ in} \cdot \text{lb})}{45,000 \text{ psi}}}^2 + \frac{3}{4} \left[\frac{180 \text{ in} \cdot \text{lb}}{60,000 \text{ psi}} \right]^2 \right]^{1/3} \quad (5.28)$$

$$D_{D1} \approx 0.82 \text{ in} \quad (5.29)$$

Because this number has benefitted by compounding safety factors in the gearing analysis and from the increase due to the retaining ring grooves, it is concluded that a shaft diameter of 0.625 in or $5/8 \text{ in}$ is sufficient. Taking into account both the case of maximum moment and maximum shear, the case of maximum moment dictates the largest diameter. Reasonably, it is estimated that a shaft of $5/8 \text{ in}$ is adequate.

In summary, shafts A, C, and D2 are all 0.5 in , shaft B has an outer diameter of 1 in and an inner diameter of $11/16 \text{ in}$, and shaft D1 has a diameter of $5/8 \text{ in}$.

5.3 Power Transmission: Keys

5.3.1 Methodology

Now that the shafts and gears are specified, the machinery component that transmits power between the two elements must be specified. Keys are simple machinery components installed between a shaft and the hub of some power-transmitting element for the purpose of transferring torque. A key is installed in an axial groove that has been machined into the shaft known as a keyseat [19]. The matching groove machined into the hub of a power-transmitting element such as a gear, flange, or sprocket is known as a keyway. There are a number of different types of keyways and keyseats to choose from. Once the type of key has been selected, there are general standards available to determine the width and height of the key. Subsequently, the length must be deemed sufficient to withstand the magnitude of shearing force endured during power transmission.

Square keys are a subset of parallel keys and are the most common types of keys for shafts up to approximately 6.5 in in diameter. The other power transmitting elements considered are pin keys, woodruff keys, and splines, but these options are ultimately discarded due to increased machining time, complexity, increased cost, or inability to transmit the amount of power required without shearing. Sometimes, the simplest solution is the best solution.

Nominal Shaft Diameter		Nominal Key Size		
Over	To (Incl.)	Width, W	Height, H	
			Square	Rectangular
5/16	7/16	3/32	3/32	
7/16	9/16	1/8	1/8	3/32
9/16	7/8	3/16	3/16	1/8
7/8	1 1/4	1/4	1/4	3/16
1 1/4	1 3/8	5/16	5/16	1/4
1 3/8	1 3/4	3/8	3/8	1/4
1 3/4	2 1/4	1/2	1/2	3/8
2 1/4	2 3/4	5/8	5/8	7/16
2 3/4	3 1/4	3/4	3/4	1/2
3 1/4	3 3/4	7/8	7/8	5/8
3 3/4	4 1/2	1	1	3/4
4 1/2	5 1/2	1 1/4	1 1/4	7/8
5 1/2	6 1/2	1 1/2	1 1/2	1
6 1/2	7 1/2	1 3/4	1 3/4	1 1/2
7 1/2	9	2	2	1 1/2
9	11	2 1/2	2 1/2	1 3/4
11	13	3	3	2
13	15	3 1/2	3 1/2	2 1/2
15	18	4		3
18	22	5		3 1/2
22	26	6		4
26	30	7		5

Note: Values in nonshaded areas preferred. Dimensions are in inches.

Figure 5.19: Key Size v. Shaft Diameter [37]

Using Figure 5.19 adapted from ANSI-ASME standard B17.1, “Keys and Keyseats,” the selected key size for the 0.5 in shafts is a square $\frac{1}{8} \times \frac{1}{8}$ in key. The selected key size for the 0.625 in shafts is a square $\frac{3}{16} \times \frac{3}{16}$ in. Now knowing that a

parallel key will be used, the keyseat type is easily selected. A profile keyseat is produced by a circular milling cutter having a width equal to the width of the key [19]. At the beginning or end of the keyseat, this technique produces a smooth radius, which results in a lower stress concentration factor. The other option is a sled runner keyseat, which is milled into a shaft with an end mill. This results in a flat-bottomed groove with one sharp, square corner at the end. Using the selected key dimensions along with the known diameters of the shafts, the dimensions for the shaft keyseat and the hub keyway are then calculated using the formulas presented in Figure 5.20:

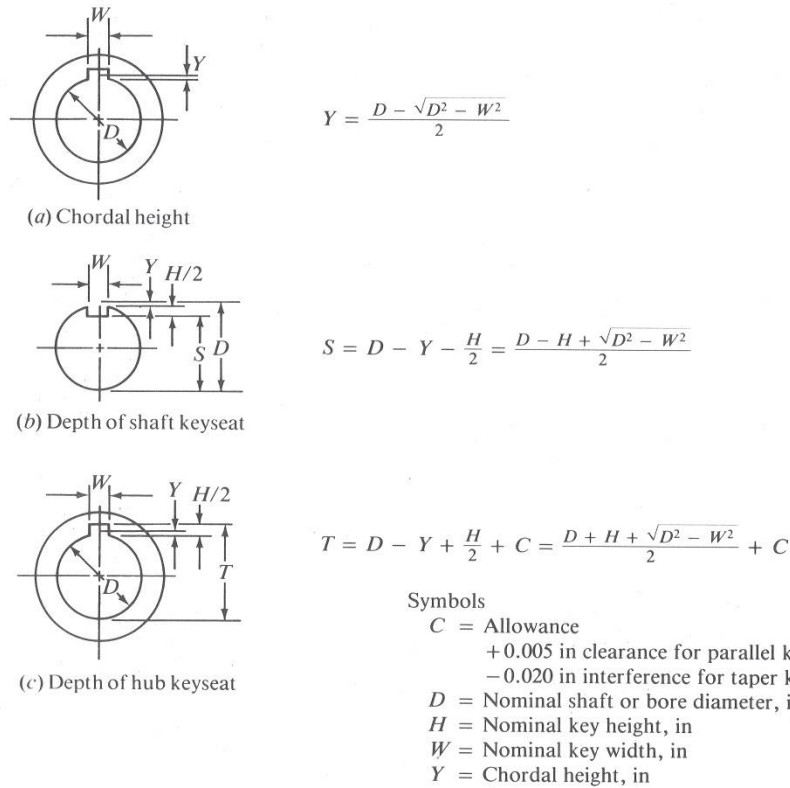


Figure 5.20: Dimensions for Parallel Keyseats and Keyways [19]

It is necessary to determine the depth of the shaft keyseat S and the depth of the hub keyway T for specification on the Tri-Wheel gears. Using the equations for S and T , these

values for the two shaft diameters selected are summarized in Table 5.1 and used to specify the proper keyseat and keyway depth on the gear machine drawings.

<i>Shaft Diameter (in)</i>	<i>S (in)</i>	<i>T (in)</i>
0.5	0.430	0.560
0.625	0.517	0.709

Table 5.1: Depth of Keyseats and Keyways

A class 2 fit between the key and the keyseat is selected for this application. According to [37], a class 2 fit is defined as a side fit (possibly clearance or interference) obtained by using keystock and keyseat tolerances as shown in Table 5.2. This is a relatively tight fit for parallel square keys and provides a guideline to ensure proper power transmission occurs through each key. The red box in this table highlights the appropriate tolerances for the parallel square keys selected for the Tri-Wheel shafts.

Type of Key	KEY WIDTH		SIDE FIT			TOP AND BOTTOM FIT			
	Over	To (Incl)	Width Tolerance		Fit Range*	Depth Tolerance			Fit Range*
			Key	Keyset		Key	Shaft Keyseat	Hub Keyseat	
Parallel	—	1-1/4	+0.001 -0.000	+0.002 -0.000	0.002 CL 0.001 INT	+0.001 -0.000	+0.000 -0.015	+0.010 +0.000	0.030 CL 0.004 CL
	1-1/4	3	+0.002 -0.000	+0.002 -0.000	0.002 CL 0.002 INT	+0.002 -0.000	+0.000 -0.015	+0.010 -0.000	0.030 CL 0.003 CL
Square	3	3-1/2	+0.003 -0.000	+0.002 -0.000	0.002 CL 0.003 INT	+0.003 -0.000	+0.000 -0.015	+0.010 -0.000	0.030 CL 0.002 CL
	—	1-1/4	+0.001 -0.000	+0.002 -0.000	0.002 CL 0.001 INT	+0.005 -0.005	+0.000 -0.015	+0.010 -0.000	0.035 CL 0.000 CL
Parallel	1-1/4	3	+0.002 -0.000	+0.002 -0.000	0.002 CL 0.002 INT	+0.005 -0.005	+0.000 -0.015	+0.010 -0.000	0.035 CL 0.000 CL
	3	7	+0.003 -0.000	+0.002 -0.000	0.002 CL 0.003 INT	+0.005 -0.005	+0.000 -0.015	+0.010 -0.000	0.035 CL 0.000 CL
Taper	—	1-1/4	+0.001 -0.000	+0.002 -0.000	0.002 CL 0.001 INT	+0.005 -0.000	+0.000 -0.015	+0.010 -0.000	0.005 CL 0.025 IN'
	1-1/4	3	+0.002 -0.000	+0.002 -0.000	0.002 CL 0.002 INT	+0.005 -0.000	+0.000 -0.015	+0.010 -0.000	0.005 CL 0.025 IN'
	3	Δ	+0.003 -0.000	+0.002 -0.000	0.002 CL 0.003 INT	+0.005 -0.000	+0.000 -0.015	+0.010 -0.000	0.005 CL 0.025 IN'

*Limits of variation. CL = Clearance; INT = Interference

Δ To (Incl) 3-1/2 Square and 7 Rectangular key widths.

All dimensions given in inches.

Table 5.2: Class 2 - Fit for Parallel and Taper Keys [37]

To complete the key analysis, the key length required to resist shearing under the given loads must be computed for a specific key material. Typically, keys are made of low carbon steel, and any material with > 10% elongation is ideal [19]. For this analysis, a common spring steel from McMaster-Carr is selected with approximate yield strength of 97,000 psi. Figure 5.21: Forces on a Parallel Key shows that the shearing force is distributed over the cross-sectional area parallel to the keyseat itself. As some torque is applied to the shaft, the shaft force acts on the key, causing a reaction from the hub on the key, which subsequently transmits the torque and power throughout the system.

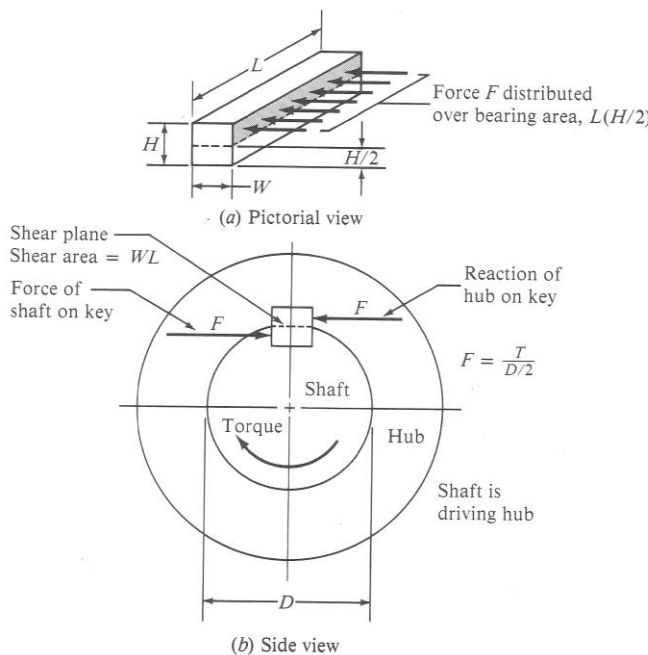


Figure 5.21: Forces on a Parallel Key [19]

When specifying a key, it is necessary to determine how the material properties of the shaft, hub, and key compare. It is important to identify the potential failure mode—compressive stress or shearing stress. In this instance, because the spring steel key has higher yield strength than the shaft, the failure is related to the compressive stress on the

surface with the lowest compressive yield strength; in this instance, the lowest yield strength belongs to the AISI 4140 steel shaft. The design stress for compression is defined as a relation between the yield strength of the shaft and the safety factor:

$$\sigma_d = \frac{s_y}{N} \quad (5.30)$$

Then, the following equation is used to calculate the key length:

$$L = \frac{4T}{\sigma_d DH} \quad (5.31)$$

where D is the shaft diameter, H is the key height, and T is the torque transmitted through the gear. This equation is then evaluated with the appropriate substitutions for the 0.5 in shaft and the 0.625 in shaft respectively as:

$$L_{0.5} = \frac{4 * 180 \text{ in} \cdot \text{lb}}{\frac{60,000 \text{ psi}}{2} * 0.5 \text{ in} * \frac{1}{8} \text{ in}} \quad (5.32)$$

$$L_{0.5} \approx 0.38 \text{ in} \quad (5.33)$$

$$L_{0.625} = \frac{4 * 180 \text{ in} \cdot \text{lb}}{\frac{60,000 \text{ psi}}{2} * 0.625 \text{ in} * \frac{3}{16} \text{ in}} \quad (5.34)$$

$$L_{0.625} \approx 0.20 \text{ in} \quad (5.35)$$

The face width of all driving gears is 0.5 in , and the face width of all tumbling gears is 0.75 in . This being said, because the computed lengths for both possible shaft diameters are less than the smallest gear face width, the decision is made to have keys that run the full face width of the gears for simplicity of installation and measuring.

Therefore, gears D1—D3 will have square, $\frac{1}{8}$ in keys of length $L = 0.5$ in. Gears T1—T2 will have square, $\frac{1}{8}$ in keys of length $L = 0.75$ in. Lastly, gear D4 will have a square, $\frac{3}{16}$ in key of length $L = 0.5$ in.

5.4 Bearing Selection

5.4.1 General Considerations

From plain surface bearings to rolling element bearings and many types in between, there is a wide variety of options available when bearings must be specified for a design. With respect to the Tri-Wheel, relatively low rotational speeds (at maximum 350 RPM) are present, and it is desirable to minimize weight, cost, and the overall thickness of the assembly. With this in mind, it is important to remember that the most highly rated bearing available is likely not necessary in many given applications. The designer must take care to specify bearings appropriately rather than over-specify beyond what is reasonable simply due to the fact that one type of bearing carries more load than another. In this section, the methodology through which the bearings are selected and the chosen material are discussed. Information regarding the specific bearings selected with part numbers from a vendor is located in Appendix F: Bill of Materials.

5.4.2 Plain Bearings

It is generally accepted that spur gears are almost always devoid of any large self-generated axial thrusts [18]. However, it is possible that the Tri-Wheel will be required to drive forward across an incline in which the right side of the robot is elevated above the

left side of the robot, for instance. In this case, there would potentially be minor axial thrust loads. For shafts C, D1, and D2, flanged sleeve bearings are thus selected and straddle-mounted to provide as even load distribution as possible. Sleeve bearings are a type of plain surface bearing—a type of bearing which allows smooth, low-friction motion between two surfaces moving relative to each other without the advantage of rolling contact. Flanged sleeve bearings, seen in Figure 5.22, are designed to handle both thrust and radial loads. While it is unlikely that there will be significant side loading, especially when considering the presence of retaining rings to be discussed in the subsequent section, the flange serves as more of a safety precaution and installation aid.



Figure 5.22: Flanged Sleeve Bearing [38]

The performance parameter required to select the appropriate flanged sleeve bearing is known as the pV Factor. This factor is actually the product of the load capacity p and the speed of operation, V and is a measure of the bearing material's ability to accommodate the frictional energy generated within the bearing. Another way to think of the pV Factor is as a comparative metric of the bearings ability to absorb energy created during rotation of a particular shaft without overheating. The load capacity p is computed as the radial load divided by the projected area of the bearing, measured in units of psi [19]:

$$p = \frac{F}{LD} \quad (5.36)$$

Here, F is the total resultant load acting on the bearing in lb, L is length of the bearing surface in contact with the shaft (including the flange), and D is the internal diameter of the bearing which makes contact with the shaft. The speed of operation V is the relative speed between the moving (shaft) and stationary (bearing) components, measured in units of ft/min. Making note that n is the rotational speed of the shaft in RPM, V is calculated as:

$$V = \frac{\pi D n}{12} \quad (5.37)$$

At each bearing labeled in Figure 5.9, Figure 5.12, and Figure 5.15 for shafts C, D2, and D1 respectively, there are radial and tangential components of the total forces on each bearing present. In order to obtain the resultant force on each bearing to use in the calculation of the resultant load F , the square root of the sum of the squares of the radial and tangential components is computed for each bearing. Using data obtained from the bending and moment diagrams of shaft C to compute the resultant bearing force, an example of this calculation for the right-hand bearing of shaft C (designated C_R) is:

$$F_D = \sqrt{D_x^2 + D_y^2} = \sqrt{75.45^2 + 103.28^2} = 127.90 \text{ lb} \quad (5.38)$$

Here, the nomenclature F_D represents the resultant bearing force on the bearing labeled as D in the free body diagram of shaft C. Bearing D is on the right hand side, and as such, the bearing shaft designation is C_R —nomenclature referencing first the shaft letter and

second the orientation on the left or right hand side of the shaft as referenced in the preceding free body diagram and shear and bending diagrams. Using this methodology, the following data in Table 5.3 is computed to describe the resultant bearing loads acting on each individual bearing and the resulting pV Factor such that an appropriate flanged sleeve bearing can be selected.

<i>Shaft designation</i>	<i>F (lb)</i>	<i>L (in)</i>	<i>D (in)</i>	<i>n (RPM)</i>	<i>p (psi)</i>	<i>V (fpm)</i>	<i>pV (psi-fpm)</i>
C _L	F _C = 434.51	0.375	0.5	160	2317.39	20.94	53,091.40
C _R	F _D = 127.90	0.375	0.5	160	682.13	20.94	14,283.80
D2 _L	D2 _E = 240.00	0.375	0.5	320	1280.00	41.80	53,504.00
D2 _R	D2 _F = 240.00	0.375	0.5	320	1280.00	41.80	53,504.00
D1 _L	D1 _G = 174.04	0.625	0.625	320	298.06	52.32	15,594.50
D1 _R	D1 _H = 165.15	0.625	0.625	320	880.80	52.32	46,083.46

Table 5.3: pV Factor Data for Shafts C, D1, and D2

It must be kept in mind that the loading used to calculate the various values of *F* has been increased substantially in the shaft analysis by the fact that the gearing spreadsheet assumes one branch of the Tri-Wheel gearing is able to tumble half the total mass of the system. In reality, there will be back wheels or back Tri-Wheels that will help to propel the vehicle forward. For this reason, these pV Factor estimates are inflated by a compounding factor of safety.

SAE 841 bronze flanged sleeve bearings are ultimately selected to meet these requirements and dimensions for the length and internal diameter. The pV maximum load estimate is 50,000. Taking into account the safety factor that has inflated values in Table 5.3, this limiting value should be more than sufficient. According to the McMaster-Carr website, SAE 841 is a porous material known as Oilite that is impregnated with

approximately 19% SAE 30 oil. This oil serves to reduce wear and prevent the bearings from requiring frequent maintenance since they are self-lubricating. Operating temperature is not concerning for this application since the bearings will be well lubricated and the shaft will not be rotating at high speeds. The lifetime of this bearing is also not a critical design factor since the Tri-Wheel has been specified for shorter bursts of operation and will very rarely be required to operate for any extended period of time at a top speed.

5.4.3 Rolling Contact Bearings

Rolling-element bearings are able to support loads using rollers or balls, operating with less friction than plain bearings. Rolling contact bearings as a broad classification references a wide array of bearings using some type of roller or spherical balls between the stationary and moving elements. These bearings are most commonly used to support rotating elements with purely radial loads such as a shaft, though some of these bearings are also designed to carry thrust loads only. For purposes of this section, radial loads include any loads acting toward the center of the bearing along a radius, and thrust loads act parallel to the axis of the shaft. Thus, the radial and tangential loads acting on the shafts described in Section 5.2 all fall under the classification of radial loads when speaking about ball bearings.

While it is desirable overall to reduce weight and simplify the design, rolling contact bearings are selected to support shafts A and B since they control the driving input and tumbling output of the entire Tri-Wheel system. For this reason, more smooth operation is desired. In addition, because shaft A slides directly through shaft B, there

must be some kind of bearing external to shaft A and inside of shaft B to provide support during rotation. Ball bearings using spherical balls to facilitate rotation are chosen for a variety of speeds (though they are particularly helpful at high speeds) and light to moderate loads. One flanged ball bearing is selected to support Shaft A at bearing A, as labeled in Figure 5.5. It is flanged to allow for ease of installation, which will be discussed in greater detail along with the housing design. On the same figure, bearing B is also a ball bearing but is a steel flange-mounted ball bearing for ease of installation in the robot chassis. Bearing B is specified by the robot design and are out of the scope of the Tri-Wheel design.

Two needle bearings will be press fit inside both ends of hollow shaft B, and shaft A will slide through them. Needle bearings are simply roller bearings with a much smaller diameter of roller. A smaller radial space is required for needle bearings to carry a specific load than is required for any other rolling contact bearing. Due to this slim profile, needle bearings will work well to provide support between the two shafts. Figure 5.23 shows a representative example of a flanged ball bearing and a needle bearing, respectively.



Figure 5.23: Flanged Ball Bearing and Needle Bearing [38]

For rolling element bearings, the basic required dynamic load rating C for a ball bearing to carry a radial design load P_d is computed simply as:

$$C = \frac{P_d f_L}{f_N} \quad (5.39)$$

where P_d is computed as the resultant square root of the sum of the squares calculated using the bearing radial and tangential forces from the shaft bending and moment diagrams. Here, a speed factor f_N and a life factor f_L are incorporated and can be determined from standard charts depending upon the speed of operation. Using Figure 5.24 for ball bearings, the maximum rated speed of 350 RPM produces values of $f_N = 0.46$ and $f_L = 1.4$.

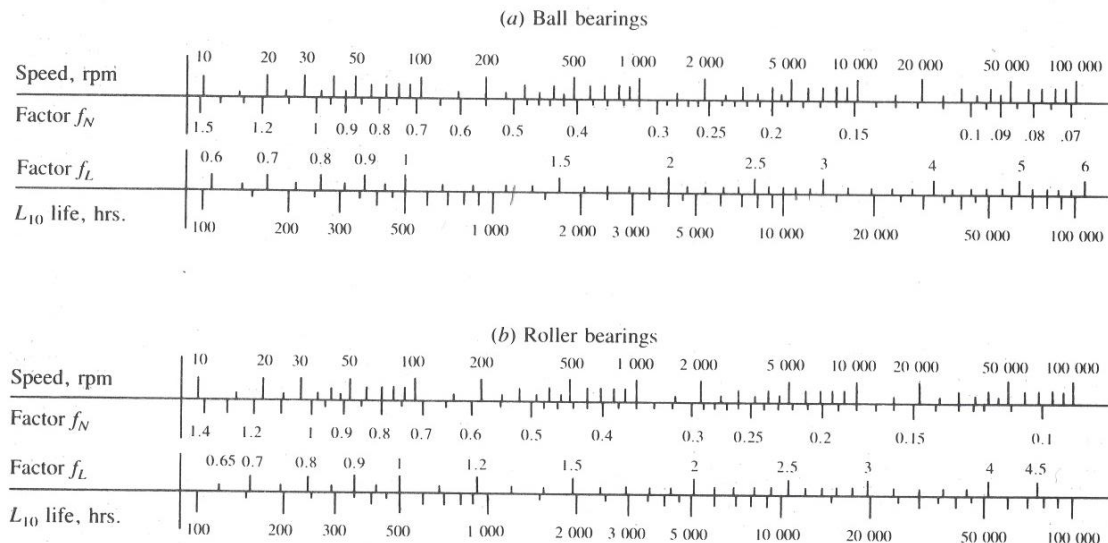


Figure 5.24: Life and Speed Factors for Ball and Roller Bearings [19]

The dynamic load rating is then calculated using the maximum force components from bearing A on shaft A as:

$$C = \frac{\sqrt{(-212.3 \text{ lb})^2 + (-77.27 \text{ lb})^2} \cdot 1.4}{0.46} \quad (5.40)$$

$$C = 687.60 \text{ lb} \quad (5.41)$$

A steel flanged ball bearing selected on McMaster Carr for this load rating has a dynamic load capacity of 820 lbs. This being the case, and factoring in again the inflation of the loads from the gearing assumptions, this bearing and loading is sufficient. The needle bearing that is selected has a dynamic load capacity of 1,550 lbs, which is more than sufficient given that this bearing is only acting as a support structure directly between two rotating parts. The steel needle roller and the ball bearing are both double-sealed in order to prevent dust or debris from entering the Tri-Wheel system and preserve lubricants. The seal on the needle bearing is made of rubber, and when the keyed shaft A is slid through the bearings, care must be taken to ensure that the seals are not ripped or torn by any sharp edges from keyways or retaining ring grooves.

5.5 Miscellaneous Assembly Components

5.5.1 Retaining Rings (Snap Rings)

Snap rings are selected for this design to restrict axial motion of mating concentric parts such as shafts, gears, and bearings. A snap ring is installed on each side of the gears both for the purpose of keeping the gear in place and for keeping the shaft from sliding out of the bearings on either side. Because there is not any significant axial loading to speak of, calculations to determine the side loading that must be withstood are not necessary.



Figure 5.25: External Retaining Ring [39]

Figure 5.25 is an external snap ring selected to fit a particular diameter A .

External snap rings are pulled open by a special installation tool (similar to pliers) so that they can be slid over the end of a shaft and release into a desired groove. On the McMaster-Carr website, the groove diameter and width as well as a standard tolerance are provided for incorporation into the shaft design. The material is black-finish steel, and appropriate sizes for the 0.5 in shafts and the 0.625 in shafts are specified. Originally, internal sleeve spacers were considered to help maintain the axial position of the different shaft elements. Upon further scrutiny, it was determined that these might present difficulties related to tolerance while the retaining ring grooves automatically allow for some extra clearance since they are specified to be wider than the retaining rings themselves.

5.5.2 Wheel-Hub Subassembly

The individual, 6 in diameter wheels specified for the Tri-Wheel mechanism are manufactured with a heavy central roller bearing in their hub. However, for purposes of this design, it is necessary for the wheel to be rotating and the same rotational speed as the shaft, and this ball bearing will not allow the power to be transmitted. In order to work around this, a number of options are considered to transmit power from shaft D1 to

the pneumatic wheel. It is first conclusively determined that the existing bearing must be removed from the existing wheel hub. A wire EDM is used to cut away a hole, preserving the rest of the hub and leaving a space for some sort of adapter, as shown in Figure 5.26.



Figure 5.26: Wheel-Hub Subassembly

Upon contacting the wheel manufacturer and obtaining the spacing for the bolt pattern already used to keep the two halves of the wheel hub together around the pneumatic tire, a simple steel flange of 0.25 in thickness is designed. Using the keyway calculations already detailed in Section 5.3, a square $\frac{3}{16} \times \frac{3}{16}$ in key with a length of 0.75 in is specified to fit in the hub and transmit power from the shaft directly to the wheel. Additional detail regarding the bolt pattern of the flange and the flange's general design is available in Appendix E.

In order for this power transmission to occur successfully, however, the wheel-hub assembly must be fastened together in such a way that the flange and the existing hub are locked in place and will not move relative to each other in operation, despite the fact

that the wheel will continuously receive reversed loading in the counterclockwise and clockwise directions depending on the Tri-Wheel's driving direction. This type of reversed loading can sometimes shake loose a variety of fasteners. In an attempt to prevent this from happening, nylon locknuts are specified to tighten up the assembly. A socket wrench is used to impart significant torque on the locknuts until the threads of the bolts are threaded into the nylon lining of the locknuts. This should clamp the subassembly together and prevent potential failure modes resulting from relative motion between the hub and flange.

5.5.3 Shear Pins

The housing of the Tri-Wheel discussed in the following section must be constrained not only by bolts and locknuts to keep the plates together. It must be constrained in some way such that when the plates can be aligned properly during assembly and such that there is no twisting of the plates relative to one another during operation, which could misalign the bearings or create other moment issues on the plates. Simple pull-out dowel pins are selected and installed between the front and back plates of the Tri-Wheel and the middle I-beam structure. The pins are removable and internally threaded on the inside, enabling them to be removed with a screw or a pull-out dowel pin tool. The selected dowel pins are precision ground, making them ideal for accurately aligning parts [40].



Figure 5.27: Alignment Dowel Pin [40]

Specific information regarding the tolerance information for the installation holes is provided by the manufacturer and taken into consideration for the machine drawings of the assembly. The selected pins are made of strong alloy steel of minimum Rockwell hardness C47 [40].

5.6 Housing Design

With all the internals of the Tri-Wheel mechanism defined, the housing that supports all these components can now be designed. Just like many of the other design processes detailed in this report, the housing for the Tri-Wheel involves some precarious optimization. It has been stated that the Tri-Wheel mechanism could be used for a variety of different purposes. What all of these missions discussed in Chapter 1 have in common is the need for a robust locomotion platform that does not fail during critical operations. However unlikely it may be, if there is a need to get inside the Tri-Wheel housing to service a component, the disassembly process must be made quick and straightforward without the use of typically unavailable, specialized tooling. This requirement has heavily influenced the overall design for the Tri-Wheel housing: an I-beam inspired center piece and two plates that attach on either side for serviceability of both sets of gears individually.

With this broad idea in mind, the next constraint to consider is the envelope size of the housing. This structure should be as small as possible while still leaving room for the appropriate tolerances necessary for the gears to rotate freely unimpeded. Additionally, a snug housing surrounding the gears must also leave room for fasteners to tighten the plates together. In order to reduce mass, AISI 6061 Aluminum is selected for

the material. To use steel or some denser, heftier substance would increase the weight of the assembly substantially and make it more difficult for the mechanism to tumble. This being said, the housing must also be strong enough to resist deformation upon experiencing a reasonable impact force. The housing must also provide a means by which to achieve satisfactory alignment of the three theoretical parts of the housing. If the holes for the bearings are not exactly concentric, binding is likely to occur, and the gears may not rotate. Lastly, the machining costs of whatever housing is selected are not, by any means, inconsequential. Reduction of cost at the expense of producing an optimal design may be required, at least for the first real Tri-Wheel assembly.



Figure 5.28: Housing Design 1

The first attempt at the Tri-Wheel housing design beyond three flat plates is shown in Figure 5.28. This piece would emerge from a large block of aluminum that has been CNC machined to the design specifications. There are a number of important design choices in this first iteration that seek to meet the previously discussed concerns and

requirements. Small extruded hubs are included around each of the bearings to provide structural support and load carrying capacity. Because the bearings are externally supported, normal sleeve bearings and ball bearings without a flange are originally specified. Each of the plates is 0.25 *in* thick to provide a sturdy but light structure. Because aluminum is not very dense, these thicker plates ultimately do not increase the overall weight of the assembly by any significant measure. Through-holes are incorporated out by the wheels and closer to the center of the mechanism to provide space for bolts that will fasten the plates together. The holes are not threaded since the aluminum is easily gouged out by repeated threading and unthreading that will be anticipated during the assembly process. The small carrier plate to the right encloses the tumbling gears with a lip for alignment, and a similar design is used for the carrier plate that encloses the driving gears on the opposite side.

While there are a number of good ideas in this configuration, they are refined further for a few important reasons. While hubs are ideal for structural support, the incorporation of both the hubs and the lip on the driving carrier plate and the tumbling carrier plate make for two two-sided parts rather than two one-sided parts. During machining, the cost to machine one side and then flip the part and realign to machine the reciprocal side increases the cost by at least an order of magnitude, according to costing estimates received.

Upon the recommendation of a machinist, the lip should actually be removed and replaced with another means of alignment since it is rather costly to maintain a constant tolerance all the way around the lip to ensure for a nice, tight fit with the center carrier structure. Lastly, the six assembly bolts situated toward the center of the assembly are not

protected by any structure on the back side of the Tri-Wheel since the extruded web from the center carrier is smaller than the tumbling plate. This could allow dust or debris to enter the system. In other failure modes, rubble could become lodged in the space between the bolts and the center carrier web, or the bolt itself could be struck with impact loading and deform.

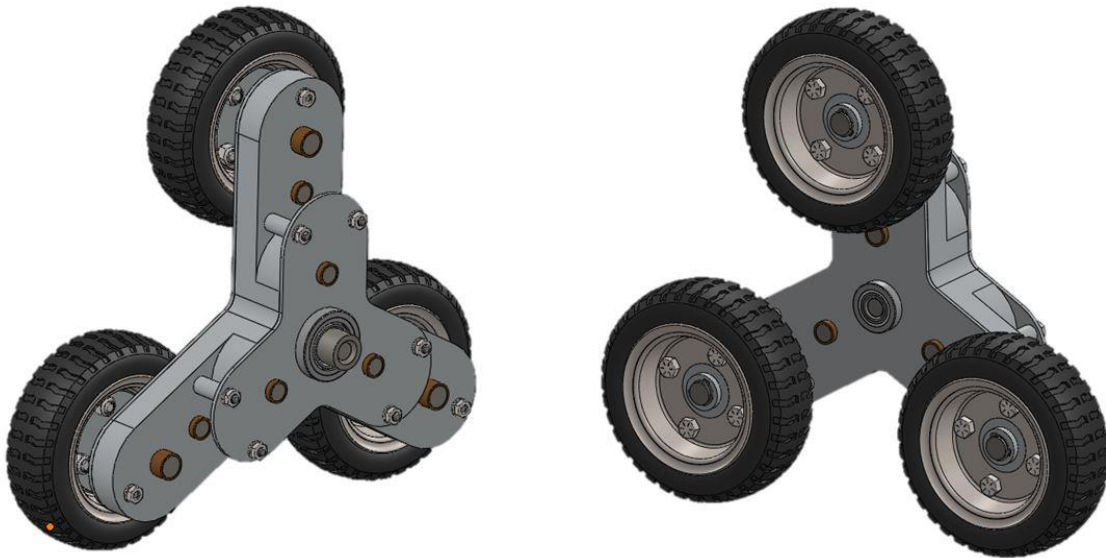


Figure 5.29: Housing Design 2

Taking these observations into consideration, a second version of the Tri-Wheel housing is produced and presented in Figure 5.29. Notice that the hubs have been removed to create a one-sided part (thereby reducing cost significantly), and the bronze Oilite bearings protrude from either side. Plastic caps are not shown in this figure but are readily available to slip over the exposed portion of bearings that poke out. These caps would prevent dust or dirt from entering the system. Because there are no hubs to support the outer portion of the bearings, counterbores are incorporated on the inside of the three components at any hole which houses a bearing. By doing this, flanged bearings can be incorporated and pressed into the housing. For assembly purposes, it is also helpful to

have a through-hole that enables the designer to see if the shaft is in proper alignment.

Note that aluminum spacer sleeves are incorporated to cover the previously exposed assembly bolts. Upon further consideration, it seems that even covering the bolts is not sufficient, as some sort of side impact could potentially bend the free edge of the tumbling plate that extends above the center carrier web.

At this point, the recommendation is also made during a design review that perhaps the carrier plates should be reduced in thickness to 0.125 in in order to reduce the thickness of the overall assembly by 0.375 in . While this recommendation was incorporated and ultimately carried through to the final produced Tri-Wheel housing design, a future version of the Tri-Wheel will likely return to the 0.25 in thick plates. When using an arbor press to press in the bearings, it is clear that a plate of this thickness is easily deformable if one is not careful. While plates of this depth are sufficient once the entire structure is assembled, sturdier plates would improve the assembly process and conclusively not increase the weight of the system significantly due to the low density of 6061 Aluminum.

Another issue presenting itself is the potential for bending or bowing out that could occur between the driving carrier plate and the matching web of the center carrier. There are nine instances of through-holes that pass through the driving gear set half of the Tri-Wheel housing. Ideally, there should be some sort of spacer or sleeve that slips over the bolts inside the housing to prevent compression or bending of the housing with some sort of impact loading. At this point, the incorporation of more aluminum spacers situated around these bolts seems to be both cost-effective and simple to install.

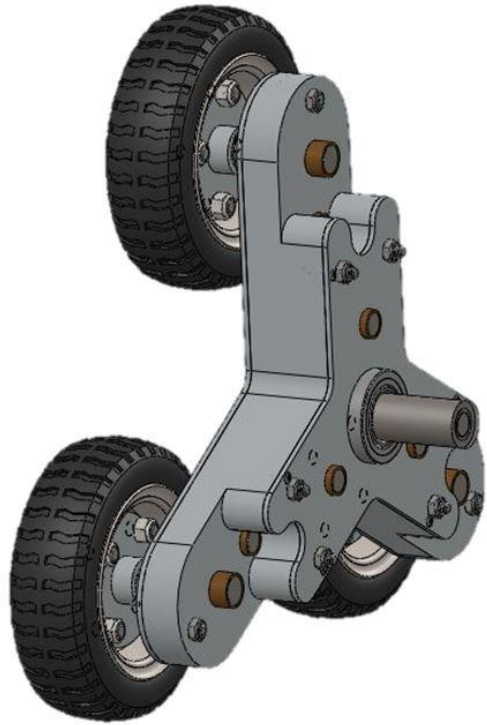


Figure 5.30: Housing Design 3

The third iteration of the housing design once again incorporates some of the suggestions and critiques from its predecessor. In order to enclose the bolts on the tumbling side of the housing, a shape that almost looks like bunny ears is incorporated into both the web and the matching plate for the tumbling gearset side of the housing. Unfortunately, this design is more complex to design with additional curves and contours that are unnecessary. The idea was to enclose them and leave as much of the tumbling side of the gearing open in order to reduce weight and still provide an access hole to the D3 shaft, but upon deliberation, it is decided that the shape is too unusual and that another strategy should be employed. Internally, aluminum spacer pieces are specified and installed within the housing.

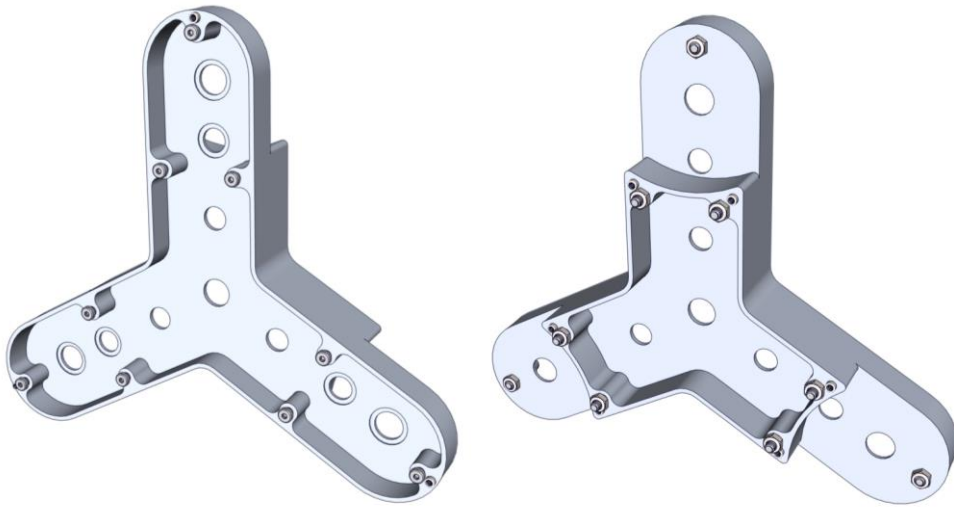


Figure 5.31: Final Housing Design Center Carrier Structure

The final housing design incorporates most of the good features and removes most of the bad design elements from the preceding housing iterations. Figure 5.32 is the final, optimized center carrier structure. Notice that the aluminum spacers have been incorporated into the actual body of this component to allow for ease of installation and precision alignment. The counterbores to locate and hold in the bearings are still present, and for the future, a chamfer will be specified on the internal edge where the shaft is seated for centering and installation purposes. The back of this structure reveals a more streamlined design that still encloses all of the bolts. On each side, there are holes included for alignment pins since the lip has been removed. These should be more cost-effective and work just as effectively.

The front and back isometric views of the driving carrier plate and the tumbling carrier plate are pictured below in Figure 5.32 and Figure 5.33, respectively. Each plate features through holes for assembly bolts as well as holes for alignment pins that will prevent the plates from twisting and help with the assembly process. The spacing of

alignment and assembly holes is carefully specified in order to prevent any interference between the fasteners and the rotating gears. Just as shown in the previous figure, counterbores are included around each of the bearing holes. Greater detail regarding the dimensions of these parts can be located in Appendix E: Machine Drawings along with the other machine drawings for the Tri-Wheel's designed components.

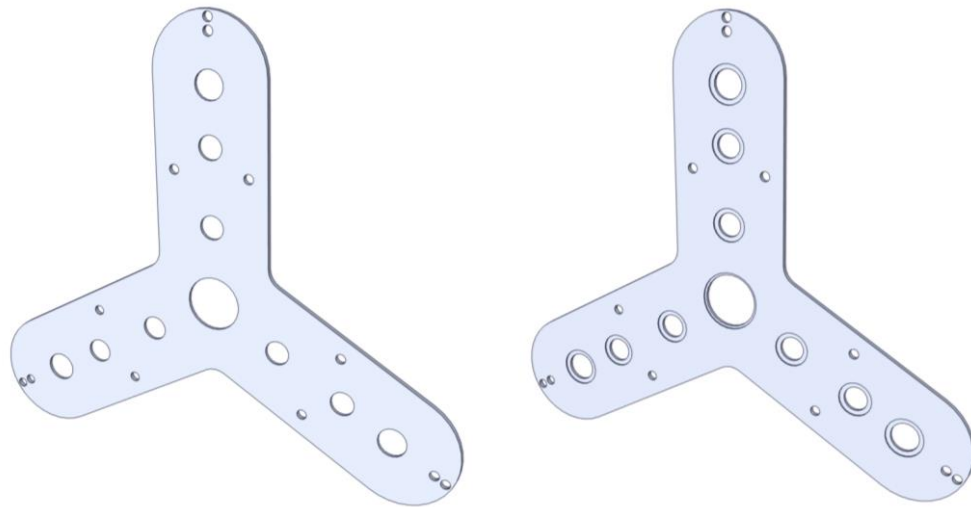


Figure 5.32: Final Housing Design Driving Carrier Plate

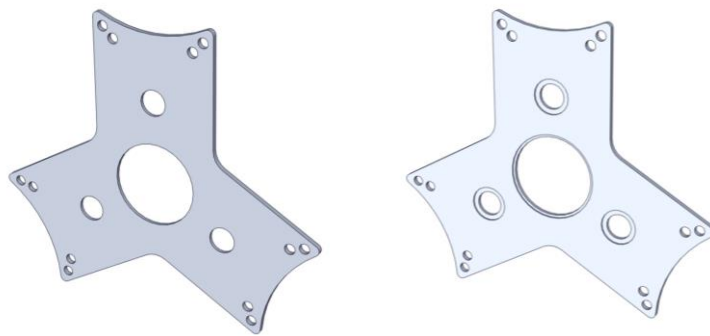


Figure 5.33: Final Housing Design Tumbling Carrier Plate

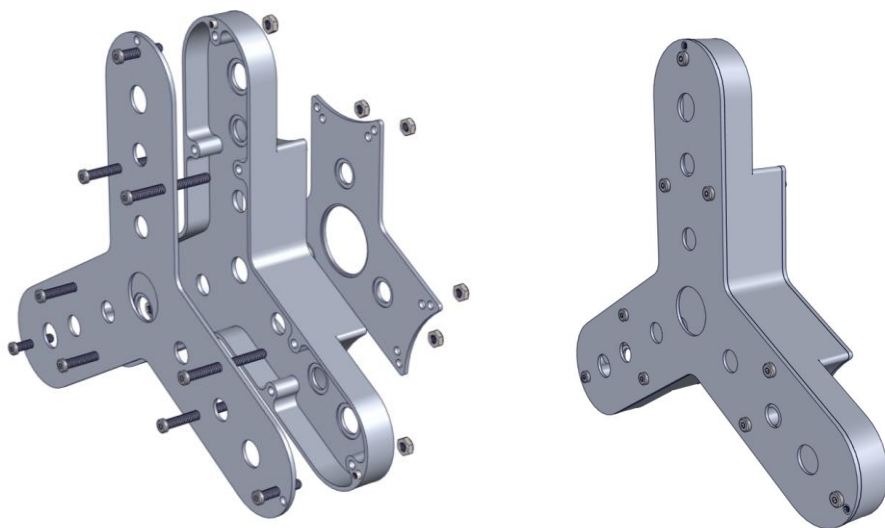


Figure 5.34: Final Housing Design Assembly

A full assembly of the Tri-Wheel housing is provided in Figure 5.34. The bolts used here have a low profile socket head to prevent any rubbing with the pneumatic wheels as they rotate. Low profile nylon locknuts are also specified to keep the entire assembly firmly tightened. Note that, while locknuts do reduce the tendency for these elements to become loose and jostled around, they are not by any means impossible to remove and can also be replaced, in keeping with the desire for ease of serviceability.

5.7 Braking Mechanism

The functionality of Tumbling Mode is contingent upon the proper selection of a brake or other clutching mechanism that can fix the hollow shaft B in space with respect to the robot chassis. In-depth analysis of multiple braking mechanisms has been conducted, but ultimately time constraints have dictated that the purchase of a pre-fabricated brake is more practical than manufacturing one from scratch. For brevity, only a list of the

concepts considered is included alongside information about the type of brake selected and purchased for the Tri-Wheel.

The basic purpose of a brake is to absorb energy. Brakes convert kinetic (translational and rotational) and potential energy into friction heat and effectively dissipate that resulting heat without developing destructively high temperatures [20]. Heat dissipation is a great concern when considering the brakes on a car. For most vehicles, braking heat is not distributed equally across all of the wheels. Instead, the heat dissipated at each brake is a function of the dynamic and static weight distribution on the wheels and the design of the entire braking system itself [41]. While these principles and concerns are not invalid for the Tri-Wheel and whichever robot chassis it is installed on, the relatively low speeds at which the mechanism will travel (roughly 6 MPH maximum) greatly reduce the energy that must be absorbed and transmitted to heat. For this reason, while it is acknowledged that this analysis could be performed, it is not a driving factor in the Tri-Wheel brake selection.

While heat dissipation is not a particularly large concern, a number of other characteristics are. One of the primary restrictions is that the brake must halt the assembly whether it is spinning in a clockwise or counterclockwise direction. Basic size constraints dictated by the robot chassis for this preliminary testing are also a concern. It is also known that the brake must be able to counter a maximum estimated 45 ft-lb of torque and bring hollow shaft B to rest from its maximum rotational speed. Lastly, it is necessary for the braking mechanism to actuate within a reasonable response time.

The types of braking mechanisms initially considered are as follows: band brake (including a differential band brake), internal cam-operated drum brake, disk brake, and

pin-in-groove brake. A band brake is initially specified and designed, but due to the time restriction, a small cam-operated drum brake is purchased. This brake functions in both directions of rotation, and utilizing a linear actuator with 32 lb of available force and bicycle cable as the lever arm, it is determined that the maximum torque requirement of 45 ft-lbs is easily satisfied.



Figure 5.35: Internals of Selected Tri-Wheel Braking Mechanism

Figure 5.35 shows the inside of the cam-operated internal drum brake purchased to install on hollow shaft B of the Tri-Wheel. This brake is typically used for a scooter, but is modified appropriately to fit this purpose. On the left side is the drum, which is attached directly to shaft B. This drum is modified to include a keyway so that it can rotate freely until the internal shoe on the right side is actuated via a small cam and pressed out against the drum to halt its rotation. The lever actuating this braking is connected to the linear actuator using a threaded rod.

6 RESULTS

6.1 Functional Assembly

The first major result of this analysis is a functional Tri-Wheel that is fully assembled and spun successfully in both directions. This is proof of the design's consideration of how the components fit together, appreciation of tolerances, and the overall design choices for this mechanism.



Figure 6.1: Completed Tri-Wheel

Figure 6.1 shows the first completed Tri-Wheel assembly. Because mechanical systems rarely go together perfectly the first time without any modification, the choice is

made to initially fabricate only two Tri-Wheels and test them on a robot chassis that supplements the other two Tri-Wheels with normal wheels of an appropriate size. The hope is that once the design is validated and tested, two more can be made in the future incorporating any changes that can improve functionality or ease of assembly.

Throughout the assembly process, NASA Glenn's Roger Tuck is instrumental in helping the Tri-Wheel transform from a box of designed components and purchased parts to a fully working mechanical system. His experience with gearing systems provides invaluable insight into the best practices for gearbox assembly and ultimately enables the Tri-Wheel to come together in completion. It is an understatement to say that much is learned through this assembly process; this knowledge will carry over to potential future versions the Tri-Wheel design.



Figure 6.2: Beginning of Assembly Process

At the beginning of the assembly process for two Tri-Wheels, the work bench is covered with carrier plates, gears, and bearings. All of the components are machined with proper material selections and heat treatments where applicable. Figure 6.2 provides a glimpse into the early stages of this process.

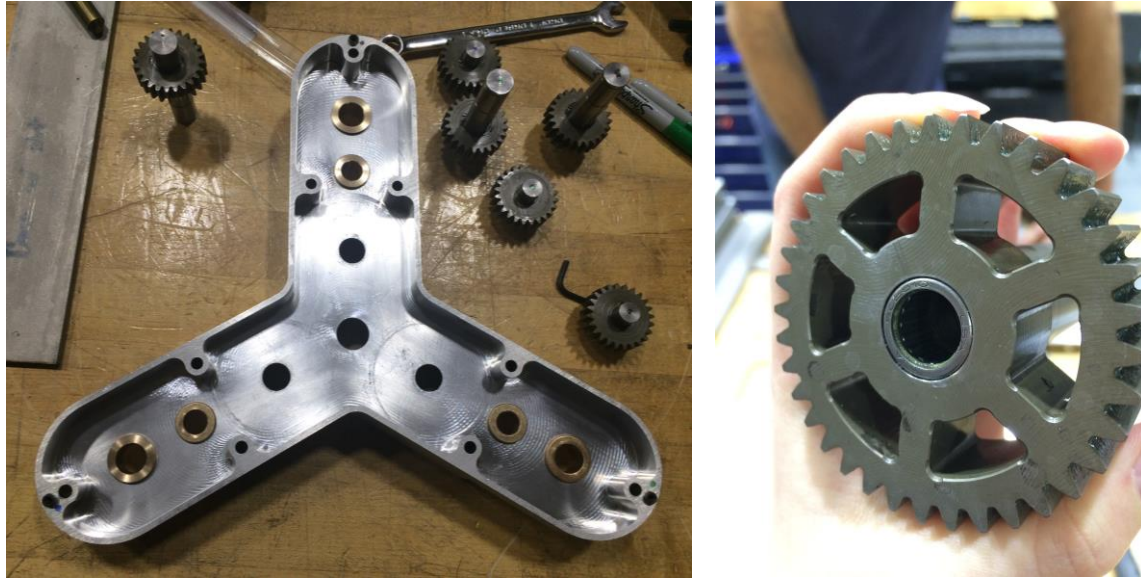


Figure 6.3: Pressed-in Bearings

The first components to be installed are the bearings. An arbor press is used to press in the flanged sleeve bearings, flanged ball bearings, and the needle bearings as depicted in Figure 6.3. The ability to efficiently press in the bearings reflects successful consideration of the tolerances necessary to achieve a proper press fit. Note that in order for the bearing holes to concentrically align through the drive, middle, and tumbling carrier plates it is desirable for the holes to be drilled simultaneously. Because it is not confirmed that this procedure has been followed, a reamer is used by hand to ensure that all of the bearings are concentric to prevent potential binding of the shafts. This also helps the shafts to rotate smoothly, as any imperfections on the inside faces of the sleeve bearings are removed.

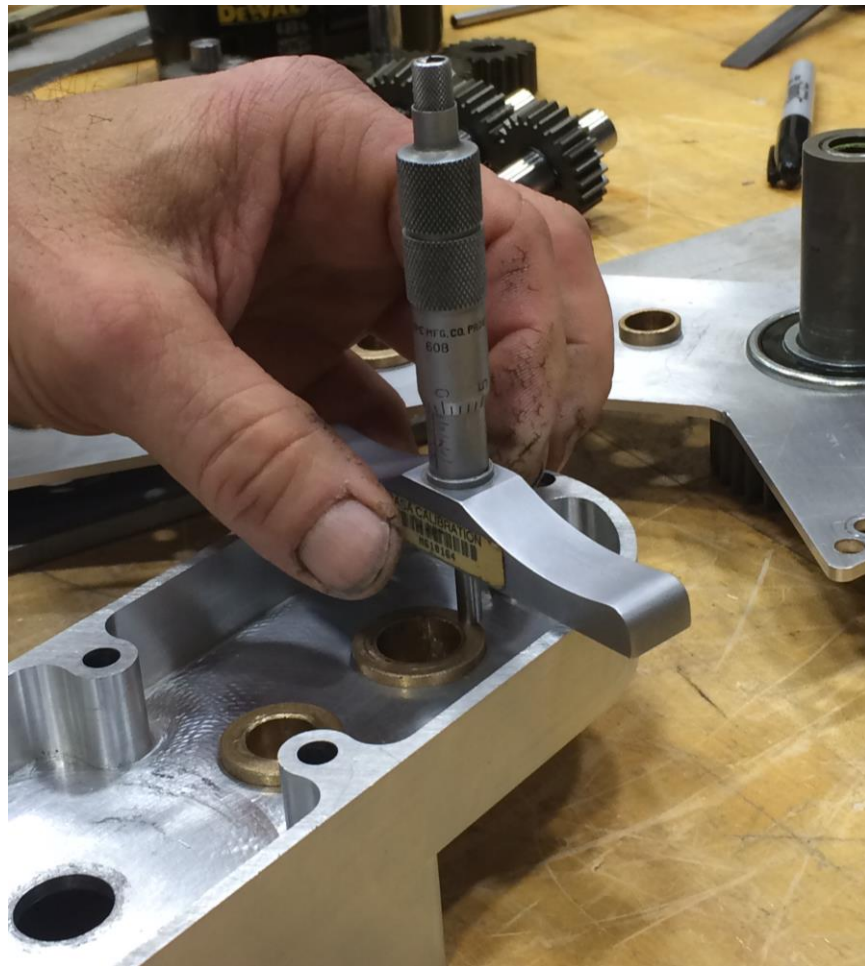


Figure 6.4: Depth Measurement with Micrometer

After installing the bearings, a micrometer is used as in Figure 6.4 to measure the depth at various points around the flange of each bearing to ensure that each one is pressed in flush at all points around the circumference. Because an arbor press is used, it is possible to press down with greater force on one half of the bearing versus the other half, leaving the flange at an angle that eats into clearance space. This measurement check validates the dimensions prescribed in the machine drawings and is a necessary step in the overall assembly process.

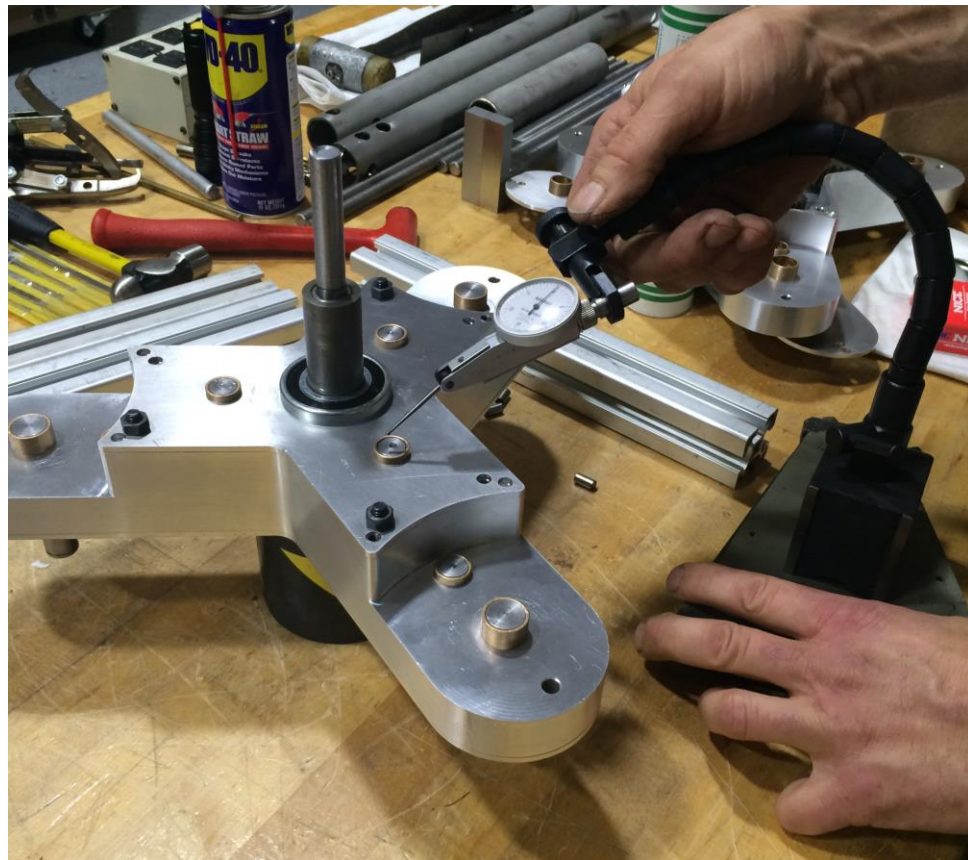


Figure 6.5: Clearance Measurement with Dial Indicator

Once the Tri-Wheel is fully assembled with gears, retaining rings, keys, dowel pins, and other small components, a dial indicator is used to measure the clearance available in each shaft subassembly, as seen in Figure 6.5. Because the ends of each shaft are left open within the bearings, it is possible to physically move the shaft back and forth axially by a small measure within the bearings. If this is not possible, clearance is not sufficient, and the gears will bind in operation. The dial indicator provides a means by which this clearance can be accounted for. In this process, it is found that the manufacturer's drawings for the sleeve bearings do not account for a fillet between the flange and the sleeve. This initially binds up the system, but a small chamfer on the inside of each bearing hole takes care of the issue and allows for proper clearance, as verified by

the use of the dial indicator. Properly specified clearances anticipated from the use of tolerance stackup analysis are validated.

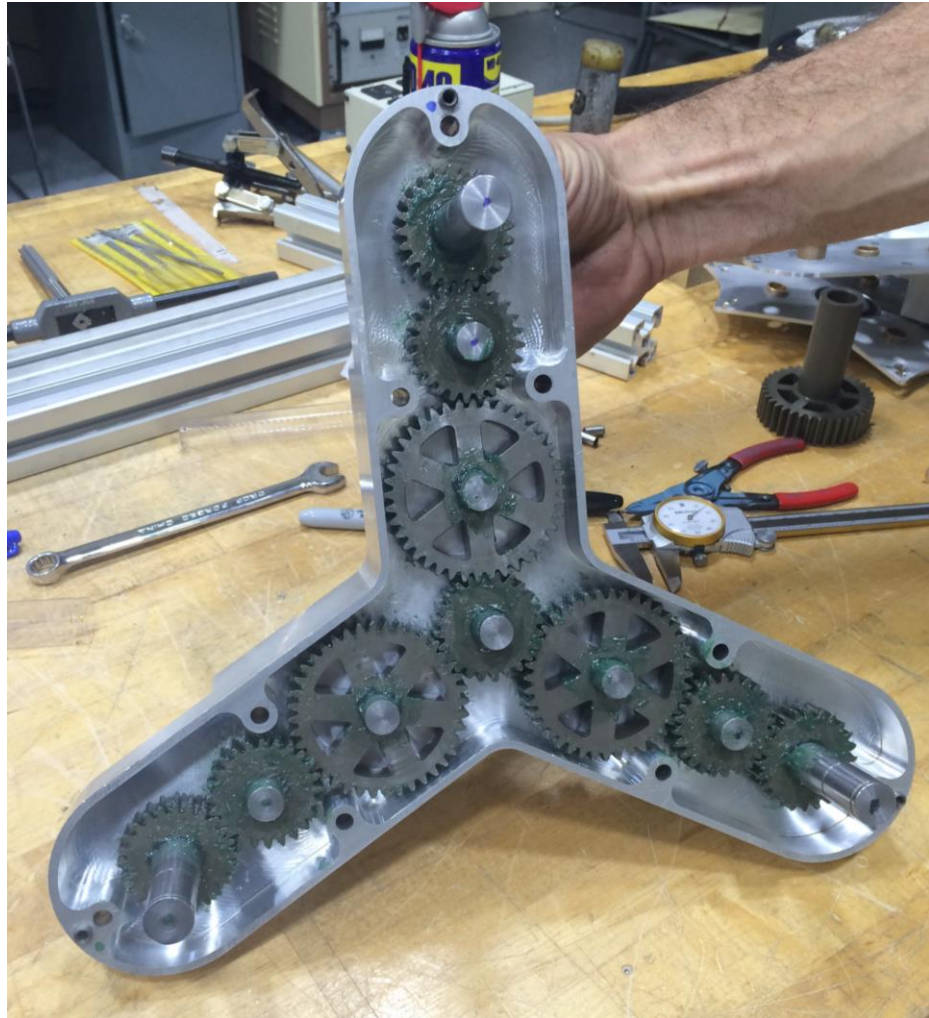


Figure 6.6: Lubricated Driving Gears

Each gear is installed individually and spun to ensure that there is not excessive friction due to its bearings or an alignment issue. Once installed, the gears are lubricated with robotics-grade grease. Lubrication is applied with a small brush on all gear teeth, around the retaining rings, and around the ends of the shafts. Extra lubrication is also placed inside the needle bearings shown in Figure 6.3. The driving gear set is shown in Figure 6.6, and the tumbling gear set is shown in Figure 6.7. Once the gears are all

installed, verification of proper meshing and adequate tolerance between the teeth is performed. The gears spin quietly and smoothly.

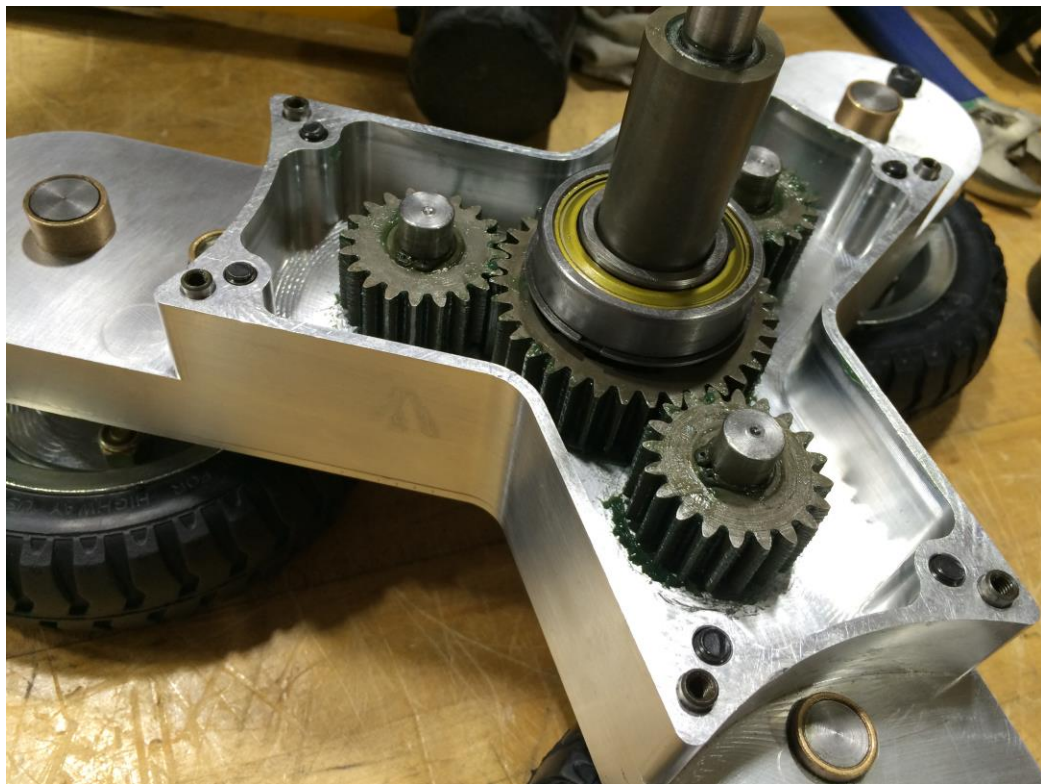


Figure 6.7: Lubricated Tumbling Gears

The last step in assembly before installing the Tri-Wheels on a robot chassis and driving with them is testing the proper gear operation and briefly running in the gear meshes to make sure that the gears are aligned and functioning properly. The Tri-Wheels are initially hooked up to a drill press via shaft A and spun in one direction. This verifies successful operation of the gears, as the spinning wheels and correct direction of spin can be observed, as shown in Figure 6.8. Next, both Tri-Wheel assemblies are run a milling machine beginning at low RPMs and increasing steadily to the maximum operating speed of roughly 350 RPM. The assemblies spin successfully. The direction of rotation is

reversed, and the same procedure is performed. This helps to run in the gears and serves as another verification of the functionality of the design.



Figure 6.8: Initial Testing of First Tri-Wheel



Figure 6.9: Run-in of Gears in Both Tri-Wheels

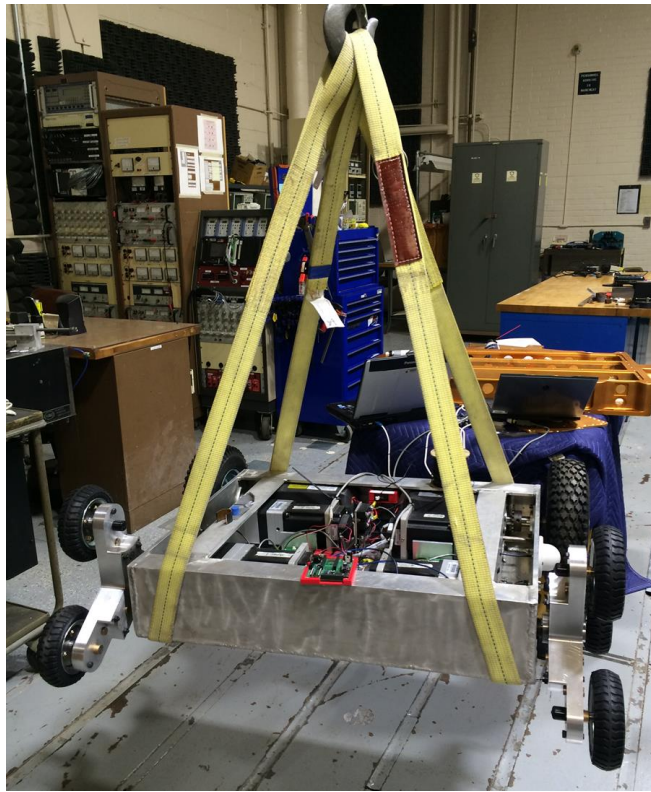


Figure 6.10: Vehicle Weighing

The last basic test involves using a calibrated fish scale and small crane to weigh the overall vehicle system, as shown in Figure 6.10. The SLOPE Lab has an existing robot chassis called Proto-Mini that is outfitted with two Tri-Wheels for testing. Again, only two Tri-Wheel assemblies are manufactured rather than the originally specified four, and the vehicle will therefore perform slightly differently. However, the back wheels are still powered and will be sufficient to establish proof of the Tri-Wheel's performance. Weighing in at 170.4 lbs, the vehicle system would still weigh less than 200 lbs if the two back wheels were substituted with two additional Tri-Wheel assemblies, as each Tri-Wheel weighs approximately 14 lbs. In confirming that the maximum weight constraint is has not been exceeded, the analysis leading to the final Tri-Wheel configuration is preserved.

6.2 Driving Mode

For the scope of this project, the predominant testing goal is the successful verification of Driving Mode and Tumbling Mode functionality, providing proof of the concept. Driving Mode is advantageous due to the increased speed it theoretically achieves. In order to corroborate the maximum speed analysis that ultimately leads to a 1:1 gear ratio, the maximum speed of the Proto-Mini/Tri-Wheel system is obtained experimentally. Most simply, velocity is the distance traveled over a given amount of time. Once the motor controllers accelerate the motor output shaft to a maximum speed of 350 RPM, it is observed that the robot travels roughly 18 ft in 2 seconds, as roughly estimated with a stopwatch, which translates to 6.1 MPH. This result is reasonably in accordance with the estimated speed of 6.21 MPH, presenting minimal losses. Losses are anticipated from two sources: first, compression of the pneumatic tires will result in a velocity less than that computed theoretically for a rigid wheel. Second, there is an RPM limit on the motor controllers that will not allow the motors to spin exactly at the maximum speed of 350 RPM. This can be changed manually for each of the four motor controllers in future testing. A time-lapsed photo of this test is provided in Figure 6.11.



Figure 6.11: Driving Mode Time Lapse

The Proto-Mini body is outfitted with two Tri-Wheels in the front and two conventional wheels in the back for testing purposes. Remember that in this mode of

operation, the Tri-Wheel assemblies are not rigidly locked in place with respect to the chassis, so the ability to pivot to contours and slopes is possible.

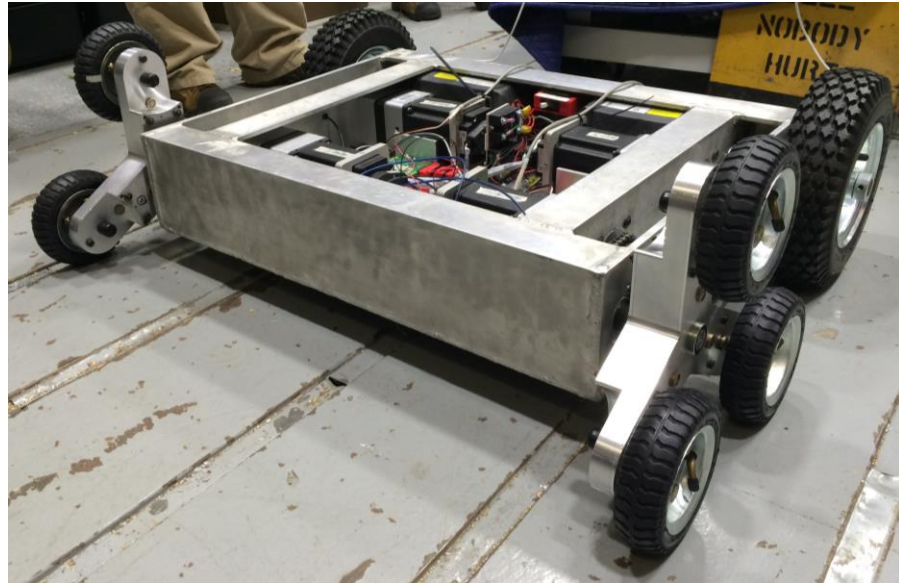


Figure 6.12: Driving Mode

Figure 6.12 is an additional view of the Proto-Mini chassis outfitted with Tri-Wheel assemblies. Using a radar gun and reflective tape, the angular velocity of the wheels when driving are recorded. With an input speed of 250 RPM from the motor controller, the wheels spin at an angular rate of roughly 248 RPM, accounting for some minor losses. The acceleration is approximated by monitoring the motor control software to see how long it takes the robot to reach its top speed and dividing the average velocity by that time. This estimation yields an acceleration of less than one second, as predicted by the Lagrangian model previously discussed. This testing confirms that Driving Mode operation exceeds minimum speed requirements, accelerates reasonably quickly as anticipated, and confirms minor frictional losses in the gearing system.

6.3 Tumbling Mode

The Tri-Wheel's tumbling functionality relies upon the production of at least 45 ft-lb of torque about each assembly, as estimated for a 200-lb robot system. This is theoretically produced using a reverted gear train resulting in a threefold increase in torque. Thus, the first metric to verify is the gear train's successful production of the expected amount of torque. A known weight is applied to a lever arm attached to the driving shaft. The resulting force transmitted through the gearing is measured with the fish scale at the end of another lever arm attached to the tumbling shaft. This confirms that there is a 3:1 increase in torque at the tumbling shaft. It is also observed in preliminary testing that one rotation of the Tri-Wheel body occurs for every three rotations of each individual wheel. Thus, the torque required to theoretically achieve Tumbling Mode is verified as present in the system. The torque of the individual gearmotors is also verified before installation to ensure that each motor functions properly.

The braking mechanism and its implementation are largely governed by the space constraints imposed by the existing Proto-Mini design. A small internal drum brake from a go-kart is utilized to halt the tumbling gear. The drum is retrofitted with a steel insert adapter that is keyed to the shaft and spins during rotation. A linear actuator capable of producing 32 lb of force is connected to the braking lever with a threaded rod and a variety of fasteners, as shown in Figure 6.13. When the linear actuator pulls on the lever, a small cam expands the brake shoe to press against the drum and halt the rotational motion of gear T1, creating a tumbling motion. This type of brake is directional, meaning that it is more effective when the Tri-Wheel is rotating in one direction over the other. In

the case of the less effective rotational direction operation, tumbling is still possible, but a larger actuation force is required.



Figure 6.13: Brake Configuration

A switch is used to extend and retract the linear actuators as required to switch between Tumbling Mode and Driving Mode. When the actuator is applied to expand the brake shoe inside the drum, gear T1 is held stationary with respect to the robot chassis, and the Tri-Wheels begin to walk forward as shown in Figure 6.14. Proto-Mini is tested ascending multiple sets of steps. Figure 6.15 provides a snapshot of the robot ascending steps of 7" rise, 11" run parameters with ease, a combination occurring in the middle of the rise-run data set presented in Chapter 3.



Figure 6.14: Tumbling Mode

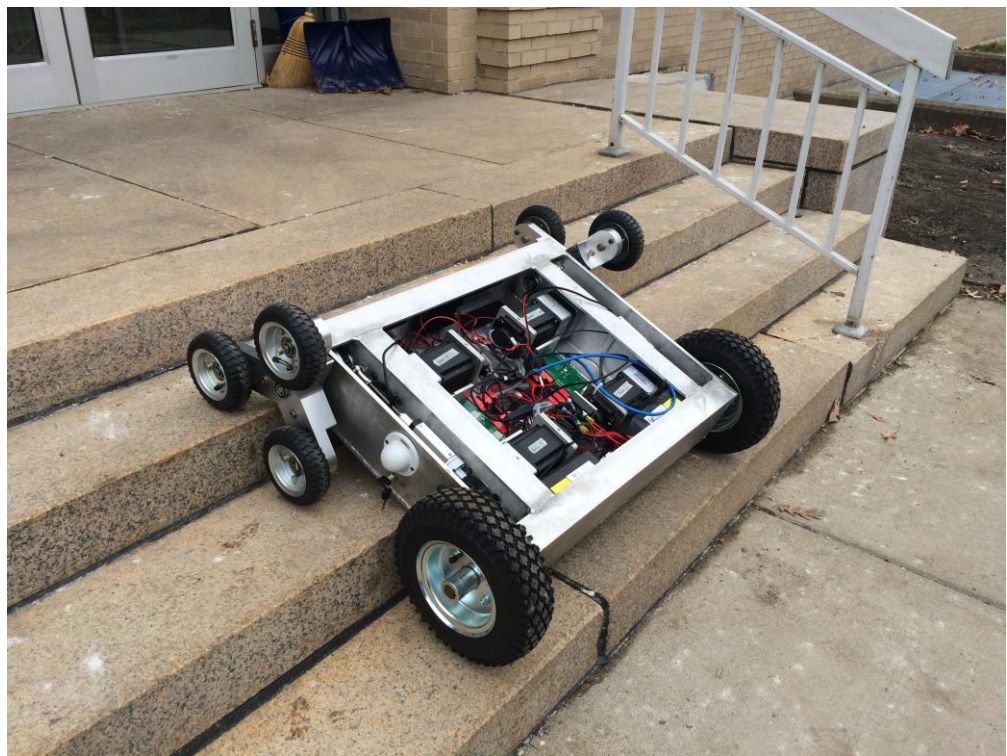


Figure 6.15: Tumbling Mode Ascending Steps - 7" Rise, 11" Run

7 CONCLUSIONS AND FUTURE WORK

7.1 Design Summary

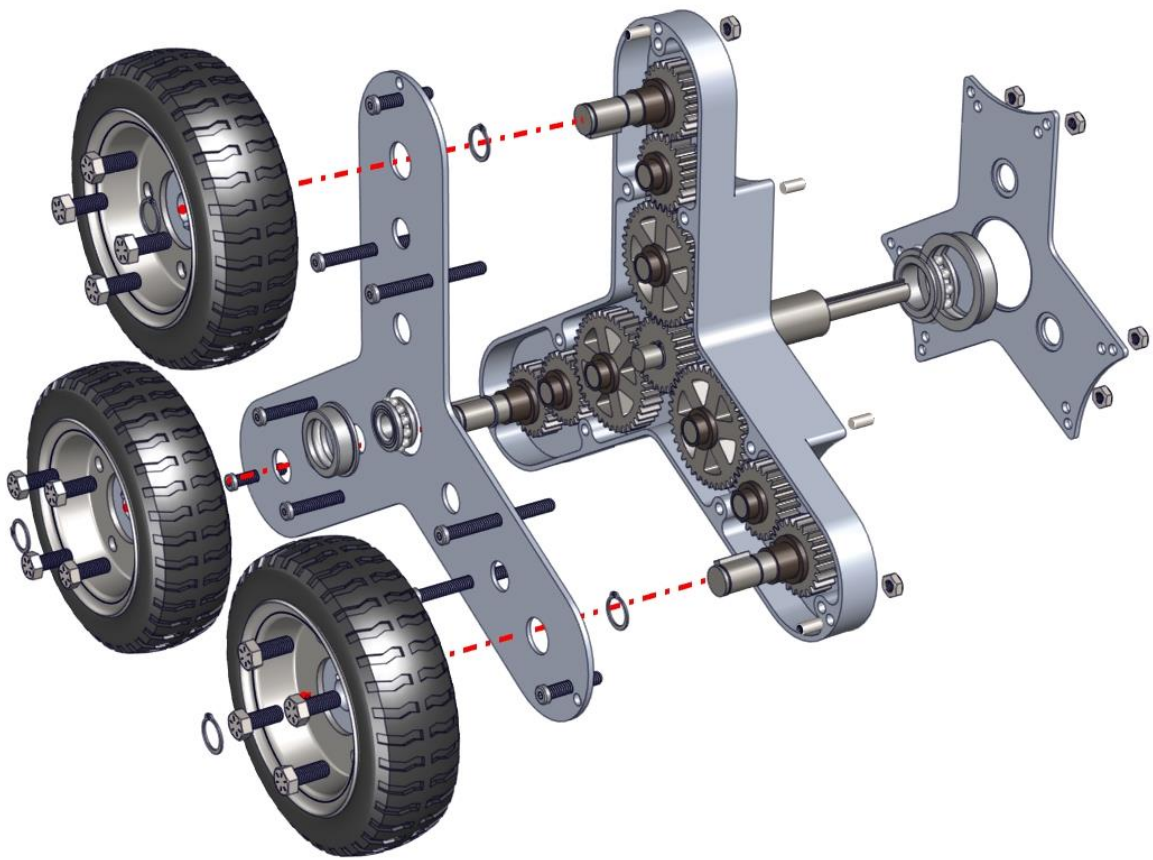


Figure 7.1: Exploded View of Complete Tri-Wheel Assembly

Figure 7.1 is a disassembled view of the final Tri-Wheel mechanism. Beginning with preliminary concepts detailed in Appendix A and ending with mechanical systems integration of all the purchased and created components, the Tri-Wheel design process has spanned a large variety of analyses and choice points.

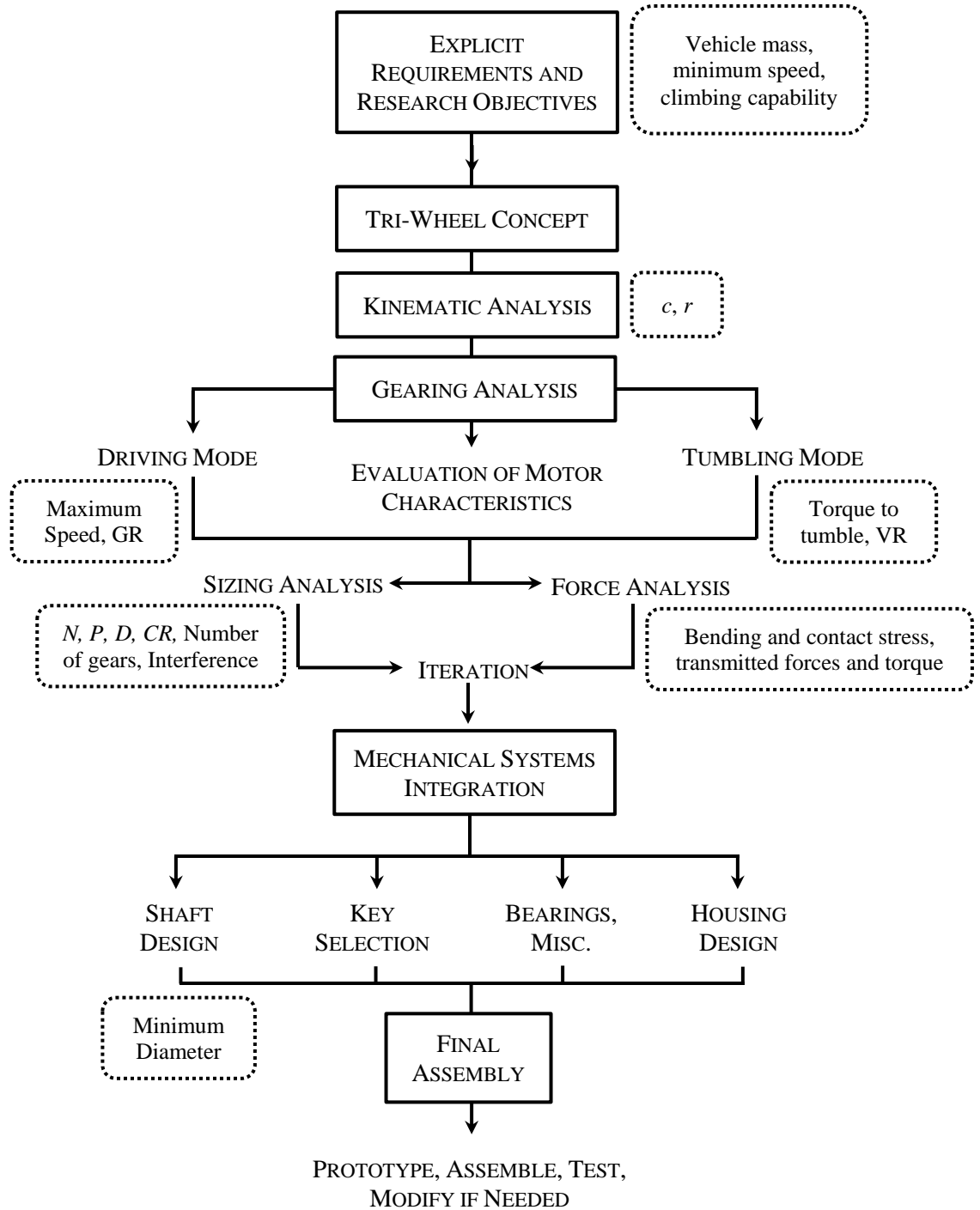


Figure 7.2: Process Diagram for Tri-Wheel Design

Figure 7.2: Process Diagram for Tri-Wheel Design provides a summary of the design process that eventually leads to this configuration. The elements within solid boxes represent major design points or broad categories under which various analyses are

performed. Elements that are not boxed at all represent important analyses or processes that occur within one of the major design categories. Any elements falling within the curved boxes with dotted lines describe some of the most important design parameters resulting from the nearby analyses or design points. While this visual aid certainly does not chronicle the entire process required for this project, it does highlight the importance of developing a logical design sequence in which certain parameters cannot be defined until others have been derived or selected. Acknowledging this early on has been critical to the successful development of the Tri-Wheel concept.

It is also important to note that the role of iteration in this process is not simply present in the gearing design, though this is unarguably where iterative optimization has been most frequently used. In addition to being a mechanical design project, this is also very much a systems integration project. At any point in the design process past the kinematic analysis (which must be fixed for all other computations and design choices to be relevant), opportunities have been seized to optimize the Tri-Wheel system as a whole by reducing weight and size, increasing functionality, and even creating a more user-friendly assembly process via the housing.

As mentioned, there have been quite a few design choices made throughout this project, and a sizeable number of derived requirements have been developed. The most fundamental design characteristics/derived requirements are included in Table 7.1 below. These metrics are the framework of the Tri-Wheel design and have conclusively led to a successful working model.

<i>Characteristic</i>	<i>Variable</i>	<i>Metric</i>
Spoke length	c	5.5 in
Individual wheel radius	r	3 in
Total number of driving gears per assembly		10
Total number of tumbling gears per assembly		4
Diametral pitch of driving gears	P_D	16
Diametral pitch of tumbling gears	P_T	14
Face width of driving gears	F_D	0.5 in
Face width of tumbling gears	F_T	0.75 in
Maximum computed linear driving speed	v_{max}	$\approx 6 \text{ MPH}$
Estimated torque required to tumble	τ_T	$\approx 45 \text{ ft-lb}$
Weight of one Tri-Wheel assembly	m_T	14 lbs
Envelope size of Tri-Wheel housing + wheels	$l \times w \times h$	$15.5 \times 4.72 \times 14.25 \text{ in}$
Driving Gear Ratio	GR_{TOT_D}	1:1
Tumbling Gear Ratio	GR_{TOT_T}	3:1

Table 7.1: Critical Design Characteristics

7.2 Conclusions

In conclusion, the Tri-Wheel mechanism has been successfully developed from a theoretical mobility solution to a fully functional proof of concept and working model. The contribution of this work is to provide a novel locomotion mechanism that enables a robot to exceed current linear speeds for robots, climb stairs and traverse obstacles, and do so keeping cost, space constraints, and robustness in mind. This design has been optimized uniquely to effectively climb a variety of standard staircase dimensions and provides functionality that is currently regarded as missing among other common locomotion concepts after assessing their capabilities. It is hopeful that technology can be implemented in other applications such as explosive ordinance disposal and perhaps even

extraterrestrial exploration. Harkening back to the research objectives declared in Chapter 1, Table 7.2 provides a summative requirement versus capability compliance assessment of these goals. The final Tri-Wheel concept either meets or exceeds each of these research objectives, as validated by the testing and installation process.

<i>Research Objective</i>	<i>Metric or Other Verification</i>	<i>Compliance</i>
Smooth and quick operation on level ground (with a linear speed of at least 3.3 MPH).	$v_{max} \approx 6 \text{ MPH}$	Exceeds
The ability to navigate rough terrain, including obstacles such as rocks or stairs of common sizes in addition to loose terrains such as sand and mud.	Testing	Meets
A robust design that will not fail mechanically during normal operations.	Testing	Meets
Full mission capability: transformation from quick motion to site of interest to high torque climbing functionality	Testing	Meets
The ability to be implemented on a previously constructed robotic platform as a hardware upgrade.	Installation on Proto-Mini	Meets
Initial sizing such that it is suitable for a robot of no greater than 150 – 200 lbs.	$m_P + 2m_T = 198.4 \text{ lb}$	Meets
Potential for implementation of a system to switch between objectives 1 and 2 above either passively, through user command, and/or autonomously.	Passive tumbling testing and successful drum brake actuation	Meets

Table 7.2: Final Requirements v. Capability Compliance

It is hopeful that this design will ultimately contribute to the overall safety of the brave first responders who help keep our communities safe. In the broader sense of science, the Tri-Wheel adds its tire tracks to the existing list of locomotion concepts, providing new functionality and potential within this field of research. Though there is room for improvement and future growth, this research has validated performance of the Tri-Wheel through preliminary testing and has subsequently corroborated the analysis leading to the final product—all while teaching its designer quite a lot along the way.

7.3 Future Work

Now that preliminary testing has been completed to verify the successful operation of the Tri-Wheel in Tumbling Mode and in Driving Mode, more detailed testing is desired to compare the Tri-Wheel platform to existing locomotion platforms, measuring its performance quantitatively against well-established concepts like wheels and tracks. Due to knowledge gained during the assembly and manufacturing processes, there are design elements that can be modified to improve ease of construction. In addition, there has been an interest expressed in developing a version of the Tri-Wheel more suitable for small robots weighing under 50 lbs. Because the sizing of the Tri-Wheel is optimized for stair climbing, a solution might come in the form of alternate material choices less massive than steel, for instance. In closure, there certainly is still work to be done regarding the Tri-Wheel concept; however, its successful development, fabrication, and testing inspires confidence in the future of this technology and its potential both to benefit those who use it and to contribute to the greater field of locomotion research.

APPENDIX A: DISCARDED LOCOMOTION CONCEPTS

Before selecting the Tri-Wheel as the design of choice to accomplish the research objectives stated in Chapter 1, a number of other options were considered. Because this research focuses primarily on the development and testing of the Tri-Wheel mechanism, it does not seem judicious to spend pages detailing all of the discarded concepts. However, in order to provide some evidence that other locomotion approaches were indeed considered, a few of these ideas (as they were named in preliminary conversation) have been included in this appendix and concisely described:

1. THE TRANSFORMING (PIN)WHEEL

This concept is largely inspired by Dr. Roger Quinn's Whegs robots. Whegs are more successful in surmounting obstacles because of the spaces between their rigid spokes that allow them to latch on to curbs and smaller obstacles. The difficulty, then, is to determine how to reap the benefits of this design for climbing obstacles but also have a more efficient means of moving on flat surfaces. If one thinks of a windmill, for example, there are gaps between the rotating blades. If those gaps were to be filled in by mating blades, the pinwheel-type structure would form an approximate circle. Thus, this design would have two offset blades of spokes that could rotate relative to each other and leave spaces open to climb obstacles but expand, rotate, and contract to fill in the gaps and form a wheel. This concept was eliminated due to the potential for debris to hinder the transformation process by lodging itself between the blades. Furthermore, the actuation

mechanism that would affect this motion would be prone to failure modes, and friction with the ground or other environmental impediments might prevent transformation between the modes altogether. This concept is too dependent upon the environment and more theoretical than practical.

2. THE TWO-SPOKED BUGGY WHEEL

This concept utilizes two wheels rather than three. Imagine the Tri-Wheel but with the top wheel removed, and that is what this concept was envisioned as. Some robot mechanisms do use this type of locomotion, particularly for lunar or extraterrestrial applications, but it does not seem as though many of these concepts utilize a substantial gear train; the wheels appear to be more passive. For the prescribed purpose of climbing stairs, it would be much less likely that a two-wheeled robot could quickly and robustly power up steps due to the large lag in rotation from the trailing ground wheel having to rotate by such a large angle and slap down on the next step or obstacle. The momentum from this motion would also likely propel the leading ground wheel backward and ultimately destabilize the vehicle.

If the wheels were not separated by an angle of 120° but rather was more like a vertical line with two wheels on either end, this design would once again be regarded as more academic in nature than practical. Just to balance while tumbling about itself, a solution to the inverted pendulum problem would be necessary to provide stability. In critical environments, this concept would not provide the robust, practical locomotion that is required. Plus, there would be hardly any ground clearance, and the mechanism could be easily end up with wheels in the air due to grades, ground contours, and debris.

3. THE BOX WHEEL

The box wheel, as it is nicknamed, is imagined with an X structure with four wheels—one at each end of the X segment. Much like the Tri-Wheel, this concept should allow for smooth motion on flat surfaces and some climbing capability. However, the X shape does not lend itself to a wide open envelope between its spokes to latch on to a step or other obstacle as a Tri-Wheel does. In addition, if a similar gear design is required in order to actuate both driving and tumbling, the extra branch of gearing would lend itself to a much heavier locomotion concept and a much heavier robot overall.

4. THE EXPANDING WHEEL

Somewhat similar to the Transforming (Pin)Wheel idea, the Expanding Wheel would be composed of tightly curved spokes offset from each other to leave a slight gap between the blades. This gap would be rather small compared to that present in either Whegs or in the (Pin)Wheel concept. When rolling, an actuating mechanism would be able to expand the wheel via linkages to extend finger-like protrusions that could help to latch on to a step. Again, this concept is much more academic in nature than functional for the task at hand. The presence of linkages and many expanding and contracting parts would present a huge opportunity for failure in the field, and this concept did not like something that would even be sturdy enough to support a robot of nearly 200 lbs. However, there are existing robots that have successfully implemented a similar concept on smaller frames. IMPASS (Intelligent Mobility Platform with Active Spoke System) is a mobile robot driven by two rimless spoke wheels. Each of the spokes can be individually actuated with intelligent motion planning to walk over uneven terrain with high mobility [42].

APPENDIX B: TRI-WHEEL DESIGN ITERATIONS

CONFIGURATION 1.0

The first prototype of the Tri-Wheel was more for proof of concept than a configuration optimized for the required conditions. Figure A.1 provides a closer look at the gearing configuration selected for this first prototype. In this arrangement, the sun gear is motor driven. The planetary gears, which are designed with twice the face width of the other gears in the system, mesh with the idler gears and braking gear simultaneously. When the braking gear rotates freely and is not clutched to become stationary, driving mode rotation occurs, and two wheels are able to roll as normal wheeled motion on flat surfaces.

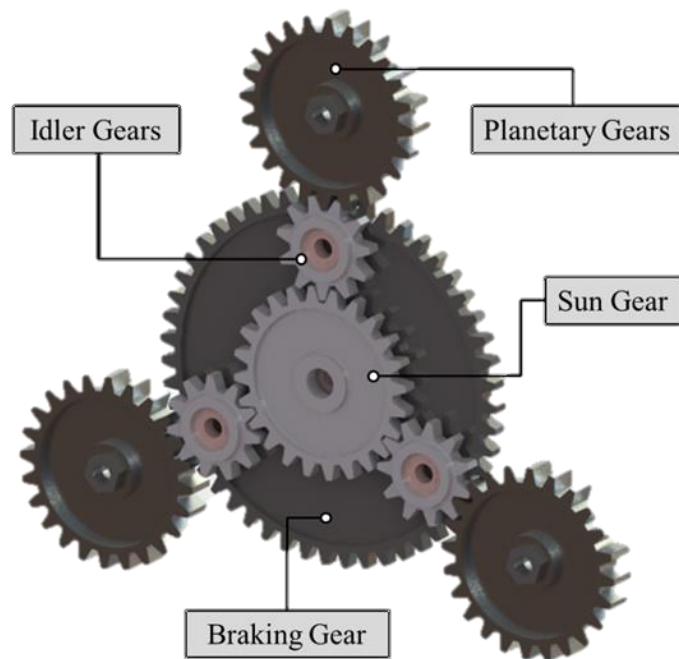


Figure A.1: Version 1.0 Gearing Configuration

When the braking gear is held, the assembly is able to rotate about a central shaft and effectively climb over objects as the wheels attached to the planetary gears are locked in place. For this design, the outer internally geared ring or “annulus” of a typical planetary gear set has been inverted and placed at the center of the mechanism to make the whole system compact and enclosable within a bell housing to prevent debris from interfering with its operation. Idler gears are utilized to ensure that the motion of tumbling mode proceeds in the same direction as the wheeled motion of driving mode, ensuring that the rotational direction of the sun and planetary gears is the same.

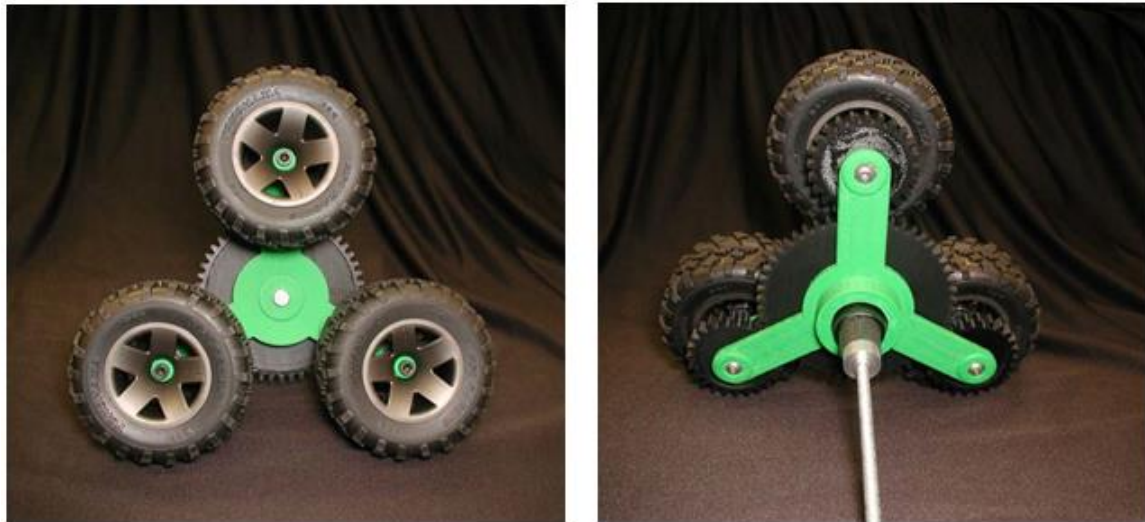


Figure A.2: Prototyped Tri-Wheel 1.0

Figure A.2 displays a rapid prototyped model of this initial configuration, which was meant to give a general notion of size and basic movement. Unfortunately, this design is impractical for stair climbing since the braking gear becomes large to the point that it protrudes into the open space between each of the three spokes attached to the wheels. Additionally, with further analysis, the face widths of these gears were determined to be much too small to resist the bending and contact stresses present within

the system. Issues with wear on the planetary gears are also a concern; because each one interfaces with an idler and the braking gear, uneven wear and loading is anticipated.

CONFIGURATION 2.0

The second Tri-Wheel configuration in Figure A.3 sought to address the issue of keeping a narrow profile within the spoke length between the centroid of the assembly and the wheel. However, in doing so, the gears at the wheels became unreasonably large and quickly presented themselves as failure points since there was very little clearance between the gears and the wheels themselves, subjecting them to a higher risk of impact loading. At the time of this design, the thought was still to keep the general configuration from Configuration 1 in which three gears were used per branch. This configuration led to the ultimate conclusion that in order to keep the gears small between the centroid of the wheel and the centroid of the Tri-Wheel, an additional gear would be required.

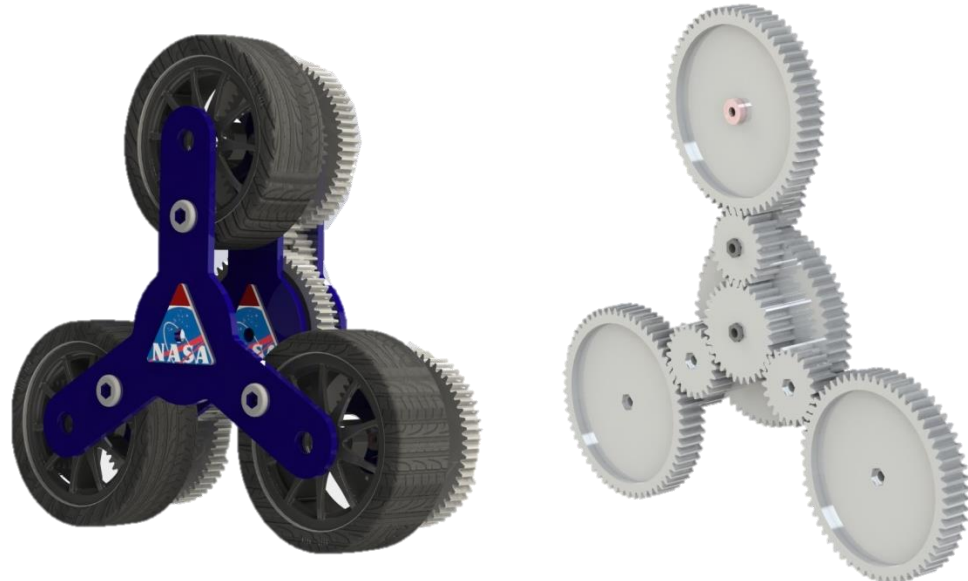


Figure A.3: Tri-Wheel 2.0 and Corresponding Gearing Configuration

Note also that the gearing configuration shown in Figure A.3 has a very small gear in the center to tumble about, which yields poor bending and contact stress properties for tumbling mode. With a fixed central tumbling gear, this configuration was also deemed to be too heavy due to the massive size of the larger gears. Even if the gears were webbed out to reduce some mass, the huge pitch diameter of nearly 5 *in* for the central tumbling gear and driving wheel gears was much too large to be practical. Because the central driving gear was so large, the envelope needed to climb stairs and tumble over obstacles between the spokes was still not large enough.

This configuration also altered the preliminary design concept by linking the two parallel gear sets for driving and tumbling modes with a shaft rather than using a single gear at the wheels with double the face width. With this modification, the wheels are permitted to spin freely while tumbling occurs, which allows the mechanism to pull itself along while tumbling via the wheels spinning in the same direction of tumbling rotation. In addition, Tri-Wheel 2.0 remedies the previously insufficient face width, but a face width of 0.75 in for each gearset is required to combat the maximum bending stresses present in tumbling mode. This increases the overall width of the Tri-Wheel gearing system unfavorably.

Lastly, it can be seen that an additional plate has been added to the front of the wheels mirroring a plate directly behind it. This sandwiches the wheels between two plates in hopes of providing extra support for the cantilevered wheels. This preliminary concept is hereafter removed because there is no convenient way to link the outer plate with the inner plate without cutting into the tumbling envelope. Without linking the two plates, the outer plate really does not provide much benefit. Car wheels are cantilevered

without a support beam linking wheels on two sides, and the loading is much greater. Therefore, with the design of a sufficiently robust housing and shafts, this outer plate is removed from future Tri-Wheel iterations.

CONFIGURATION 3.0

Tri-Wheel configuration 3.0 in Figure A.4 is designed with a specified face width of 0.5 *in* in order to reduce overall width. This configuration shrinks the envelope size of all driving gears (the leftmost set of gears shown in the isometric drawing of Figure A.5) and increases the size of the tumbling gear at the center to reduce bending and contact stresses present during tumbling mode.



Figure A.4: Tri-Wheel 3.0

However, if you review the power flow diagrams carefully in Figure 13, the wheels in driving mode are actually spinning in the opposite direction of the entire assembly as it rotates about its central shaft in tumbling mode. Initially, it was assumed

that an odd number of tumbling gears including the central braking gear in each leg of the Tri-Wheel (for instance, three gears shown in the rightmost set of gears in the isometric drawing of Figure A.5 was required. However, this gear set does not necessarily behave as a typical configuration. Because the central gear will be held stationary, it does not count as a conventional gear necessarily, and must be treated as a fixed rigid body. Thus, in order to have the same direction of spin for the wheels in driving mode and the whole assembly in tumbling mode, there must be an odd number of gears in each leg of the tumbling gear set, less the central gear.

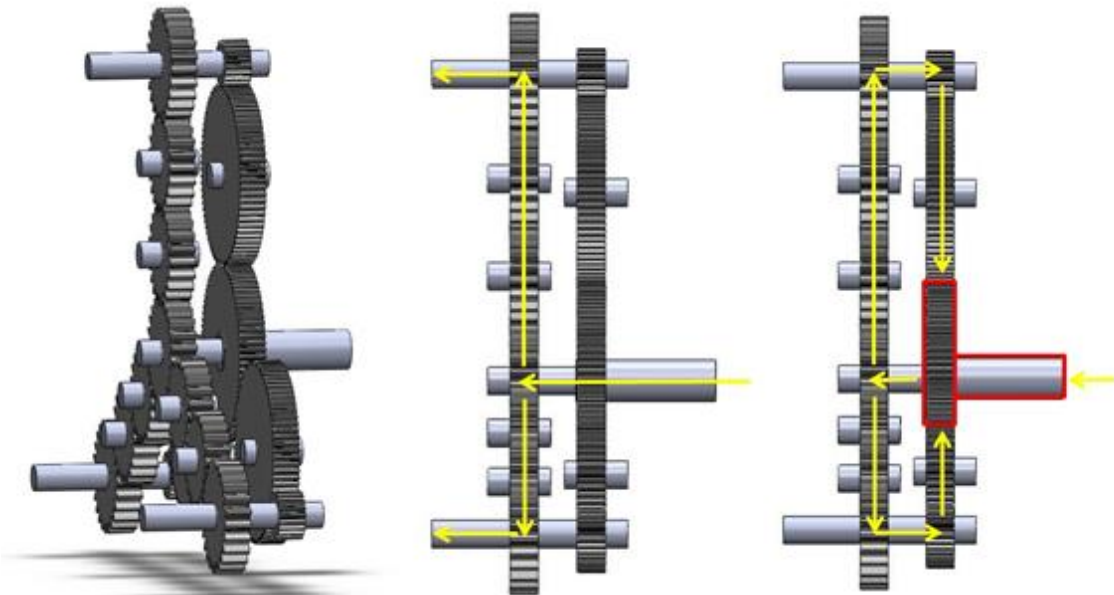


Figure A.5. Tri-Wheel 3.0 Driving Mode and Tumbling Mode, Respectively

It is also evident in this design (as in the previous designs) that the shaft linking the driving and tumbling gearsets is located at the wheel rather than right next to the central drive and tumbling shafts. For future designs, the relocation of the connecting shaft is a redesign choice made to reduce the weight of the overall Tri-Wheel system, eliminating a number of gears entirely and decreasing the envelope size of all the gears. Rather than trying to increase the torque required to tumble only through the tumbling

gears, future designs take advantage of the reverted gear train concept which allows part of the 3-fold increase in torque to occur through the driving gears and a fraction of the torque increase to occur through the tumbling gears.

While a number of intermediate designs exist between configurations 1.0, 2.0, and 3.0, these particular arrangements highlight some of the most important lessons learned and design changes incorporated throughout the iterative gear design process.

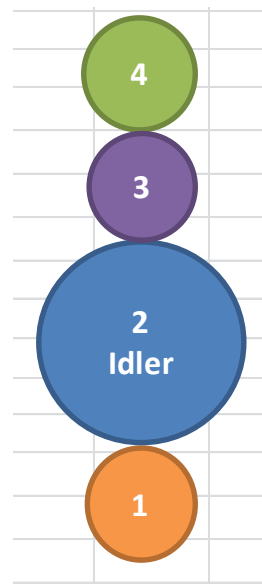
APPENDIX C: GEARING SPREADSHEET

The following pages contain the gearing design spreadsheet used to iteratively compute design values of interest in a pursuit to optimize the Tri-Wheel gearing. The driving gear train spreadsheet is presented first, followed by the tumbling gear train spreadsheet. Due to the paper sizing restrictions stipulated for this report, the presentation of one complete spreadsheet on a single page is not practical, as the text becomes rather small. For reference of the overall setup, the entire spreadsheet for one set of gears is first presented on a single page and then broken down into individual components that are easier to read and interpret.

The nomenclature and units used throughout this spreadsheet are identical to those described in Chapter 4: Design of Gearing System. Many of these common symbols can also be located in the Symbols section of this paper. Please note that the spreadsheet values included in this appendix only reflect the values computed for the Tri-Wheel in its case of maximum torque. Because this point of operation (in Tumbling Mode) imposes the greatest stresses upon the system, these parameters are utilized throughout the design or specification of shafts, bearings, and many other elements of the Tri-Wheel mechanism.

GEAR SPREADSHEET: DRIVING MODE (MAX POWER AND TORQUE)														
General Parameters														
INPUT - SIZING				INPUT - FORCE ANALYSIS										
c_{TOTAL}	5.5	c_{TOTAL}	5.500	m	200.000	$J_{1, 1-2}$	0.350	τ	15.000	\dot{W}	0.868	τ_T	45.833	
GR_{TOTAL}	1.00	c_{1-2}	2.000	GR_{GM}	10	$J_{2, 1-2}$	0.390	$\tau_T \cos(30)$	39.693					
N_2	40.0	c_{2-3}	2.000	η_M	0.960	$J_{3, 2-3}$	0.390							
N_3	24.0	c_{3-4}	1.500	RPM_M	3038	$J_{3, 3-4}$	0.330							
P	16.0	GR_{1-2}	-1.667	RPM_{GM}	303.800	$J_{4, 3-4}$	0.310							
ϕ	20.0	GR_{2-3}	-0.600	K_o	1.250	I_{1-2}	0.095							
r_{wheel}	3.0	GR_{3-4}	-1.000	K_v	0.900	I_{2-3}	0.090							
		b_{\min}	0.500	K_s	1.000	I_{3-4}	0.080							
		b_{\min}	0.563	K_m	1.200	C_p	2300.000							
		b_{\max}	0.875											
Determine pitch diameters and number of teeth.														
N_1	N_2	N_3	N_4	r_1	r_2	r_3	r_4	d_1	d_2	d_3	d_4			
24.000	40.000	24.000	24.000	0.750	1.250	0.750	0.75	1.500	2.500	1.500	1.500			
Check for interference. If $A > a$, then interference will not occur. 'a' is addendum for standard full-depth gear.														
r_{b1}	r_{b2}	r_{b3}	r_{b4}			a		$A1_{(1-2)}$	$A2_{(1-2)}$					
0.705	1.175	0.705	0.705			0.063		0.232	0.109					
$r_{\text{amax}, 1 (1-2)}$	$r_{\text{amax}, 2 (1-2)}$	$r_{\text{amax}, 2 (2-3)}$	$r_{\text{amax}, 3 (2-3)}$	$r_{\text{amax}, 3 (3-4)}$	$r_{\text{amax}, 4 (3-4)}$			$A2_{(2-3)}$	$A3_{(2-3)}$					
0.982	1.359	1.359	0.982	0.872	0.872			0.109	0.232					
								$A2_{(3-4)}$	$A3_{(3-4)}$					
								0.122	0.122					
Calculate contact ratio to check for smoothness of operation. CR > 1 is acceptable. CR > 1.6 is recommended.														
p_b	r_{a1}	r_{b1}	r_{a2}	r_{b2}	r_{a3}	r_{b3}	r_{a4}	r_{b4}				CR_{1-2}	CR_{2-3}	CR_{3-4}
0.185	0.813	0.705	1.313	1.175	0.813	0.705	0.813	0.705				1.658	1.658	1.602
Gear Force and Torque Analysis. *NOTE: All subsequent analysis is based off of rounded values of gear sizing (bold)														
V	F_t	F_r	τ_1	τ_2	τ_3	τ_4	R_f		τ		τ_T		$\tau_T \cos(30)$	
119.302	240.000	87.353	15.000	-25.000	15.000	-15.000	255.403		15.000		45.833		39.693	
Gear Tooth Contact and Bending Stress * $S_t < S_{\text{sat}}$ and $S_c < S_{\text{ac}}$ for satisfactory design														
Simplified Formulas:				$S_{t, 1}$	$S_{t, 2, 1-2}$	$S_{t, 2, 2-3}$	$S_{t, 3, 2-3}$	$S_{t, 3, 3-4}$	$S_{t, 4}$	S_{at}	$S_{c, 1}$	$S_{c, 2, 1-2}$	$S_{c, 2, 2-3}$	$S_{t, 3, 2-3}$
				21,943	19,692	19,692	21,943	23,273	24,774	5,000-75,000	133,488	103,399	106,351	137,298
											145,465	145,465	145,465	30,000 - 255,000
Formulas with Constants:				$S_{t, 1}$	$S_{t, 2, 1-2}$	$S_{t, 2, 2-3}$	$S_{t, 3, 2-3}$	$S_{t, 3, 3-4}$	$S_{t, 4}$	S_{at}	$S_{c, 1}$	$S_{c, 2, 1-2}$	$S_{c, 2, 2-3}$	$S_{t, 3, 2-3}$
				29,623	26,585	26,585	29,623	31,418	33,445	5,000-75,000	155,099	120,139	159,526	159,526
											169,015	169,015	169,015	30,000 - 255,000

GEAR SPREADSHEET: DRIVING MODE (MAX POWER AND TORQUE)										
General Parameters										
INPUT - SIZING					INPUT - FORCE ANALYSIS					
c_{TOTAL}	5.5	c_{TOTAL}	5.500		m	200.000	$J_{1, 1-2}$	0.350	τ	15.000
GR_{TOTAL}	1.00	c_{1-2}	2.000		τ_M	1.563	$J_{2, 1-2}$	0.390	\dot{W}	0.868
N_2	40.0	c_{2-3}	2.000		GR_{GM}	10	$J_{2, 2-3}$	0.390	τ_T	45.833
N_3	24.0	c_{3-4}	1.500		η_M	0.960	$J_{3, 2-3}$	0.350	$\tau_T \cos(30)$	39.693
P	16.0	GR_{1-2}	-1.667		RPM_M	3038	$J_{3, 3-4}$	0.330		
ϕ	20.0	GR_{2-3}	-0.600		RPM_{GM}	303.800	$J_{4, 3-4}$	0.310		
r_{wheel}	3.0	GR_{3-4}	-1.000		K_o	1.250	I_{1-2}	0.095		
		b_{min}	0.500		K_v	0.900	I_{2-3}	0.090		
		b_{min}	0.563		K_s	1.000	I_{3-4}	0.080		
		b_{max}	0.875		K_m	1.200	C_p	2300.000		



Determine pitch diameters and number of teeth.														
N ₁	N ₂	N ₃	N ₄		r ₁	r ₂	r ₃	r ₄		d ₁	d ₂	d ₃	d ₄	
24.000	40.000	24.000	24.000		0.750	1.250	0.750	0.75		1.500	2.500	1.500	1.500	
Check for interference. If A > a, then interference will not occur. 'a' is addendum for standard full-depth gear.														
r _{b1}	r _{b2}	r _{b3}	r _{b4}					a		A1 ₍₁₋₂₎	A2 ₍₁₋₂₎			
0.705	1.175	0.705	0.705					0.063		0.232	0.109			
r _{amax, 1 (1-2)}	r _{amax, 2 (1-2)}	r _{amax, 2 (2-3)}	r _{amax, 3 (2-3)}	r _{amax, 3 (3-4)}	r _{amax, 4 (3-4)}					A2 ₍₂₋₃₎	A3 ₍₂₋₃₎			
0.982	1.359	1.359	0.982	0.872	0.872					0.109	0.232			
P _b	r _{a1}	r _{b1}	r _{a2}	r _{b2}	r _{a3}	r _{b3}	r _{a4}	r _{b4}		CR ₁₋₂	CR ₂₋₃	CR ₃₋₄		
0.185	0.813	0.705	1.313	1.175	0.813	0.705	0.813	0.705		1.658	1.658	1.602		
Calculate contact ratio to check for smoothness of operation. CR > 1 is acceptable. CR > 1.6 is recommended.														
V	F _t	F _r	τ ₁	τ ₂	τ ₃	τ ₄	R _f		τ		τ _T	τ _{T cos(30)}		
119.302	240.000	87.353	15.000	-25.000	15.000	-15.000	255.403		15.000		45.833	39.693		

Gear Tooth Contact and Bending Stress *S _t < S _{at} and S _c < S _{ac} for satisfactory design													
Simplified Formulas:				Formulas with Constants:									
S _{t, 1}	S _{t, 2, 1-2}	S _{t, 2, 2-3}	S _{t, 3, 2-3}	S _{t, 3, 3-4}	S _{t, 4}	S _{at}	S _{c, 1}	S _{c, 2, 1-2}	S _{c, 2, 2-3}	S _{t, 3, 2-3}	S _{t, 3, 3-4}	S _{t, 4}	S _{ac}
21,943	19,692	19,692	21,943	23,273	24,774	5,000-75,000	133,488	103,399	106,351	137,298	145,465	145,465	30,000 - 255,000
S _{t, 1}	S _{t, 2, 1-2}	S _{t, 2, 2-3}	S _{t, 3, 2-3}	S _{t, 3, 3-4}	S _{t, 4}	S _{at}	S _{c, 1}	S _{c, 2, 1-2}	S _{c, 2, 2-3}	S _{t, 3, 2-3}	S _{t, 3, 3-4}	S _{t, 4}	S _{ac}
29,623	26,585	26,585	29,623	31,418	33,445	5,000-75,000	155,099	120,139	159,526	159,526	169,015	169,015	30,000 - 255,000

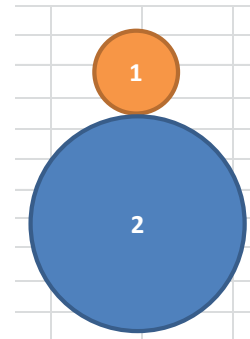
GEAR SPREADSHEET: TUMBLING MODE (MAXIMUM POWER AND TORQUE)								
General Parameters								
INPUT - SIZING			INPUT - FORCE ANALYSIS					
c_{TOTAL}	2.000		$c_{\text{TOTAL,NEW}}$	2.000		m	200.000	$J_{1, 1-2}$
GR_{TOTAL}	1.8		$c_{1-2, \text{NEW}}$	2.000		RPM_M	182	$J_{2, 1-2}$
P	14.0		$GR_{1-2, \text{NEW}}$	-1.800		K_o	1.250	I_{1-2}
ϕ	20.0		b_{\min}	0.750		K_v	0.950	C_p
r_{wheel}	3.0		b_{\max}	1.000		K_s	1.000	τ
			c_{1-2}	2.000		K_m	1.200	\dot{W}
			GR_{1-2}	-1.800				τ_T
								$\tau_{T \cos(30)}$
								39.693
Determine pitch diameters and number of teeth.								
r_1	r_2		d_1	d_2		N_1	N_2	
0.714	1.286		1.429	2.571		20.000	36.000	
Rounded:								
r_1	r_2		d_1	d_2		N_1	N_2	
0.714	1.286		1.429	2.571		20.000	36.000	
Check for interference. If $A > a$, then interference will not occur. 'a' is addendum for standard full-depth gear.								
r_{b1}	r_{b2}		$r_{\max, 1 (1-2)}$	$r_{\max, 2 (1-2)}$		a	$A1_{(1-2)}$	$A2_{(1-2)}$
0.671	1.208		0.958	1.388		0.071	0.244	0.103
0.671	1.208		0.958	1.388		0.071	0.244	0.103
Calculate contact ratio to check for smoothness of operation. CR > 1 is acceptable. CR > 1.6 is recommended.								
p_b	r_{a1}	r_{b1}	r_{a2}	r_{b2}			CR_{1-2}	
0.211	0.786	0.671	1.357	1.208			1.625	
0.211	0.786	0.671	1.357	1.208			1.625	
Gear Force and Torque Analysis *NOTE: All subsequent analysis is based off of rounded values of gear sizing (bold)								
V	F_t	F_r	τ_1	τ_2	R_f		τ	τ_T
68.173	420.000	152.867	-25.000	45.000	446.955		-25.000	45.833
								39.693
Gear Tooth Contact and Bending Stress * $S_t < S_{at}$ and $S_c < S_{ac}$ for satisfactory design								
Simplified Formulas:								
$S_{t, 1}$	$S_{t, 2, 1-2}$	S_{at}				$S_{c, 1}$	$S_{c, 2, 1-2}$	S_{ac}
24,500	20,632	5,000-75,000				147,744	110,122	30,000 - 255,000
Formulas with Constants:								
$S_{t, 1}$	$S_{t, 2, 1-2}$	S_{at}				$S_{c, 1}$	$S_{c, 2, 1-2}$	S_{ac}
34,913	29,400	5,000-75,000				176,367	131,456	30,000 - 255,000

GEAR SPREADSHEET: TUMBLING MODE (MAXIMUM POWER AND TORQUE)							
General Parameters							
INPUT - SIZING		INPUT - FORCE ANALYSIS					
c_{TOTAL}	2.000	$c_{TOTAL, NEW}$	2.000	m	200.000	$J_{1, 1-2}$	0.320
GR_{TOTAL}	1.8	$c_{1-2, NEW}$	2.000	RPM_M	182	$J_{2, 1-2}$	0.380
P	14.0	$GR_{1-2, NEW}$	-1.800	K_o	1.250	I_{1-2}	0.095
ϕ	20.0	b_{min}	0.750	K_v	0.950	C_p	2300.000
r_{wheel}	3.0	b_{max}	1.000	K_s	1.000	τ	-25.000
		c_{1-2}	2.000	K_m	1.200	\dot{W}	0.868
		GR_{1-2}	-1.800			τ_T	45.833
						$\tau_T \cos(30)$	39.693

Determine pitch diameters and number of teeth.							
r_1	r_2	d_1	d_2	N_1	N_2		
0.714	1.286	1.429	2.571	20.000	36.000		
Rounded:							
r_1	r_2	d_1	d_2	N_1	N_2		
0.714	1.286	1.429	2.571	20.000	36.000		

Check for interference. If $A > a$, then interference will not occur. 'a' is addendum for standard full-depth gear.							
r_{b1}	r_{b2}	$r_{amax, 1 (1-2)}$	$r_{amax, 2 (1-2)}$	a	$A1_{(1-2)}$	$A2_{(1-2)}$	
0.671	1.208	0.958	1.388	0.071	0.244	0.103	
0.671	1.208	0.958	1.388	0.071	0.244	0.103	

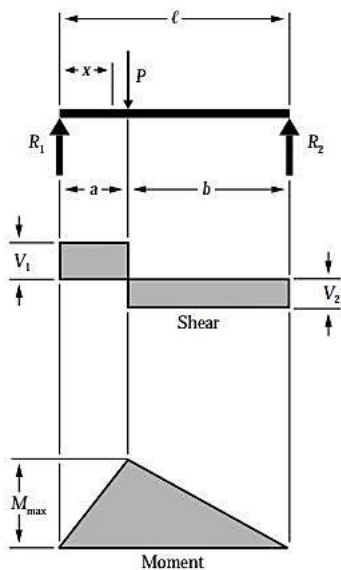
Calculate contact ratio to check for smoothness of operation. CR > 1 is acceptable. CR > 1.6 is recommended.								
p_b	r_{a1}	r_{b1}	r_{a2}	r_{b2}			CR₁₋₂	
0.211	0.786	0.671	1.357	1.208			1.625	
0.211	0.786	0.671	1.357	1.208			1.625	
Gear Force and Torque Analysis *NOTE: All subsequent analysis is based off of rounded values of gear sizing (bold)								
V	F_t	F_r	τ₁	τ₂	R_f		τ	τ_T
68.173	420.000	152.867	-25.000	45.000	446.955		-25.000	45.833
								39.693
Gear Tooth Contact and Bending Stress *S _t < S _{at} and S _c <S _{ac} for satisfactory design								
Simplified Formulas:								
S _{t, 1}	S _{t, 2, 1-2}	S _{at}				S _{c, 1}	S _{c, 2, 1-2}	S _{ac}
24,500	20,632	5,000-75,000				147,744	110,122	30,000 - 255,000
Formulas with Constants:								
S _{t, 1}	S _{t, 2, 1-2}	S _{at}				S _{c, 1}	S _{c, 2, 1-2}	S _{ac}
34,913	29,400	5,000-75,000				176,367	131,456	30,000 - 255,000



APPENDIX D: SHEAR AND MOMENT FORMULAS

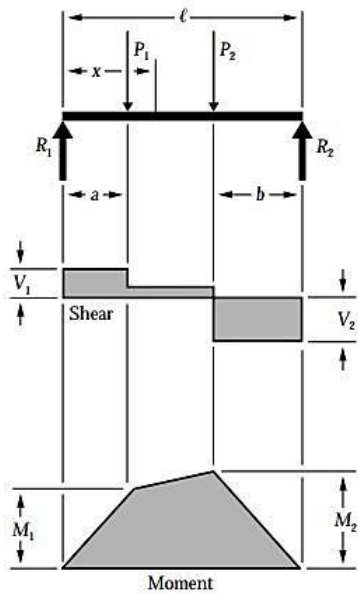
The following shear and moment formulas are utilized in the computation of the minimum diameter required to withstand the given shaft loading described in Chapter 5. This information is taken from The American Wood Council's ANSI/AF&PA NDS-2005 standard [43]. These formulas provided guidance for quick computations of the shear stresses and bending moments present in each of the Tri-Wheel's shafts. However in some instances, these equations were modified, and the techniques of making cuts in the beam and evaluating the forces and moments about that cut were also employed.

1. Simple Beam – Concentrated Load at Any Point



$$\begin{aligned}
 R_1 &= V_1 \text{ (max when } a < b) & = \frac{Pb}{\ell} \\
 R_2 &= V_2 \text{ (max when } a > b) & = \frac{Pa}{\ell} \\
 M_{\max} \text{ (at point of load)} & & = \frac{Pab}{\ell} \\
 M_x \text{ (when } x < a) & & = \frac{Pbx}{\ell} \\
 \Delta_{\max} \left(\text{at } x = \sqrt{\frac{a(a+2b)}{3}} \text{ when } a > b \right) & & = \frac{Pab(a+2b)\sqrt{3a(a+2b)}}{27EI\ell} \\
 \Delta_a \text{ (at point of load)} & & = \frac{Pa^2b^2}{3EI\ell} \\
 \Delta_x \text{ (when } x < a) & & = \frac{Pbx}{6EI\ell}(\ell^2 - b^2 - x^2) \\
 \Delta_x \text{ (when } x > a) & & = \frac{Pa(\ell-x)}{6EI\ell}(2\ell x - x^2 - a^2)
 \end{aligned}$$

2. Simple Beam – Two Unequal Concentrated Loads Unsymmetrically Placed



$$R_1 = V_1 \dots \dots \dots \dots \dots = \frac{P_1(\ell - a) + P_2 b}{\ell}$$

$$R_2 = V_2 \dots \dots \dots \dots \dots = \frac{P_1 a + P_2 (\ell - b)}{\ell}$$

$$V_x \left(\text{when } x > a \text{ and } x < (\ell - b) \right) \dots = R_1 - P_1$$

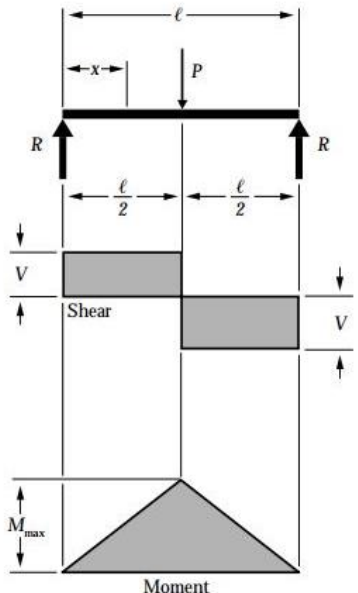
$$M_1 \left(\text{max when } R_1 < P_1 \right) \dots \dots \dots = R_1 a$$

$$M_2 \left(\text{max when } R_2 < P_2 \right) \dots \dots \dots = R_2 b$$

$$M_x \left(\text{when } x < a \right) \dots \dots \dots = R_1 x$$

$$M_x \left(\text{when } x > a \text{ and } x < (\ell - b) \right) \dots = R_1 x - P_1(x - a)$$

3. Simple Beam – Concentrated Load at Center



$$R = V \dots \dots \dots \dots \dots = \frac{P}{2}$$

$$M_{\max} \left(\text{at point of load} \right) \dots \dots \dots = \frac{P\ell}{4}$$

$$M_x \left(\text{when } x < \frac{\ell}{2} \right) \dots \dots \dots = \frac{Px}{2}$$

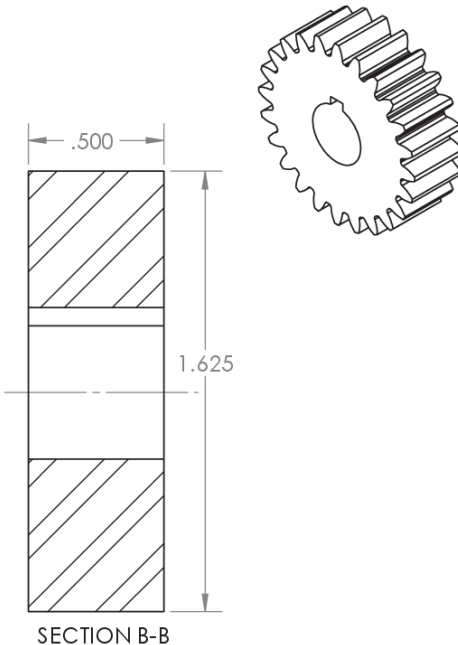
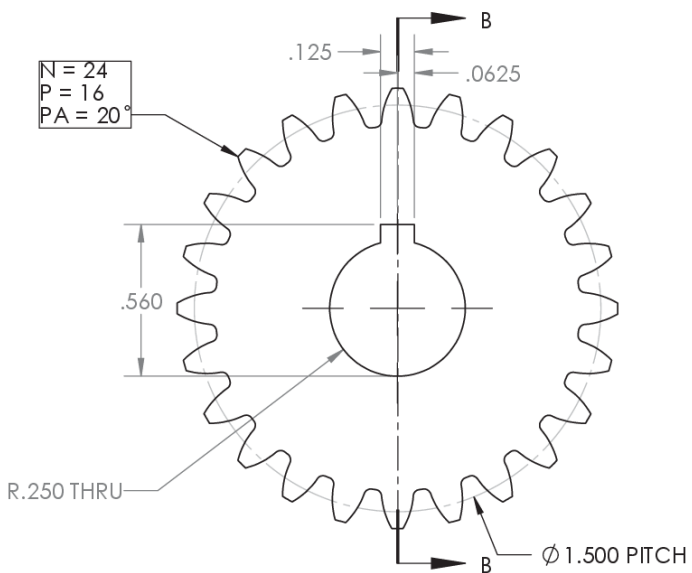
$$\Delta_{\max} \left(\text{at point of load} \right) \dots \dots \dots = \frac{P\ell^3}{48EI}$$

$$\Delta_x \left(\text{when } x < \frac{\ell}{2} \right) \dots \dots \dots = \frac{Px}{48EI} (3\ell^2 - 4x^2)$$

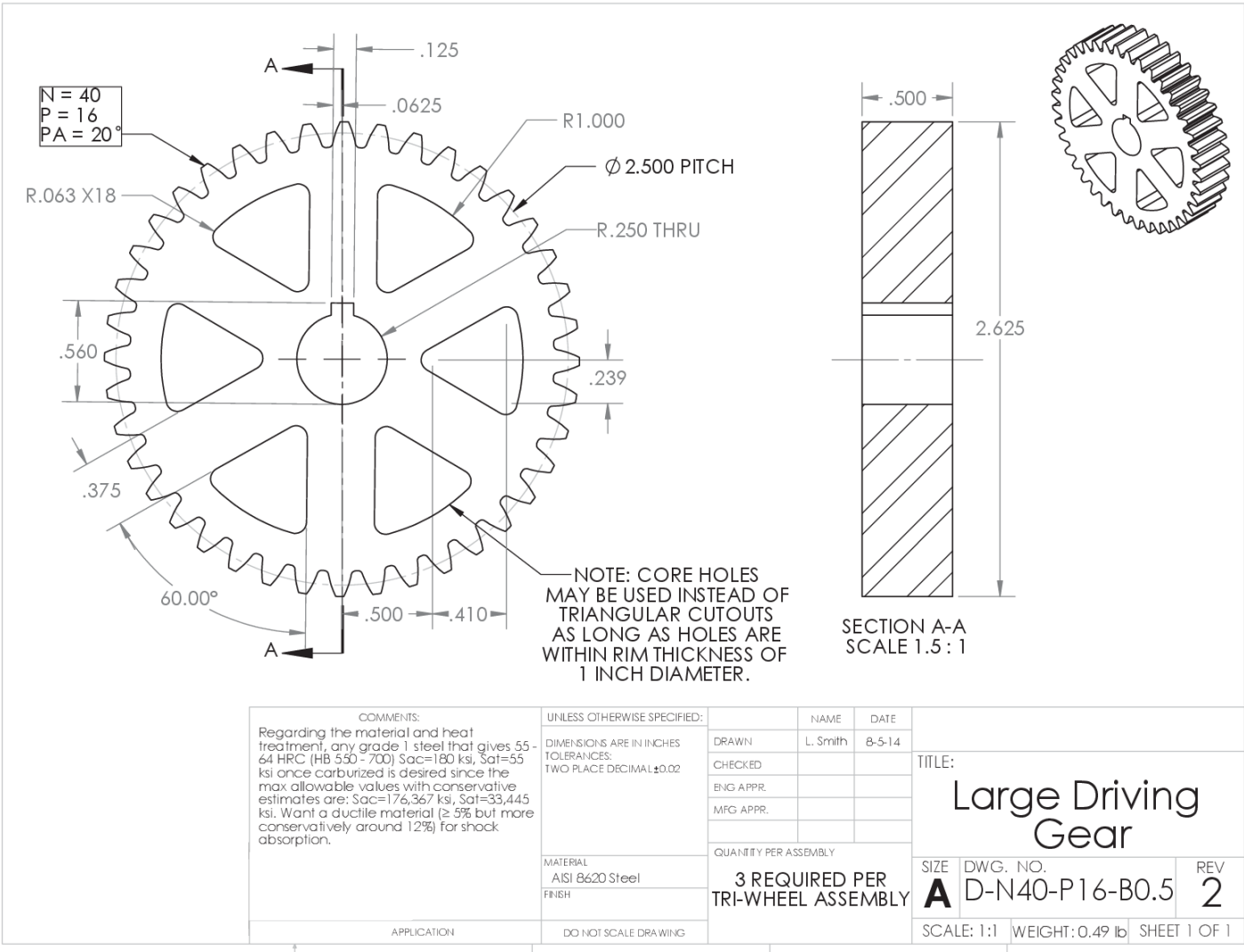
APPENDIX E: MACHINE DRAWINGS

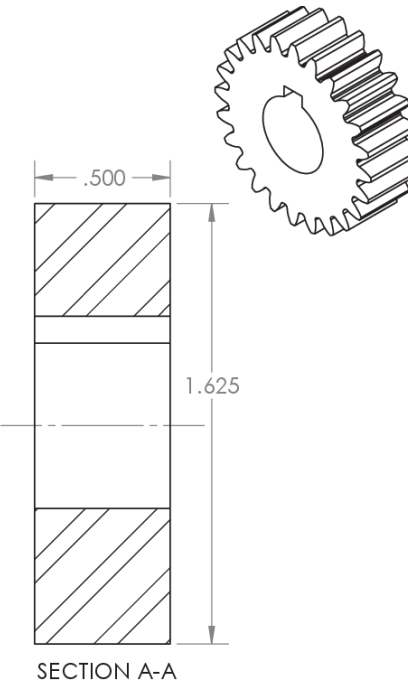
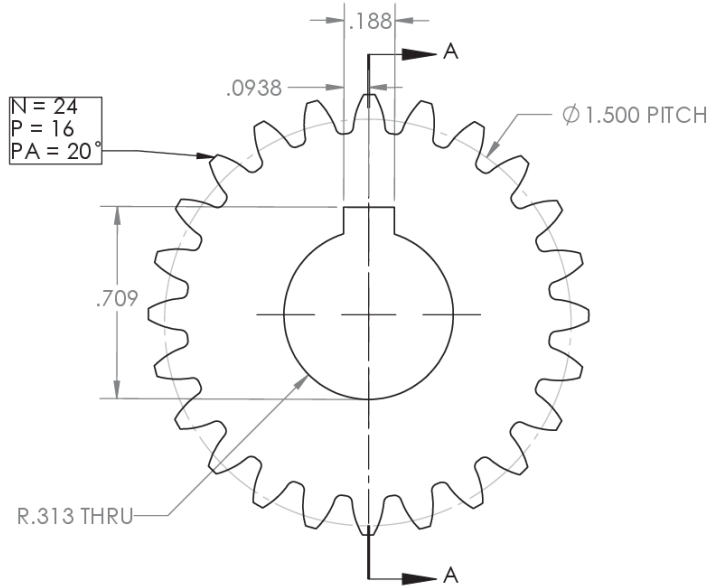
Each of the components in the Tri-Wheel that is not a purchased part has a corresponding machine drawing. These drawings were used by manufacturers to produce the gears, shafts, housing, and a few other miscellaneous components that have gone into the most recent Tri-Wheel prototype. Basic information regarding tolerances necessary to achieve certain press fits and slip fits are not included in the drawings. Instead, the type of fit required is specified. All of the bearings require press fits into the housing, and the gears are designed to be a slip fit on to the shaft. The drawings included in this appendix are listed in the following order:

- 1. Gears** – D1/D3, D2, D4, T1, T2
- 2. Shafts** – A, C, D1, D2
- 3. Housing Components** – Tumbling Carrier Plate, Driving Carrier Plate, Center Carrier Structure
- 4. Subassemblies** – A/B, C, D1, D2
- 5. Miscellaneous** – Wheel Flange



COMMENTS:		UNLESS OTHERWISE SPECIFIED:		NAME L. Smith	DATE 8-5-14	TITLE: Small Driving Gear Center & Idlers			
		DIMENSIONS ARE IN INCHES TOLERANCES: TWO PLACE DECIMAL ± 0.02							
		DRAWN	CHECKED						
		ENG APPR.	MFG APPR.						
		QUANTITY PER ASSEMBLY							
		4 REQUIRED PER TRI-WHEEL ASSEMBLY							
MATERIAL AISI 8620 Steel	SIZE A	DWG. NO. D-N24-P16-B0.5		REV 2					
FINISH	SCALE: 2:1	WEIGHT: 0.22 lb		SHEET 1 OF 1					
APPLICATION	DO NOT SCALE DRAWING								





SECTION A-A

COMMENTS:

Regarding the material and heat treatment, any grade 1 steel that gives 55-64 HRC (HB 550 - 700) Sac=180 ksi, Sat=55 ksi once carburized is desired since the max allowable values with conservative estimates are: Sac=176,367 ksi, Sat=33,445 ksi. Want a ductile material ($\geq 5\%$ but more conservatively around 12%) for shock absorption.

UNLESS OTHERWISE SPECIFIED:

DIMENSIONS ARE IN INCHES
TOLERANCES:
TWO PLACE DECIMAL ± 0.02

MATERIAL
AISI 6620 Steel
FINISH

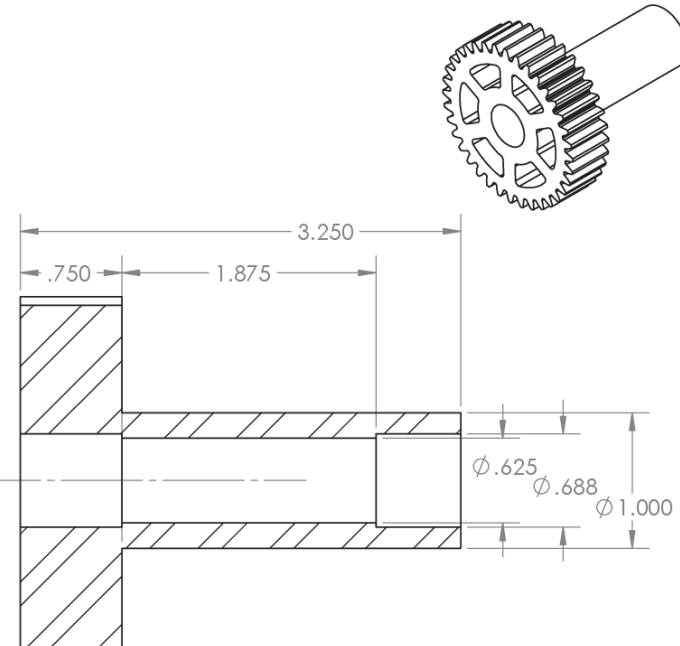
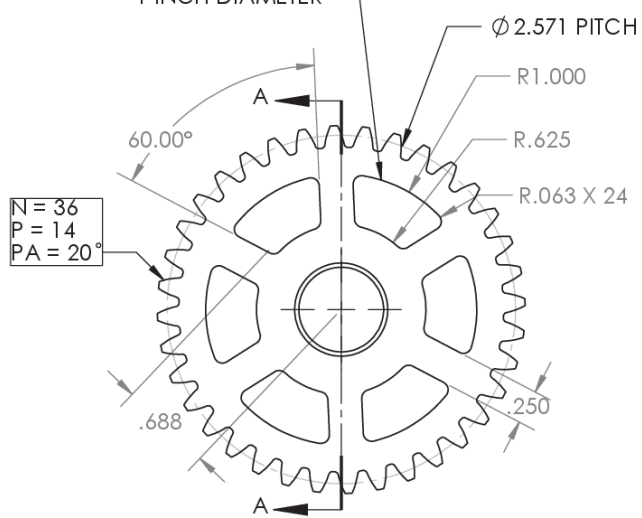
QUANTITY PER ASSEMBLY
3 REQUIRED PER
TRI-WHEEL ASSEMBLY

SIZE DWG. NO.
A D-N24-P16-B0.625 REV
2

SCALE: 2:1 WEIGHT: 0.20 lb SHEET 1 OF 1

TITLE: **Small Driving Gear - Wheel**

NOTE: CORE HOLES
MAY BE USED INSTEAD OF
TRIANGULAR CUTOUTS
AS LONG AS HOLES ARE
WITHIN RIM THICKNESSES OF
1 INCH DIAMETER



SECTION A-A
SCALE 1 : 1

COMMENTS:
Regarding the material and heat treatment,
any grade 1 steel that gives 55 - 64 HRC (HB
550 - 700) Sac=180 ksi, Sat=55 ksi once
carburized is desired since the max
allowable values with conservative estimates
are: Sac=176,367 ksi, Sat=33,445 ksi. Want a
ductile material ($\geq 5\%$ but more
conservatively around 12%) for shock
absorption.

UNLESS OTHERWISE SPECIFIED:
DIMENSIONS ARE IN INCHES
TOLERANCES:
TWO PLACE DECIMAL ± 0.02

MATERIAL
AISI 8620 Steel

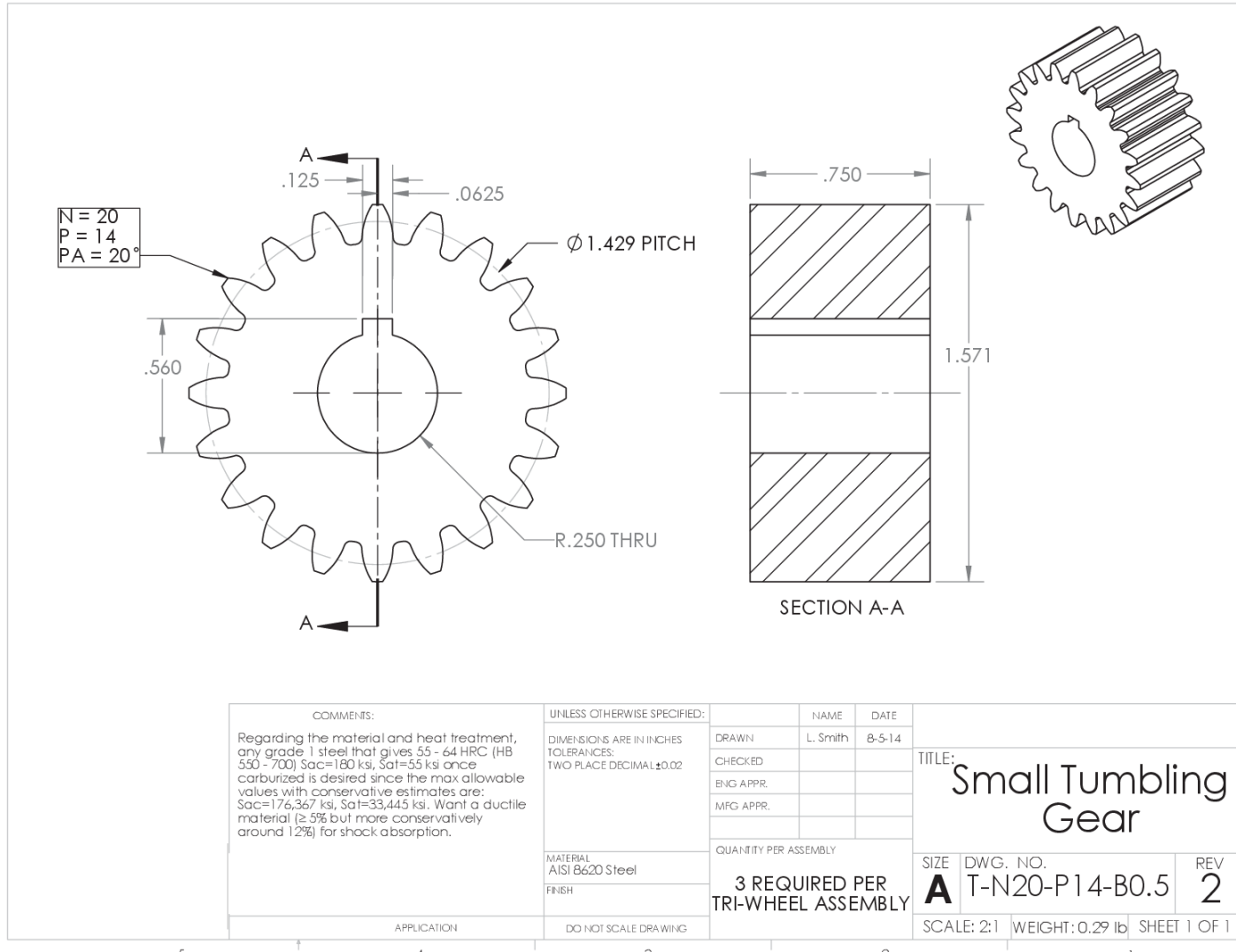
FINISH

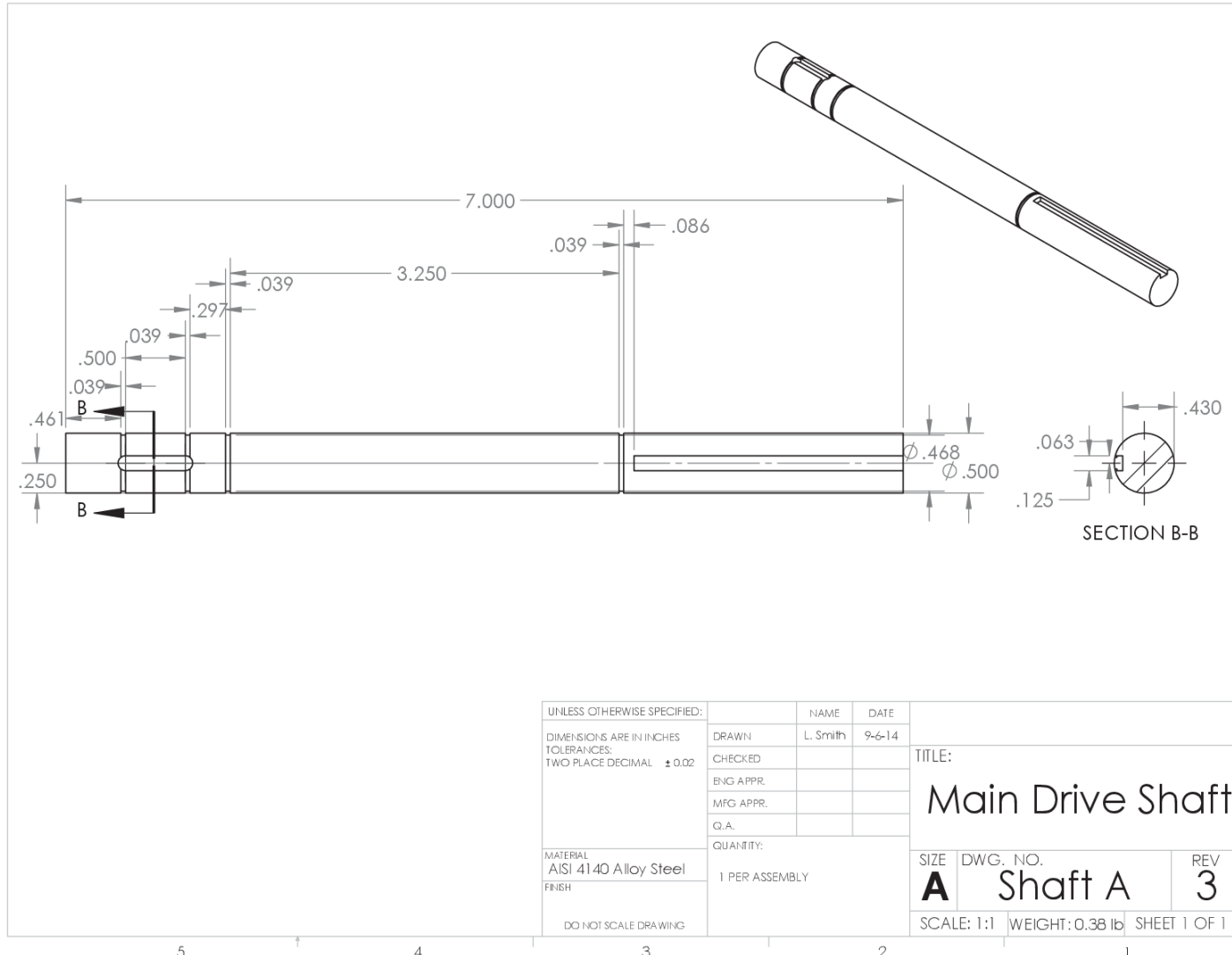
DO NOT SCALE DRAWING

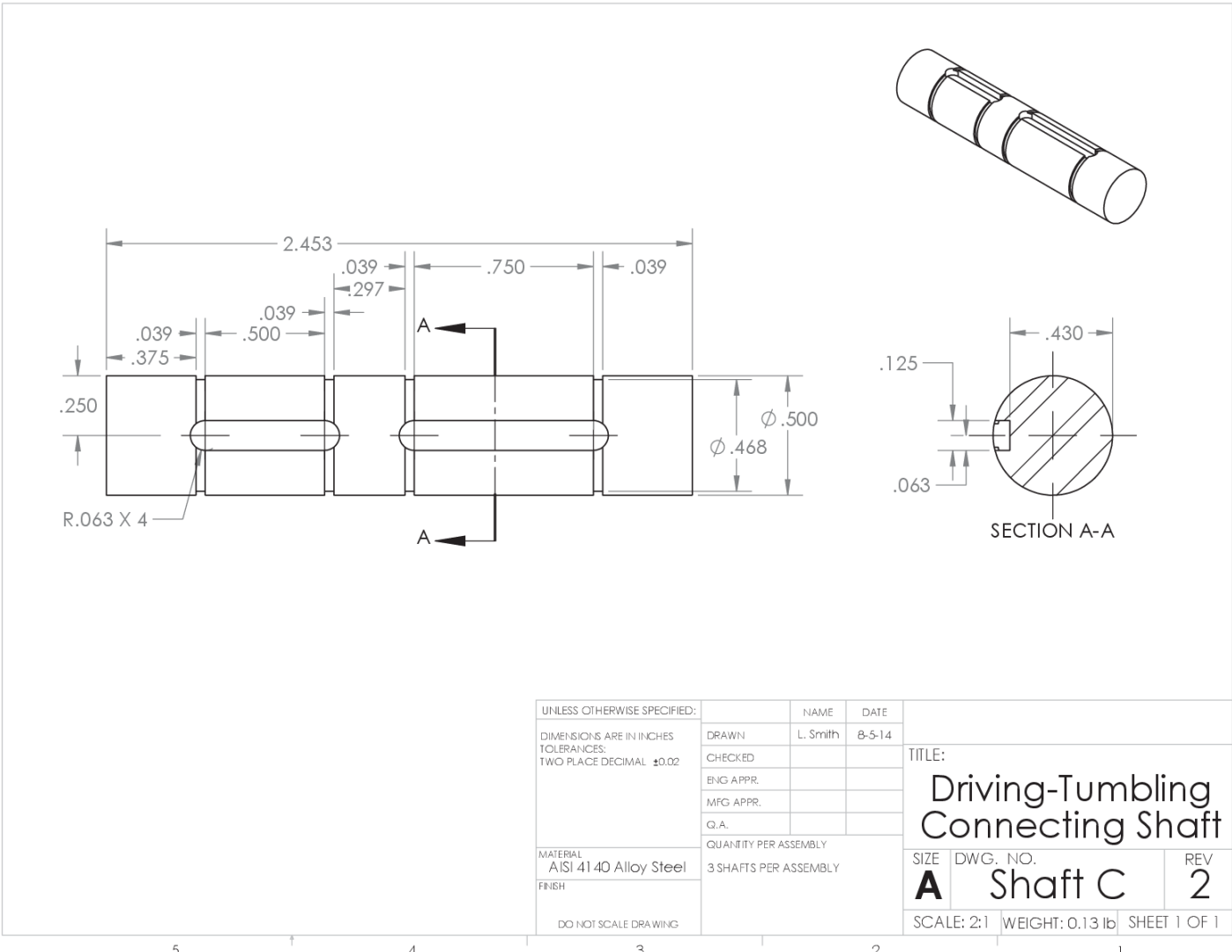
1 REQUIRED
PER ASSEMBLY

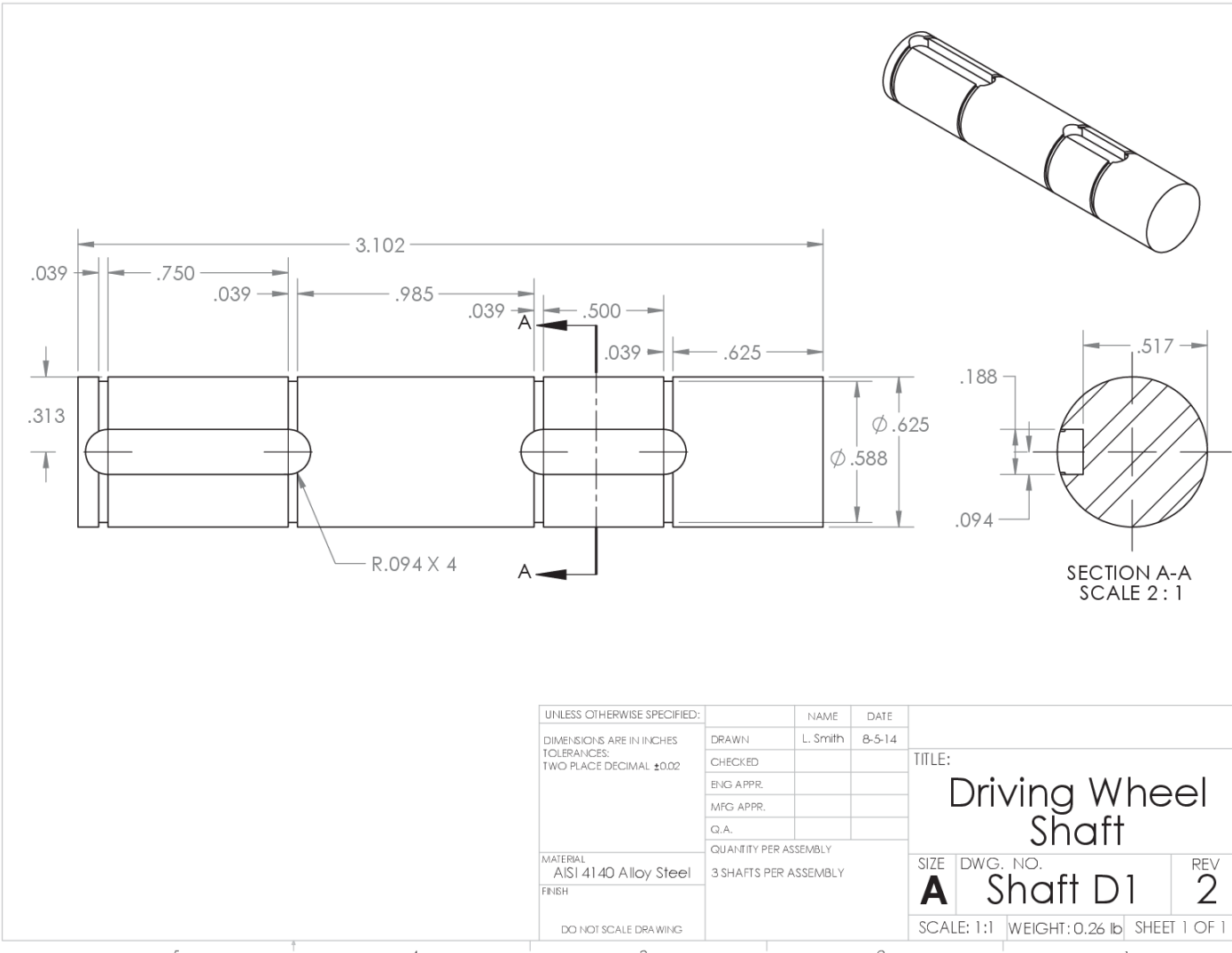
TITLE:
Center Tumbling
Gear

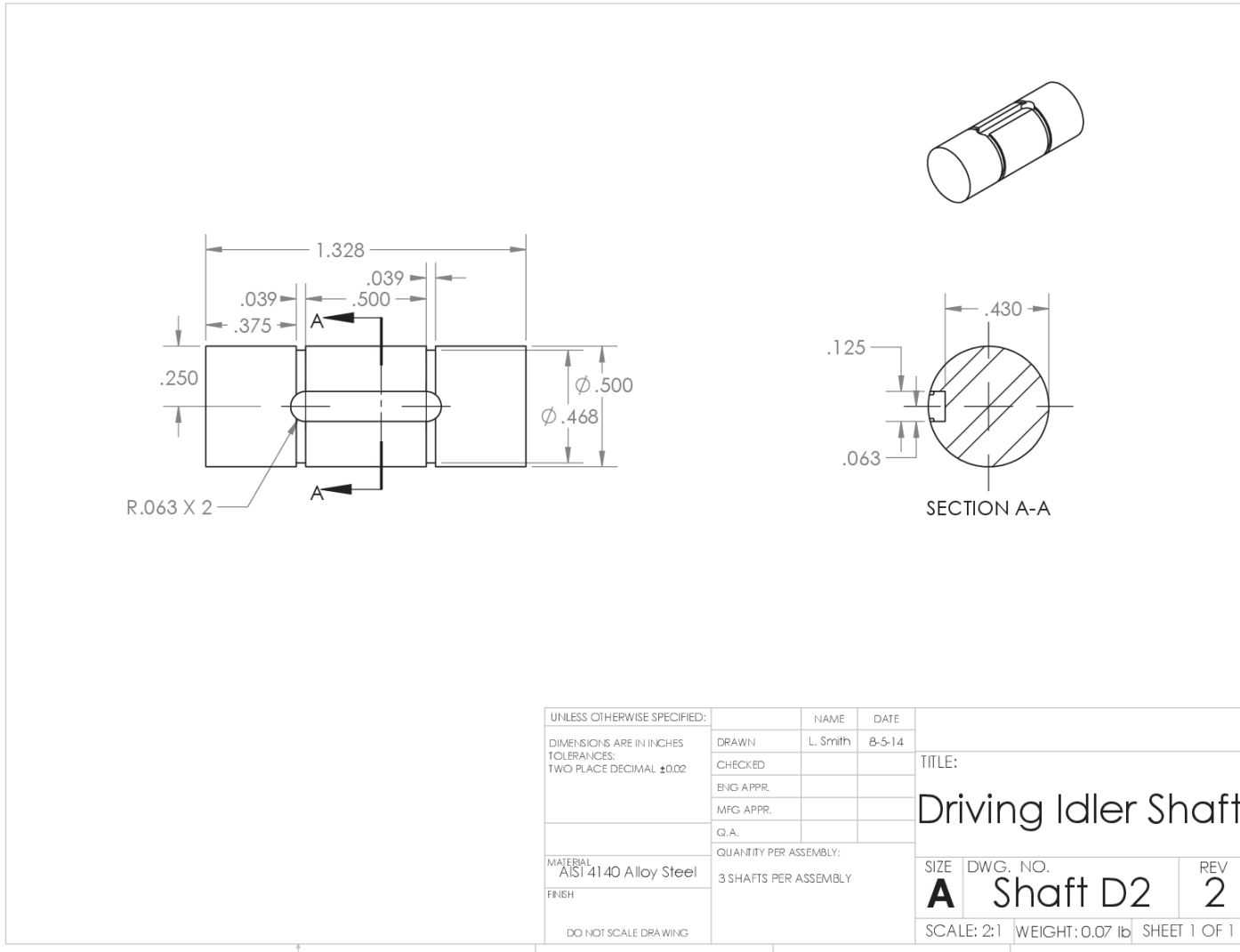
SIZE	DWG. NO.	REV
A	T-N36-P14	2
SCALE: 1:2	WEIGHT: 1.06 lb	SHEET 1 OF 1

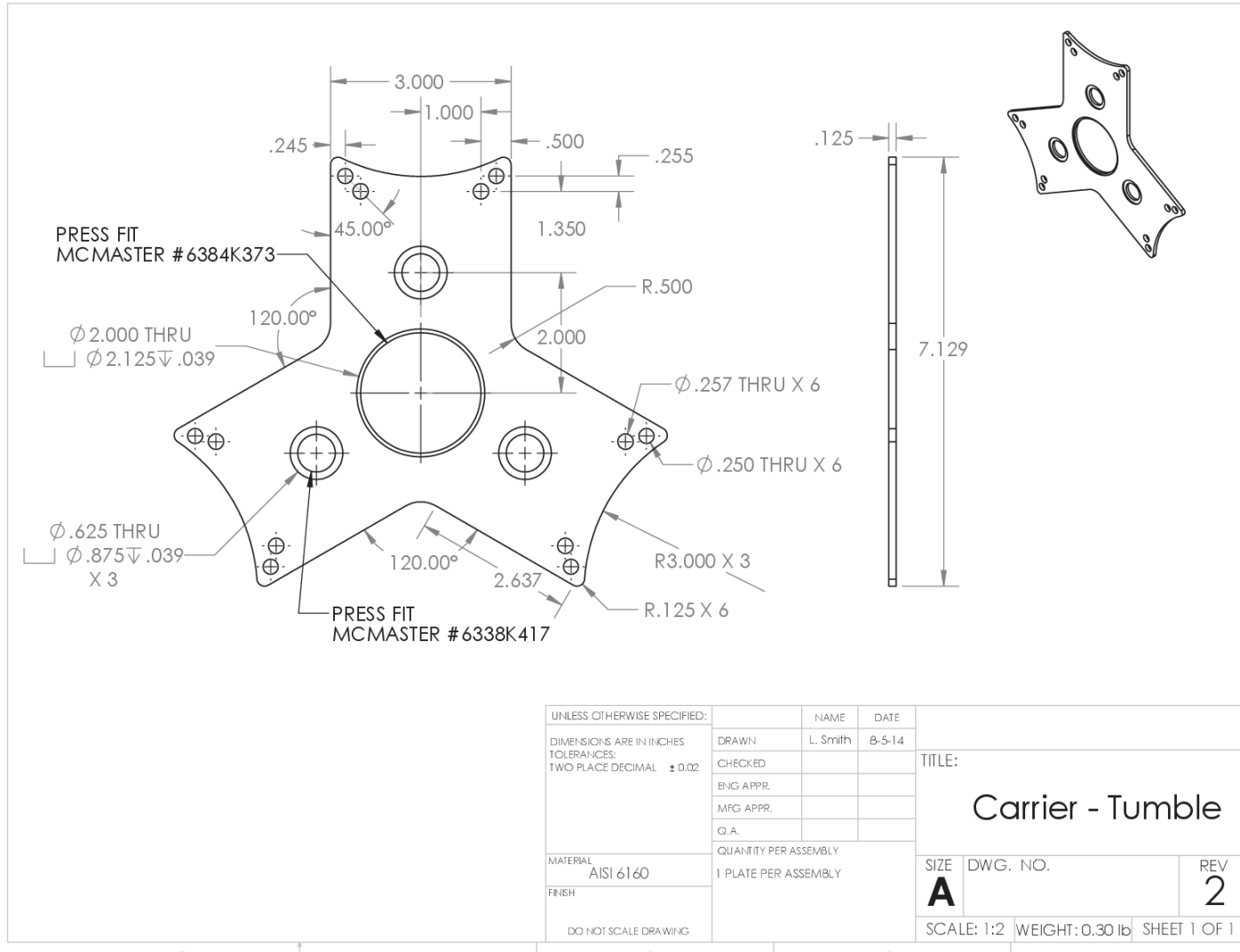


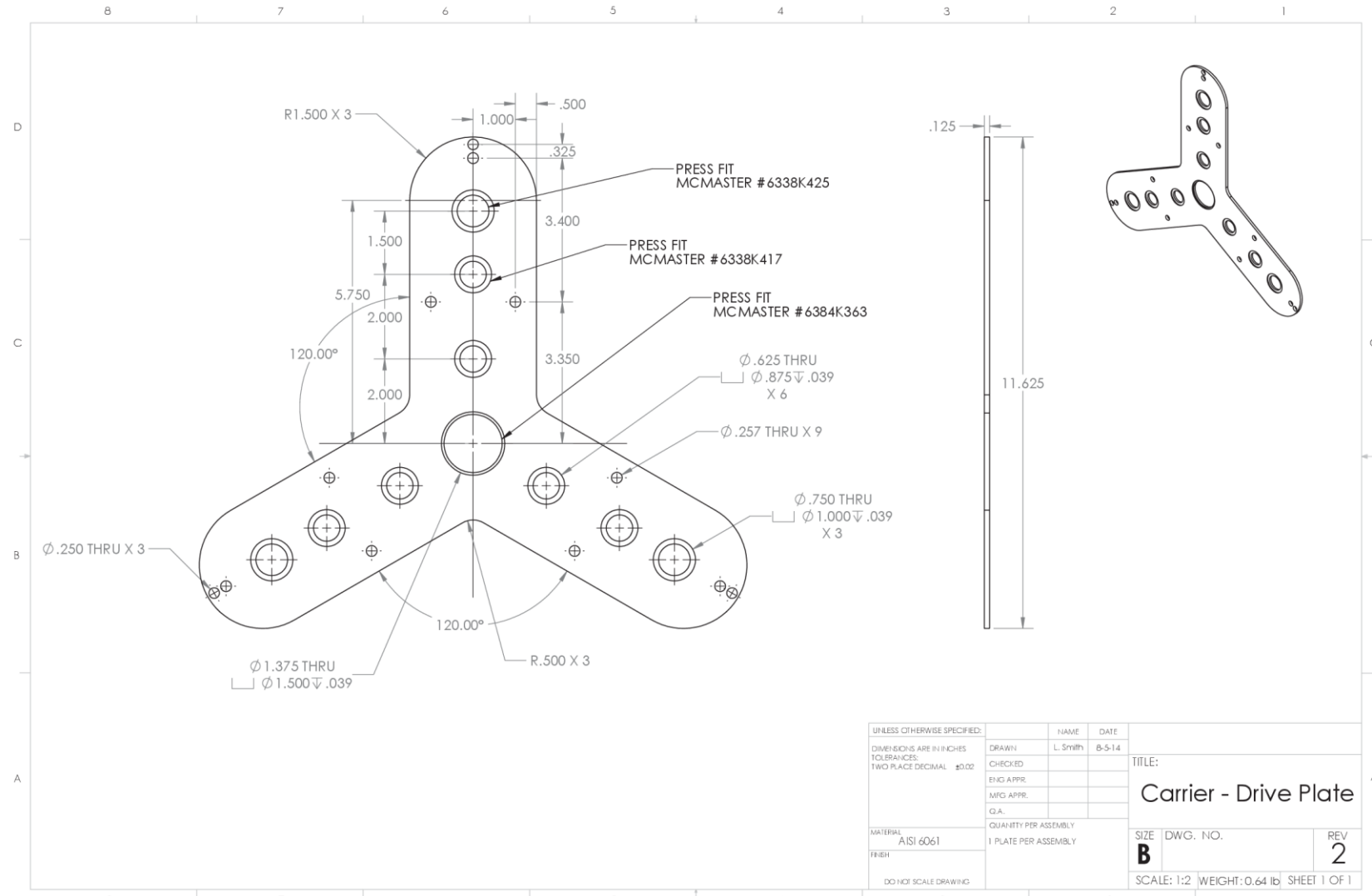


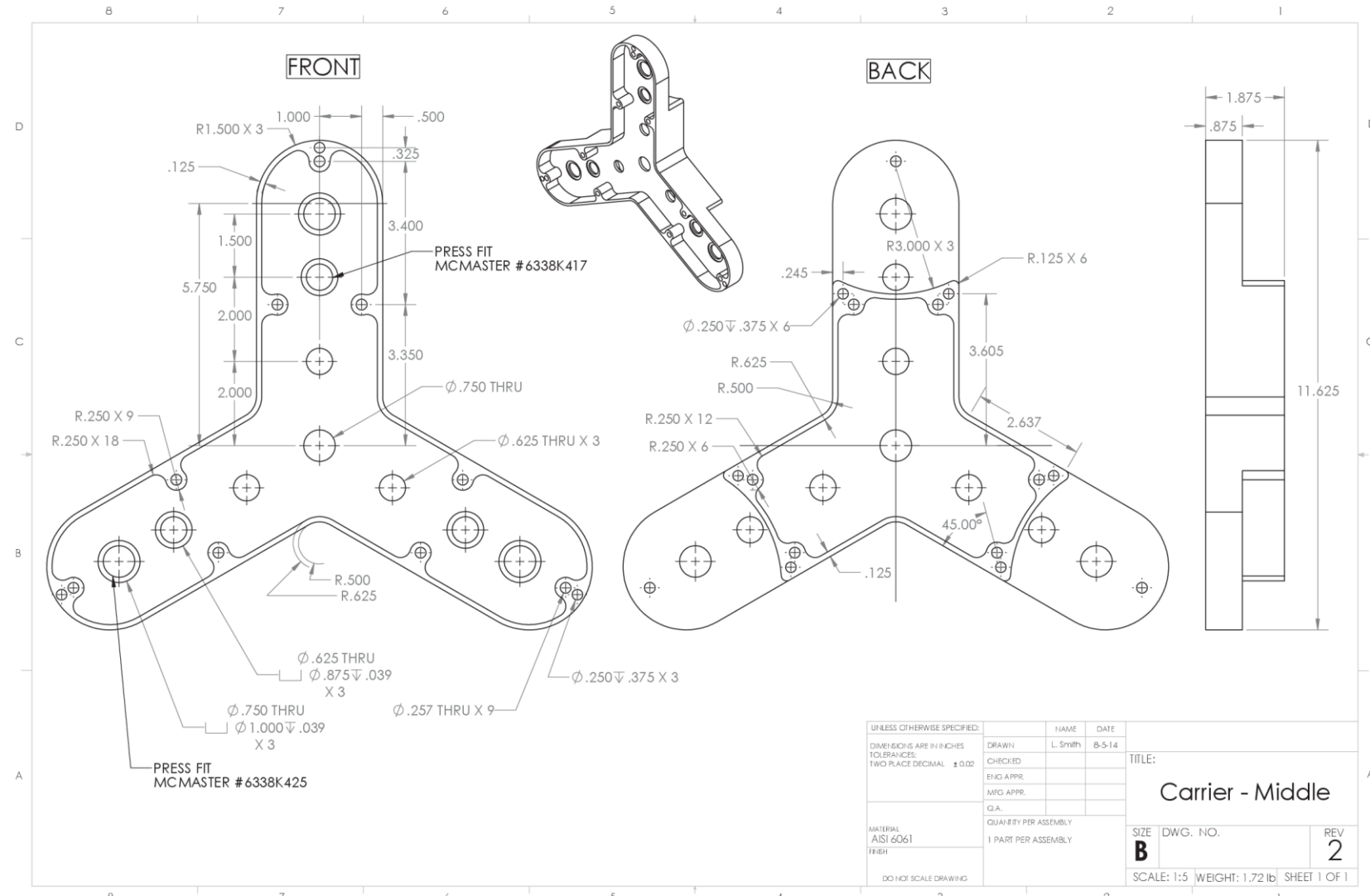


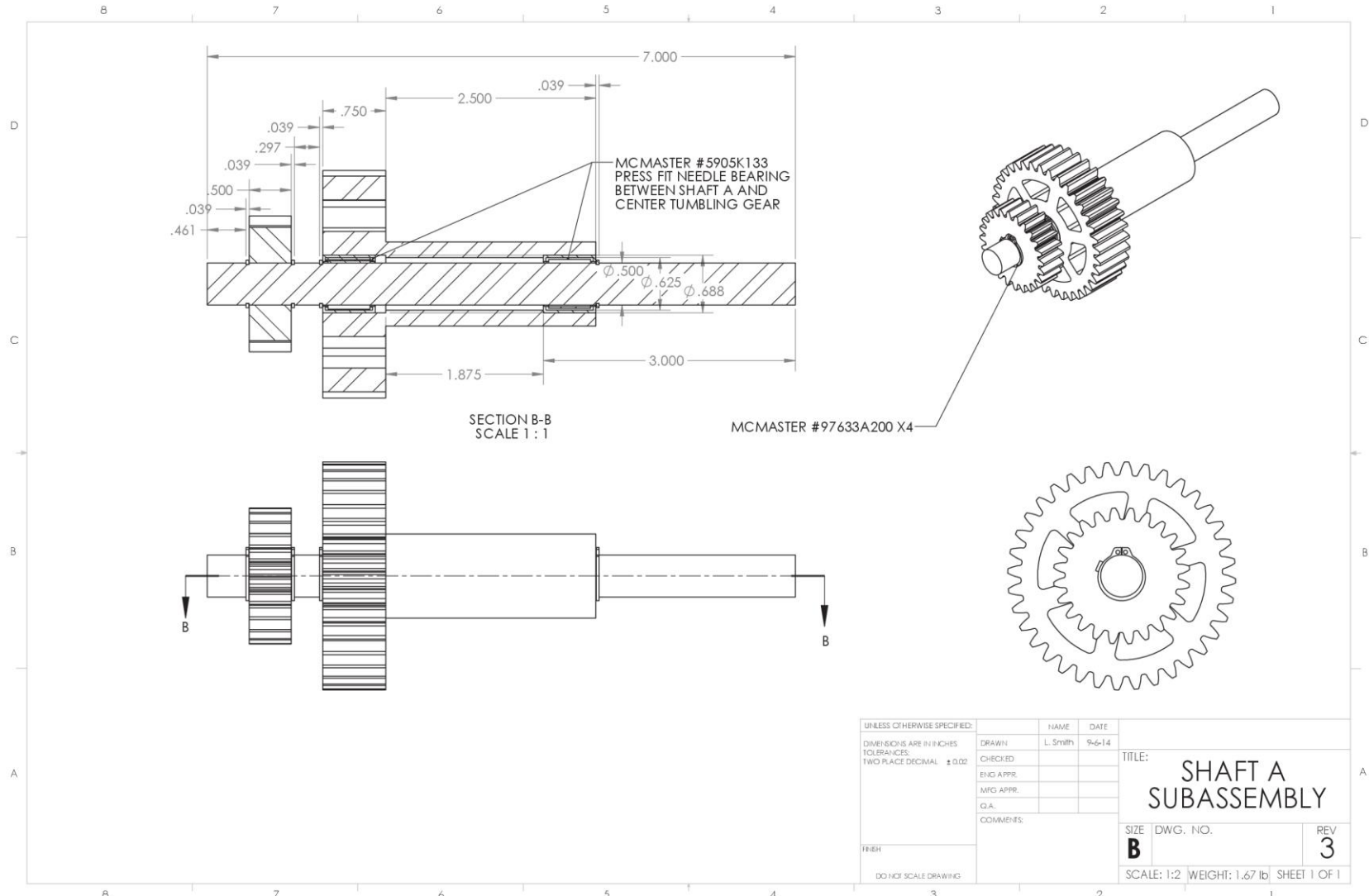


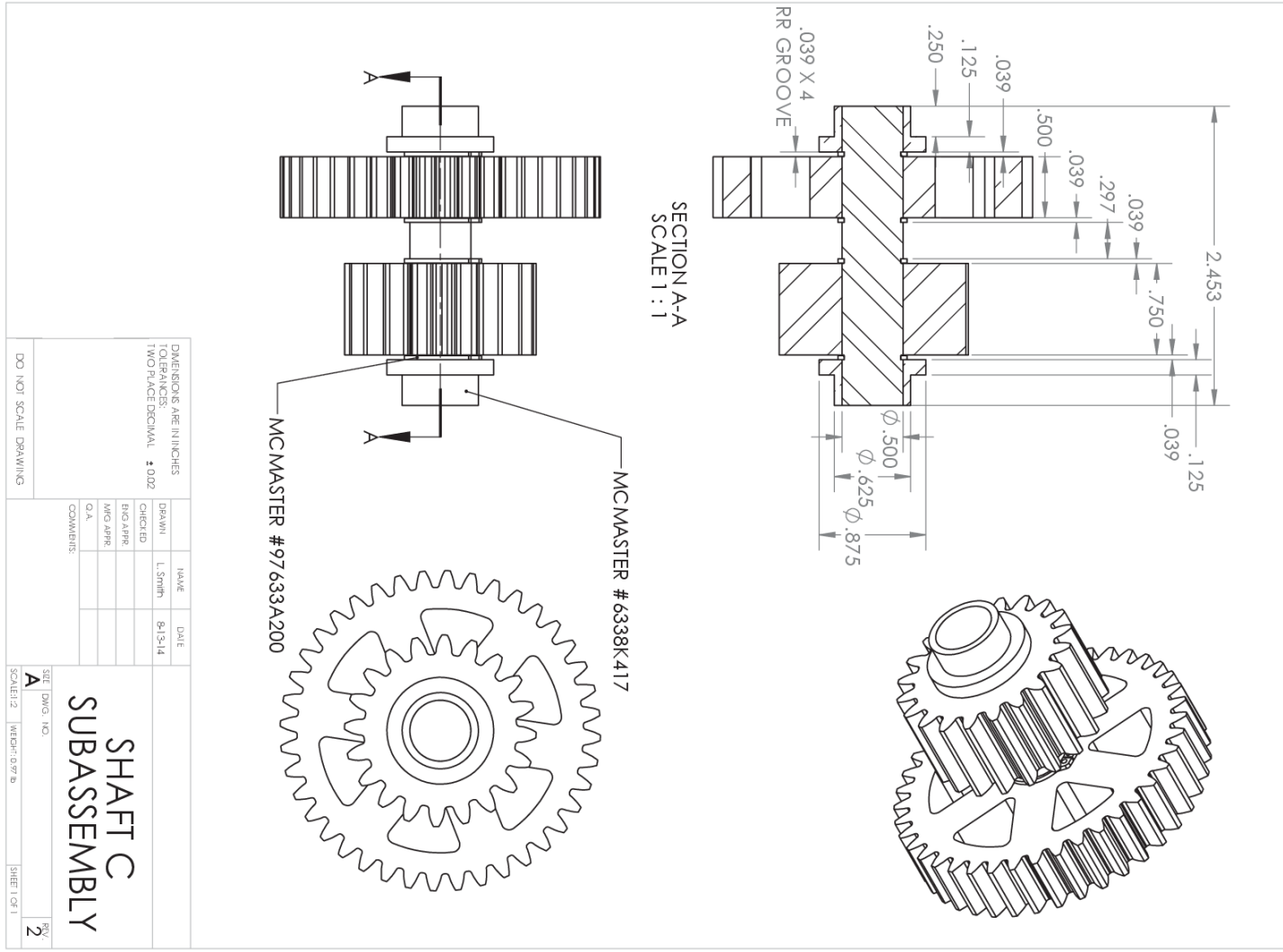


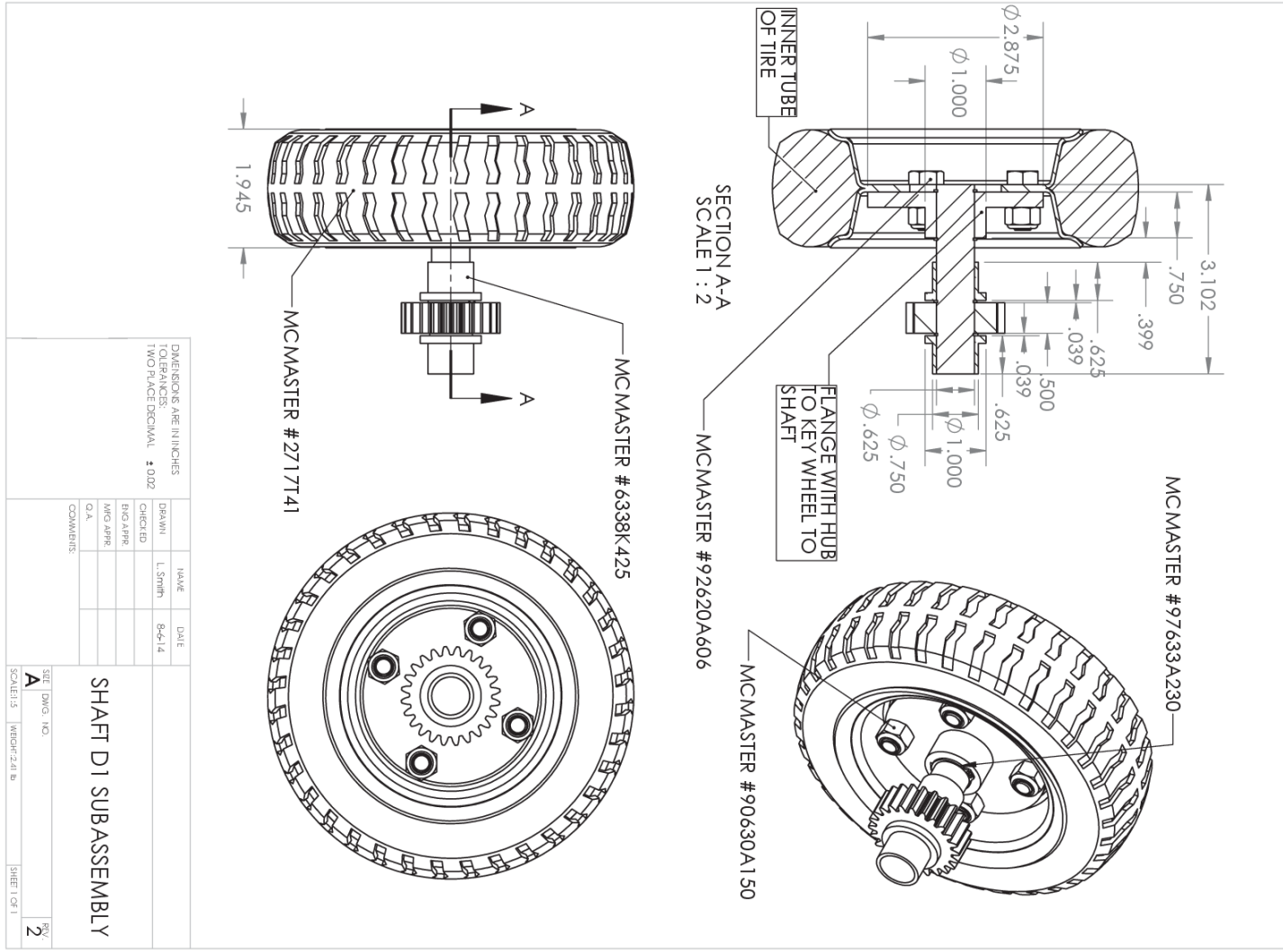


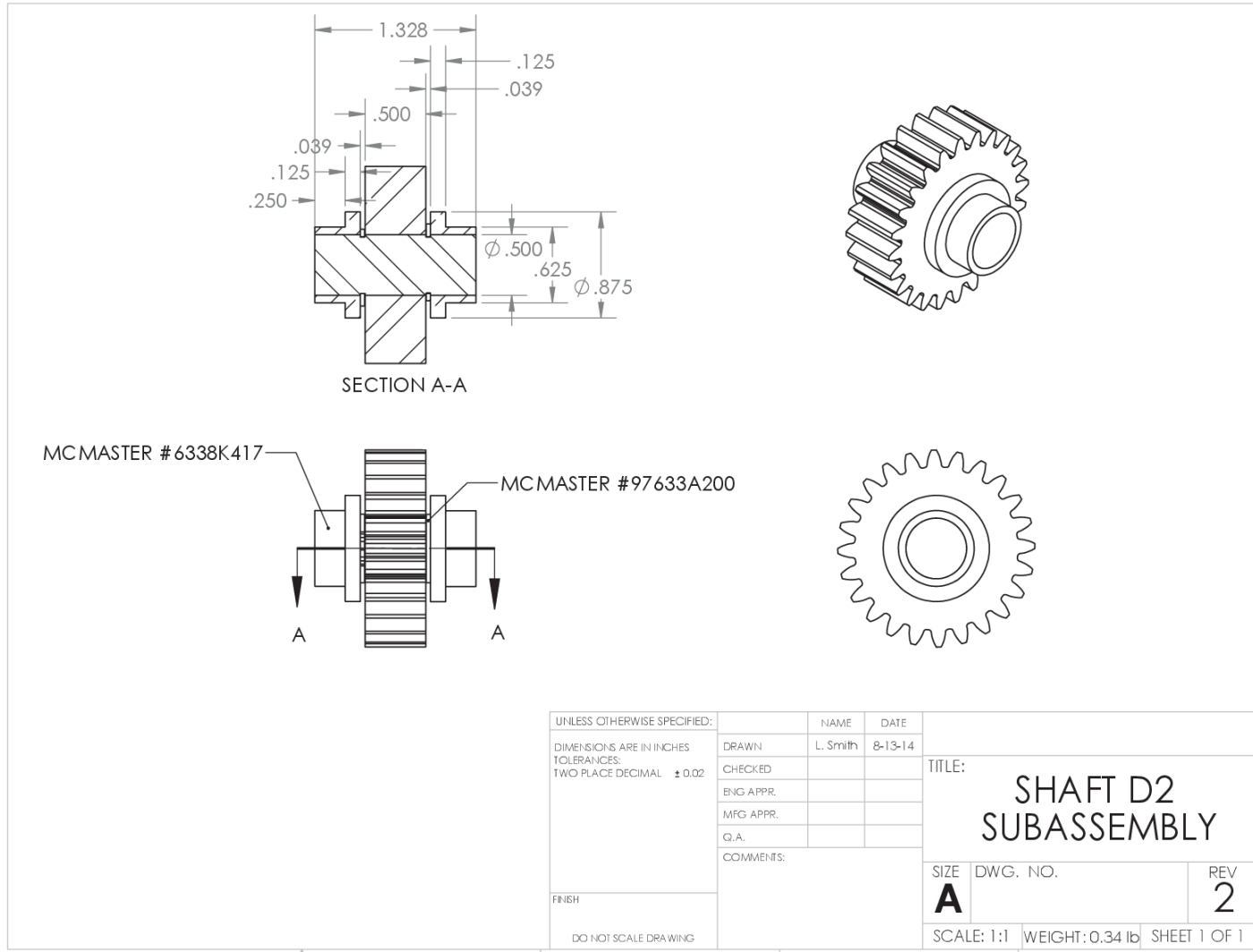


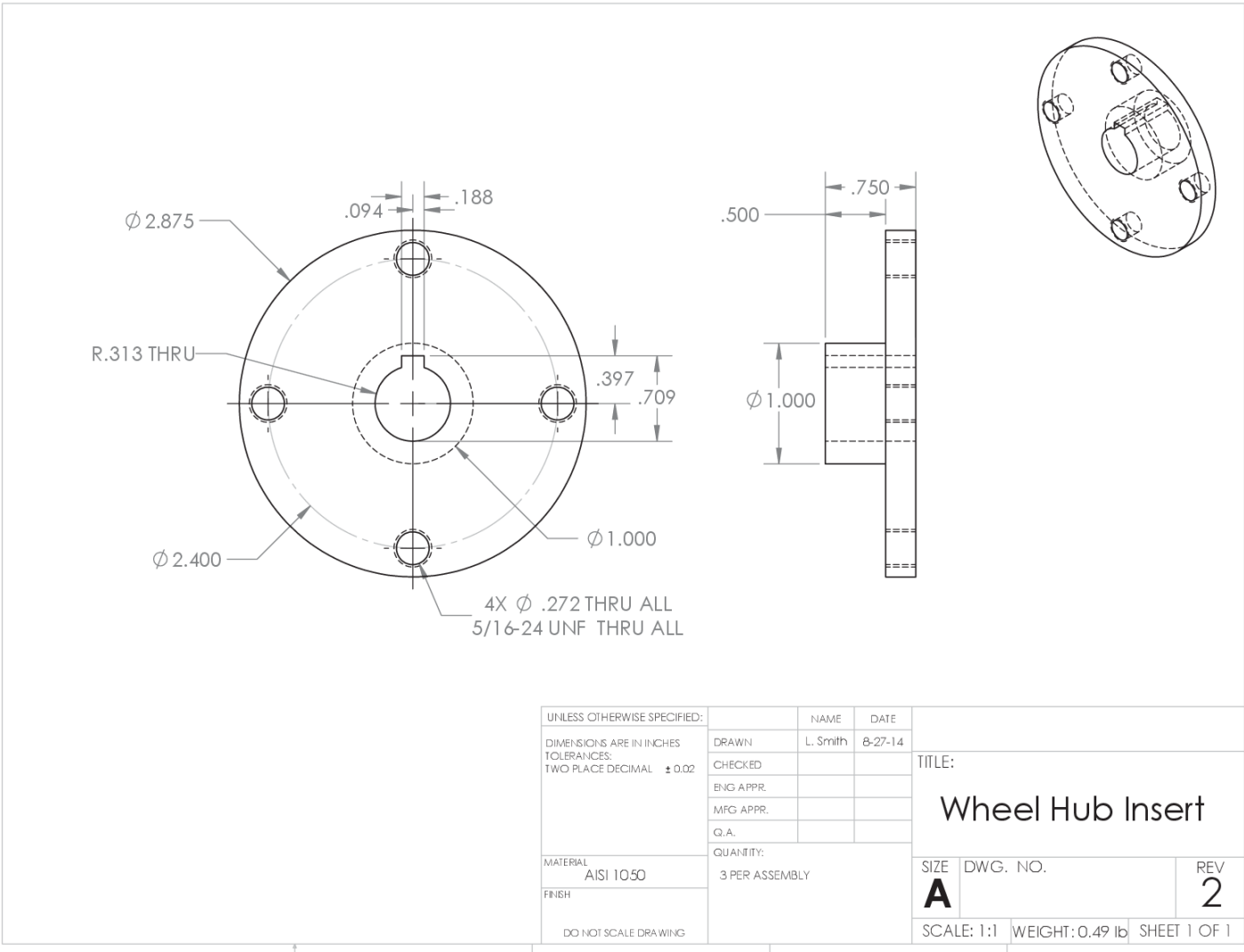












APPENDIX F: BILL OF MATERIALS

Component	Quantity	Cost/Unit	Total Cost	Part Number
Small Driving Gear - Center & Idlers	8	41	328	D-N24-P16-B0.5
Large Driving Gear - Connectors	6	100	600	D-N40-P16-B0.5
Small Driving Gear - Wheel	6	47	282	D-N24-P16-B0.625
Large Tumbling Gear - Center	2	268	536	T-N36-P14
Small Tumbling Gear - Connectors	6	55	330	T-N20-P14-B0.5
Shaft D1 - Wheels	6	115	690	R258-TGP
Shaft D2 - Idlers	6	83	498	
Shaft C - Connectors	6	115	690	R212-TGP
Shaft A - Drive Shaft	2	78	156	
Key - 0.5" Shaft	14	2.07/12"	2.07	98535A130
Key - 0.5" Shaft	6			
Key - 0.625" Shaft	6	2.77/12"	2.77	98535A140
Key - 0.625" Shaft	6			
Flanged Sleeve Bearing - 0.625" Shaft	12	1.28	15.36	6338K425
Flanged Sleeve Bearing - 0.5" Shaft	24	1.12	26.88	6338K417
Flanged Ball Bearing Drive Shaft	2	11.57	23.14	6384K363
Flanged Ball Bearing Tumble Shaft	2	19.9	39.8	6384K373
Steel Needle-Roller Bearings	4	10.88	43.52	5905K133
Housing - Carrier Middle	2	689	1378	
Housing - Carrier Drive Plate	2	179	358	
Housing - Carrier Tumble Plate	2	157	314	
Wheel Flange	6	64	384	
Wheels	6	21.92	131.52	2717T41

Long Low-Profile Alloy Steel Socket Head Cap Screw	12	2.92	35.04	92220A206
Short Low-Profile Alloy Steel Socket Head Cap Screw	6	8.20/25	8.2	92220A205
Nylon-Insert Thin Hex Locknut	9	4.94/50	4.94	90101A230
High-Strength Steel Cap Screw - FLANGE	12	8.58/50	8.58	92620A579
Nylon-Insert Hex Locknut - FLANGE	24	3.80/20	7.6	97135A220
Retaining Ring - 0.5" Shaft		10.13/100	10.13	97633A200
Retaining Ring - 0.625" Shaft		12.45/100	12.45	97633A230
Standard Pull-Out Dowel Pin	18	1.58	28.44	97175A309
TOTAL			6944.44	

BIBLIOGRAPHY

- [1] J. Kuntz, "Congratulations to NASA Glenn and Cleveland Fire Department on a hot robotic item: editorial," *The Plain Dealer*, April 27, 2011. [Online]. Available: http://www.cleveland.com/opinion/index.ssf/2011/04/congratulations_to_nasa_glen_n.html. [Accessed April 12, 2012].
- [2] S. Böttcher, Principles of robot locomotion, Seminar ‘Human robot interaction.’
- [3] A. Seenii, B. Schafer, B. Rebele and N. Tolyarenko, "Robot Mobility Concepts for Extraterrestrial Surface," in *Aerospace Conference, 2008 IEEE*, Big Sky, MT.
- [4] Northrop Grumman, "Mobile Armed Dismount Support System," MADSS datasheet, 2013.
- [5] C. Behn, I. Zeidis and K. Zimmerman, "Wheeled Locomotion Systems -- Rolling," in *Mechanics of Terrestrial Locomotion With a Focus on Non-pedal Motion Systems*, New York, Springer, 2009, pp. 73-124.
- [6] Northrop Grumman, “Remotec Andros F6,” Andros F6 datasheet.
- [7] U. Saranli, M. Buehler and D. E. Koditschek, "RHex - A Simple and Highly Mobile Hexapod Robot," *International Journal of Robotics Research*, 2001.
- [8] Y.-S. Kim, G.-P. Jung, K. Haan, K.-J. Cho and C.-N. Chu, "Wheel Transformer: A Wheel-Leg Hybrid Robot with Passive Transformable Wheels," *IEEE Transactions on Robotics*, no. 99, pp. 1-12, 20 November 2014.
- [9] Biologically Inspired Robotics, “Whogs,” Case Western Reserve University. [Online]. Available: <http://biorobots.case.edu/projects/whegs/>. [Accessed April 25, 2012].
- [10] F. Cordes, T. M. Roehr and F. Kirchner, "RIMRES: A Modular Reconfigurable Heterogeneous Multi-Robot Exploration System," *International Symposium on*

Artificial Intelligence, Robotics and Automatoin in Space, 2012.

- [11] R. W. Forsyth and J. P. Forsyth, "Design and Development of the TerraStar Marginal-Terrain Amphibian," 1968.
- [12] "All-Terrain Hex-Limbed Extra-Terrestrial Explorer," NASA Jet Propulsion Laboratory, [Online]. Available: <http://athlete.jpl.nasa.gov/>. [Accessed 25 April 2012].
- [13] N. Carey, "Establishing Pedestrian Walking Speeds," Portland State University ITE Student Chapter, Portland, 2005.
- [14] D. Greenwood, Principles of Dynamics, 2 ed., Upper Saddle Ridge: Prentice Hall, Inc., 1988.
- [15] R. M. Murray, Z. Li and S. S. Sastry, A Mathematical Introductoin to Robotic Manipulation, Boca Raton: Taylor & Francis Group, LLC, 1994.
- [16] P. Davis, "Stair Safety: A Review of the Literature and Data Concerning Stair Climbing Geometry and Other Characteristics," NAHB Research Center, Upper Marlboro, 1992.
- [17] P. Dollan, B. Donnelley and K. Kanagasabapathy, "VEX Robotics Design System," Innovation First International, Inc., 2012. [Online]. Available: <http://curriculum.vexrobotics.com/>. [Accessed 12 September 2013].
- [18] D. W. Dudley, Gear Handbook: The Design, Manufacture, and Application of Gears, 1 ed., New York: Mc-Graw-Hill Book Company, 1962.
- [19] R. L. Mott, Machine Elements in Mechanical Design, New York: Macmillan Publishing Company, 1992.
- [20] R. C. Juvinall and K. M. Marshek, Fundamentals of Machine Component Design, 2 ed., John Wilen & Sons, Inc., 1991.
- [21] Anaheim Automation, Inc., "BLY34 Series - Brushless DC Motors," 2011. [Online]. Available: <http://www.anheimautomation.com/products/brushless/brushless-motor-item.php?sID=150&pt=i&tID=96&cID=22>. [Accessed 1 September 2014].
- [22] J. A. Collins, Mechanical Design of Machine Elements and Machines: A Failure

Prevention Perspective, New York: John Wiley & Sons, Inc., 2002.

- [23] G. A. David and M. B. Histand, Introduction to Mechatronics and Measurement Systems, 4 ed., New York: McGraw-Hill, 2007.
- [24] J. McLester and P. St. Pierre, Applied Biomechanics: Concepts and Connections, Belmont: Thomson Wadsworth, 2008.
- [25] "Engineering-abc.com," [Online]. Available: <http://www.tribology-abc.com/abc/cof.htm#rolweerstand>. [Accessed 12 October 2013].
- [26] J. L. Meriam and L. G. Kraige, Engineering Mechanics Volume 2: Dynamics, 6 ed., Hoboken: John Wiley & Sons, Inc., 2007.
- [27] "Air-Ride Wheel for Casters: 2717T41," McMaster-Carr, [Online]. Available: <http://www.mcmaster.com/#2717t41=u8gia4>. [Accessed 20 October 2013].
- [28] P. J. Blau, Friction Science and Technology: From Concepts to Applications, Danvers: CRC Press, 2009.
- [29] J. E. Shigley and L. D. Mitchell, Mechanical Engineering Design, 4 ed., New York: McGraw-Hill, Inc., 1983.
- [30] J. J. Coy, D. P. Townsend and E. V. Zaretsky, "Gearing," NASA Reference Publication 1152, Cleveland, 1985.
- [31] American Gear Manufacturers Association , "Fundamental Rating Factors and Calculation Methods for Involute Spur and Helical Gear Teeth," American Gear Manufacturers Association, 2004.
- [32] American Gear Manufacturers Association , "Geometry Factors for Determining the Pitting Resistance and Bending Strength of Spur, Helical and Herringbone Gear Teeth," American Gear Manufacturers Association, Alexandria, 1989.
- [33] AZO Materials, "AISI 8620 Alloy Steel (UNS G86200)," 2014. [Online]. Available: <http://www.azom.com/article.aspx?ArticleID=6754>. [Accessed 5 June 2014].
- [34] C. H. Logue and R. Trautschold, American Machinist Gear Book, Simplified Tables and Formulas for Designing, and Practical Points in Cutting All Commercial Types of Gears, 3 ed., New York: McGraw-Hill Book Co. Inc., 1922.

- [35] C. R. Thomas and V. S. Hillsman, "Simple Word Rules for the Determination of Gear Force Directions," in *1993 IEEE Frontiers in Education Conference*, 1993.
- [36] McMaster-Carr, "Air-Ride Wheel for Casters: Black, 6" x 2", 1/2" Axle, Ball Bearing, 200 lb Capacity," [Online]. Available: <http://www.mcmaster.com/#2717t41/=uhxdrt>. [Accessed 11 September 2014].
- [37] American National Standards Institute, "ANSI-ASME B17.1-1967: Keys and Keyseats," 2003.
- [38] "Bearings," McMaster-Carr, 8 November 2014. [Online]. Available: <http://www.mcmaster.com/#bearings/=ui81vr>.
- [39] McMaster-Carr, "Black-Finish Steel External Retaining Ring for 1/2" Shaft Diameter," [Online]. Available: <http://www.mcmaster.com/#97633a200/=uia2lc>. [Accessed 11 November 2014].
- [40] McMaster-Carr, "Standard Pull-Out Dowel Pin-Alloy Steel, 1/4" Diameter, 1/2" Length, 8-32 Thread," 8 November 2014. [Online]. Available: <http://www.mcmaster.com/#97175a309/=uial9x>.
- [41] H. A. Rothbart, Mechanical Design Handbook, New York: McGraw-Hill, 1996.
- [42] B. J. Jeans and D. Hong, "IMPASS: Intelligent Mobility Platform with Active Spoke System," *IEEE International Conference on Robotics and Automation*, pp. 1605-1606, 17 May 2009.
- [43] American Forest and Paper Association, "Beam Design Formulas With Shear and Moment Diagrams," American Wood Council, Washington, D.C., 2005.